

Synthesis and Characterization of Noble Metal Doped Structured Oxides for Water Gas Shift Reaction and CO Oxidation

Thesis Submitted to AcSIR for the Award of the Degree of
DOCTOR OF PHILOSOPHY
in Chemistry



By

Rajesh T

Registration Number: 10CC11J26022

Under the guidance of

Dr. R. Nandini Devi

**Catalysis and Inorganic Chemistry Division
CSIR- National Chemical Laboratory, Pune - 411008, India**

February 2015



हीरक जयन्ती वर्ष 2009-10

राष्ट्रीय रासायनिक प्रयोगशाला

(वैज्ञानिक तथा औद्योगिक अनुसंधान परिषद)

डॉ. होमी भाभा मार्ग, पुणे - 411 008. भारत

NATIONAL CHEMICAL LABORATORY

(Council of Scientific & Industrial Research)

Dr. Homi Bhabha Road, Pune - 411 008. India.


Certificate

This is to certify that the work incorporated in this Ph.D. thesis entitled Synthesis and Characterization of Noble Metal Doped Structured Oxides for Water Gas Shift Reaction and CO Oxidation submitted by Mr. Rajesh T to Academy of Scientific and Innovative Research (AcSIR) in fulfillment of the requirements for the award of the Degree of Doctor of Philosophy, embodies original research work under my supervision/guidance. I further certify that this work has not been submitted to any other University or Institution in part or full for the award of any degree or diploma. Research material obtained from other sources has been duly acknowledged in the thesis. Any text, illustration, table etc., used in the thesis from other sources, have been duly cited and acknowledged.


(Student)


(Supervisor)

Communication
Channels


NCL Level DID : 2590
NCL Board No. : +91-20-25902000
EPABX : +91-20-25893300
+91-20-25893400

FAX

Director's Office : +91-20-25902601
COA's Office : +91-20-25902660
COS&P's Office : +91-20-25902664

WEBSITE

www.ncl-india.org

DECLARATION BY RESEARCH SCHOLAR

I hereby declare that the work incorporated in this thesis entitled "**Synthesis and Characterization of Noble Metal Doped Structured Oxides for Water Gas Shift Reaction and CO Oxidation**" submitted by me for the degree of Doctor of Philosophy to the AcSIR is the record of the work I have carried out at the Catalysis and Inorganic Chemistry Division, CSIR-National Chemical Laboratory, Pune - 411 008 under the supervision of Dr. R. Nandini Devi is original and has not formed the basis of award of any degree or diploma. All the materials from other sources have been duly acknowledged in the thesis.

Date: 09-02-2015



Rajesh T
Catalysis and Inorganic Chemistry Division
CSIR-National Chemical Laboratory
Pune-411008

.....*Dedicated to*

my Parents

Acknowledgement

I would like to express my deepest gratitude to my supervisor Dr. R. Nandini Devi for her invaluable guidance, continuous encouragement, and unconditional support. I am grateful to her for introducing me to the fascinating field of solid state and structural chemistry. I am indebted to her for giving me liberty to carry out my research work independently throughout the course. Without her encouragement, constant inspiration and constructive criticism, I could not have finished my doctoral degree. Working with her was really a great pleasure and fetched me a lot of learning experience.

My heartfelt thanks to Dr. C. V. V. Satyanarayana for valuable discussions and advises. Also I acknowledge him for the various characterization and reactor facilities provided throughout the course of the programme. I am thankful to Dr. C. S. Gopinath for useful discussions, valuable advises and fruitful collaboration work. I would like to express my gratitude to Dr. A. K. Rajarajan (BARC, Mumbai), Anuj Upadhyay, Dr. Anil K. Sinha, and Dr. Sudip K. Deb (RRCAT, Indore) for collaborative work. I would like to thank Mr. P. S. R. Krishna and A. B. Shinde (BARC, Mumbai) for the neutron data collection and help in analysis and Dr. Thirunavukkarasu (IIT Madras, India), Dr. T. Shripathi (UGC-DAE CSR Indore) & Dr S. N. Jha (ARPES beamline, RRCAT, Indore) for XPS data. I am thankful to my Doctoral Advisory Committee (DAC) members Dr. Rahul Banerjee, Dr. Paresh L. Dhepe and Dr. C. V. V. Satyanarayana for continuously monitoring the progress of the research work and for scientific discussions. I sincerely acknowledge the help provided by, Dr. T. Raja, Dr. C. P. Vinod Dr. P. A. Joy, Dr. Kumar Vanka, and Dr. T. G. Ajith Kumar. I am also thankful to Dr. K. R. Patil for XPS, Dr. Naren, Anuj, Pandiraj, Sahithi for HRTEM and Ketan for SEM. I acknowledge Mr. P. K. Mane and Mr. S. S. Deo for technical support during my PhD.

It gives me great pleasure to thank my labmates Dr. Kala Raj, Dr. Atul, Dr. Anupam Samanta, Jijil, Leena, Soumya, Sumona, Santosh Khokarale, Dhruva Bhuyan, Sourik, Athira, , Shibin, Monojit, Satej and Pranav Ghore for their kind help and support, invaluable discussions which we shared and maintaining a lively environment in the laboratory during every walk of life in the laboratory to achieve this goal and also thank to trainee students, Remya, Hanna, Remith, Rajith, Ali, Surya, Prakrithi, Saranya, Anantha, Shivesh, Sandhya, Akhil and Fessy.

I would like to express my sincere thanks to Reji N. K. for all the help rendered for the catalysis and reactor set up. I am grateful to Ms. Violet Samuel for her help. I am thankful to my colleagues and friends, Eldho, Dr. Suresh, Alson, Venugopal, Dr. Vijaya Das, Dr. Rajeesh kumar, Sreekuttan, Arun Torris, Anumon, Roshna, Aany, Hilda, Priya, Harindranath, Anu, Rahul, Mufsir, Renny, Dr. Sadique, Dr. Shijo, Dr. Prasanna Kumara, Renjith, Eldhose, Jijo, Hareesh, Gireesh, Dr. Srinivasa Rao, Hanumanth, Richa Bobade, Dr. Narasimha Rao, Nishitha, Srikanth, Atul, Laxmi, Lalit, Jay, Pranjal, Amlan, Dr. Ramakanta Sahu, Deepa, Manoj, Anup Tathod, Presnjith, Sanil, Richa, Tanusree, Sagar, Sandeep, Aneesh, Shoy, Jitesh, Prithi, Dr. Edwin, Jino, Dr. Shivaranjini, Dr. Trupthi, Dr. Swathi, Atul, Vyshag, Sunil, Sreedhala, Ashok, Periyasami, Manikandan, Aswathi, Dr. Khaja, Dr. Vijay, Mangesh, Govind, Jaya, Bindhu, Lenin, Mohan, Ram Sunder, Manjunath, Sharath K, Kiran, Sarath, Prajitha, Dr. Nisha, Dhanya, Bihag, Jaya .C Jose, Nishamol, Unnikrishanan, Joby, Anjali, Dr. Bhogesh, Rashid, Dr. Prakash Chandra, Bausaheb Tawade, Tamboli Majid, Krishanu, Shyam and Innaih for their invaluable help and for spending wonderful time with them.

I would like to express my appreciation to my junior friends Rajeesh, Pranav, Sanoop, Kabeer, Robin, Thomas, Manu, Betsy, Sabareesh, Jeevan and Yadu, for spending wonderful time with them.

It gives me great pleasure to thank my parents and family members, for their love and unconditional support. Finally, my thanks are due to University Grants Commission, Government of India, for awarding the research fellowship, and to Dr. S. Sivaram, former Director and Dr. Sourav Pal, Director, CSIR-National Chemical Laboratory, to carry out my research work and extending all possible infrastructural facilities, and to allow me to submit this work in the form of a thesis for the award of Ph.D. degree. I would also like to acknowledge Department of Science and Technology, India for providing the timely financial support to participate in "CAPoC 9" conference in Belgium.

.....Rajesh

Table of Contents

Abstract	v
List of figures	ix
List of tables	xvii
Abbreviations	xviii

1. Introduction and Literature Survey

1.1.	Noble metal catalysis	1
1.2.	Sintering of nanoparticles and catalyst deactivation	4
1.3.	Important noble metal catalysed heterogeneous reactions	9
1.3.1.	Water gas shift (WGS) reaction	10
1.3.2.	CO oxidation	15
1.4.	Catalytic activity of ionic noble metal species in heterogeneous reactions	18
1.5.	Role of solid state compounds in heterogeneous catalysis	20
1.6	Scope and objective of thesis	26
	References	28

2. Synthesis, Characterisation and WGS Activity Studies of Pt and Y Doped BaCeO₃ Catalysts: Activity of Cationic Pt and Role of Oxygen Vacancies towards WGS Reaction

2A. Synthesis, Characterisation, WGS Activity and Reactor Shut down Studies of BaCe_{1-x}Pt_xO_{3-δ}; (x = 0.02, 0.04 and 0.06): Activity and Stability of Cationic Pt

2A.1.	Introduction	38
2A.2.	Experimental section	39
2A.2.1.	Synthesis of BaCe _{1-x} Pt _x O _{3-δ} (x = 0.02, 0.04 & 0.06)	39
2A.2.2.	Characterisation	39
2A.2.3.	Catalytic testing	41

2A.3.	Results and discussion	42
2A.3.1.	Synthesis and structural characterisation	42
2A.3.2.	Catalytic activity and structural correlation	51
2A.4.	Conclusions	62
	References	63

2B. Synthesis, Characterisation and WGS Activity Studies of $\text{BaCe}_{0.98-x}\text{Y}_x\text{Pt}_{0.02}\text{O}_{3-\delta}$; (x = 0.02, 0.04, 0.06, 0.10, 0.20, and 0.30): Role of Oxygen Vacancies on WGS Activity

2B.1.	Introduction	66
2B.2.	Experimental section	67
2B.2.1.	Synthesis of $\text{BaCe}_{0.98-x}\text{Y}_x\text{Pt}_{0.02}\text{O}_{3-\delta}$ (x = 0.02, 0.04, 0.06, 0.10, 0.20 & 0.30)	67
2B.2.2.	Characterisation	67
2B.2.3.	Catalytic set up	68
2B.3.	Results and discussion	69
2B.3.1.	Synthesis and structural characterisation	69
2B.3.2.	Catalytic activity testing	81
2B.4.	Conclusions	92
	References	93

3. Synthesis, Characterisation and WGS Activity Studies of $\text{LaB}_{1-x}\text{Pt}_x\text{O}_{3-\delta}$; (B = Mn, Fe, and Co): Activity and Stability of Cationic Pt

3.1.	Introduction	95
3.2.	Experimental section	96
3.2.1.	Synthesis	96
3.2.2.	Characterisation	97
3.2.3.	Catalytic testing	98
3.3.	Results and discussion	98

3.3.1.	Pt doping in LaMnO ₃ system	99
3.3.1.1.	Synthesis	99
3.3.1.2.	Structural characterisation	100
3.3.1.3.	Textural characterisation	103
3.3.1.4.	Surface characterisation	104
3.3.1.5.	Catalytic activity	105
3.3.1.6.	Surface and structural characterisation of spent catalysts	106
3.3.2.	Pt doping in LaFeO ₃ and LaCoO ₃ systems	109
3.3.2.1.	Structural characterisation	109
3.3.2.2.	Surface characterisation	116
3.3.2.3.	Catalytic activity and structural correlation	118
3.3.2.4.	Characterisation of spent catalysts	121
3.4.	Conclusions	123
	References	125

4. Synthesis, Characterisation, WGS and CO Oxidation Activity of Ag₂Cu₂O₃ and Ag₂Cu₂O₄: Catalytic Activity of Compounds with Low Coordinated Metal Centers

4.1.	Introduction	129
4.2	Experimental section	130
4.2.1.	Synthesis	130
4.2.2.	Characterisation	130
4.2.3.	Catalytic testing	131
4.3.	Results and discussion	131
4.3.1.	Structural characterisation and WGS activity studies	131
4.3.2.	CO oxidation activity studies	135
4.4.	Conclusions	136

References	137
------------	-----

5. Summary and Conclusions

5.1	Summary	139
-----	---------	-----

5.2	Conclusions	142
-----	-------------	-----

Publications/Symposia/Conference

Appendix

Abstract

Metal particles dispersed on inorganic oxide surfaces have been the mainstay of industrially important heterogeneous catalytic processes. However, agglomeration or sintering under reaction conditions often leads to deterioration of catalytic properties. This problem has been plaguing many catalytic processes, the water gas shift (WGS) reaction and CO oxidation being foremost among them. WGS reaction is an intermediate CO clean up step in fuel processing for generating hydrogen feed for fuel cells, whereby not only CO concentration is reduced but hydrogen content in the feed also is enriched by its reaction with water. Even a slight deactivation of the WGS catalyst may have dire consequences in downstream utilisation modules like fuel cells or Pt electrodes, which get poisoned by small fluctuations in CO concentration.

Pt and Au supported on CeO_2 are reported to be highly active for WGS reaction. However, severe sintering on stream and subsequent deactivation also is reported in these systems. Hence an alternative catalyst system that is resistant to agglomeration and sintering is highly desirable. Recently, seminal work by Li *et al.* concluded that partially ionic noble metal species are responsible for WGS activity in oxide supported Au and Pt catalysts. As an extension to this, the logic followed in this work is that noble metal cations stabilised by doping in stable lattice types like perovskites (ABO_3) can also be WGS active. Moreover, pathways of sintering encountered in conventional supported catalysts can be minimised in such systems by simply space-separating the active centers. BaCeO_3 based perovskites can be a potential candidate for this on account of its proton conducting properties and redox properties of cerium. Lanthanum perovskites with B site occupied by first row transition metal ions can also be considered as they can be synthesised at lower temperature ranges making overall textural properties ideal for catalysis and B can be a range of elements which will enable us to study their combined effects along with Pt on WGS.

For WGS reaction with supported noble metal catalysts, a mechanism involving oxygen vacancies in conjunction with CO adsorption on Pt nanoparticle surfaces has been

proposed. Though there is agreement between the researchers about the role of oxygen vacancies in the mechanism, reports establishing its participation unambiguously are not available. Perovskite structure accommodates a variety of substitutions often leading to the formation of oxygen vacancies and thus can be utilised to investigate the effect of oxygen vacancies on catalytic activity. Doped BaCeO_3 solid electrolytes make the ideal choice as they are well known protonic and oxide ion conductors because of oxide ion vacancies, caused by doping on the Ce^{4+} site.

Compounds with active sites in low coordination geometries can be envisaged to be conducive for catalysis since the unsaturated metal sites form ideal catalytic sites via coordination of reactant molecules. However, surprisingly, catalytic applications of these types of materials are rarely investigated.

The thesis will be presented in five chapters, a brief summary of which is given below.

Chapter 1 presents a general introduction to noble metal catalysis and catalyst deactivation due to sintering of nanoparticles. The chapter further reviews the available literature on some industrially important heterogeneous reactions like WGS reaction and CO oxidation where supported metal catalysts are important. Some of the reports of the catalytic activity of the ionic noble metal species are also presented here. In addition, a brief introduction to the solid state compounds such as perovskites that have attracted considerable interest in catalysis in the recent times are also discussed. Finally the scope and objective of the theses are stated.

Chapter 2 is divided into two parts.

Chapter 2A describes the stabilisation of cationic Platinum in the lattice sites of BaCeO_3 perovskite. It presents the synthesis of $\text{BaCe}_{1-x}\text{Pt}_x\text{O}_{3-\delta}$ and its structural evaluation by various characterisation methods and in situ studies, in relation to the WGS reaction. This catalyst system is found to efficiently isolate cationic Pt species that are stable under reducing conditions even at high temperatures. Cationic Pt stabilised in the BaCeO_3 lattice is found to be active for WGS reaction. This catalyst system is found to be stable and

withstand various shut down conditions employed such as N₂, reformat feed and reformat feed along with steam.

Chapter 2B presents an attempt to induce more oxygen vacancies in the BaCe_{0.98}Pt_{0.02}O_{3-δ} catalyst system by yttrium doping and to examine the role of oxygen vacancies in the mechanism of WGS reaction. The progressive doping of yttrium in the B-site of BaCe_{0.98}Pt_{0.02}O_{3-δ} system has led to the systematic creation of oxygen vacancies. The materials are characterised using various techniques and their WGS activities are compared. BaCe_{0.92}Pt_{0.02}Y_{0.06}O_{3-δ} having the least distorted Ce/Y/PtO₆ octahedra, exhibited maximum WGS activity in the series indicating dependence on not the concentration of oxygen vacancies but on their crystallographic characteristics. Extensive in-situ powder XRD studies under reducing, oxidising and conditions similar to WGS reaction indicated that vacancy sites are involved in the mechanism of WGS reaction.

Chapter 3 describes in detail the synthesis, characterisation and WGS activity of LaB_{1-x}Pt_xO_{3-δ} system where B is Mn, Fe, and Co. X-ray based characterisation techniques indicated cationic Pt stabilisation in the lattice sites of Fe and Co perovskites. In the case of Mn, highly sintered metallic Pt particles are observed. Pt/LaMnO₃ system exhibited very poor WGS activity. WGS activities of LaB_{0.96}Pt_{0.04}O_{3-δ} where B = Fe and Co, are found to be very high, but a small amount of methanation is observed in the case of Co perovskites. It is also observed that methanation could be decreased and WGS enhanced when perovskites are used, in comparison with mixed oxides. Ionic Pt species in tandem with oxygen vacancies capable of acting as water adsorption sites might be enhancing their WGS activity suppressing CO or CO₂ hydrogenation.

Chapter 4 presents the synthesis of low coordination compounds, Ag₂Cu₂O₃ and Ag₂Cu₂O₄ and their catalytic activity towards two different important reactions; WGS reaction and CO oxidation, to study the activity of coordinatively unsaturated active metals. When Ag₂Cu₂O₃ is used as catalyst for WGS reaction, very high initial CO oxidation activity without any hydrogen production is observed with simultaneous decomposition of the catalyst. However when used for CO oxidation, the structure is retained with the appearance of a small percentage of metallic Ag. Interestingly, the oxygen rich Ag₂Cu₂O₄

catalyst did not show any activity in CO oxidation under WGS conditions and decomposed to metallic Ag and Cu. The compound shows CO oxidation activity under oxidising conditions, but decomposes to Ag and CuO. This indicates that lattice oxygen takes part in oxidising CO in the case of $\text{Ag}_2\text{Cu}_2\text{O}_3$, consequently destroying the structure whereas, this does not occur in case of $\text{Ag}_2\text{Cu}_2\text{O}_4$.

Chapter 5: Summary and conclusion

This chapter summarises the results and conclusions based on the work reported in the thesis. Altogether, this thesis reports the stabilisation of cationic noble metal species in stable lattices against sintering and establishes its catalytic activity towards WGS reaction. In addition it also demonstrates that oxygen vacancies are involved in the mechanism of WGS reaction and the catalytic activity depends not on the concentration of oxygen vacancies but on their crystallographic characteristics.

List of Figures

Figure 1.1.	Noble metal nanoparticles dispersed on oxide supports, (A) Au on TiO ₂ , (B) Pt on ZrO ₂ , and (C) Pd on γ -Al ₂ O ₃ . Adapted from ref. [29-31]	4
Figure 1.2.	Low voltage SEM image of a Pt/alumina model nanocatalyst shows formation of large Pt islands due to the sintering of Pt nanoparticles during the high temperature reduction process on certain crystallographic faces of the polycrystalline alumina support. Inset shows unchanged particles. Adapted from ref. [61]	5
Figure 1.3.	Schematic representation of the various stages involved in the formation and growth of particles. Adapted from ref. [53]	6
Figure 1.4.	CO exit concentration of 2% Pt/CeO ₂ -ZrO ₂ at 228 °C for WGS reaction, Reformate composition 5.98 % CO, 7.4 % CO ₂ , 31.82 % H ₂ , 28.86 % N ₂ & 26 % H ₂ O. Adapted from ref. [98]	13
Figure 1.5.	Possible reaction schemes for the CO oxidation reaction over supported Au catalysts. Adapted from ref. [135]	17
Figure 1.6.	Schematic representation showing the leaching of metallic Au or Pt from the surface of Au or Pt supported on Ce _{1-x} La _x O ₂ . Adapted from ref. [151]	19
Figure 1.7.	Structure of a cubic CaTiO ₃ perovskite	22
Figure 1.8.	Structure of (A) Ag ₂ Cu ₂ O ₃ and (B) Ag ₂ Cu ₂ O ₄	26
Figure 2A.1.	Flow diagram of the catalytic reactor setup	42
Figure 2A.2.	(A) PXRD patterns of (a) BaCeO ₃ , (b) 0.8 wt% Pt impregnated BaCeO ₃ , and BaCe _{1-x} Pt _x O _{3-δ} with (c) x = 0.02, (d) x = 0.04, and (e) x = 0.06, (B) 2 θ region where Pt(111) reflection appear, and (C) PXRD patterns of (a) BaCe _{0.98} Pt _{0.02} O _{3-δ} , (b) after dil. HNO ₃ wash, and (c) after heating at 400 °C for 1 h	43

Figure 2A.3.	(A) PXRD patterns of $\text{BaCe}_{1-x}\text{Pt}_x\text{O}_{3-\delta}$ (a) $x = 0.08$ and (b) $x = 0.10$, and (B) 2θ region where Pt(111) reflection appear	44
Figure 2A.4.	Rietveld refinement of PXRD data for $\text{BaCe}_{1-x}\text{Pt}_x\text{O}_{3-\delta}$ with (a) $x = 0.02$, (b) $x = 0.04$ and (c) $x = 0.06$. Red line represents experimental data, green line is the Rietveld fit and pink line represents difference plot. Vertical lines at the top of the figure are the expected positions for the impurity phases BaCO_3 and CeO_2	46
Figure 2A.5.	(A) Rietveld refinement of constant wave neutron diffraction data for $\text{BaCe}_{1-x}\text{Pt}_x\text{O}_{3-\delta}$ with (a) $x = 0.02$, (b) $x = 0.04$ and (c) $x = 0.06$. Red line represents experimental data, black line is the Rietveld fit and the blue line is for the difference plot. Vertical lines (brown and green) at the top represent the expected positions for the impurity phases BaCO_3 and CeO_2 , (B) crystal structure of $\text{BaCe}_{1-x}\text{Pt}_x\text{O}_{3-\delta}$ with $x = 0.02$ and (C) cell volume and octahedron volumes of $\text{BaCe}_{1-x}\text{Pt}_x\text{O}_{3-\delta}$ as a function of substitution x	49
Figure 2A.6.	(A) & (D) HRTEM images, (B) & (E) lattice planes and (C) electron diffraction pattern of 2 mol% Pt doped BaCeO_3	50
Figure 2A.7.	CO conversion measured over $\text{BaCe}_{1-x}\text{Pt}_x\text{O}_{3-\delta}$ with A) $x = 0.02$, B) $x = 0.04$ and C) $x = 0.06$ under WGS reaction conditions. Reformate composition: 39.8 % H_2 , 34.9 % N_2 , 10.2 % CO and 15.2 % CO_2 , steam to CO ratio 4.5, GHSV of 5000 h^{-1}	51
Figure 2A.8.	(A) PXRD patterns of 2 mol% Pt doped BaCeO_3 a) before and b) after WGS reaction, (B) 2θ region where Pt(111) reflections appear.	52
Figure 2A.9.	In situ variable temperature PXRD patterns of $\text{BaCe}_{1-x}\text{Pt}_x\text{O}_{3-\delta}$ with (A) $x = 0.02$, (B) $x = 0.04$, (C) $x = 0.06$, (D) $x = 0.08$, and (E) $x = 0.10$ under 10 % H_2/N_2 ; (a) RT, (b) 100°C , (c) 200°C , (d) 300°C , (e) 400°C , (f) 500°C , (g) 600°C , (h) RT; (F) 2θ region where Pt(111) reflection appear (a) $x = 0.02$, (b) $x = 0.04$, (c) $x = 0.06$, (d) $x =$	53

	0.08, and (e) $x = 0.10$. Expected peak position for Pt (111) is indicated as dashed line	
Figure 2A.10.	(A) Pt-4f XP spectra of 2 mol% Pt doped BaCeO ₃ a) before, b) after 1 st cycle and c) after 2 nd cycle of WGS reaction, (B) Ce-3d XP spectra of 2 mol% Pt doped BaCeO ₃ a) before, b) after 1 st cycle and c) after 2 nd cycle of WGS reaction	54
Figure 2A.11.	WGS activities of BaCe _{0.98} Pt _{0.02} O _{3-δ} obtained before and after shut down under (A) nitrogen, (B) reformat feed and (C) reformat feed with steam up to 80 °C and keeping for 1 h	57
Figure 2A.12.	PXRD patterns of BaCe _{0.98} Pt _{0.02} O _{3-δ} (a) before and after reactor shut down under (b) nitrogen, (c) reformat feed and (d) reformat feed with steam up to 80 °C and keeping for 1 h	58
Figure 2A.13.	In situ PXRD patterns of BaCe _{0.98} Pt _{0.02} O _{3-δ} under reformat mixture saturated with water vapour up to 400 °C and then reactor shut down under (A) nitrogen, (B) reformat feed and (C) reformat feed saturated with water vapour up to 80 °C and keeping for 1 h. (a) RT, (b) 100 °C, (c) 200 °C, (d) 300 °C, (e) 350 °C, (f) 400 °C and (g) RT. (D) 2 θ region where reflections corresponding to Pt(111) appear, taken with long duration per step after (a) condition I, (b) condition II, and (c) condition III	59
Figure 2A.14.	Pt-4f XP spectra of BaCe _{0.98} Pt _{0.02} O _{3-δ} (a) before and after reactor shut down under (b) nitrogen, (c) reformat feed and (d) reformat feed with steam up to 80 °C and keeping for 1 h; Black: observed, red: fitted, blue; Pt(II)	60
Figure 2A.15.	Ce-3d XP spectra of BaCe _{0.98} Pt _{0.02} O _{3-δ} . (a) before and after reactor shut down under (b) nitrogen, (c) reformat feed and (d) reformat feed with steam up to 80 °C and keeping for 1 h. Black: observed, red: fitted, brown: Ce(IV) and pink: Ce(III)	61

Figure 2B.1.	Crystal structure of $\text{BaCe}_{0.98-x}\text{Y}_x\text{Pt}_{0.02}\text{O}_{3-\delta}$	70
Figure 2B.2.	(A) PXRD patterns of (a) BaCeO_3 , $\text{BaCe}_{0.98-x}\text{Y}_x\text{Pt}_{0.02}\text{O}_{3-\delta}$ with (b) $x = 0$, (c) $x = 0.02$, (d) $x = 0.04$, (e) $x = 0.06$, (f) $x = 0.10$, (g) $x = 0.20$ and (h) $x = 0.30$; (B) 2θ region showing peaks corresponding to (202) and (040) planes showing the orthorhombic to monoclinic transition as Y concentration increases	70
Figure 2B.3.	Pt-4f XP spectra of $\text{BaCe}_{0.98-x}\text{Y}_x\text{Pt}_{0.02}\text{O}_{3-\delta}$ with (a) $x = 0.06$, (b) $x = 0.10$ and (c) $x = 0.20$	72
Figure 2B.4.	Rietveld profile fits for the PXRD patterns of $\text{BaCe}_{0.98-x}\text{Y}_x\text{Pt}_{0.02}\text{O}_{3-\delta}$ with (a) $x = 0.02$, (b) $x = 0.04$, (c) $x = 0.06$, (d) $x = 0.10$, (e) $x = 0.20$ and (f) $x = 0.30$. Red line represents experimental data, green line is the Rietveld fit and pink line represents difference plot. Vertical lines at the top of the figure are the expected positions for the impurity phases BaCO_3 and CeO_2	73
Figure 2B.5.	(A) Pseudo-cubic cell volume, BO6 octahedron volume and (B) Pseudo-cubic cell parameters $\blacksquare = a$, $\bullet = b$, and $\blacktriangle = c$ of $\text{BaCe}_{0.98-x}\text{Y}_x\text{Pt}_{0.02}\text{O}_{3-\delta}$ as a function of substitution x as obtained from Rietveld refinement of PXRD data. BO6 octahedron volume was calculated considering total volume of four component tetrahedra	76
Figure 2B.6a.	(A, B, & D) HRTEM images and (C, E & F) lattice fringes of $\text{BaCe}_{0.92}\text{Y}_{0.06}\text{Pt}_{0.02}\text{O}_{3-\delta}$	80
Figure 2B.6b.	(G, H, & I) HRTEM images and (J, K & L) lattice fringes of $\text{BaCe}_{0.78}\text{Y}_{0.20}\text{Pt}_{0.02}\text{O}_{3-\delta}$.	80
Figure 2B.7.	Specific activities of $\text{BaCe}_{0.98-x}\text{Y}_x\text{Pt}_{0.02}\text{O}_{3-\delta}$ ($x=0$ to 0.3) under WGS conditions. Reformate composition: 40.3% H_2 , 35.1% N_2 , 10.1% CO and 14.5% CO_2 with a steam to CO ratio of 4.5 and GHSV 5000 h^{-1} .	83
Figure 2B.8.	Thermogravimetric profile under air for $\text{BaCe}_{0.98-x}\text{Y}_x\text{Pt}_{0.02}\text{O}_{3-\delta}$ ($x=0$)	83

	to 0.3)	
Figure 2B.9.	(A) PXRD patterns of $\text{BaCe}_{0.98-x}\text{Y}_x\text{Pt}_{0.02}\text{O}_{3-\delta}$, before (a) $x = 0.02$, (b) $x = 0.04$, (c) $x = 0.06$, (d) $x = 0.10$, (e) $x = 0.20$ and (f) $x = 0.30$ and after (a') $x = 0.02$, (b') $x = 0.04$, (c') $x = 0.06$, (d') $x = 0.10$, (e') $x = 0.20$ and (f') $x = 0.30$ WGS reaction. (B) 2θ region corresponding to [202] and [040] planes of $\text{BaCe}_{0.98-x}\text{Y}_x\text{Pt}_{0.02}\text{O}_{3-\delta}$ before e) $x = 0.2$, f) $x = 0.3$ and after e') $x = 0.2$, f') $x = 0.3$ WGS reaction. Dotted line refers to the [202] peak.	85
Figure 2B.10.	In situ high temperature PXRD patterns of $\text{BaCe}_{0.98-x}\text{Y}_x\text{Pt}_{0.02}\text{O}_{3-\delta}$ with (A) $x = 0.02$, (B) $x = 0.04$, (C) $x = 0.06$, (D) $x = 0.10$, (E) $x = 0.20$ and (F) $x = 0.30$; (a) RT, (b) 150 °C, (c) 300 °C, (d) 450 °C, (e) 600 °C, (f) 750 °C, (g) 900 °C, (h) RT under 5% H_2/Ar ; (G) 2θ region where peak for metallic Pt(111) appear for $\text{BaCe}_{0.98-x}\text{Y}_x\text{Pt}_{0.02}\text{O}_{3-\delta}$ with (a) $x = 0.02$, (b) $x = 0.04$, (c) $x = 0.06$, (d) $x = 0.10$, (e) $x = 0.20$ and (f) $x = 0.30$ taken at 900 °C with slow scan speed	86
Figure 2B.11.	In situ high temperature powder XRD patterns of $\text{BaCe}_{0.98-x}\text{Y}_x\text{Pt}_{0.02}\text{O}_{3-\delta}$ with (A) $x = 0.02$, (B) $x = 0.04$, (C) $x = 0.06$, (D) $x = 0.10$, (E) $x = 0.20$ and (F) $x = 0.30$; (a) RT, (b) 150 °C, (c) 300 °C, (d) 450 °C, (e) 600 °C, and (f) 750 °C under 10% O_2/He	87
Figure 2B.12.	Cell volume of $\text{BaCe}_{0.98-x}\text{Y}_x\text{Pt}_{0.02}\text{O}_{3-\delta}$ under A) 5 % H_2/Ar and B) 10 % O_2/He with ■: $x = 0.02$, ●: $x = 0.04$, ▲: $x = 0.06$, ▼: $x = 0.10$, ◀: $x = 0.20$ and ▶: $x = 0.30$	88
Figure 2B.13.	In situ PXRD patterns of $\text{BaCe}_{0.98-x}\text{Y}_x\text{Pt}_{0.02}\text{O}_{3-\delta}$ with (A) $x = 0.06$ and (B) $x = 0.20$, (C) 2θ region showing monoclinic-orthorhombic transition for $x=0.20$ under reformat gas mixture of 40.3% H_2 , 35.1% N_2 , 10.1% CO and 14.5% CO_2 saturated with water vapour; (D) In situ PXRD patterns of $\text{BaCe}_{0.78}\text{Y}_{0.20}\text{Pt}_{0.02}\text{O}_{3-\delta}$ and (E) 2θ region showing monoclinic-orthorhombic transition for $x=0.20$	90

	under helium saturated with water vapour; (a) RT, (b) 100 °C, (c) 200 °C, (d) 300 °C, (e) 400 °C, and (f) RT	
Figure 2B.14.	Cell volume of $\text{BaCe}_{0.98-x}\text{Y}_x\text{Pt}_{0.02}\text{O}_{3-\delta}$ ■: $x = 0.06$ and ●: $x = 0.20$ under reformate gas mixture of 40.3% H_2 , 35.1% N_2 , 10.1% CO and 14.5% CO_2 saturated with water vapour	91
Figure 3.1.	(A)PXR patterns of $\text{LaB}_{1-x}\text{Pt}_x\text{O}_{3-\delta}$ (B = Fe, Co and Mn). For Fe (a) $x = 0.02$, (b) $x = 0.04$, (c) $x = 0.06$; for Co (d) $x = 0.02$, (e) $x = 0.04$ and for Mn (f) $x = 0.02$ and (g) $x = 0.04$. (B) 2θ region where Pt(111) reflection appear	98
Figure 3.2.	(A) PXR patterns of (a) LaMnO_3 , and 4 mol% Pt doped LaMnO_3 calcined at (b) 600 °C, (c) 700 °C and (d) 900 °C; (B) 2θ region where Pt(111) reflections appear	100
Figure 3.3.	Rietveld refinement of PXR patterns of 4 mol% Pt doped LaMnO_3 synthesised at (A) 600 °C, (B) 700 °C and (C) 900 °C	102
Figure 3.4.	(A) HRTEM images of MP600; (B) LaMnO_3 lattice showing (110) plane (C, D) amorphous structure, (E-G) PtO_2	104
Figure 3.5.	(A) Pt 4f and (B) Mn 2p XP spectra of MP600. Black: observed, red: fitted, green; Pt(IV), Brown: Mn(III), blue: Mn(IV) and pink: satellite peaks	105
Figure 3.6.	CO conversion measured over Pt doped LaMnO_3 calcined at ■: 600 °C, ●: 700 °C and ▲: 900 °C under WGS conditions. Reformate composition 40.3 % H_2 , 35.1 % N_2 , 10.1 % CO and 14.5 % CO_2 ; steam to CO ratio 4.5 and GHSV 5000 h^{-1} . Total amount of Pt is considered for calculating the conversions	106
Figure 3.7.	(A) Pt 4f and (B) Mn 2p XP spectra of MP600 after WGS reaction; Black: observed, red: fitted, violet: Pt(0), orange: Pt(II), brown: Mn(III), blue: Mn(IV) and pink: satellite peaks	107

Figure 3.8.	(A) PXRD pattern of MP600 (a) before and (b) after WGS reaction, and (B) 2θ region where Pt(111) reflection appear	108
Figure 3.9.	(A, B) HRTEM images of MP600 after WGS reaction showing lattices of (C) PtO (D) LaMnO ₃ showing (020) planes, (E) metallic Pt and (F) PtO ₂	109
Figure 3.10.	Pt L3 XANES spectra of (a) LaFe _{0.94} Pt _{0.06} O _{3-δ} and (b) LaMn _{0.96} Pt _{0.04} O ₃ . The spectra are normalised by the incident intensity to a step edge of unity	111
Figure 3.11a.	Rietveld refinement of the synchrotron XRD pattern of LaCo _{1-x} Pt _x O _{3-δ} with (A) x = 0.02, and (B) x = 0.04	112
Figure 3.11b.	Rietveld refinement of the synchrotron XRD pattern of LaFe _{1-x} Pt _x O _{3-δ} with (A) x = 0.02, (B) x = 0.04 and (C) x = 0.06	113
Figure 3.12.	Cell volume and octahedron volume plots of LaB _{1-x} Pt _x O _{3-δ} ; (A) B = Fe and (B) B = Co as a function of substitution x as obtained from Rietveld refinement of synchrotron XRD data.	115
Figure 3.13.	HRTEM images of LaB _{0.96} Pt _{0.04} O _{3-δ} , (A) B= Fe and (B) B = Co	116
Figure 3.14.	(A) Pt-4f and (B) Co-2p XP spectra of LaCo _{0.96} Pt _{0.04} O _{3-δ} and (C) Pt-4f and (D) Fe-2p XP spectra of LaFe _{0.96} Pt _{0.04} O _{3-δ}	117
Figure 3.15.	CO conversion measured over ■:LaFe _{0.96} Pt _{0.04} O _{3-δ} , ●: 3 wt% Pt impregnated LaFeO ₃ , and ▲: 3 wt% Pt impregnated La ₂ O ₃ -Fe ₂ O ₃ catalysts under WGS conditions. Reformate composition of 37.9 % H ₂ , 13.5 % CO, 19.6 % CO ₂ and balance N ₂ with a steam to CO ratio of 4.5 and GHSV 5000 h ⁻¹	119
Figure 3.16.	(A) CO conversion measured over ■: LaCo _{0.96} Pt _{0.04} O _{3-δ} , ●: 3 wt% Pt impregnated LaCoO ₃ , and ▲: 3 wt% Pt impregnated La ₂ O ₃ -Co ₃ O ₄ catalysts under WGS conditions. Reformate composition of 37.9 %	120

	H ₂ , 13.5 % CO, 19.6 % CO ₂ and balance N ₂ with a steam to CO ratio of 4.5 and GHSV 5000 h ⁻¹ . (B) Methane formation observed with the Co catalysts under the same conditions described above	
Figure 3.17.	CO conversion measured over ■: LaFeO ₃ and ●:LaCoO ₃ catalysts under WGS conditions. Reformate composition of 37.9 % H ₂ , 13.5 % CO, 19.6 % CO ₂ and balance N ₂ with a steam to CO ratio of 4.5 and GHSV 5000 h ⁻¹	121
Figure 3.18.	PXRD patterns of LaFe _{0.96} Pt _{0.04} O _{3-δ} (a) before and (b) after WGS reaction and LaCo _{0.96} Pt _{0.04} O _{3-δ} (c) before and (d) after WGS reaction	122
Figure 3.19.	(A) Pt-4f and (B) Co-2p XP spectra of LaCo _{0.96} Pt _{0.04} O _{3-δ} and (C) Pt-4f and (D) Fe-2p XP spectra of LaFe _{0.96} Pt _{0.04} O _{3-δ} after WGS reaction	123
Figure 4.1.	PXRD patterns of (a) Ag ₂ Cu ₂ O ₃ and (b) Ag ₂ Cu ₂ O ₄	131
Figure 4.2.	PXRD patterns of Ag ₂ Cu ₂ O ₃ (a) before, (b) after WGS reaction, after subjecting to (c) steam with N ₂ and (d) reformate mixture alone; *: Ag, ^: Cu	132
Figure 4.3.	In situ high temperature PXRD patterns of Ag ₂ Cu ₂ O ₃ (a) RT, (b) 50 °C, (c) 100 °C, (d) 150 °C, (e) 200 °C and (f) RT, under 10% H ₂ /N ₂ ; *: Ag, ^: Cu	133
Figure 4.4.	PXRD patterns of Ag ₂ Cu ₂ O ₄ (a) before and (b) after WGS reaction; *: Ag, ^: Cu	134
Figure 4.5.	CO conversion measured over ■: Ag ₂ Cu ₂ O ₃ and ●: Ag ₂ Cu ₂ O ₄ . GHSV: 20000 h ⁻¹ ; CO: O ₂ = 1: 3	135
Figure 4.6.	PXRD patterns of (a) Ag ₂ Cu ₂ O ₃ and (c) Ag ₂ Cu ₂ O ₄ before and (b) Ag ₂ Cu ₂ O ₃ and (d) Ag ₂ Cu ₂ O ₄ after CO oxidation. #: CuO and *: Ag.	136

List of Tables

Table 1.1.	Tmelting, T _{Tamman} and T _{Huttig} values (in K) of some metals and their compounds. Adapted from ref [53]	8
Table 2A.1.	Crystal structures of BaCe _{1-x} Pt _x O _{3-δ} as obtained from Rietveld refinement of PXRD data	47
Table 2A.2.	Crystal structures of BaCe _{1-x} Pt _x O _{3-δ} as obtained from Rietveld refinement of neutron diffraction data	48
Table 2B.1.	Concentrations of Pt and Y in BaCe _{0.98-x} Y _x Pt _{0.02} O _{3-δ} obtained from ICP-AES analysis	69
Table 2B.2.	Crystal structures of BaCe _{0.98-x} Y _x Pt _{0.02} O _{3-δ} as obtained from Rietveld refinement of PXRD data	74
Table 2B.3.	Bond lengths and bond angles for BaCe _{0.98-x} Y _x Pt _{0.02} O _{3-δ} as obtained from the Rietveld refinement of PXRD data	77
Table 2B.4a.	O-Ba bond lengths of BaCe _{0.98-x} Y _x Pt _{0.02} O _{3-δ} ; x ≤ 0.1 obtained from Rietveld refinement of PXRD patterns	78
Table 2B.4b.	O-Ba bond lengths of BaCe _{0.98-x} Y _x Pt _{0.02} O _{3-δ} ; x ≥ 0.1 obtained from Rietveld refinement of PXRD patterns	79
Table 2B.5.	Surface area obtained from N ₂ adsorption	81
Table 3.1.	Pt concentrations of 4 mol% Pt doped LaMnO ₃ calcined at different temperatures, obtained from ICP-AES analysis	100
Table 3.2.	Crystal structures of Pt doped and impregnated LaMnO ₃ as obtained from Rietveld refinement of PXRD data	103
Table 3.3.	Pt concentrations determined using ICP-AES technique	110
Table 3.4a.	Crystal structures of LaCo _{1-x} Pt _x O _{3-δ} as obtained from Rietveld refinement of synchrotron XRD data	114
Table 3.4b.	Crystal structures of LaFe _{1-x} Pt _x O _{3-δ} as obtained from Rietveld refinement of synchrotron XRD data	114
Table 3.5.	Surface area analysis of LaB _{0.96} Pt _{0.04} O _{3-δ} , (B = Fe and Co)	116

List of Abbreviations

ADXRD	Angle Dispersive X-Ray Diffraction
BET	Braunauer-Emmett-Teller
DFT	Density Functional Theory
GC	Gas Chromatography
GHSV	Gas Hour Space Velocity
HRTEM	High Resolution Transmission Electron Microscopy
HTS	High Temperature Shift
ICP-AES	Inductively Coupled Plasma-Atomic Emission Spectroscopy
JCPDS	Joint Committee on Powder Diffraction Standards
LTS	Low Temperature Shift
MIEC	Mixed Ionic And Electronic Conduction
PEM	Polymer Electrolyte Membrane
PXRD	Powder X-ray Diffraction
SEM	Scanning Electron Microscopy
SOFC	Solid Oxide Fuel Cells
SSITKA-	Steady-State Isotopic Transient Kinetic Analysis - Diffuse Reflectance
DRIFTS	Infrared Fourier Transform Spectroscopy
SMSI	Strong Metal-Support Interactions
SXRD	Synchrotron X-ray Diffraction
TEM	Transmission Electron Microscopy
TPD	Temperature-Programmed Desorption
TPO	Temperature-Programmed Oxidation
TPR	Temperature-Programmed Reduction
TOF-SIMS	Time-of-Flight Secondary Ion Mass Spectroscopy
TWC	Three-Way Catalysts
UHV	Ultra High Vacuum
WGS	Water Gas Shift
XANES	X-Ray Absorption Near Edge Spectroscopy
XPS	X-Ray Photoelectron Spectroscopy

Chapter 1

Introduction and Literature Survey

1.1. Noble metal catalysis

Heterogeneous catalytic reactions have paramount importance in the production of useful chemicals, synthesis of fine compounds and environmental cleanup, accounting for the production of more than 80 % of all the chemical products [1-2]. Historically, catalysts involving oxides have been used primarily for gas phase reactions in the petroleum and petrochemical industries [3]. Later, these are found to be effective in promoting a number of synthetically useful reactions. Nowadays, metal oxides represent one of the most important and widely employed categories of solid catalysts, either as active phases or supports [4-5]. Metal oxides are utilized for their acid-base and redox properties. Oxide catalysts are either electrical insulators with stoichiometric M:O ratios where cationic material has a single valence (eg., MgO, Al₂O₃ and SiO₂ and the more complex zeolites) or semiconductors in which the metallic species is relatively easily cycled between two valence states (eg., different positive oxidation states as in Fe₂O₃, CeO₂, TiO₂, CuO or NiO, or the interconversion between the positive ion and neutral metal such as in ZnO). The former materials act as solid acids or bases while the latter are most commonly used in oxidations. Simple oxide catalysts are employed either in the bulk state or supported on an inert oxide material. Among these metal oxide catalysts, those of transition metals are important due to their low cost of production, easy regeneration and selective action [6]. The catalytic activity can be attributed to the presence of partially filled d-orbitals of the metal ion and to the effect of the oxide ligand field on these orbitals. Of the oxides of rare-earth elements, CeO₂ has attracted considerable attention in recent years in industrial catalysis [7-9].

The current industrial heterogeneous catalysts usually consist of metals and amorphous or crystalline oxide phases [10-11]. These can be conveniently classified into main components, promoters and supports. Main components participate directly in the catalytic transformation of molecules and promoters are used to modify and improve the performance of main components. The high surface area supports, on the surface of which main components and promoters are spread are said to perform several functions such as it (1) increases the dispersion of catalytic metal phase to ensure maximum utilization, (2) enhances the thermal stability of the active component

toward agglomeration by binding them to the surface, and (3) occasionally promotes the catalytic properties of the active phase. In some cases, the supports directly and chemically take part in catalysis. In addition, high catalyst performance often requires chemical interactions between the active component and the support (such as strong metal support interaction (SMSI) properties) [12-13]. Mass and heat transfer also depends on geometrical structure of supports.

Mixed metal oxides consisting combinations of two or more metallic ions in varying proportions defined by a strict stoichiometry, are considered as important materials for catalysis [14]. These have been extensively used as catalysts and catalyst supports for a wide variety of reactions. It is often established that catalysts with active components dispersed on mixed metal oxides often exhibit superior activity than those supported on single oxides [15, 16]. The mixed oxide formation helps to alter the acid-base and redox properties as well as to increase the thermal, chemical, and mechanical stability. For eg., $\text{TiO}_2\text{-ZrO}_2$ mixed oxides make use of the properties of both TiO_2 (which is catalytically active and act as a support) and ZrO_2 (acid-base properties) [17]. In addition, the strong interaction between them may result in the generation of new catalytic sites and thus extend their application.

Even though catalysis by the above mentioned oxides and mixed oxides has several advantages like easy removal of catalyst materials, possible use of high temperatures etc. compared to homogeneous catalysis, it suffered lack of selectivity for a long period of time. In addition, the mechanistic aspects are very difficult to understand. But the use of transition metal nanoparticles as catalysts changed the scenario as the reactions involve metal surface activation and catalysis at the nanoscale bring selectivity and efficiency [18]. The sizes of the nanoparticles vary from one nanometer to several tens or hundreds of nanometers, but various reports suggest that the most active in catalysis are only 1-10 nm in size, i.e. they contain a few tens to a few hundred atoms only [19-21]. In many common solids with particle sizes on the micrometer length scale or larger, the number of atoms in the external surface is negligible compared to the number of internal atoms. Thus, the particle exhibits the properties of the bulk material and the physical and chemical properties are not

affected by the variations in the particle size in this size range. But when the particle size is reduced sufficient enough to result in a significant ratio between the number of atoms on the external surface to that within the bulk, then, the properties of the material may vary as a function of the dimensions of the particles. Although these effects are expected to arise below particle sizes of hundreds of nanometers, they will be significant only at the size of a few nanometers. The variation in the properties arises since a significant fraction of the total number of atoms is on the surface and hence coordinatively undersaturated, making them behave differently when compared to those in the interior of the particle in these size range. Atoms in the external surface have the ability to bind with adsorbates due to the presence of unsaturated coordination. This field has attracted a considerable amount of attention recently, as catalysts involving them are selective, efficient, and recyclable, meeting the modern requirements for green catalysts [22-23].

Transition group metals including noble metals are frequently used as catalysts and their intrinsic catalytic capabilities can be ascribed to the optimum degree of d-band vacancy [24]. Even though many of the transition metal nanoparticles are reported to be active for several reactions, the most studied are those of noble metals viz. Ru, Rh, Pd, Pt and Au [25-29]. The reason why precious metals could be used for commercial application in spite of the cost, is that they can be highly dispersed on appropriate supports and are less prone to oxidation. For eg., figure 1.1 displays such highly dispersed Au, Pt and Pd nanoparticles on high surface area oxide supports [30-32]. As mentioned earlier, it is desirable to have the active noble metal nanoparticles with controlled size and dispersion for catalysis applications. This is achieved to an extent by supporting the nanoparticles on high surface area supports. Recent developments have also enabled facile synthesis of metal nanoparticles with tunable particle size, shape and composition [33, 34].

There is a large number of reports concerning the catalytic activities of noble metal nanoparticles dispersed on a variety of metal oxides, viz. SiO₂, Al₂O₃, TiO₂, ZrO₂, MgO, ZnO, and CeO₂ [35-41]. Platinum, palladium, iridium, copper, silver and other

transition metals are highly active, promoting many different types of organic reactions including hydrogenations, oxidations, C – C bond formation, etc. [42].

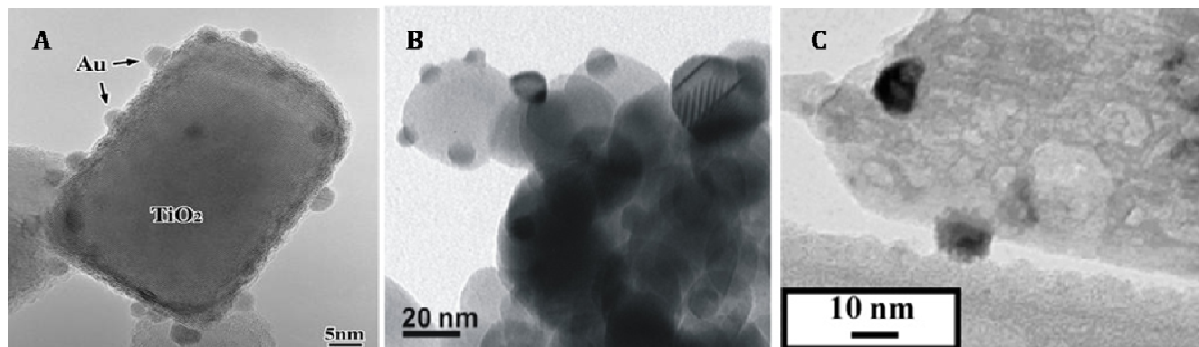


Figure 1.1. Noble metal nanoparticles dispersed on oxide supports, (A) Au on TiO₂, (B) Pt on ZrO₂, and (C) Pd on γ -Al₂O₃. Adapted from ref. [29-31].

The three-way catalyst (TWC) based on combinations of Pt, Pd and Rh is efficient in removing CO and NO_x from gasoline engines at temperatures from 400 °C to 800 °C [43-44]. One or more noble metals can be active for a particular reaction, but their activity and selectivity can be different from one another. Noble metals viz. rhodium, platinum and palladium are excellent catalysts for total oxidation of hydrocarbons and carbon monoxide [45]. However, silver and copper are found to be efficient for partial oxidation reactions such as ethylene epoxidation [46], conversion of methanol to formaldehyde [47, 48] and partial oxidation of methanol [49, 50]. Till the late 90s, gold was considered to be catalytically inactive. However, the seminal contribution of Prof. Masatake Haruta in Tokyo Metropolitan University established the extreme catalytic activity of gold nanoparticles (with size below 5 nm) towards aerobic oxidation of CO to CO₂ at low temperatures [51, 30]. Despite the very clear advantages of the noble metal based catalysts in terms of activity and selectivity, issues pertaining to stability and deactivation vis-à-vis agglomeration and sintering plague these systems [52].

1.2. Sintering of nanoparticles and catalyst deactivation

The study of catalyst deactivation is of great practical importance because of its high economic consequences. Catalysts undergo deactivation mainly by four different

ways: (1) poisoning, (2) fouling, (3) sintering, and (4) volatilization [53, 54]. Even though metal nanoparticles are promising heterogeneous catalysts, poor thermal stability limits their use to low temperature conditions and presents a hurdle towards widespread industrial application [55]. The catalytically active nanoparticles undergo sintering or coalescence to minimize their surface energies under reaction conditions, especially at high reaction temperatures. Sintering, the loss of active catalyst surface area due to crystallite growth of the supported metals, is an important mode of deactivation in supported metal nanoparticle catalysts, which is found to be most severe in case of noble metals [56]. Thermal stability of these catalysts becomes a critical problem especially in industrially important high temperature catalytic reactions, such as catalytic combustion [57], reforming of hydrocarbons [58] and automobile exhaust control [59] etc.

For example, the coalescence of platinum nanoparticle catalysts used in proton exchange membrane fuel cells results in a reduction of the electrochemically active surface area which leads to catalyst deactivation and subsequent reduction in cell performance after several cycles [60]. Figure 1.2 displays the SEM images of Pt/ Al_2O_3 catalyst depicting the preferential growth of Pt particles on certain crystallographic faces of the support during high-temperature reduction [61].

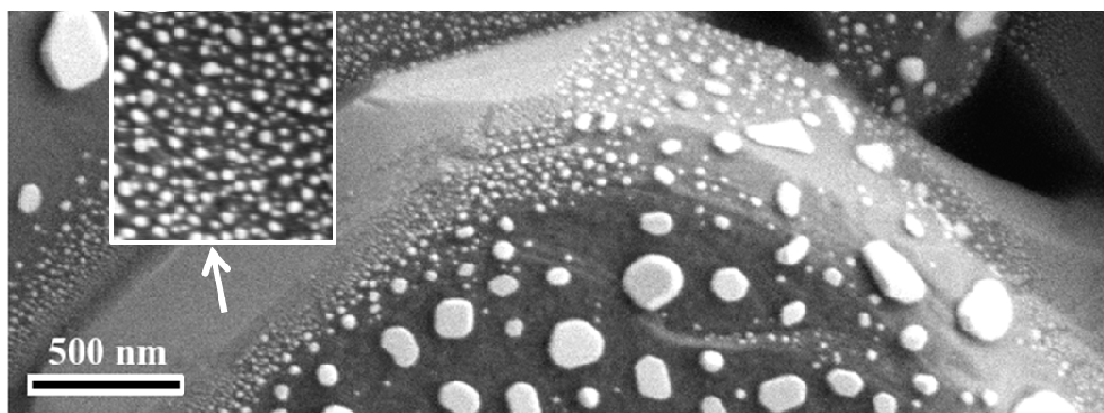


Figure 1.2. Low voltage SEM image of a Pt/alumina model nanocatalyst shows formation of large Pt islands due to the sintering of Pt nanoparticles during the high temperature reduction process on certain crystallographic faces of the polycrystalline alumina support. Inset shows unchanged particles. Adapted from ref. [61].

Sintering of supported metal catalysts is proposed to involve complex physical and chemical phenomena constituting a number of different rate-limiting steps (figure 1.3) as follows [53, 54, 62],

1. The dissociation and emission of metal atoms from metal crystallites.
2. The adsorption and trapping of metal atoms on the support surface.
3. The diffusion or hopping of metal atoms, and/or metal crystallites across support surface.
4. The wetting of the support surface by metal particles.
5. The nucleation of metal particles.
6. The coalescence of metal particles and/or bridging of two metal particles.
7. The capture of atoms by metal particles.
8. The vaporization of metal atom, and volatilization of metals as complexes.

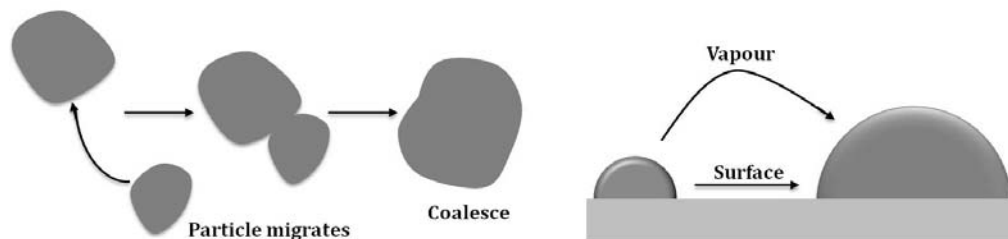


Figure 1.3. Schematic representation of the various stages involved in the formation and growth of particles. Adapted from ref. [53].

However, the exact steps involved in a particular sintering process mainly depends on reaction conditions, time, and catalyst formulation. The detailed understanding of sintering mechanism requires knowledge of surface diffusional processes, metal-support interfacial phenomena, solid-state reactions on the surface and the energetics of metal-metal and metal-surface interactions [63].

Metal crystallite growth is proposed to occur by two principal modes, i.e. atomic migration and crystallite migration [64-66]. In the case of atomic migration, atoms detach and migrate from one crystallite to another through the surface or gas phase and collide with another metal crystallite. Since larger crystallites are more stable on

account of the greater metal-metal bond energies compared to the metal-support interaction, small crystallites diminish and the larger ones increase in size. This growth of large crystallites at the expense of smaller ones is referred to as “Ostwald ripening”. Crystallite migration involves the diffusion of entire crystallites along the surface of the support, followed by collision with other ones and final coalescence. These two mechanisms can occur simultaneously and be coupled with each other during sintering. Sintering may directly lead to particle growth and coalescence, shape deformation and change in composition of the active nanoparticles, which eventually results in deactivation of the nanocatalysts.

Both atomic and crystallite diffusion mechanisms require the breaking of bonds (either between metal atoms or between the crystallite and the underlying surface), and higher temperature will hence result in faster diffusion and increased mobility. The position of the particle on the surface of the support is also crucial for sintering. A particle on a ‘valley’ position is stable, while that on a flat surface is highly unstable with respect to sintering [53].

As already mentioned, sintering is strongly temperature dependent and the key mechanism involved is the surface diffusion. It can be assumed that solid-state diffusion becomes faster when the temperature is closer to the melting point indicating that a relation exists between melting point and the sintering steps [53]. Two temperatures viz. Tamman and Huttig temperatures, at which sintering may occur are suggested to be dependent on the melting point by the following semiempirical relations,

$$T_{\text{Huttig}} = 0.3T_{\text{melting}}$$

$$T_{\text{Tamman}} = 0.5T_{\text{melting}}$$

Atoms at defects become mobile at Huttig temperature and when the Tamman temperature is reached, atoms from the bulk will exhibit mobility. The direct consequence of these relations is that metals with higher melting points tend to show better resistance to sintering which also means that the increase in the melting point of

a nanoparticle by some means improves catalyst stability. Tamman and Hüttig temperatures for some metals and compounds are given in table 1.1 [53].

Table 1.1. T_{melting} , T_{Tamman} and $T_{\text{Hüttig}}$ values (in K) of some metals and their compounds. Adapted from ref [53].

Compound	T_{melting} (K)	T_{Tamman} (K)	$T_{\text{Hüttig}}$ (K)
Pt	2028	1014	608
PtO	823	412	247
PtO ₂	723	362	217
Pd	1828	914	548
Ru	2723	1362	817
Ag	1233	617	370
Au	1336	668	401
Cu	1356	678	407

The temperature at which the solid becomes mobile depends on various other factors such as texture, size and morphology of the metal particle and the support. For eg., sintering of metal nanoparticles on highly porous Al₂O₃ is much more severe than on moderately porous Al₂O₃ [53]. Particles with small sizes may become mobile at temperatures much lower than that indicated by the Tamman or Hüttig temperatures.

Other than the temperature and size, the sintering of metal nanoparticles is affected by many factors that lead to a change in the surface energy of the particle such as the atmosphere and the shape and composition of the metal nanocrystallite. The stability of the nanoparticle is also affected by the properties of the particle itself, the loading or dispersion of the metal on a support and metal-support interaction [54].

Several reports suggest that sintering is more severe in oxidizing atmosphere than in inert or reducing atmospheres for Pt-supported catalysts [67, 68], however, this cannot be generalized since the rate of dispersion also depends on Pt loading and these effects may be related to changes in surface structure due to adsorbed species such as H, O or OH in H₂, O₂ or H₂O-containing atmospheres, respectively [69]. Strong metal-support interactions (SMSI) also affect the spreading, wetting and redispersion of the supported metals. For eg., NiO/SiO₂ is thermally more stable in air than NiO/SiO₂ in H₂ atmosphere owing to the strong interaction of NiO with SiO₂ [69]. Supports like CeO₂ and La₂O₃ are suggested to stabilise the noble metal atoms in automotive exhaust converters due to a strong, localized chemical interaction [70, 71].

In reducing atmosphere, metal crystallite stability generally decreases with decreasing metal melting temperature, i.e. in the order Ru > Ir > Rh > Pt > Pd > Ni > Cu > Ag [62]. But this order may be affected by relatively stronger metal-support interactions; the stability of Pt on various supports in vacuum is Pt/Al₂O₃ > Pt/SiO₂ > Pt/C. In oxidizing atmospheres, stability of metal particle depends on the volatility of metal oxides and the strength of the metal oxide-support interaction. Metal stability for noble metals in air decreases in the order Rh > Pt > Ir > Ru. Ru is the least stable because of the formation of volatile RuO₄ [62].

1.3. Important noble metal catalysed heterogeneous reactions

As mentioned in section 1.1, noble metal based catalysts are used in innumerable industrially important reactions. Of these, water gas shift reaction and CO oxidation are very relevant in the current scenario of energy scarcity and requirement for pollution abatement. Moreover, both reactions are simple with common mechanistic reaction steps which make them ideal for studying fundamental aspects of catalysis. Indeed a lot of studies are conducted on these reactions using variety of catalysts. In spite of the fact that these reactions are extensively studied for years, their mechanism and the active species involved remain under debate.

1.3.1. Water gas shift (WGS) reaction

The demand for hydrocarbon fuels is increasing day by day despite the limited supply of hydrocarbon resources in the world. In this scenario, the concept of the hydrogen economy, in which hydrogen with its high energy density would replace the fossil fuels, is proposed to solve some of the negative effects of using hydrocarbon fuels [72]. Many researchers argue that hydrogen can be an environmentally cleaner source of energy, particularly in transportation applications, without release of pollutants or carbon dioxide. Fuel cells, which use hydrogen as fuel, are attractive as they are far more efficient than the internal combustion engines [73]. Fuel cells require high-purity hydrogen because the impurities would quickly degrade the life of the fuel cell stack. There are two primary uses for hydrogen today: about half of annual production being used in making nitrogen fertilisers via the Haber process and rest to convert low-grade crude oils into transport fuels. Currently more than 90 % of the hydrogen is industrially produced from steam reforming, which uses fossil fuels such as natural gas, oil, or coal. However, reforming hydrocarbon fuels for hydrogen production yields reformat streams containing CO, which, because of its strong adsorption to the electrode surface poisons the Pt anode in the Polymer Electrolyte Membrane (PEM) fuel cell at concentrations above 100 ppm [74, 75]. Water Gas Shift (WGS) reaction is used to increase and adjust the H₂/CO molar ratio in the synthesis gas and to remove CO from the gas effluents [76-77]. In the WGS reaction, the carbon monoxide is reacted with steam to produce hydrogen and carbon dioxide (CO₂).



The WGS reaction is important for industrial hydrogen production as well as an integral component of fuel processing for fuel cell applications. As the reaction is moderately exothermic, low temperature favors a high equilibrium conversion of CO. Two adiabatic stages are employed to achieve the highest feasible conversion: a high temperature shift (HTS) at 310–450 °C with a catalyst based on iron oxide structurally promoted with chromium oxide, followed by a low temperature shift (LTS) in the temperature range of 210– 240 °C, where the typical industrial catalyst is copper with

zinc oxide and aluminum oxide as support materials [78-80]. These two stages help to take advantage of kinetics and thermodynamics. High temperature shift is used to make the reaction kinetically favourable. By cooling the syngas between the HTS and LTS stages, an active catalyst can take advantage of the thermodynamic equilibrium at low temperature. This two stage WGS configuration results in an exit CO concentration of much less than 1 %. However, these commercial Fe/Cr and Cu/Zn/Al based catalysts, prior to the operation must undergo a pretreatment using a specific process to control reduction of the oxides to the catalytically active state. Improper activation affects the activity and life of the catalysts. During shut down, care must be taken to avoid steam condensation and to minimize the re-oxidization of the catalysts [81]. Also the copper catalyst undergoes deactivation at temperatures higher than 300 °C, as the copper particles sinter because of surface migration. Another important issue is regarding the size of the fuel cell reformer. The present stationary commercialized reformers are very large; however, for transport and domestic household applications, compactness and fast response are necessary. The transition to hydrogen based energy will be possible only after the development of efficient and stable catalysts which overcome the above said drawbacks of the current commercial catalysts.

Precious metal based catalysts are being actively studied in recent years for fuel cell applications [82-85]. The WGS reaction orders on precious metal catalysts are favourable for high CO conversions [86]. These catalyst systems usually do not require a lengthy reduction process and are stable to condensing water [87]. They are stable when subjected to air during start up and shut down operations and can withstand temperature upsets. Moreover they are generally more resistant to poisoning than base metal catalysts. Their superior activity enables to build compact reactors which permit a rapid response to transient conditions. Although several oxides are used as supports for precious metals, reducible oxides are found to be the best. Ceria (Au, Cu or Pt on CeO₂), titania (Au, Pd or Pt on TiO₂), and Fe₂O₃ (Au) based catalysts are highly active for low temperature WGS reaction [88-92]. Ceria-based WGS catalysts have attracted attention recently because of the high oxygen-storage capacity of ceria and modified ceria [82, 93, 94]. In addition, it acts as a stabilizer of noble metal as well as a promoter

of the reaction. The multiple stable oxidation states, +3 and +4 for Ce, allow it to undergo oxidation and reduction relatively easily. It helps to maintain the dispersion of the catalytic metals.

However, various deactivation mechanisms including increased blocking of the active surface by formation of carbonates, formates, or hydroxycarbonates, sintering of metal nanoparticles, loss of contact between the metal and the support and irreversible over reduction of support under WGS conditions are reported in supported metal catalyst systems [95-101]. Sintering of the metal particles is considered as one of the major deactivation mechanisms in WGS reaction. At various operating conditions of the WGS reaction, like start up, shut down, numerous redox cycles, temperature excursions etc., the catalysts tend to lose their activity by the loss of surface area. Dr. Robert J. Farrauto and coworkers in Columbia University investigated the aging of Pt-based ZrO₂-CeO₂ supported WGS catalysts under steady-state operation, high temperature stress and start up–shut down conditions using activity testing, transmission electron microscopy (TEM), IR spectroscopy and chemisorption techniques [98]. In their study, they observed significant aging for both steady-state operation at low temperature (228–260 °C) (figure 1.4.) and high temperature cycling (380–450 °C). The loss of activity was attributed to the sintering of Pt particles as evidenced from CO chemisorption and TEM analysis. In another report, Wang *et al.* have conducted an accelerated aging test for Pd on ceria catalysts under WGS conditions [99]. They observed substantial catalyst deactivation after the test cycles. In order to account for the deactivation, they subjected the catalysts to various conditions, and found that heating the catalyst to high temperature in pure CO results in a dramatic reduction in the activity. The measurement of Pd dispersion using CO adsorption reveals that the activity reduction indeed results from the loss of metal surface area in CO. Also they found out a linear relationship of WGS reaction rates with Pd surface area over a wide range of Pd particle sizes. The results from various research groups indicate that it is worthwhile to develop advanced WGS catalysts that are more active than the commercial non-noble metal based catalysts and also stable under the reaction conditions.

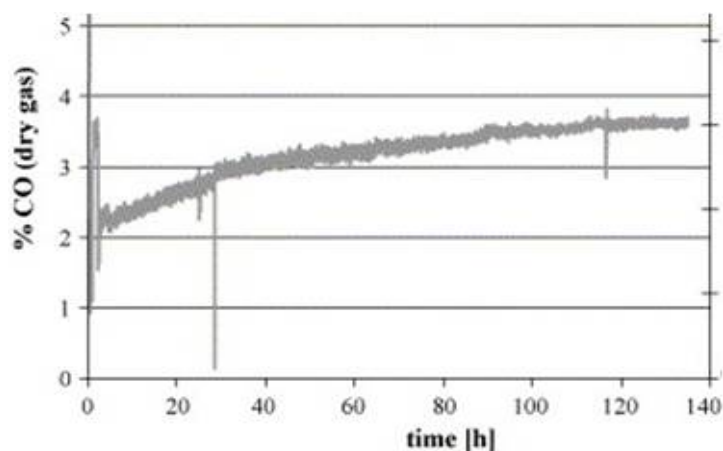


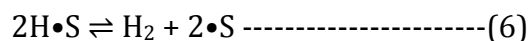
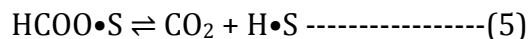
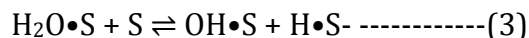
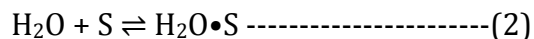
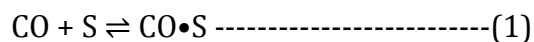
Figure 1.4. CO exit concentration of 2 % Pt/CeO₂-ZrO₂ at 228 °C for WGS reaction, Reformate composition 5.98 % CO, 7.4 % CO₂, 31.82 % H₂, 28.86 % N₂ & 26 % H₂O. Adapted from ref. [98].

However, gaining insights regarding the nature of the active sites, the reaction mechanism and limiting steps for the reaction is important for the design and optimization of stable and efficient WGS catalysts. There is a lot of controversy over the mechanism of WGS reaction. Two general mechanistic schemes have been proposed,

1. Associative Mechanism and
2. Regenerative (redox) Mechanism

The associative mechanism is a Langmuir-Hinshelwood type mechanism consisting adsorption and desorption steps where the adsorbed carbon monoxide and water on the catalyst surface, interact to form a surface intermediate, which breaks down to form reaction products [102-107]. Even though many researchers support this mechanism, there is still no agreement about the nature of the intermediate. Some reports suggest the participation of formate intermediate [103-105] while others are consistent with a mechanism involving carboxyl intermediate [106, 107]. Shido and Iwasawa, with the help of IR spectroscopy and temperature-programmed desorption (TPD), concluded that bidentate formate, produced by the reaction of CO with terminal hydroxyl groups on the ceria, is the intermediate species for the ceria-supported Rh catalysed WGS reaction [102]. Rhodes *et al.* proposed formate species as intermediate

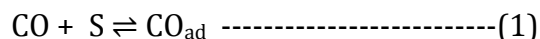
species for the Cu–chromite catalyst [108]. The steps involved in the associative mechanism with formate species as intermediate are given below.

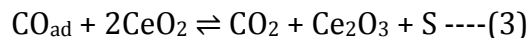


where S represents adsorption sites on the metal. Jacobs et al. investigated the low-temperature WGS reaction over the Pt/CeO₂ catalyst by SSITKA–DRIFTS and confirmed that formate is the active intermediate [104]. Density function theory (DFT) calculations on Pt(111) along with experimental studies indicate the involvement of a carboxylate (OCOH) intermediate for the alumina-supported platinum clusters for the WGS reaction [109]. Gokhale et al. has proposed that water gas shift reaction proceeds through the carboxyl mechanism on Cu(111) [110].

The regenerative or redox mechanism, in which adsorbed water decomposes to form adsorbed atomic oxygen that subsequently oxidizes carbon monoxide have been reported on less inert oxide supports [82, 90, 111]. The rate of WGS reaction is significantly higher over ceria-supported Pt, Pd, and Rh, even though the metals are not easily oxidized by water. In contrast, the oxidation of Ce₂O₃ by water to yield hydrogen is thermodynamically favorable and is observed in low pressure adsorption studies. The redox mechanism is a co-operative mechanism, involving the oxidation of adsorbed CO on the metal by labile oxygen of the support, followed by dissociative adsorption of H₂O on the oxygen vacancy on ceria that leads to the formation of hydrogen.

The overall reaction steps on a CeO₂ supported metal catalyst is suggested to occur in the following steps.





where S represents adsorption sites on the metal. Mainly kinetic studies provide evidence for the redox mechanism. But TPD studies indicate that CO adsorbed on metals can be oxidized by oxygen from ceria [112]. Cu- and Ni-containing La doped ceria catalysts is reported to proceed through the redox mechanism for low-temperature WGS reaction [90]. Kalamaras et al. supports the redox mechanism with the help of detailed SSITKA-DRIFTS, and other transient ^{18}O -isotopic exchange experiments, for the WGS reaction on the Pt/TiO₂ catalyst [111]. WGS reaction over a series of ceria-supported, transition metals (Pd/ceria, Ni/ceria, Fe/ceria, Co/ceria, and Pd/silica. Pd/ceria) are suggested to involve redox mechanism [86].

1.3.2. CO oxidation

Carbon monoxide (CO) is one of the most common air pollutants. Catalytic CO oxidation by oxygen is of utmost importance for the reduction of CO in the atmosphere [113].

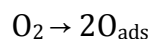
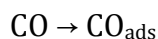


Moreover it finds application in the preferential oxidation of CO in hydrogen rich stream produced mainly by reforming of natural gas followed by the WGS reaction to reduce the amount of CO, as small amount of CO (0.5–2.0 wt%) can poison the Pt-based anode in the polymer electrolyte membrane (PEM) fuel cell [114].

Furthermore the CO oxidation reaction is one of the most investigated heterogeneous reactions and it has been studied extensively on various noble metals. CO oxidation on Pt-group metal surfaces is often considered as an ideal probing reaction to understand fundamental steps involved in the heterogeneous reaction as its mechanism consists of steps such as molecular adsorption or desorption of reactants, dissociative adsorption of reactants, surface reaction, etc. [115].

Currently the removal of CO from automobile exhaust is accomplished by the oxidation of CO in catalytic converters using supported Pt, Pd and Rh catalysts [116]. CO

oxidation on single crystal surfaces of Pt-group metals (Rh, Pt, Pd and Ru) at low pressures has been well-studied using traditional Ultra High Vacuum (UHV) surface science probes [115]. At low pressure conditions, Langmuir–Hinshelwood reaction mechanism is generally accepted for CO oxidation, whereby co-adsorbed CO and O atoms react to form CO₂ [113, 117, 118]. This reaction scheme is shown below



It is understood from various studies that CO inhibits O₂ adsorption more effectively than the inhibition of CO adsorption by surface oxygen [119, 120]. This has a direct consequence on the CO₂ production rate and puts the limit of minimal CO surface coverage for better conversion at low temperatures. The increase in CO partial pressures results in increase in the temperature at which maximum CO conversion occurs. However, higher temperatures cause high CO desorption rate and here activity is affected due to inhibition of CO adsorption by oxygen and to decreased lifetimes of CO species on the surface. But Ru behaves differently towards CO oxidation when compared to the Pd, Pt and Rh [121-123]. It exhibits the least activity of all the Pt-group metals at low pressures but most active at high pressures. The higher reactivity of Ru at high pressures is attributed to the tendency of the surface to be covered with oxygen atoms more facilely than Rh, Pd, Pt. But some investigators suggested that only one reactant needs to be adsorbed on the catalyst while the other in the gas phase reacts with the adsorbed one, following Eley-Rideal mechanism [124]. However, there is general agreement that the oxidation mechanism changes with temperature.

Even though gold has been considered as an inert heterogeneous catalyst till the late 90s because of its completely filled 5d shell and the relatively high first ionisation potential, gold particles smaller than 5 nm, highly dispersed on metal oxides (Fe₂O₃, Co₃O₄, TiO₂, NiO, ZrO₂, Mn₂O₃) are reported to be extremely active for CO oxidation even at temperatures lower than room temperature [51, 125-127]. However, its catalytic

activity was found to be strongly affected by the preparation method and the pretreatment conditions used as it is strongly dependant on the particle size [128, 129]. A synergistic mechanism is suggested for the CO oxidation involving the gold and metal oxide interface, with the oxide support playing a necessary part in the reaction [130-132]. CO is adsorbed on a metallic gold site near to a metal oxide site occupied by an adsorbed O molecule. The reaction may then proceed via a carbonate like intermediate species which ultimately decomposes to CO₂. But the dissociative adsorption of oxygen is hindered at temperatures below 400 °C due to a high energy barrier, even though CO adsorbs at low temperatures (T<150 K) [133]. Moreover when atomic oxygen is present, CO oxidation takes place readily [134]. To explain the activity for CO oxidation, several models have been proposed for oxygen adsorption on supported Au particles [135] and are visualized in figure. 1.5.

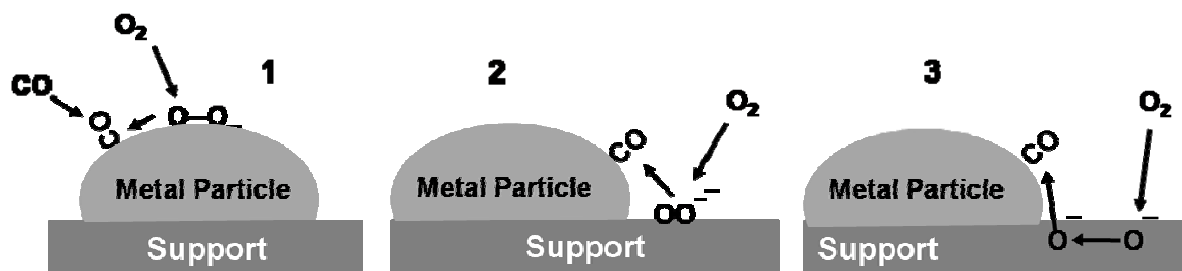


Figure 1.5. Possible reaction schemes for the CO oxidation reaction over supported Au catalysts. Adapted from ref. [135].

1) The reaction proceeds with the O₂ dissociation occurring either by the formation of a four-centered CO-O₂ surface complex on a common Au site or on a defect site on the metal surface or on small, flat-shaped particles with different electronic structure [136-138].

2) Adsorption of oxygen occurs on the support (or at the metal-support interface) near to the metal particle possibly on oxygen vacancies near to metal particles as O₂⁻ [139, 140].

3) On the support, the adsorbed oxygen dissociates immediately to produce lattice oxygen, which subsequently reacts at the interface or after a spillover of oxygen to the gold metal [132, 141].

Other proposed active sites include small Au clusters possessing nonmetallic electronic properties due to quantum-size effect [142], surface step and strain defects [143], and an ensemble of Au^+-OH^- and metallic Au atoms [144]. According to model (3), metallic Au activates the oxygen molecule, and Au cation with a hydroxyl ligand provides the pathway for the oxidation of CO. It is the requirement of such an ensemble that makes the activity of a catalyst very sensitive to the preparation details and pretreatment conditions. Generally it is believed that since CO adsorbs much more strongly to metals than to their oxides, CO oxidation takes place on metallic surfaces. However, some recent reports with the help of in situ spectroscopic techniques, revealed the presence of oxidic Pt, Pd, and Ru under CO oxidation reaction conditions [145, 146].

1.4. Catalytic activity of ionic noble metal species in heterogeneous reactions

In the case of WGS reaction, research works are underway to understand the active species. There is a disagreement in the research community regarding the oxidation states of the active metal species. Most of the earlier researchers are in agreement with a zerovalent state [86, 108, 147]. However, some of the recent reports suggest that metal particles with ionic character are active for WGS reaction. Prof. M. Flytzani-Stephanopoulos and co-workers in Tufts University were able to show, by selective leaching studies, that only ionic gold and platinum bound to ceria are active for the WGS reaction and metallic particles do not participate in the reaction [148-150]. They deposited nanosized gold or platinum onto a La-doped cerium oxide support and then calcined the material in air at 400 °C. The resulted metal nanoparticles were removed from the surface of the material using basic sodium cyanide solution (figure 1.6.). This procedure removed more than 90 % of the metallic loading from ceria. The surface of the leached materials, as analyzed with the help of X-ray photoelectron

spectroscopy, was found to consist of ionic Au or Pt as the major or only Au or Pt species. Electron microscopy also detected no gold clusters.

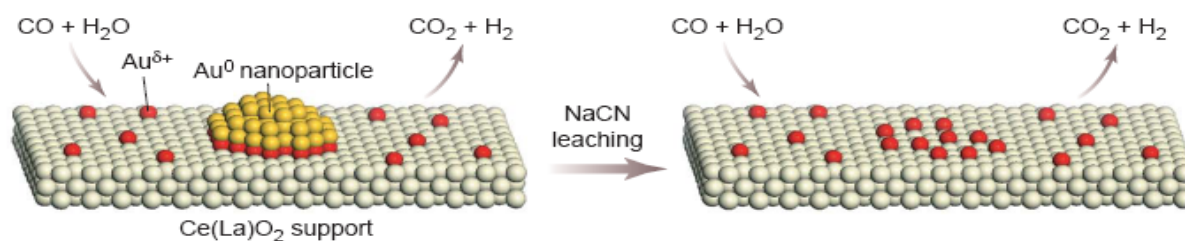


Figure 1.6. Schematic representation showing the leaching of metallic Au or Pt from the surface of Au or Pt supported on Ce_{1-x}La_xO₂. Adapted from ref. [151].

When used as catalysts for WGS reaction, both the parent and leached (Au or Pt on ceria) catalysts exhibited similar rates of CO₂ production. In addition, the apparent activation energy for the reaction was determined to be the same for both the parent and leached catalysts. However, the rate of the reaction measured over the support alone was much lower than the noble metal-containing catalysts, with a much higher activation energy. Since the removed Au in the parent catalyst neither increased the rate nor changed the activation energy of the reaction, it was concluded that only ionic Au present on the leached catalysts is active.

Also, it is reported based on computational studies that stable oxidized gold clusters at ceria-oxygen defects are active sites [152]. They demonstrated with the help of density functional theory that the empty non bonding f states of ceria helps the oxidation of Au and only Au^{δ+} can adsorb CO sufficiently strongly for subsequent catalysis, and that a combination of several such Au^{δ+} in the vicinity of an O vacancy does catalyze the WGS conversion.

Since metal particles often have positively charged atoms at the metal-support interface, various reports propose the unique role of cationic interfacial gold species. A study using EXAFS analysis indicated that the presence of a partially oxidized Pt species with coordination lower than octahedral for the Pt/Al₂O₃ catalyst, is responsible for generating high CO oxidation activity [153]. Time-of-flight secondary ion mass spectroscopy (TOF-SIMS) studies of Au/γ-Al₂O₃ and Au/TiO₂ catalysts showed the

presence of oxidized Au clusters of AuO^- , AuOH^- and AuO_2^- , which together with the metallic gold are suggested to act as the active site for CO oxidation [154]. Prof. Avelino Corma's group in the Institute of Chemical Technology (ITQ-CSIC-Polytechnical University of Valencia) stabilized Au(III) on nanocrystalline CeO_2 and Y_2O_3 and found that the catalytic activity of the catalyst towards CO oxidation is directly proportional to the concentration of Au(III) surface species [155]. In another report, XANES and TPR-TPO techniques suggested that both Au(I) and Au(0) are present in MgO-supported gold catalysts for CO oxidation and it was also observed that both the catalytic activity and the surface concentration of Au(I) were found to decrease with increasing CO partial pressure demonstrating that the catalytic sites incorporate Au(I) [156].

1.5. Role of solid state compounds in heterogeneous catalysis

The attempts to design new solid catalysts for a variety of industrial processes are now converging on a generally applicable strategy to develop well defined active centers which are spatially separated [157]. Such single-site catalysts, which are similar to the metal-centered homogenous catalysts and enzymes, enable element-efficient catalysis. This approach has been demonstrated through the use of active cationic species substituted for the cations in the metal oxides. In the preceding section, various reports suggesting the activity of cationic metals are presented, but the nature of the active center was not established with certainty. Moreover in conventional catalysts, only the atoms present on the surface of the noble metal particles act as adsorption sites. The complete dispersion of noble metals is possible only by its incorporation as ions in the lattices of oxides. Some attempts to synthesize such dispersed ionic noble metal catalysts are already reported.

Pioneering work from Prof. M. S. Hegde's group in Indian Institute of Science reported synthesis of Pt, Pd, Cu or Rh doped CeO_2 , TiO_2 or $\text{Ce}_{1-x}\text{Ti}_x\text{O}_2$ structures and their activities in CO and hydrocarbon oxidation and NO_x reduction [158-161]. They observed that the rates are 15-30 times higher for the ionic catalysts than for the same amount of noble metal loaded on an oxide support catalyst. In another report, $\text{Au}_x\text{Ti}_{1-x}\text{O}_2$ was synthesized and used as catalysts for CO oxidation [162]. They

demonstrated with the help of DFT that gold ion prefers to substitute a five-coordinated Ti atom on the surface rather than the bulk Ti atom. Several such doped oxide catalysts performing various catalytic reactions are there in the literature viz. $\text{Cu}_x\text{Ce}_{1-x}\text{O}_2$ catalysing NO reduction with NH_3 , $\text{Pt}_x\text{Ce}_{1-x}\text{O}_2$ performing the WGS reaction, $\text{Fe}_x\text{Ce}_{1-x}\text{O}_2$ catalysing N_2O decomposition and $\text{Ce}_{0.9}\text{Cu}_{0.1}\text{O}_2$ catalysing the steam reforming of methanol [163-166]. In all of these systems, the doped oxide is a better catalyst than metal impregnated oxide.

Of the oxide systems, perovskites occupy an important position with multiple catalytic reactions attributed to them due to a wide window available for doping and creation of oxygen vacancies which may help the activity. The term 'perovskite' was originally used for the mineral CaTiO_3 which was discovered and named after Russian mineralogist, Count Lev Aleksevich von Perovski by Gustav Rose in 1839 from samples obtained in the Ural Mountains. Goldschmidt who produced the first synthetic perovskites in 1926 used the term perovskite to describe a class of compounds with same stoichiometry and connectivity as those in CaTiO_3 . The crystal structure of a BaTiO_3 type orthorhombic perovskite was solved by H. D. Megaw in 1945 [167]. The perovskite structure has the general formula ABX_3 where A commonly stands for rare earth and alkaline earth ions (La, Ba, Sr, Ca etc.) and B represents usually transition metal ions (Cr, Mn, Co, Fe, Ce etc.) and X is an anion, most commonly oxygen. The structure of a cubic perovskite is shown in figure 1.7. The cation occupying the A-site has a coordination number of twelve (cuboctahedral coordination) while the B ion is located in the centre of an octahedron of oxygen ions (six fold coordination). The easiest way to visualize the structure is in terms of the BO_6 octahedra which share corners infinitely in all 3 dimensions and the A cations occupy every hole created by 8 such octahedra.

The strict relative ion size requirements for stability of the cubic structure cause slight buckling and distortion which produce several lower-symmetry structures (e.g. tetragonal, orthorhombic, etc.), in which the coordination numbers of A, B or both ions are reduced [168].

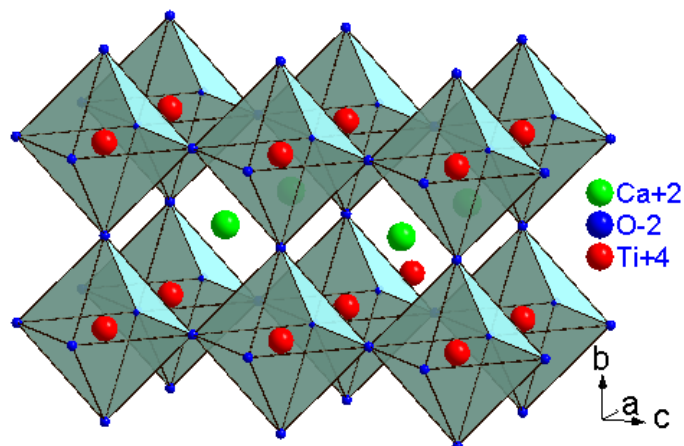


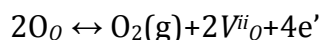
Figure 1.7. Structure of a cubic CaTiO_3 perovskite.

Furthermore the flexibility of bond angles inherent in the perovskite structure may result in distortions including displacement of the cations out of the centers of their coordination polyhedra, and distortions of the octahedra driven by electronic factors (Jahn-Teller distortions). Various factors such as changes in temperature or oxygen partial pressure, and a size mismatch of the A and B cations contribute to the distortion. The Goldschmidt tolerance factor (t) which predicts the stability of the perovskite structure can be calculated from the ionic radii of ions present on the A and B sites [169], as

$$t = (r_A + r_O) / \sqrt{2} (r_B + r_O)$$

r_A , r_B and r_O represents the ionic radius of the ions on the A, B and oxygen sites respectively.

When the value of tolerance factor is close to unity, symmetry is predicted to be cubic. Values in the range of 0.74 - 1 indicate the possibility of a distorted crystal structure. However, a real crystal often contains intrinsic defects like oxygen vacancies due to equilibrium between lattice oxygen and gas phase oxygen. According to Kroger-Vink notation



Where O_o represents lattice oxygen, $O_2(g)$ is gas phase oxygen, V^{i}_o is an oxygen vacancy, and e' is an electron in the conduction band.

The concentration of oxygen vacancies in a pure perovskite material depends generally on factors like temperature, total pressure and oxygen partial pressure [170]. Extrinsic vacancies in these compounds can be introduced by doping A and B-site ions with lower valence ions. Perovskite structures readily accept substitution of different ions on each site producing wide range of compositions resulting in variety of physical properties making them one of the most frequently encountered in solid-state inorganic chemistry. The structure accommodates most of the metal ions in the periodic table in different combinations.

Perovskite materials, doped on the A and B sites to create oxygen vacancies allow mixed ionic and electronic conduction (MIEC). These mixed conductors owing to their unusual high tolerance for oxygen ion vacancies are used as cathode or ideal electrolyte materials in solid oxide fuel cells (SOFC) and in membranes for oxygen separation and for chemical production [171, 172]. Perovskites such as $BaZrO_3$ and $SrZrO_3$ are currently being proposed as electrolytes for SOFCs [173,174]. Moreover they have wide range of technological applications such as in sensors, memory devices (RAM), superconductors, amplifiers, and electro-optical devices [175]. Moreover they exhibit many interesting properties such as colossal magnetoresistance, ferroelectricity, superconductivity, charge ordering, spin dependent transport, high thermopower and the interplay of structural, magnetic and transport properties [175]. Synthetic perovskites are suggested as possible inexpensive base materials for high-efficiency commercial photovoltaics.

The unique crystal structure, nonstoichiometry in oxygen content, acid-base property, redox nature, and thermal stability of perovskites allow it to be effective in exhaust abatement, hydrogenation, oxidations and photocatalysis [176-179]. Recently, perovskites are found to catalyse biomass conversion such as glycerol to syngas [180]. In addition, perovskites offer the possibility of preparing a large series of isomorphous solids for the study of the effect of partial substitution of A and B cations on catalytic

behavior. The stability of these oxides at elevated temperatures makes them ideal to use in many areas where other formulations fail, e.g., high temperature catalytic combustion.

Recently considerable attention has been given to transition-metal based perovskites on account of their possible utility as catalysts [181-183]. The drawback of low surface area for these materials can be overcome by performing substitutions on the cationic site or by developing active perovskite type oxides by new synthesis methods. Various metal ions including noble metals can be used for partial substitution of metal ions in perovskite. Pd doped perovskite, $\text{LaCo}_{1-x}\text{Pd}_x\text{O}_3$ ($x = 0, 0.1$ and 0.3) is reported to be good catalysts for catalytic removal of NO_x and diesel soot [184].

Moreover catalytic activity of perovskites can be enhanced by the addition of small amounts of noble metals. Noble metals such as Pt, Pd or Rh supported on LaMnO_3 perovskites are found to be active for the total oxidation of methane [185]. Pd in the $\text{LaFe}_{0.95}\text{Pd}_{0.05}\text{O}_3$ and $\text{BaCe}_{1-x}\text{Pd}_x\text{O}_3$ catalyst are reported to move in and out of the lattice depending on the atmosphere [186, 187].

Various methods can be used to synthesize perovskite phases like solid state method, citrate-gel method, sol-gel method, co-precipitation method etc [188]. Solid state methods utilise starting materials in the form of oxides, carbonates, or acetates of the metal cations of interest. Accurately weighed powders depending on the stoichiometric ratio are mixed and ground well and calcined at a temperature high enough to decompose the starting material. The mixture is again reground and heated at elevated temperatures and the heating cycles are repeated until structure formation. Rate of heating is important for the crystallization of some perovskites. Materials prepared by solid-state reaction consists of highly agglomerated large sized particles and high impurity contents due to their inherent problems such as heterogeneous solid phase reaction and high reaction temperature [189]. Hence this method is not suitable for material preparation for catalysis type of applications.

Many wet chemical synthesis routes are developed to generate high purity, homogeneous, reactive ultrafine powders at low temperatures. The advantage of wet

chemical methods is the quasi-atomic dispersion of constituent components in a liquid precursor, which facilitates synthesis of the crystallized powder with submicron particles and high purity at low temperatures. However, sol-gel and coprecipitation methods require controlled chemical conditions such as pH, reagent concentration, reaction medium, and chelating properties of ligands [190-192]. Stoichiometric deviations and formation of biphasic solid solutions are observed when coprecipitation and sol-gel methods are used. The advantage of the citrate-gel method is its simplicity for obtaining powders of high purity and possibility to hold the initial stoichiometry. Citrate gel method is used mostly as it yields phase pure, almost homogeneously distributed particles [193]. Synthesis of perovskites using citrate process involves calcination of amorphous citrate complex precursors. An aqueous solution of citric acid is added to the aqueous mixture of metal nitrates in proper molar ratios according to the desired perovskite composition. The removal of water from the solution results in a gel type of amorphous citrate precursor, the heating of which results in its decomposition and formation of the crystalline perovskite phase. Instead of citric acid, glycine, urea etc. are also used. The advantage of this method is that a homogenous mixture of the cations is obtained and the perovskite is formed at a relatively lower temperature. Surface area of the perovskite is important for catalysis application and large surface area materials can often be achieved by reducing the synthesis temperatures.

Another important family of compounds worth exploring contains noble metals in low coordinated sites which present coordinatively unsaturated sites conducive for catalysis. Ag and Cu in metallic form are highly active for various reactions. But the presence of these elements in coordinatively unsaturated sites presents an interesting prospect in catalysis. Recently P. Gomez-Romero et al. synthesized the compound $\text{Ag}_2\text{Cu}_2\text{O}_3$, an oxide in which both Ag and Cu coexist [194-195]. This compound consists of alternating chains of edge-sharing square-planar CuO_4 units and zigzag chains of linearly coordinated AgO_2 units (figure 1.8A). These chains run parallel to *a* and *b* axes, consecutively, presenting three dimensional array of tunnels. The coordination of the metals is typical of Cu(II) and Ag(I). This structure can be chemically and

electrochemically oxidized to $\text{Ag}_2\text{Cu}_2\text{O}_4$ in which the metal oxidation states and coordination geometry are retained in which the charge is delocalized among silver and copper with their formal oxidation states larger than the usual Ag(I) and Cu(II), but an O atom is intercalated such that the open channel structure is changed to a layered structure (figure 1.8B) [196-198].

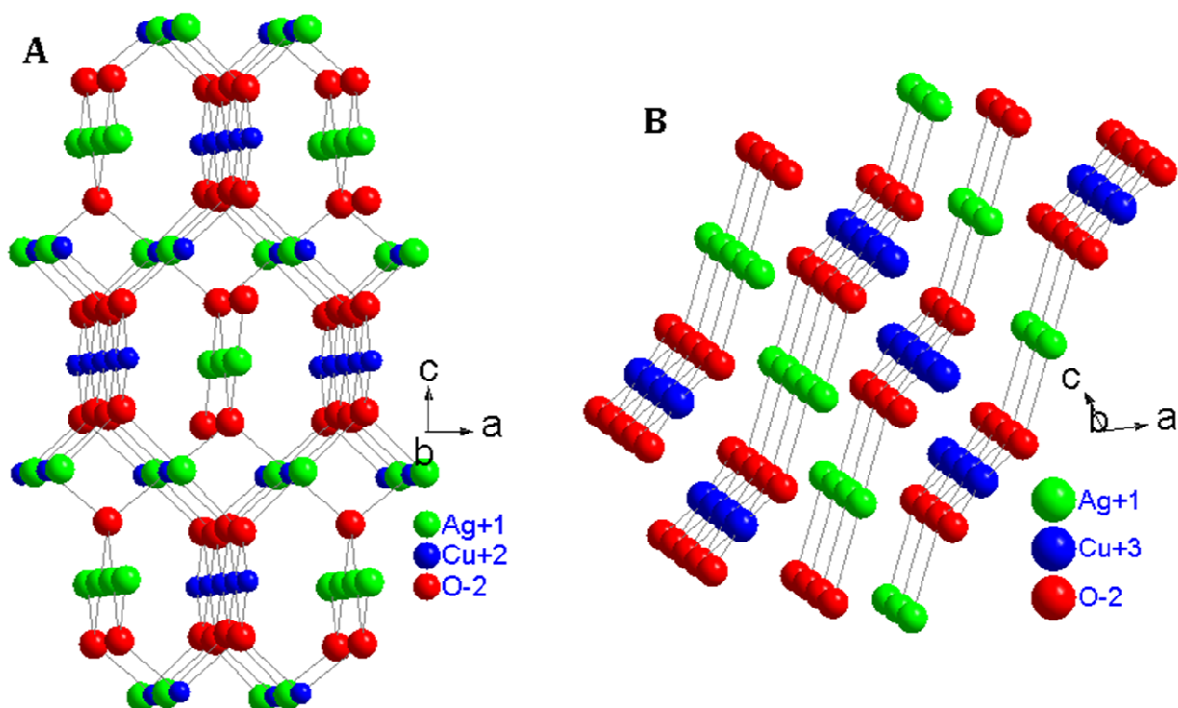


Figure 1.8. Structure of (A) $\text{Ag}_2\text{Cu}_2\text{O}_3$ and (B) $\text{Ag}_2\text{Cu}_2\text{O}_4$.

The evidences of ionic mobility and disorder in these systems points to a rather flexible structure that can lead to a variety of intercalation reactions. Even though copper and silver based catalysts are already tested for WGS as well as CO oxidation reactions, low coordination compounds based on them have not been studied as catalysts for these processes.

1.6. Scope and objective of thesis

It is already stated that although supported noble metal particles are extremely active for a variety of heterogeneous reactions, their deactivation by sintering of nanoparticles under reaction conditions presents a hurdle for their widespread

application. The deterioration of catalytic activity of supported Pt and Au catalysts by sintering is prominent in the case of Water gas shift reaction and CO oxidation. This scenario demands an alternative catalyst system that is resistant to sintering. Some recent works demonstrated that partially ionic noble metal species are responsible for WGS activity in oxide supported Au and Pt catalysts. As an extension to this, the logic followed in this work is that noble metal cations stabilized by doping in stable lattice types like perovskites (ABO_3) can also be WGS active and sinter resistant. $BaCeO_3$ perovskite can be an ideal candidate for doping noble metals like Pt on account of appropriate ionic sizes and high tolerance factor due to the multiple valence of Ce. Lanthanum perovskites with first row transition metal ions occupying B-site can also be considered, as they can be synthesised at relatively lower temperatures making overall textural properties suitable for catalysis. Moreover a range of elements which themselves are active for many reactions is possible in the B-site which will enable to study their combined effects along with Pt on WGS.

Most of the studies regarding the WGS reaction concentrate on the structural and redox aspects of the catalysts. The WGS reaction mechanism is proposed to involve oxygen vacancies for supported noble metal catalysts. However, reports establishing their participation unambiguously are not available. Perovskite structure is flexible enough to allow a wide range of substitutions which leads to the formation of oxygen vacancies. So, doped perovskites can be used as catalysts to investigate the role of oxygen vacancies on WGS activity. Doped $BaCeO_3$ can be an ideal choice as they are well known for their protonic and oxide ion conduction through the oxide ion vacancies, caused by doping on the Ce^{4+} site.

Recently many low coordination compounds are reported which possess fascinating properties making them useful for various applications. However, their catalytic properties are hardly investigated. The presence of coordinatively unsaturated active metals in these compounds makes these materials ideal for catalysis. The recently developed Ag and Cu based mixed oxides are reported to have variety of properties. Coordinatively unsaturated active metals like Cu and Ag in these materials

make it worthwhile to study their catalytic activity and stability under different conditions.

Based on these facts, the following specific works were selected for the present thesis,

1. Synthesis, characterisation, WGS activity and stability studies of Pt doped BaCeO₃.
2. Study the stability of cationic Pt in the lattice under various possible shut down conditions.
3. Synthesis, characterisation, stability and WGS activity studies of Pt and Y codoped BaCeO₃ to understand the role of oxygen vacancy on catalytic activity.
4. Synthesis, characterisation and WGS activity studies of LaB_{1-x}Pt_xO₃ (B = Mn, Fe and Co).
5. Compare WGS activities of the Pt doped perovskites with Pt impregnated perovskites and mixed oxides.
6. Characterization and WGS activity studies of Pt doped LaMnO₃ synthesised at various calcination temperatures.
7. Synthesis, characterisation, CO oxidation and WGS activity studies of Ag₂Cu₂O₃ and Ag₂Cu₂O₄.

References

1. Ross, J. R. H. Chapter 1 - Heterogeneous Catalysis - Chemistry in Two Dimensions. In Heterogeneous Catalysis; Elsevier: Amsterdam; 2012.
2. Bartholomew, C. H.; Farrauto, R. J. Fundamentals of Industrial Catalytic Processes; John Wiley and Sons, Inc. New Jersey; 2006.
3. Fierro, J. L. G. Metal Oxides: Chemistry and Applications; Taylor & Francis Group: Boca Raton, Florida; 2006.
4. Deutschmann, O.; Knozinger, H.; Kochloefl, K.; Turek, T. Heterogeneous Catalysis and Solid Catalysts; Wiley-VCH Verlag GmbH & Co. KGaA, Weinheim; 2009.
5. Moulijn, J. A.; van Leeuwen, P. W. N. M.; van Santen, R. A. Catalysis-An Integrated Approach to Homogeneous, Heterogeneous and Industrial Catalysis; Elsevier, Amsterdam; 1993.
6. Rao, C. N. R. *Annu. Rev. Phys. Chem.* **1989**, *40*, 291.

7. Trovarelli, A.; de Leitenburg, C.; Boaro, M.; Dolcetti, G. *Catal. Today* **1999**, *50*, 353.
8. Bernal, S.; Calvino, J. J.; Cauqui, M. A.; Gatica, J. M.; Larese, C.; Perez Omil, J. A.; Pintado, J. M. *Catal. Today* **1999**, *50*, 175.
9. Di Monte, R.; Kaspar, J. *Top. Catal.* **2004**, *28*, 47.
10. Bartholomew, C. H.; Farrauto, R. J. *Fundamentals of Industrial Catalytic Processes*, 2nd ed: Wiley and Sons: Hoboken, NJ, 2006.
11. Hagen, J. *Industrial Catalysis - A Practical Approach*, 2nd ed.; Wiley-VCH: Weinheim, Germany, 2006.
12. Bond, G. C.; Burch, R.; Birkett, M. D.; Kuhn, A. T.; Webb, G. Strong metal-support interactions. In *Catalysis: Volume 6*; The Royal Society of Chemistry, 1983.
13. Tauster, S. J.; Fung, S. C.; Garten, R. L. *J. Am. Chem. Soc.* **1978**, *100*, 170.
14. Misono, M.; Makoto, M. Chapter 2 - Chemistry and Catalysis of Mixed Oxides. In *Studies in Surface Science and Catalysis*; Elsevier; Amsterdam; 2013.
15. Di Monte, R.; Kaspar, J. *Catal. Today* **2005**, *100*, 27.
16. Abdelkader, A.; Daly, H.; Saih, Y.; Morgan, K.; Mohamed, M. A.; Halawy, S. A.; Hardacre, C. *Int. J. Hydrogen Energ.* **2013**, *38*, 8263.
17. Reddy, B. M.; Khan, A. *Catal. Rev.-Sci. Eng.* **2005**, *47*, 257.
18. Astruc, D. Transition-Metal Nanoparticles in Catalysis: From Historical Background to the State-of-the Art. In *Nanoparticles and Catalysis*; Wiley-VCH Verlag GmbH & Co. KGaA: Weinheim, 2008.
19. Xia, Y.; Yang, H.; Campbell, C. T. *Acc. Chem. Res.* **2013**, *46*, 1671.
20. Valden, M.; Lai, X.; Goodman, D. W. *Science* **1998**, *281*, 1647
21. Schlogl, R.; Abd Hamid, S. B. *Angew. Chem. Int. Ed.* **2004**, *43*, 1628.
22. Bell, A. T. *Science* **2003**, *299*, 1688.
23. Sambur, J. B.; Chen, P. *Annu. Rev. Phys. Chem.* **2014**, *65*, 395.
24. Hammer, B. *Top. Catal.* **2006**, *37*, 3.
25. Karim, A. M.; Prasad, V.; Mpourmpakis, G.; Lonergan, W. W.; Frenkel, A. I.; Chen, J. G.; Vlachos, D. G. *J. Am. Chem. Soc.* **2009**, *131*, 12230.
26. Pecchi, G.; Reyes, P.; Gomez, R.; Lopez, T.; Fierro, J. L. G. *Appl. Catal. B: Environ.* **1998**, *17*, L7.

27. Epling, W. S.; Hoflund, G. B. *J. Catal.* **1999**, *182*, 5.
28. Manasilp, A.; Gulari, E. *Appl. Catal. B: Environ.* **2002**, *37*, 17.
29. Grisel, R. J. H.; Nieuwenhuys, B. E. *J. Catal.* **2001**, *199*, 48.
30. Haruta, M. *Catal. Today* **1997**, *36*, 153.
31. Cuenya, B. R. *Thin Solid Films* **2010**, *518*, 3127.
32. Parres-Esclapez, S.; Illan-Gomez, M. J.; de Lecea, C. S.-M. n.; Bueno-Lopez, A. *Appl. Catal. B: Environ.* **2010**, *96*, 370.
33. Ahmadi, T. S.; Wang, Z. L.; Green, T. C.; Henglein, A.; El-Sayed, M. A. *Science* **1996**, *272*, 1924.
34. Roucoux, A.; Schulz, J. r.; Patin, H. *Chem. Rev.* **2002**, *102*, 3757.
35. Burch, R.; Bond, G. C.; Webb, G. Structure and properties of supported noble metal catalysts. In *Catalysis: Volume 7*; The Royal Society of Chemistry, 1985.
36. Liguras, D. K.; Kondarides, D. I.; Verykios, X. E. *Appl. Catal. B: Environ.* **2003**, *43*, 345.
37. Rioche, C.; Kulkarni, S.; Meunier, F. C.; Breen, J. P.; Burch, R. *Appl. Catal. B: Environ.* **2005**, *61*, 130.
38. Panagiotopoulou, P.; Kondarides, D. I. *J. Catal.* **2004**, *225*, 327.
39. Santos, V. P.; Carabineiro, S. A. C.; Tavares, P. B.; Pereira, M. F. R.; Orfao, J. J. M.; Figueiredo, J. L. *Appl. Catal. B: Environ.* **2010**, *99*, 198.
40. Qin, D.; Lapszewicz, J. *Catal. Today* **1994**, *21*, 551.
41. Fageria, P.; Gangopadhyay, S.; Pande, S. *RSC Adv.* **2014**, *4*, 24962.
42. Rylander, P. N. *Organic Syntheses with Noble Metal Catalysts*; Academic press, New York ; 1973.
43. Gandhi, H. S.; Graham, G. W.; McCabe, R. W. *J. Catal.* **2003**, *216*, 433.
44. He, H.; Dai, H. X.; Ng, L. H.; Wong, K. W.; Au, C. T. *J. Catal.* **2002**, *206*, 1.
45. Yao, Y.-F. *J. Catal.* **1984**, *87*, 152.
46. Nguyen, N. L.; de Gironcoli, S.; Piccinin, S. *J. Chem. Phys.* **2013**, *138*, 184707.
47. Qian, M.; Liauw, M. A.; Emig, G. *Appl. Catal. A: Gen.* **2003**, *238*, 211.
48. Chen, A. K.; Masel, R. *Surf. Sci.* **1995**, *343*, 17.
49. Mo, L.; Zheng, X.; Yeh, C.-T. *Chem. Commun.* **2004**, 1426.

50. Alejo, L.; Lago, R.; Pena, M. A.; Fierro, J. L. G. *Appl. Catal. A: Gen.* **1997**, *162*, 281.
51. Haruta, M.; Yamada, N.; Kobayashi, T.; Iijima, S. *J. Catal.* **1989**, *115*, 301.
52. Fuentes, G. A.; Bartholomew, C. H. *Catalyst Deactivation*; Elsevier, Amsterdam; 1997.
53. Moulijn, J. A.; van Diepen, A. E.; Kapteijn, F. *Appl. Catal. A: Gen.* **2001**, *212*, 3.
54. Forzatti, P.; Lietti, L. *Catal. Today* **1999**, *52*, 165.
55. Bartholomew, C. H.; Spivey, J. J.; Agarwal, S. K. Model catalyst studies of supported metal sintering and redispersion kinetics. In *Catalysis: Volume 10*; The Royal Society of Chemistry, 1993.
56. Cao, A.; Lu, R.; Veser, G. *Phys. Chem. Chem. Phys.* **2010**, *12*, 13499.
57. Euzen, P.; Le Gal, J.-H.; Rebours, B.; Martin, G. r. *Catal. Today* **1999**, *47*, 19.
58. Borgna, A.; Le Normand, F.; Garetto, T.; Apesteguia, C. R.; Moraweck, B. *Catal. Lett.* **1992**, *13*, 175.
59. Birgersson, H.; Eriksson, L.; Boutonnet, M.; Jaras, S. G. *Appl. Catal. B: Environ.* **2004**, *54*, 193.
60. Shao-Horn, Y.; Sheng, W. C.; Chen, S.; Ferreira, P. J.; Holby, E. F.; Morgan, D. *Top. Catal.* **2007**, *46*, 285.
61. Liu, J. *Microsc. Microanal.* **2003**, *9(Suppl 2)*, 290.
62. Bartholomew, C. H. *Appl. Catal. A: Gen.* **2001**, *212*, 17.
63. Campbell, C. T. *Acc. Chem. Res.* **2013**, *46*, 1712.
64. Wynblatt, P.; Gjostein, N. A. *Prog. Solid State Chem.* **1975**, *9*, 21.
65. Harris, P.J. F. *Int. Mater. Rev.* **1995**, *40*, 97.
66. Granqvist, C. G.; Buhrman, R. A. *J. Catal.* **1976**, *42*, 477.
67. Flynn, P. C.; Wanke, S. E. *J. Catal.* **1975**, *37*, 432.
68. Fiedorow, R. M. J.; Chahar, B. S.; Wanke, S. E. *J. Catal.* **1978**, *51*, 193.
69. C.H. Bartholomew, in: *Catalyst Deactivation, Studies in Surface Science and Catalysis*, vol. 88, Elsevier, Amsterdam; 1994.
70. Chen, J.; Heck, R. M.; Farrauto, R. J. *Catal. Today* **1992**, *11*, 517
71. Oudet, F.; Vejux, A.; Courtine, P. *Appl. Catal.* **1989**, *50*, 79.

72. Eliasson, B.; Bossel, U. "The Future of the Hydrogen Economy: Bright or Bleak?", Proceedings, The Fuel Cell World, Lucerne / Switzerland, July 2002.
73. BMW Group Clean Energy ZEV Symposium. September 2006, p. 12.
74. Baschuk, J. J.; Li, X. *Int. J. Energy Res.* **2001**, *25*, 695.
75. Igarashi, H.; Fujino, T.; Watanabe, M. *J. Electroanal. Chem.* **1995**, *391*, 119.
76. Newsome, D. S. *Catal. Rev.-Sci. Eng.* **1980**, *21*, 275.
77. Grenoble, D. C.; Estadt, M. M.; Ollis, D. F. *J. Catal.* **1981**, *67*, 90.
78. Ratnasamy, C.; Wagner, J. P. *Catal. Rev.* **2009**, *51*, 325.
79. Byron Smith R. J.; Muruganandam, L.; Murthy S. S. *Int. J. Chem. React. Eng.* **2010** *8*, 1.
80. Ladebeck, J. R.; Wagner, J. P. Catalyst development for water-gas shift, , Volume 3, Part 2, pp 190–201, in Handbook of Fuel Cells – Fundamentals, Technology and Applications, John Wiley & Sons, Ltd, Chichester; 2003.
81. Ruettinger, W.; Ilinich, O.; Farrauto, R. J. *J. Power Sources* **2003**, *118*, 61.
82. Bunluesin, T.; Gorte, R. J.; Graham, G. W. *Appl. Catal. B: Environ.* **1998**, *15*, 107.
83. Panagiotopoulou, P.; Papavasiliou, J.; Avgouropoulos, G.; Ioannides, T.; Kondarides, D. I. *Chem. Eng. J.* **2007**, *134*, 16.
84. Catalano, J.; Guazzone, F.; Mardilovich, I. P.; Kazantzis, N. K.; Ma, Y. H. *Ind. Eng. Chem. Res.*, **2012**, *52*, 1042.
85. Basinska, A.; Domka, F. *Appl. Catal. A: Gen.* **1999**, *179*, 241.
86. Hilaire, S., Wang, X., Luo, T., Gorte, R. J., and Wagner, J. P. *Appl. Catal. A: Gen.* **2001**, *215*, 271.
87. Li, Y.; Fu, Q.; Flytzani-Stephanopoulos, M. *Appl. Catal. B: Environ.* **2000**, *27*, 179.
88. Barrio, L.; Zhou, G.; Gonzalez, I. D.; Estrella, M.; Hanson, J.; Rodriguez, J. A.; Navarro, R. M.; Fierro, J. L. G. *Phys. Chem. Chem. Phys.* **2012**, *14*, 2192.
89. Kim, Y. T.; Park, E. D.; Lee, H. C.; Lee, D.; Lee, K. H. *Appl. Catal. B: Environ.* **2009**, *90*, 45.
90. Y. Li, Qi Fu and M. Flytzani-Stephanopolos, *Appl. Catal. B: Environ.* **2000**, *27*, 179.
91. Panagiotopoulou, P.; Kondarides, D. I. *Catal. Today* **2006**, *112*, 49.

92. Boccuzzi, F.; Chiorino, A.; Manzoli, M.; Andreeva, D.; Tabakova, T. *J. Catal.* **1999**, *188*, 176.
93. Trovarelli, A. *Catalysis by Ceria and Related Materials*, Catalytic Science Series, vol. 2, Imperial College Press, London; 2002.
94. Trovarelli, A. *Catal. Rev.-Sci. Eng.* **1996**, *38*, 439
95. Kim, C.H.; Thompson, L.T. *J. Catal.* **2005**, *230*, 66.
96. Fu, Q.; Deng, W.; Saltsburg, H.; Flytzani-Stephanopoulos, M. *Appl. Catal. B: Environ.* **2005**, *56*, 57.
97. Liu, X.; Ruettinger, W.; Xu, X.; Farrauto, R. *Appl. Catal. B: Environ.* **2005**, *56*, 69.
98. Ruettinger, W.; Liu, X.; Farrauto, R. *J. Appl. Catal. B: Environ.* **2006**, *65*, 135.
99. Wang, X.; Gorte, R. J.; Wagner, J. P. *J. Catal.* **2002**, *212*, 225.
100. Goguet, A.; Burch, R.; Chen, Y.; Hardacre, C.; Hu, P.; Joyner, R. W.; Meunier, F. C.; Mun, B. S.; Thompsett, D.; Tibiletti, D. *J. Phys. Chem. C* **2007**, *111*, 16927.
101. Zalc, J. M.; Sokolovskii, V.; Loffler, D. G. *J. Catal.* **2002**, *206*, 169.
102. T. Shido and Y. Iwasawa, *J. Catal.* **1993**, *141*, 71
103. Jacobs, G.; Graham, U. M.; Chenu, E.; Patterson, P. M.; Dozier, A.; Davis, B. H. *J. Catal.* **2005**, *229*, 499.
104. Jacobs, G.; Patterson, P. M.; Graham, U. M.; Sparks, D. E.; Davis, B. H. *Appl. Catal. A: Gen.* **2004**, *269*, 63.
105. Jacobs, G.; Patterson, P. M.; Williams, L.; Chenu, E.; Sparks, D.; Thomas, G.; Davis, B. H. *Appl. Catal. A: Gen.* **2004**, *262*, 177.
106. Rodriguez, J. A.; Senanayake, S. D.; Stacchiola, D.; Liu, P.; Hrbek, J. *Acc. Chem. Res.* **2014**, *47*, 773.
107. Grabow, L. C.; Gokhale, A. A.; Evans, S. T.; Dumesic, J. A.; Mavrikakis, M. *J. Phys. Chem. C* **2008**, *112*, 4608.
108. Rhodes, C.; Hutchings, G. J.; Ward, A. M. *Catal. Today* **1995**, *23*, 43.
109. Flaherty, D. W.; Yu, W.-Y.; Pozun, Z. D.; Henkelman, G.; Mullins, C. B. *J. Catal.* **2011**, *282*, 278.
110. Gokhale, A. A.; Dumesic, J. A.; Mavrikakis, M. *J. Am. Chem. Soc.* **2008**, *130*, 1402.
111. Kalamaras, C. M.; Americanou, S.; Efstathiou, A. M. *J. Catal.* **2011**, *279*, 287.

112. Zafiridis, G. S.; Gorte, R. J. *J. Catal.* **1993**, *139*, 561.
113. Royer, S.; Duprez, D. *Chem. Cat. Chem.* **2011**, *3*, 24.
114. Liu, K.; Wang, A.; Zhang, T. *ACS Catal.* **2012**, *2*, 1165.
115. McClure, S. M.; Goodman, D. W. *Chem. Phys. Lett.* **2009**, *469*, 1.
116. Santra, A. K.; Goodman, D. W. *Electrochim. Acta.* **2002**, *47*, 3595.
117. Freund, H.-J.; Meijer, G.; Scheffler, M.; Schlogl, R.; Wolf, M. *Angew. Chem. Int. Ed.* **2011**, *50*, 10064.
118. Engel, T.; Ertl, G. *Adv. Catal.* **1979**, *28*, 1.
119. Jones, I. Z.; Bennett, R. A.; Bowker, M. *Surf. Sci.* **1999**, *439*, 235.
120. Engel, T.; Ertl, G. *J. Chem. Phys.* **1978**, *69*, 1267.
121. Stampfl, C.; Scheffler, M. *Surf. Sci.* **1999**, *433–435*, 119.
122. Peden, C. H. F.; Goodman, D. W. *J. Phys. Chem.* **1986**, *90*, 1360.
123. Lee, H. -I.; White, J. M. *J. Catal.* **1980**, *63*, 261.
124. Peden, C. H. F.; Goodman, D. W.; Weisel, M. D.; Hoffmann, F. M. *Surf. Sci.* **1991**, *253*, 44.
125. Yang, J. H.; Henao, J. D.; Raphulu, M. C.; Wang, Y.; Caputo, T.; Groszek, A. J.; Kung, M. C.; Scurrrell, M. S.; Miller, J. T.; Kung, H. H. *J. Phys. Chem. B* **2005**, *109*, 10319.
126. Knell, A.; Barnickel, P.; Baiker, A.; Wokaun, A. *J. Catal.* **1992**, *137*, 306.
127. Wang, L.-C.; Liu, Q.; Huang, X.-S.; Liu, Y.-M.; Cao, Y.; Fan, K.-N. *Appl. Catal. B: Environ.* **2009**, *88*, 204.
128. Choudhary, T. V.; Goodman, D. W. *Top. Catal.* **2002**, *21*, 25.
129. Bamwenda, G. R.; Tsubota, S.; Nakamura, T.; Haruta, M. *Catal. Lett.* **1997**, *44*, 83.
130. Grisel, R. J. H.; Nieuwenhuys, B. E. *Catal. Today* **2001**, *64*, 69.
131. Bamwenda, G. R.; Tsubota, S.; Nakamura, T.; Haruta, M. *Catal. Lett.* **1997**, *44*, 83.
132. Grunwaldt, J.-D.; Baiker, A. *J. Phys. Chem. B* **1999**, *103*, 1002.
133. Canning, N. D. S.; Madix, R. J. *Surf. Sci.* **1984**, *141*, 240.
134. Bondzie, V. A.; Campbell, C. T. *J. Vac. Sci. Technol., A* **1999**, *17*, 1717.
135. Schubert, M. M.; Hackenberg, S.; van Veen, A. C.; Muhler, M.; Plzak, V.; Behm, R. J. *J. Catal.* **2001**, *197*, 113.
136. Haruta, M. *Catal. Surv. Asia* **1997**, *1*, 61.

137. Mavrikakis, M.; Stoltze, P.; Nørskov, J. K. *Catal. Lett.* **2000**, *64*, 101.
138. Valden, M.; Pak, S.; Lai, X.; Goodman, D. W. *Catal. Lett.* **1998**, *56*, 7.
139. Liu, H.; I. Kozlov, A.; P. Kozlova, A.; Shido, T.; Iwasawa, Y. *Phys. Chem. Chem. Phys.* **1999**, *1*, 2851.
140. Bollinger, M. A.; Vannice, M. A. *Appl. Catal. B: Environ.* **1996**, *8*, 417.
141. Tripathi, A. K.; Kamble, V. S.; Gupta, N. M. *J. Catal.* **1999**, *187*, 332.
142. Valden, M.; Lai, X.; Goodman, D. W. *Science* **1998**, *281*, 1647.
143. Mavrikakis, M.; Stoltze, P.; Nørskov, J. K. *Catal. Lett.* **2000**, *64*, 101.
144. Costello, C. K.; Kung, M. C.; Oh, H. S.; Wang, Y.; Kung, H. H. *Appl. Catal. A: Gen.* **2002**, *232*, 159.
145. Hendriksen, B. L. M.; Frenken, J. W. M. *Phys. Rev. Lett.* **2002**, *89*, 046101-1.
146. Chen, M. S.; Cai, Y.; Yan, Z.; Gath, K. K.; Axnanda, S.; Goodman, D. W. *Surf. Sci.* **2007**, *601*, 5326.
147. Gorte, R. J.; Zhao, S. *Catal. Today* **2005**, *104*, 18.
148. Fu, Q.; Saltsburg, H.; Flytzani-Stephanopoulos, M. *Science* **2003**, *301*, 935.
149. Fu, Q.; Kudriavtseva, S.; Saltsburg, H.; Flytzani-Stephanopoulos, M. *Chem. Eng. J.* **2003**, *93*, 41.
150. Fu, Q.; Deng, W.; Saltsburg, H.; Flytzani-Stephanopoulos, M. *Appl. Catal., B: Environ.* **2005**, *56*, 57.
151. Davis, R. J. *Science* **2003**, *301*, 926.
152. Liu, Z.; Jenkins, S. J.; King, D. A. *Phys. Rev. Lett.* **2005**, *94*, 196102.
153. Alayon, E. M. C.; Singh, J.; Nachtegaal, M.; Harfouche, M.; Bokhoven, J. A. v. *J. Phys. Conf. Ser.* **2009**, *190*, 012152.
154. Carrettin, S.; Corma, A.; Iglesias, M.; Sanchez, F. *Appl. Catal. A: Gen.* **2005**, *291*, 247.
155. Fu, L.; Wu, N. Q.; Yang, J. H.; Qu, F.; Johnson, D. L.; Kung, M. C.; Kung, H. H.; Dravid, V. P. *J. Phys. Chem. B* **2005**, *109*, 3704.
156. Guzman, J.; Gates, B. C. *J. Am. Chem. Soc.* **2004**, *126*, 2672.
157. Thomas, J. M. *J. Chem. Phys.* **2008**, *128*, 182502.
158. Hegde, M. S.; Madras, G.; Patil, K. C. *Acc. Chem. Res.* **2009**, *42*, 704.
159. Baidya, T.; Dutta, G.; Hegde, M. S.; Waghmare, U. V. *Dalton Trans.* **2009**, *3*, 455.

160. Bera, P.; Patil, K. C.; Jayaram, V.; Subbanna, G. N.; Hegde, M. S. *J. Catal.* **2000**, *196*, 293.
161. Gayen, A.; Priolkar, K. R.; Sarode, P. .; Jayaram, V.; Hegde, M. S.; Emura, S. *Chem. Mater.* **2004**, *16*, 2317.
162. Chretien, S.; Metiu, H. *Catal. Lett.* **2006**, *107*, 143.
163. Bera, P.; Priolkar, K. R.; Sarode, P. R.; Hegde, M. S.; Emura, S.; Kumashiro, R.; Lalla, N. P. *Chem. Mater.* **2002**, *14*, 3591.
164. Bera, P.; Malwadkar, S.; Gayen, A.; Satyanarayana, C. V. V.; Rao, B. S.; Hegde, M. S. *Catal. Lett.* **2004**, *96*, 213.
165. Perez-Alonso, F. J.; Melian-Cabrera, I.; Lopez Granados, M.; Kapteijn, F.; Fierro, J. L. *G. J. Catal.* **2006**, *239*, 340.
166. Shan, W.; Feng, Z.; Li, Z.; Zhang, J.; Shen, W.; Li, C. *J. Catal.* **2004**, *228*, 206.
167. Megaw, H. D. *Nature* **1945**, *155*, 484.
168. Woodward, P. M. *Acta Cryst.* **1997**, *B53*, 32.
169. Goldschmidt, V. M. *Naturwissenschaften.* **1926**, *14*, 477.
170. Smyth, D. M. *Annu. Rev. Mater. Sci.* **1985**, *15*, 329.
171. Pfaff, E. M.; Kaletsch, A.; Broeckmann, C. *Chem. Eng. Technol.* **2012**, *35*, 455.
172. Gellings, P. J.; Bouwmeester, H. J. M. *Catal. Today* **1992**, *12*, 1-101.
173. Ryu, K. H.; Haile, S. M. *Solid State Ionics* **1999**, *125*, 355.
174. Zajac, W.; Rusinek, D.; Zheng, K.; Molenda, J. *Cent. Eur. J. Chem.* **2013**, *11*, 471.
175. Pena, M. A.; Fierro, J. L. G. *Chem. Rev.* **2001**, *101*, 1981.
176. Hibbert, D. B. *Catal. Rev.-Sci. Eng.* **1992**, *34*, 391.
177. Petunchi, J. O.; Ulla, M. A.; Marcos, J. A.; Lombardo, E. A. *J. Catal.* **1981**, *70*, 356.
178. Seiyama, T. *Catal. Rev.-Sci. Eng.* **1992**, *34*, 281.
179. Maegli, A. E.; Hisatomi, T.; Otal, E. H.; Yoon, S.; Pokrant, S.; Gratzel, M.; Weidenkaff, A. *J. Mater. Chem.* **2012**, *22*, 17906.
180. Liu, S. -K.; Lin, Y. -C. *Ind. Eng. Chem. Res.* **2012**, *51*, 16278.
181. Lombardo, E. A.; Ulla, M. A. *Res. Chem. Intermediat.* **1998**, *24*, 581.
182. Suntivich, J.; Gasteiger, H. A.; Yabuuchi, N.; Nakanishi, H.; Goodenough, J. B.; Shao-Horn, Y. *Nat. Chem.* **2011**, *3*, 546.

183. Labhsetwar, N.; Biniwale, R. B.; Kumar, R.; Rayalu, S.; Devotta, S. *Catal. Surv. Asia* **2006**, *10*, 55.
184. Yao, W.; Wang, R.; Yang, X. *Catal. Lett.* **2009**, *130*, 613.
185. Giebeler, L.; Kießling, D.; Wendt, G. *Chem. Eng. Tech.* **2007**, *30*, 889.
186. Nishihata, Y.; Mizuki, J.; Akao, T.; Tanaka, H.; Uenishi, M.; Kimura, M.; Okamoto, T.; Hamada, N. *Nature* **2002**, *418*, 164.
187. Li, J.; Singh, U. G.; Bennett, J. W.; Page, K.; Weaver, J. C.; Zhang, J.; Proffen, T.; Rappe, A. M.; Scott, S. L.; Seshadri, R. *Chem. Mater.* **2007**, *19*, 1418.
188. Zhu, J.; Li, H.; Zhong, L.; Xiao, P.; Xu, X.; Yang, X.; Zhao, Z.; Li, J. *ACS Catal.* **2014**, *4*, 2917.
189. Schaak, R. E.; Mallouk, T. E. *Chem. Mater.* **2002**, *14*, 1455.
190. Zeng, Y.; Lin, Y. S.; Swartz, S. L. *J. Membrane Sci.* **1998**, *150*, 87.
191. Mori, M.; Sammes, N. M.; Tompsett, G. A. *J. Power Sources* **2000**, *86*, 395.
192. Huang, K.; Feng, M.; Goodenough, J. B. *J. Am. Ceram. Soc.* **1996**, *79*, 1100.
193. Deganello, F.; Marci, G.; Deganello, G. *J. Eur. Ceram. Soc.* **2009**, *29*, 439.
194. Gomez-Romero, P.; Tejada-Rosales, E. M.; Palacin, M. R. *Angew. Chem. Int. Ed.* **1999**, *38*, 524.
195. Tejada-Rosales, E. M.; Rodriguez-Carvajal, J.; Casan-Pastor, N.; Alemany, P.; Ruiz, E.; El-Fallah, M. S.; Alvarez, S.; Gomez-Romero, P. *Inorg. Chem.* **2002**, *41*, 6604.
196. Curda, J.; Klein, W.; Jansen, M. *J. Solid State Chem.* **2001**, *162*, 220.
197. Curda, J.; Klein, W.; Liu, H.; Jansen, M. *J. Alloys Compd.* **2002**, *338*, 99.
198. Munoz-Rojas, D.; Oro, J.; Gomez-Romero, P.; Fraxedas, J.; Casan-Pastor, N. *Electrochem. Commun.* **2002**, *4*, 684.
199. Munoz-Rojas, D.; Fraxedas, J.; Oro, J.; Gomez-Romero, P.; Casan-Pastor, N. *Cryst. Eng.* **2002**, *5*, 459.
200. Munoz-Rojas, D.; Fraxedas, J.; Gomez-Romero, P.; Casan-Pastor, N. *J. Solid State Chem.* **2005**, *178*, 295.

Chapter 2

Synthesis, Characterisation and WGS Activity Studies of Pt and Y Doped BaCeO₃ Catalysts: Activity of Cationic Pt and Role of Oxygen Vacancies towards WGS Reaction

Part A

**Synthesis, Characterization, WGS Activity and
Reactor Shut down Studies of $\text{BaCe}_{1-x}\text{Pt}_x\text{O}_{3-\delta}$;
($x = 0.02, 0.04$ and 0.06): Activity and Stability of
Cationic Pt**

2A.1. Introduction

The concept of stabilization of noble metals via incorporation into stable lattices like perovskites to address the problem of sintering associated with supported metal catalysts is already introduced in the chapter 1. Some attempts to stabilize the noble metals in the fluorite and perovskite lattices are already reported. Nishihata et al. reported that, in the Pd doped LaFeO₃ perovskite, Pd occupies the B-site of the perovskite structure in oxidative atmospheres and it segregates out to form metallic particles in the reductive atmospheres and display catalytic activity [1]. This reversible movement of Pd minimises the probability of agglomeration and growth of the metal particles. As mentioned in chapter 1, section 1.5, Prof. Seshadri's group attempted to stabilize Pd in BaCeO₃ and found that square planar Pd(II) substitute the octahedral Ce(IV) with the concomitant creation of oxygen vacancies [2, 3]. Moreover they also observed that the Pd species ingress and egress from the lattice depending on the conditions that the catalysts are subjected to, viz, oxidising or reducing, respectively.

However in the work described in this chapter, attempt is to stabilize the noble metal inside the perovskite lattice and to establish the catalytic activity of noble metal cations present in the lattice sites. The advantage of this strategy is that it does not lead to structural variations with reaction conditions, but provides an active sinter resistant catalyst. However the selection of appropriate perovskite lattice is crucial as the harsh reducing conditions employed in the WGS reaction may directly affect the structure of the perovskite or may lead to the egression of metallic Pt particles. BaCeO₃ presents an ideal candidate system to investigate such type of lattice incorporated noble metal ion activity. BaCeO₃ and its doped systems are well studied for proton conduction, where the mechanism involves dissociative adsorption of water similar to the steps involved in the WGS reaction mechanism [4-8]. Moreover the well known redox and substitution tolerance properties of cerium can be exploited [9-11]. In addition, one can make use of the oxygen vacancies present in the system to facilitate the water dissociation steps. So the focus of the work is to dope Pt in the Ce-site of BaCeO₃, study the structure using various techniques, establish the activity of the cationic platinum towards WGS reaction. In addition, the work is extended to demonstrate the stability of the above

system under different shut down conditions which are proposed to be contributing towards catalyst deactivation.

2A.2. Experimental Section

2A.2.1. Synthesis of BaCe_{1-x}Pt_xO_{3-δ} (x = 0.02, 0.04 & 0.06)

Combustion method using citric acid as fuel was employed to synthesise the Pt doped and undoped perovskites. In a typical synthesis procedure, barium nitrate (0.003 mol) (Aldrich) was dissolved in 50 ml water. Citric acid monohydrate (0.012 mol) (Merck) followed by ceric ammonium nitrate (0.003 mol) (Aldrich) were added to synthesise undoped BaCeO₃. Appropriate concentration of tetraammineplatinum (II) nitrate (Aldrich) was added for the Pt doped sample. Ammonia solution was used to adjust the pH of the solution to 7. The solution was then heated to 90 °C to get a gel which was then heated at 400 °C for 1 h to remove organic and volatile components. The obtained powder was ground well and then calcined at 900 °C for 6 h to get the perovskite.

2A.2.2. Characterization

The principles of all the techniques used throughout the work are briefly discussed in the Appendix. Structural characterization using powder X-ray diffraction (PXRD) was carried out in a PANalytical X'pert Pro dual goniometer diffractometer. The radiation used was Cu K α (1.5418 Å) at 40 kV and 30 mA with a Ni filter. The data was collected using a flat holder in Bragg–Brentano geometry with 1° slit at the source side. An X'celerator solid state detector with step size of 0.008° and time per step of 45.72 s was employed. Rietveld refinement of the PXRD patterns was done by means of the GSAS-EXPGUI program [12]. The initial refinement of background and scale factors was followed by that of cell parameters and positional parameters. Variable temperature in-situ XRD experiments were carried out in an Anton-Paar XRK900 reactor under 10 % H₂/N₂. The XRD patterns in the 2 θ range 18-90° and 38-44° were collected with step size of 0.008° and time per step of 45.72 s and with step size of 0.008° and time per step of 100 s respectively. For the shut down experiments inside the Anton-Paar XRK900

reaction chamber, reformat feed with a composition of 40.3 % H₂, 10.1 % CO, 14.5 % CO₂ and balance N₂ saturated with water vapour by bubbling the feed through a flask containing water was used. The experiments were carried up to 400 °C with data collection done at intervals of 100 °C after passing for half an hour at each temperature with a step size of 0.008° and time per step of 42.5 s for the 2θ range 26.5-84.5° and step size of 0.008° and a time per step of 100 s for the 2θ range 38-42° respectively.

Neutron diffraction patterns were acquired at room temperature on the profile analysis spectrometer T1015 attached to Dhruva reactor. Neutrons of constant wavelength, 1.2443 Å were used and the detection of the scattered neutrons were done using an array of five ³He linear position sensitive detectors covering a range of 6 to 137°. The Rietveld refinement of the neutron data was carried out using FullProf software [13]. The starting model consisted of BaCeO₃ (space group Pnma) and an impurity phase of CeO₂ in the case of 2 and 4 mol% Pt doped samples and BaCO₃ phase in the case of the sample with 6 mol% Pt. Initially scale factor was refined followed by lattice parameters and preceded through profile factors, atomic positions, thermal factors and occupancies. Finally the oxygen occupancy is varied along with all the other parameters to get the final fit.

HRTEM observations of the samples were done with the help of FEI Tecnai TF-30 electron microscope, operating at 300 kV. Samples for the observations were prepared by placing a drop of the suspension of the sample in isopropanol onto a carbon-coated copper mesh 200 grid and then evaporating the solvent. The concentrations of platinum present in the samples were determined by ICP-AES technique on Spectro Arcos, FHS-12. A clear solution of the materials in aqua regia was used for the analysis.

The surface characterization was done using X-ray photoelectron spectroscopy (XPS) with a multiprobe system (Omicron Nanotechnology, Germany) equipped with a dual Mg/Al X-ray source and a hemispherical analyzer operating in constant analyzer energy (CAE) mode. The spectra were obtained with pass energy of 50 eV for survey scan and individual scans. The Mg K α X-ray source was operated at 300 W and 15 kV.

The base pressure in the analyzing chamber was maintained at 1×10^{-10} mBar. The binding energy of 285 eV for adventitious carbon was taken as the reference binding energy for charge correction. The surface characterization of the samples used for the shut down study was carried out with a VSW scientific instrument (UK) with twin anode facility. An Al K α source (resolution ~ 0.9 eV) was employed. The detection of photoelectrons was done using a concentric hemispherical analyzer with a pass energy of 40 eV. For adventitious carbon, 285 eV was taken as the reference binding energy for charge correction. XPSPEAK41 software was used to perform data processing. A Shirley type of background is used and the spectra were deconvoluted using a mixture of Gaussian and Lorentzian lines.

2A.2.3. Catalytic testing

The set up for the evaluation of catalytic activity consists of a vertical, down flow, fixed bed tubular metal reactor, having length of 24 cm and internal diameter 0.9 cm placed inside a furnace (BTRS, Autoclave Engineers). Schematic representation of the set up is shown in figure 2A.1. About 0.3 cc of the catalyst in the particle size range of 10-20 mesh was loaded in to the tubular reactor that has a thermo well inserted to the center of the catalyst bed. A Cr-Al thermocouple was used to continuously monitor the temperature. A reformat mixture feed with a composition of 39.8 % H₂, 34.9 % N₂, 10.2 % CO and 15.2 % CO₂ (For the shut down studies, the reformat composition used was 40.3 % H₂, 35.1 % N₂, 10.1 % CO and 14.5 % CO₂) with steam to CO ratio 4.5 was used at a gas hour space velocity (GHSV) of 5000 h⁻¹. Water was sent to the reactor using an ISCO model 500D syringe pump, which was preheated and converted to steam by an inbuilt oven in the reactor. All the runs were carried out under atmospheric pressure. In a typical experiment, the temperature was gradually increased to 250 °C with a constant heating rate of 2 °C min⁻¹ under N₂. Activity was measured at intervals of 25 °C. At each temperature, the reformat mixture and steam were allowed to pass through the catalyst for half an hour. The gases were analyzed using a NUCON gas chromatograph equipped with a Carbosphere column and a thermal conductivity detector.

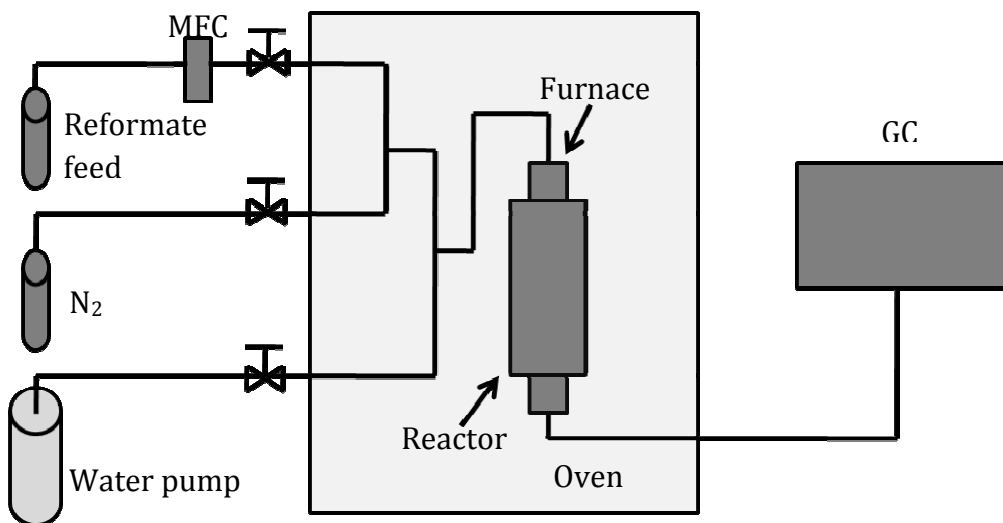


Figure 2A.1. Flow diagram of the catalytic reactor setup for WGS reaction.

2A.3. Results and discussion

2A.3.1. Synthesis and structural characterization

Most of the reports utilise solid state method employing high temperatures for the synthesis of doped or undoped BaCeO₃ [14-19]. Since the application of the material in this study is on catalysis, solution based citrate gel combustion method was used for the synthesis with phase formation at relatively lower temperatures enabling the particle size and morphologies ideal for the aforementioned application. The synthesis involves the combustion of the constituent metal nitrates with citric acid and then the structure formation after calcination at high temperatures. The molar concentrations of Pt were allowed to increase progressively as 2, 4 and 6 at the Ce site in the materials. This results in the final compositions of BaCe_{1-x}Pt_xO_{3-δ} (x = 0.02, 0.04 and 0.06) corresponding to the Pt weight percentages, 1.19, 2.38 and 3.56 respectively. ICP-AES analysis was used to determine the Pt concentrations in the synthesized materials and the obtained concentrations (1.02, 2.11 and 3.17 wt% respectively) are similar to the theoretical values. Structural characterization of all the Pt doped materials were done using PXRD and the corresponding diffraction patterns along with those of the parent perovskite and 0.8 wt% Pt impregnated perovskite are given in figure 2A.2A.

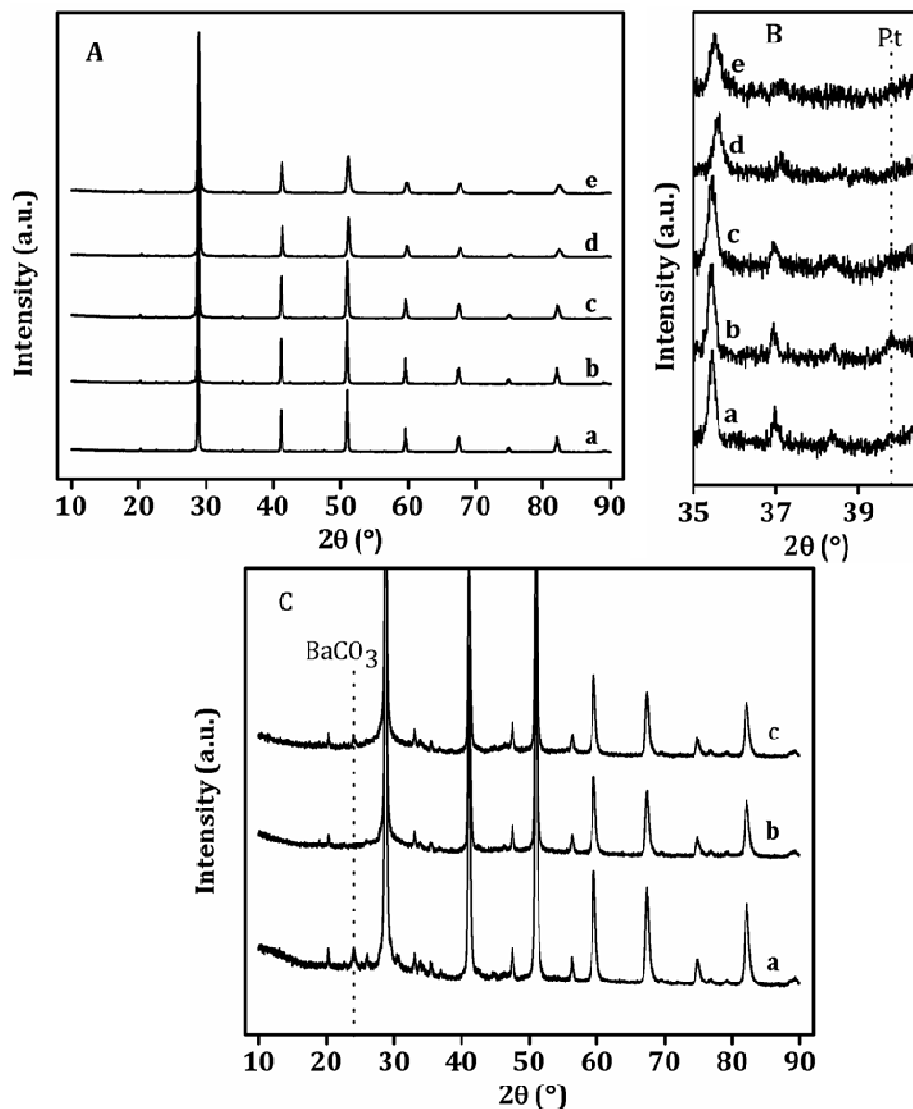


Figure 2A.2. (A) PXRD patterns of (a) BaCeO₃, (b) 0.8 wt% Pt impregnated BaCeO₃, and BaCe_{1-x}Pt_xO_{3-δ} with (c) $x = 0.02$, (d) $x = 0.04$, and (e) $x = 0.06$, (B) 2θ region where Pt(111) reflection appear and (C) PXRD patterns of (a) BaCe_{0.98}Pt_{0.02}O_{3-δ}, (b) after dil. HNO₃ wash, and (c) after heating at 400 °C for 1 h.

The PXRD patterns of all the Pt doped materials were consistent with orthorhombic space group and the patterns could be matched with that of BaCeO₃ [JCPDS: 82-2425] [20]. The PXRD pattern of the BaCeO₃ perovskite impregnated with 0.8 wt% Pt shows peaks corresponding to the metallic Pt clearly showing that even this small weight percentage of Pt can be detectable with PXRD (figure. 2A.2B). The PXRD

patterns of none of the Pt doped BaCeO₃ displayed any reflections corresponding to the fcc Pt suggesting that Pt ions are incorporated in the lattice sites of the perovskite. However trace amounts of BaCO₃ and CeO₂ were found to be present in all these samples. The 2 mol% Pt doped sample was washed with dil. HNO₃ to remove the BaCO₃ and the PXRD patterns (Figure. 2A.2C) show almost complete disappearance of peaks corresponding to the BaCO₃. However the peaks of BaCO₃ reappeared when the sample was heated at 400 °C in air. The segregation of BaCO₃ in barium containing compounds is already reported [21-23].

The knowledge of the tolerance limit for the Pt incorporation in BaCeO₃ is essential and to understand that, the Pt molar concentrations were further increased to 8 and 10 mol% corresponding to weight percentages of 4.73 and 5.89 respectively. PXRD patterns of the sample (figure 2A.3) with 8 mol% Pt, indicates complete stabilization of cationic Pt in the lattice while that of the 10 mol% Pt doped sample shows that a small percentage of metallic Pt egress out of the lattice pointing that ionic Pt substitution is not possible after this concentration. Quantitative analysis using Rietveld refinement revealed that only 0.3 wt% of Pt is out of the lattice.

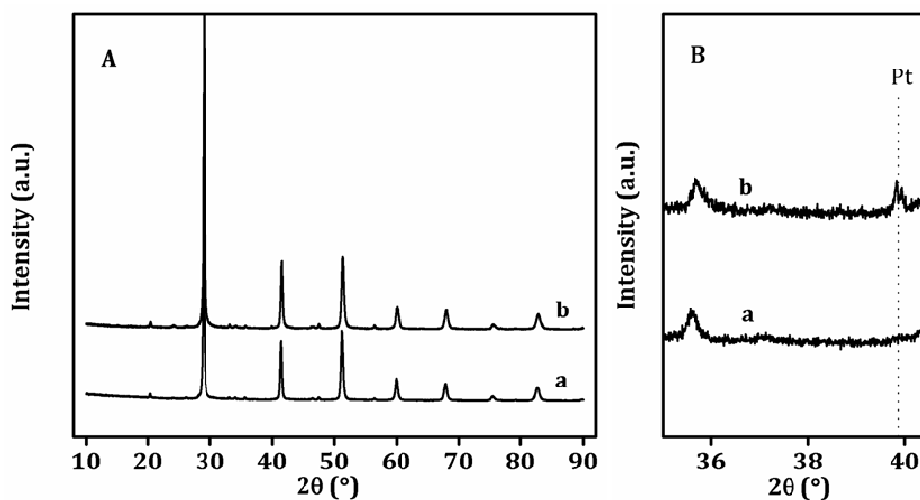


Figure 2A.3. (A) PXRD patterns of BaCe_{1-x}Pt_xO_{3-δ} (a) $x = 0.08$ and (b) $x = 0.10$, and (B) 2θ region where Pt(111) reflection appear.

Detailed Rietveld refinement has been done using GSAS-EXPGUI program on PXRD patterns of all the Pt doped samples to obtain quantitative information. Even though the pure BaCeO₃ has orthorhombic structure, substitution by Zr or Y in higher amount in this compound results in structure distortions to monoclinic $I2/m$ or rhombohedral $R\bar{3}c$ systems [24-25]. However the comparison of the experimental patterns of the doped sample with those of the simulated patterns of the various space groups revealed that the structure retained the $Pnma$ space group. Hence the refinement was carried out based on the $Pnma$ model. The resulted plots of the refinement are shown in figure 2A.4 and the parameters obtained are listed in table 2A.1. Pt occupancies are fixed based on the elemental analysis.

In an earlier work mentioned in section 2A.1., incorporation of Pd was attempted in BaCeO₃ lattice and it is suggested to occupy square planar geometry when doped in the Ce site [2]. In a similar way, the incorporation of Pt can have an effect on the coordination geometry of the B-site ion. The replacement of Ce(IV) by Pt(II) ion can be easily identified from the XRD as the crystallographic radii of octahedral Ce(IV) is 1.01 Å and that of square planar coordinated Pt(II) is 0.76 Å. Moreover this substitution can lead to the creation of oxygen vacancies to balance the charge. The estimation of oxygen vacancies created is of paramount importance to understand the substitution and to determine the properties of the material. When compared to the X-rays, neutron has higher scattering cross section for oxygen. Moreover the accurate measurement of the occupancy of oxygen is not possible with X-rays, since X-ray diffraction involves scattering from electron cloud and hence depend on atomic number and therefore the contribution of oxygen towards the scattering is lesser in presence of heavier elements. However the scattering cross section for neutron is almost same for all the elements and hence the determination of atomic oxygen positions is possible [26]. Hence neutron diffraction patterns of all the Pt doped BaCeO₃ samples were acquired and the Rietveld refinement of the patterns were carried out using Fullprof program. The refinement fits are shown in figure 2A.5A and the parameters obtained are listed in table 2A.2.

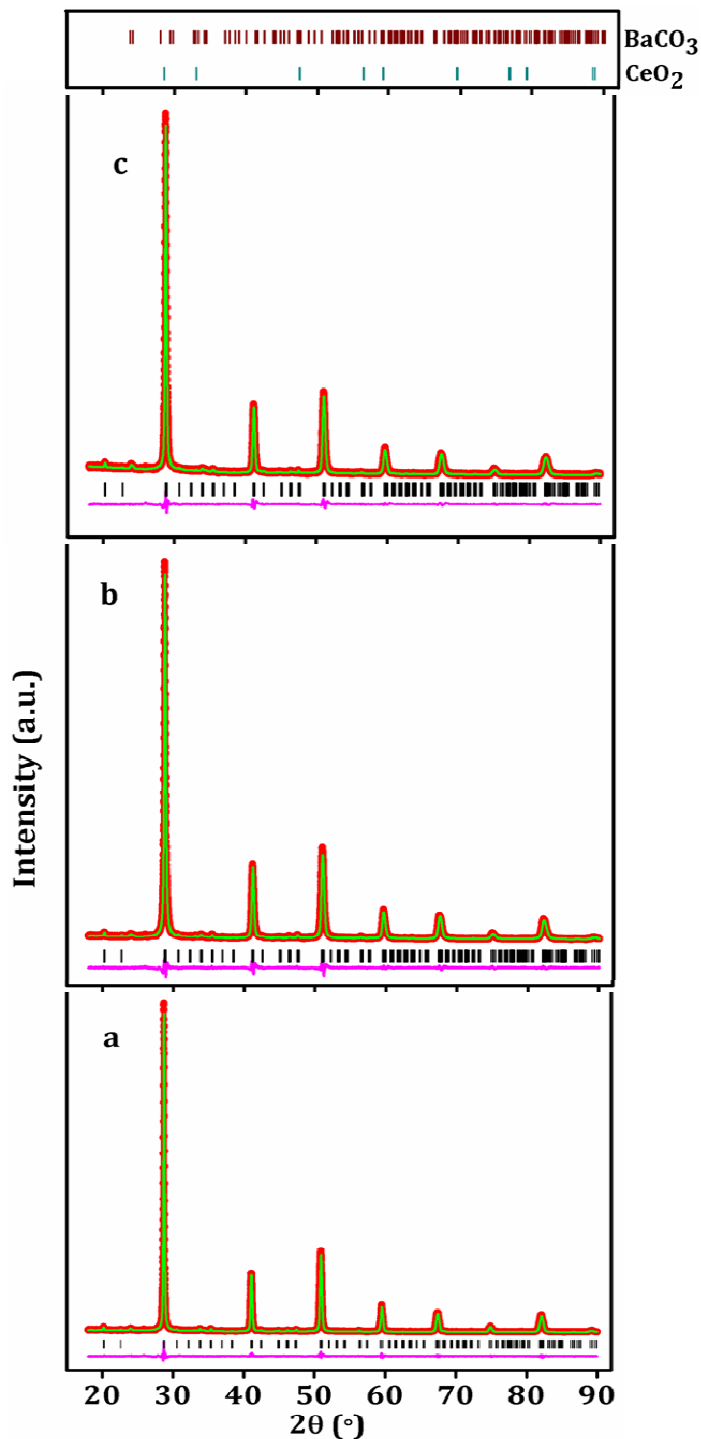


Figure 2A.4. Rietveld refinement of PXRD data for BaCe_{1-x}Pt_xO_{3- δ} with (a) $x = 0.02$, (b) $x = 0.04$ and (c) $x = 0.06$. Red line represents experimental data, green line is the Rietveld fit and pink line represents difference plot. Vertical lines at the top of the figure are the expected positions for the impurity phases BaCO₃ and CeO₂.

Table 2A.1. Crystal structures of BaCe_{1-x}Pt_xO_{3-δ} as obtained from Rietveld refinement of PXRD data.

Parameters	BaCe _{1-x} Pt _x O _{3-δ}		
	x = 0.02	x = 0.04	x = 0.06
χ^2	1.205	1.822	1.847
wRp (%)	6.27	8.00	6.04
Rp (%)	4.38	5.95	4.45
a(Å)	6.2052(1)	6.1791(1)	6.1704(1)
b(Å)	8.7624(1)	8.7929(3)	8.7778(2)
c(Å)	6.2249(0)	6.2128(2)	6.2022(2)
Ba x	0.4846(1)	0.5151(2)	0.4857(3)
y	0.25	0.25	0.25
z	0.0045(3)	0.0016(13)	-0.0047(7)
O1 x	0.5028(18)	0.5121(27)	0.4803(33)
y	0.25	0.25	0.25
z	0.5799(22)	0.5981(36)	0.5915(44)
O2 x	0.2279(24)	0.2771(27)	0.2296(38)
y	0.0342(11)	0.0271(20)	0.0247(20)
z	0.2758(21)	0.2346(40)	0.2707(47)
Pt (occ.)	0.0171	0.0355	0.0534
O1 (occ.)	1	1	1
O2 (occ.)	1	1	1
Ba (Uiso)	0.0223(3)	0.0248(4)	0.0229(5)
Ce (Uiso)	0.0153(3)	0.0165(4)	0.0156(4)
BaCO ₃ (wt%)	2.72	2.77	4.30
CeO ₂ (wt%)	1.21	1.94	1.15
Ce and Pt at (0,0,0)			

Table 2A.2. Crystal structures of BaCe_{1-x}Pt_xO_{3-δ} as obtained from Rietveld refinement of neutron diffraction data.

Parameters	BaCe _{1-x} Pt _x O _{3-δ}		
	x = 0.02	x = 0.04	x = 0.06
χ^2	1.85	1.95	1.41
wRp (%)	3.83	3.69	3.08
Rp (%)	3.04	2.92	2.43
a	6.2077(24)	6.1718(35)	6.1726(31)
b	8.7792(33)	8.7579(49)	8.7423(56)
c	6.2284(21)	6.2027(28)	6.2001(35)
Ba x	0.4795(29)	0.5196(28)	0.4954(41)
y	0.25	0.25	0.25
z	-0.0025(37)	-0.0021(56)	0.0098(39)
O1 x	0.5164(30)	0.4742(23)	0.5123(47)
y	0.25	0.25	0.25
z	0.5863(21)	0.5792(19)	0.5753(24)
O2 x	0.2298(19)	0.2354(25)	0.2310(21)
y	0.0336(10)	0.0317(12)	0.0323(13)
z	0.2750(17)	0.2671(23)	0.2721(21)
O1 (occ.)	0.876(23)	0.936(29)	0.986(34)
O2 (occ.)	1.048(37)	0.980(39)	0.899(41)
Pt (occ.)	0.02	0.04	0.06
Ba(Uiso)	1.029(192)	1.139(184)	0.937(152)
Ce(Uiso)	0.619(135)	0.451(130)	0.453(124)
Pt(Uiso)	0.619(135)	0.451(130)	0.453(124)
O1(Uiso)	0.325(213)	0.083(175)	0.855(320)
O2(Uiso)	1.723(176)	2.179(224)	0.968(200)

Ce and Pt at (0,0,0)

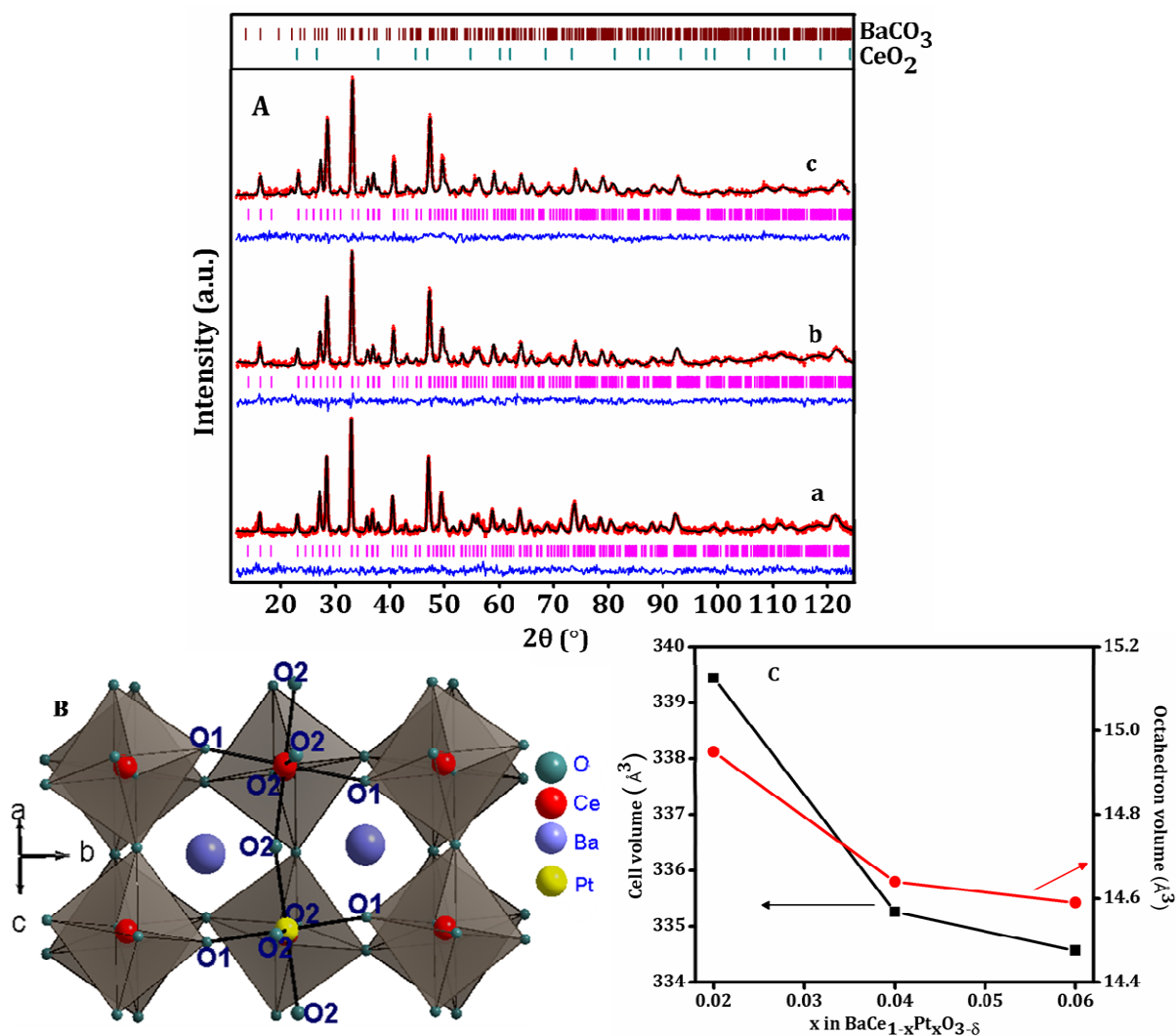


Figure 2A.5. (A) Rietveld refinement of constant wave neutron diffraction data for $\text{BaCe}_{1-x}\text{Pt}_x\text{O}_{3-\delta}$ with (a) $x = 0.02$, (b) $x = 0.04$ and (c) $x = 0.06$. Red line represents experimental data, black line is the Rietveld fit and the blue line is for the difference plot. Vertical lines (brown and green) at the top represent the expected positions for the impurity phases BaCO_3 and CeO_2 , (B) crystal structure of $\text{BaCe}_{1-x}\text{Pt}_x\text{O}_{3-\delta}$ with $x = 0.02$ and (C) cell volume and octahedron volumes of $\text{BaCe}_{1-x}\text{Pt}_x\text{O}_{3-\delta}$ as a function of substitution x .

The cell and atomic position parameters were found to be similar to that obtained from PXRD refinement. However occupancies of oxygen atoms were also refined here. The overall oxygen vacancies were found to be increasing with the Pt

substitution. However the vacancies are created in O₂ sites along the ac plane pointing to the square planar Pt-O geometry in the (101) planes as shown in figure 2A.5B. The cell volumes and the octahedral volumes obtained from the crystallographic data is plotted in figure 2A.5C as a function of substitution x in BaCe_{1-x}Pt_xO_{3-δ}. The decrease in cell volume with Pt substitution indicates the replacement of Ce(IV) with Pt(II). In addition, the fact that the volume of the BO₆ octahedron gradually decreases with Pt concentration in the materials further supports the increased incorporation of Pt in the Ce site. The nonlinear decrease in both the cell volume and octahedron volume with substitution and the deviation of amount of oxygen vacancies created from theoretical values can be attributed to the combined effect of increased concentrations of Ce(III), Pt(II) and oxygen vacancies.

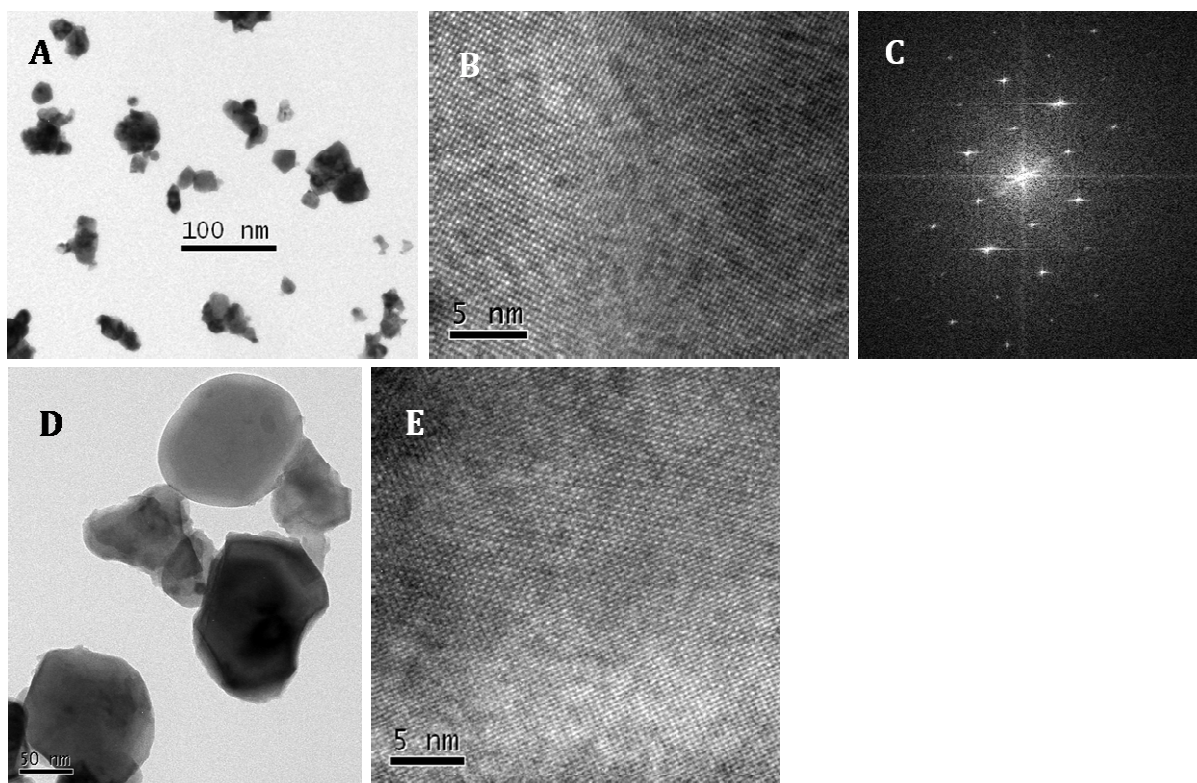


Figure 2A.6. (A) & (D) HRTEM images, (B) & (E) lattice planes and (C) electron diffraction pattern of 2 mol% Pt doped BaCeO₃.

HRTEM was used to understand the size and morphology of the particles as well as to look for the presence of any metallic Pt particles. Representative images of 2 mol%

Pt doped samples are shown in figure 2A.6. The particles are irregularly shaped with average size less than 100 nm. A number of images were analyzed with the help of Digital Micrograph software to determine the lattice spacing. No lattices of metallic Pt other than the lattices of the perovskite were identified in these images. Electron diffraction patterns were also obtained and the analysis of the lattice spacing shows diffraction from perovskite exclusively.

2A.3.2. Catalytic activity and structural correlation

Various deactivation mechanisms are proposed with different noble metal supported catalysts [27-35]. The factors that contribute to the catalyst deactivation include highly reducing atmosphere, startup and shut down conditions, temperature excursions, presence of steam during shut down etc. So the catalytic activity studies were carried out for all the Pt doped catalysts for two cycles of WGS reaction and the data are displayed in figure 2A.7.

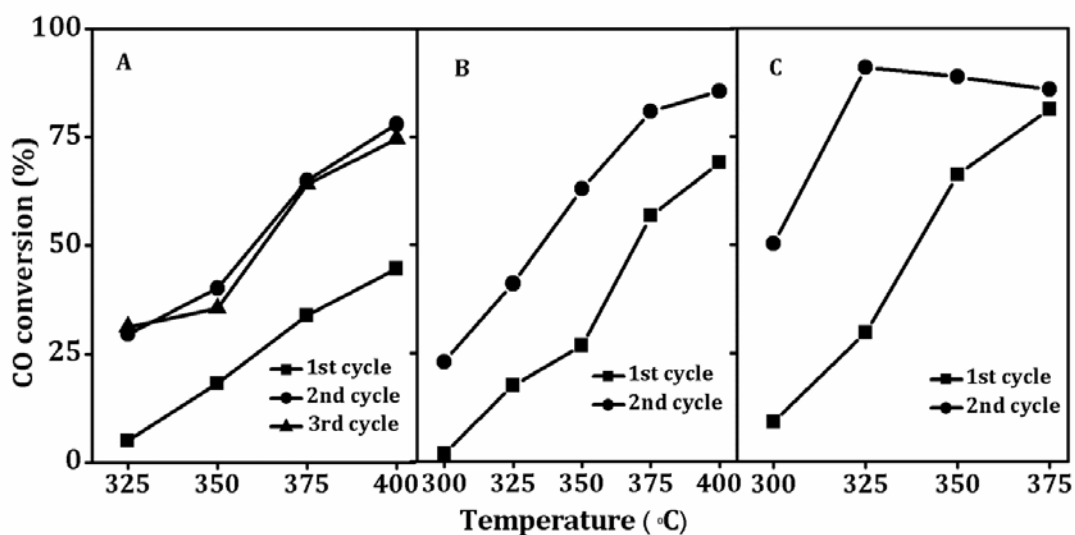


Figure 2A.7. CO conversion measured over BaCe_{1-x}Pt_xO_{3-δ} with A) x = 0.02, B) x = 0.04 and C) x = 0.06 under WGS reaction conditions. Reformate composition: 39.8 % H₂, 34.9 % N₂, 10.2 % CO and 15.2 % CO₂, steam to CO ratio 4.5, GHSV of 5000 h⁻¹.

The catalysts with 2 mol% Pt was only moderately active for the first cycle of reaction. However an increase in activity can be observed with increase in the molar

concentration of Pt as there is sufficient concentration of Pt species on the surface of the catalyst. After the data collection for the first cycle of reaction up to 400 °C, WGS feed and steam were switched off and nitrogen was passed through the catalyst for 20 minutes at 400 °C and then the catalysts were allowed to cool to room temperature in air. The activity data were collected for the second cycle and it can be noticed that there is a remarkable enhancement in the activity for all the Pt doped catalysts when compared to their first cycle activity. The activity was determined for the third cycle for the 2 mol% Pt substituted sample and the activity was similar to that obtained for the second cycle.

The stability of BaCeO₃ is reported to be poor in CO₂ containing atmospheres at temperatures 600-800 °C [36]. So the spent catalysts recovered under nitrogen atmosphere was analysed with the help of PXRD. Figure 2A.8 shows that the structure retained even under the harsh reaction conditions of WGS and no reflections corresponding to the metallic Pt was observed. This indicates that cationic Pt is stabilized in the lattice irrespective of the conditions exposed, unlike those reported in the case of Pd doped perovskites [2].

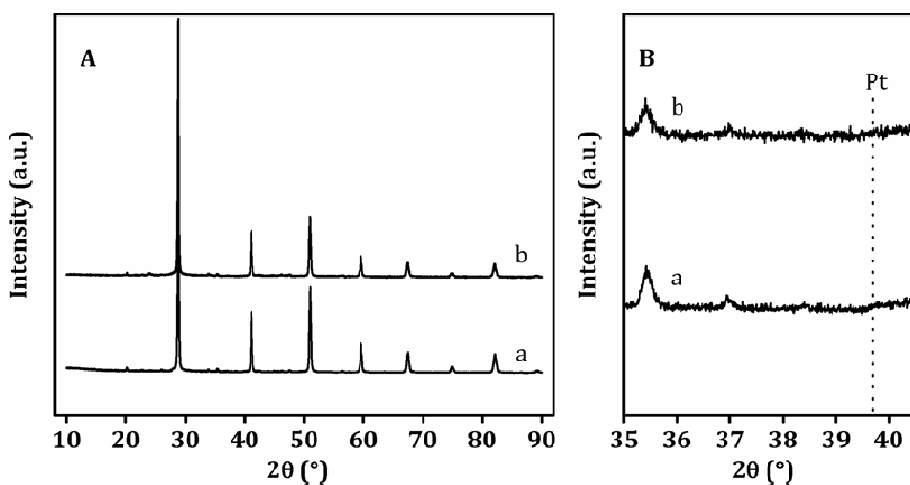


Figure 2A.8. (A) PXRD patterns of 2 mol% Pt doped BaCeO₃ a) before and b) after WGS reaction, (B) 2 theta region where Pt(111) reflections appear.

The stability of all the Pt doped compounds was further examined using in situ high temperature XRD experiments under reducing atmospheres and the results are shown in figure 2A.9.

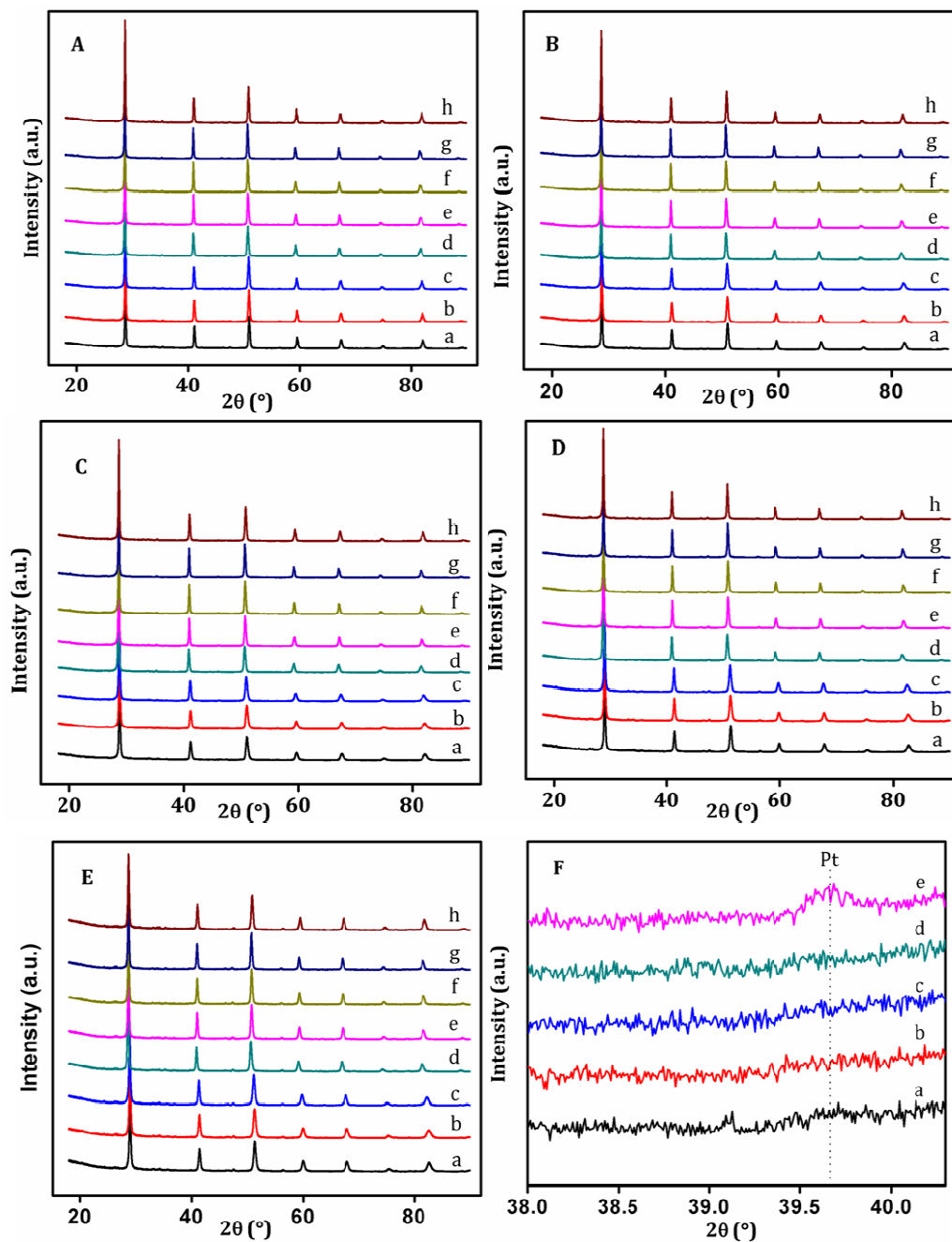


Figure 2A.9. In situ variable temperature PXRD patterns of BaCe_{1-x}Pt_xO_{3-δ} with (A) $x = 0.02$, (B) $x = 0.04$, (C) $x = 0.06$, (D) $x = 0.08$, and (E) $x = 0.10$ under 10 % H₂/N₂; (a) RT, (b) 100 °C, (c) 200 °C, (d) 300 °C, (e) 400 °C, (f) 500 °C, (g) 600 °C, (h) RT; (F) 2θ region where Pt(111) reflection appear (a) $x = 0.02$, (b) $x = 0.04$, (c) $x = 0.06$, (d) $x = 0.08$, and (e) $x = 0.10$. Expected peak position for Pt (111) is indicated as dashed line.

Again no structural change or collapse is observed up to 600 °C for compounds containing up to 6 mol% Pt under 10 % H₂/N₂. Moreover the two-theta region of the intense reflection corresponding to (111) plane of metallic Pt is scanned with very slow scan speed and the results suggest stabilization of ionic Pt at these conditions also. In situ variable temperature experiments were done on 8 and 10 mol% Pt doped samples also under 10 % H₂/N₂. The sample with 8 mol% Pt was found to be stable under the conditions up to 600 °C, while quantitative analysis with Rietveld refinement indicates that the percentage of metallic Pt increases from 0.33 to 0.6 for the 10 mol% Pt substituted sample. This clearly establishes that ~9.5 mol% of Pt can be stabilized in the BaCeO₃ lattice.

Analysis of the surface of the catalysts before and after WGS reaction is essential to identify the species responsible for the activity. Moreover any surface segregation of metallic platinum not distinguishable in PXRD can also be determined. As an example, the surface analysis of 2 mol% Pt doped sample before and after shut down cycles was carried out and the Pt-4f spectra of the samples are shown in figure 2A.10A.

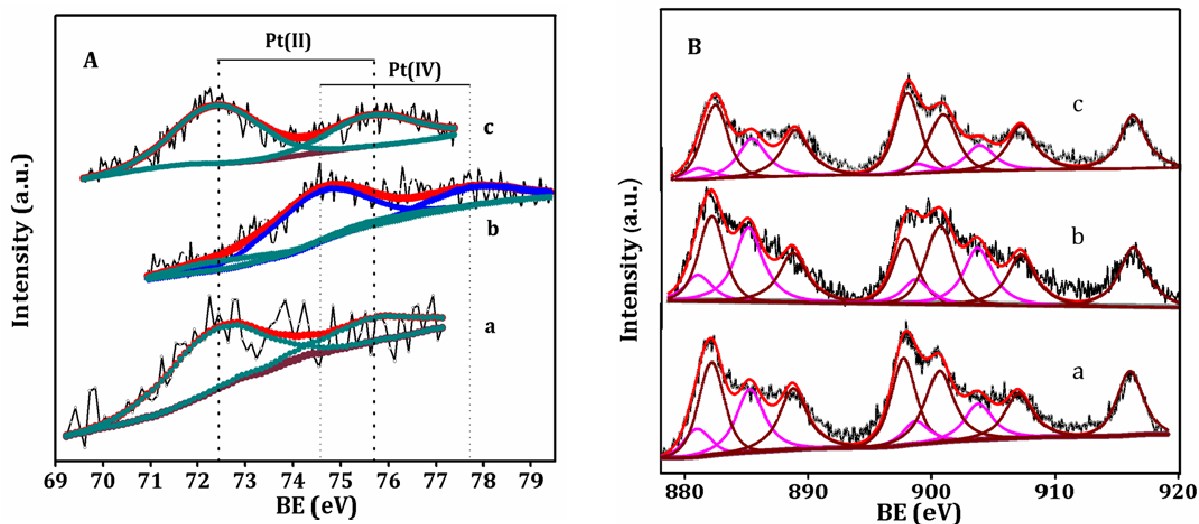


Figure 2A.10. (A) Pt-4f XP spectra of 2 mol% Pt doped BaCeO₃ (a) before, (b) after 1st cycle and (c) after 2nd cycle of WGS reaction and (B) Ce-3d XP spectra of 2 mol% Pt doped BaCeO₃ (a) before, (b) after 1st cycle and (c) after 2nd cycle of WGS reaction.

An examination of the Pt-4f spectrum of the fresh catalyst shows a weak and broad peak at binding energy 72.4 eV. This suggests the presence of Pt(II) species with very low concentration on the surface. According to the literature, peak corresponding to metallic Pt appears at around 71.2 eV [37, 38]. However no peaks are observed in that region showing the absence of metallic platinum in the fresh catalyst. Interestingly after the first shut down, concentration of Pt(II) species diminished and the surface was predominantly found to contain Pt(IV) species as evidenced by the appearance of a peak at 74.6 eV. However the overall surface Pt concentration increases after the first cycle. But the surface Pt again changes its oxidation state to +2 after the second cycle, leaving the overall Pt concentration more or less similar. The significant point to be noticed is that the surface was not found to consist of metallic Pt in any of the fresh or spent catalysts. These results point to the stabilization of cationic platinum in the BaCeO₃ lattice against the harsh reducing and shut down conditions. A semi quantitative estimation of the changes occurring to the concentration of surface Pt in between the cycles may help to understand the change in activity. Thus the Pt:Ce ratio was determined using the ratio of area of peak corresponding to Pt4f_{7/2} to the total area of the Ce3d_{5/2} peaks. The ratio for the fresh catalyst was 0.07 which increased to 0.09 after shut down under air. This enrichment of the cationic platinum on the surface might have resulted in the enhanced activity of the catalyst for the second cycle. The reversible changes occur to the oxidation states from Pt(II) and Pt(IV) in between cycles makes it difficult to say the contribution of a particular state towards activity as the second and third cycle displays similar activity. The change of oxidation state of platinum between shut down cycles can be attributed to the interaction with the atmospheric components during shutdown.

As Ce is a redox system, it is necessary to examine the changes occurring to it between cycles and the Ce-3d spectra of 2 mol% Pt doped BaCeO₃ catalyst before and after WGS reaction are shown in figure 2A.10B. The presence of many satellite peaks due to shake up, shake down and multiplet splitting effects complicates the Ce-3d XP spectrum. The peaks at ~882.5, 888.9, 898.2, 901, 907.5 and 916.7 eV represents Ce(IV) state while those at ~880.5, 885.7, 898.8 and 903.7 eV are due to the presence of Ce(III)

species [39-41]. The first three peaks of Ce(IV) represent 3d⁵/2 states while the last three stand for 3d³/2 states. Similarly for Ce(III) the first two represent 3d⁵/2 and last two corresponds to 3d³/2 states. The peaks of Ce(IV) at ~882.5, 888.9 eV are due to a mixture of (5d 6s)⁰ 4f² 02p⁴ and (5s 6d)⁰ 4f¹ 02p⁵ configurations and peak at ~898.2 eV is due to (5d 6s)⁰ 4f⁰ 02p⁶ final state. The peaks at ~880.5 and 885.7 eV are due to a mixture of (5d 6s)⁰ 4f² 02p⁴ and (5d 6s)⁰ 4f¹ 02p⁵ configurations in Ce(III). The Ce 3d³/2 structures can be explained in a similar way. However valuable information regarding the changes occurring to the Ce state can be extracted from the ratio of intensity of Ce(IV) peak at 916 eV and Ce(III) peak at 886 eV. It can be found that Ce(IV)/Ce(III) ratio decreases after first shut down compared to the fresh catalyst suggesting significant reduction of Ce(IV) to Ce(III) state. But the ratio increases after second shut down. These changes in oxidation state of cerium between shut down cycles are in exact correspondence to that observed in the Pt-4f spectra.

The ionic Pt incorporated in the BaCeO₃ lattice was proven to be stable under WGS reaction conditions and air shut down process. But various other shut down conditions including the passage of steam and reformat feed are practiced and hence various deactivation mechanisms of the catalysts due to the formation of surface hydroxyls, blocking of active sites by carbonate etc. are also possible [42, 43]. So we selected the 2 mol% Pt doped sample and subjected this catalyst to three different possible shut down conditions and compared the WGS activities. The catalyst was subjected to the WGS reaction conditions for 265 minutes up to a maximum temperature of 400 °C and then (I) reformat mixture feed and steam were switched off and nitrogen was passed through the catalyst and allowed to cool to RT, (II) steam alone was switched off and the catalyst was allowed to cool to RT under reformat feed, and (III) the catalyst was allowed to cool down to 80 °C under the reaction atmosphere itself, i.e. comprising reformat feed and steam and kept at this temperature with same atmospheres for 1 h and then cooled down to RT after switching off steam. The WGS activities obtained for cycles before and after all the shut down conditions employed are displayed in figure 2A.11.

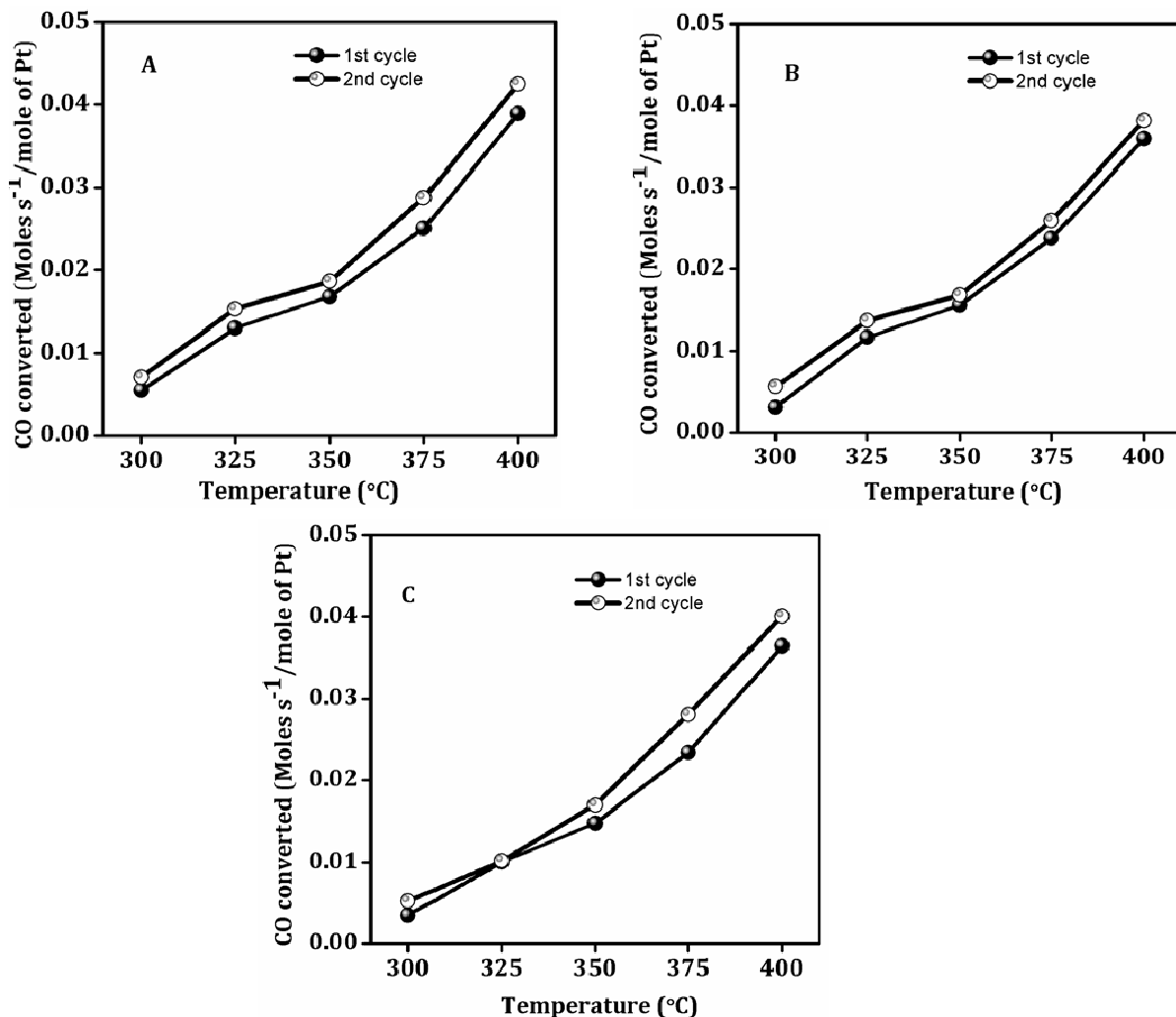


Figure 2A.11. WGS activities of BaCe_{0.98}Pt_{0.02}O_{3-δ} obtained before and after shut down under A) nitrogen, B) reformate feed and C) reformate feed with steam up to 80 °C and keeping for 1 h.

It can be understood from the figure that there is no substantial change in the activity before and after shut down cycles. This observation is different from the earlier one with a remarkable enhancement in the activity after oxidative shut down process.

Structural characterization of the catalysts after the shut down cycle was done by PXRD and the diffraction patterns of the spent catalysts are shown in figure 2A.12 in comparison with that of the fresh catalyst.

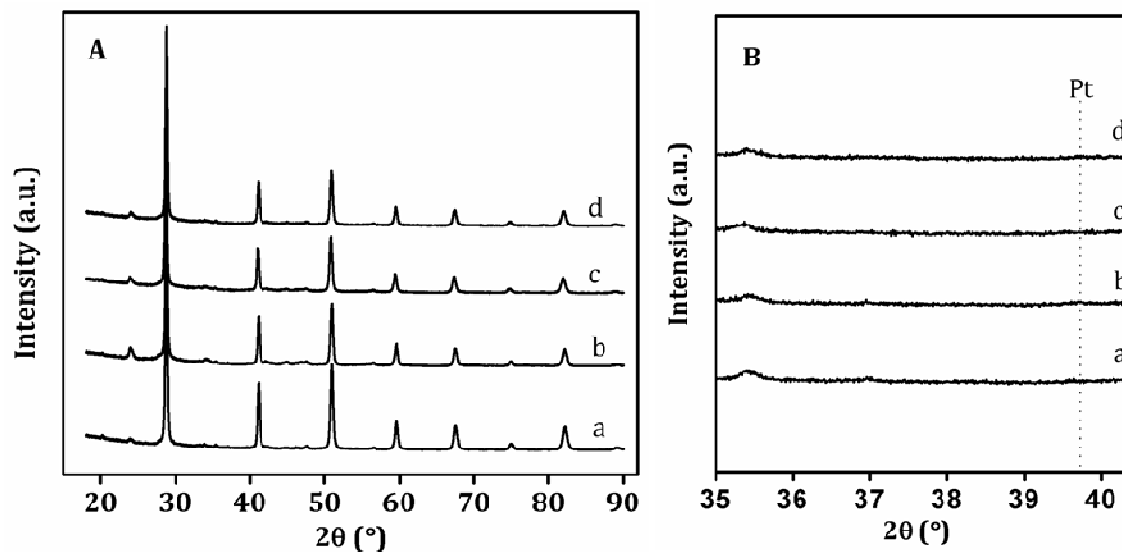


Figure 2A.12. PXRD patterns of BaCe_{0.98}Pt_{0.02}O_{3-δ} a) before and after reactor shut down under b) nitrogen, c) reformat feed and d) reformat feed with steam up to 80 °C and keeping for 1 h.

No structural change is observed for the catalyst under the conditions used. However a small increase in the amount of the barium carbonate is observed for the spent catalysts, the formation of which can be attributed to the presence of CO₂ in the feed. Also the segregation of BaCO₃ was found to be highest for the catalyst shut down under nitrogen atmosphere directly indicating that reformat feed and steam help to reduce the carbonate formation. The formation of carbonate on the surface of Au/CeO₂ catalyst was reported to block the active sites resulting in catalyst deactivation [43]. However in our case we are not observing any deactivation, as the carbonate is removed as BaCO₃ and thus active sites are not blocked. The formation of small amount of BaCO₃ may lead to the creation of A-site vacancy in the perovskite with the simultaneous formation of oxygen vacancy to balance the charge and thus the structure retains the stability. Moreover the absence of reflections corresponding to metallic Pt in the PXRD pattern suggests that ionic Pt incorporated withstand all the shut down conditions followed.

The stability of the BaCe_{0.98}Pt_{0.02}O_{3-δ} under the shut down conditions was further investigated with the help of variable temperature in situ XRD experiments. The WGS

experimental conditions were mimicked by passing reformat feed saturated with water vapour through an in situ reaction chamber containing the sample up to the temperatures used in the activity studies and then allowed to cool down to RT by following the shut down procedures I, II and III listed earlier. The powder XRD patterns collected are shown in figure 2A.13. The structural stability of the sample is again highlighted and no egress of metallic Pt is observed.

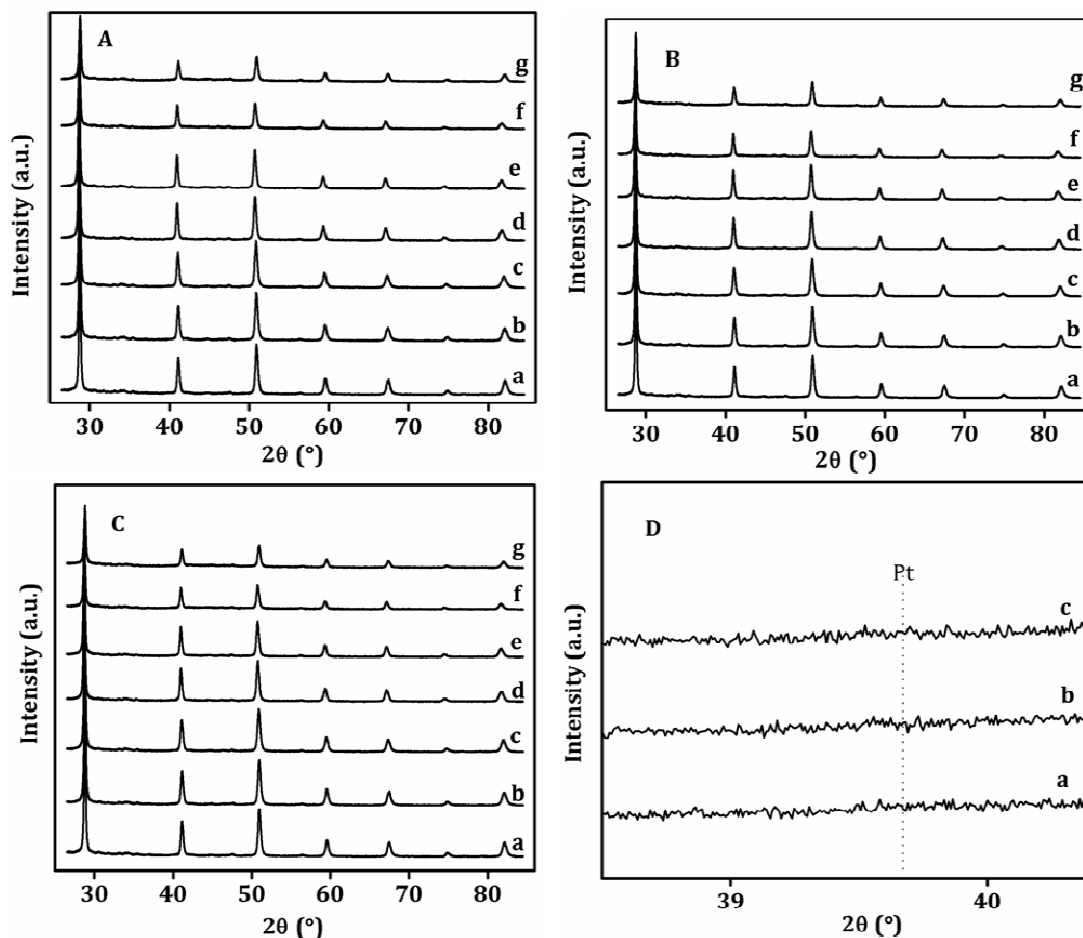


Figure 2A.13. In situ PXR patterns of BaCe_{0.98}Pt_{0.02}O_{3- δ} under reformat mixture saturated with water vapour up to 400 °C and then reactor shut down under (A) nitrogen, (B) reformat feed and (C) reformat feed saturated with water vapour up to 80 °C and keeping for 1 h. (a) RT, (b) 100 °C, (c) 200 °C, (d) 300 °C, (e) 350 °C, (f) 400 °C and (g) RT; (D) 2 θ region where reflections corresponding to Pt(111) appear, taken with long duration per step after (a) condition I, (b) condition II, and (c) condition III.

The behavior of the surface of the catalyst towards the different shut down conditions followed are to be investigated and the Pt-4f spectra of the 2 mol% Pt doped sample shut down under the various conditions are compared with that of the fresh catalyst and are shown in figure 2A.14. The appearance of a peak at ~ 72.9 eV in the XP spectrum of the fresh catalyst points to the presence of Pt(II) species on the surface. The Pt-4f XP spectra of all the spent catalysts also suggest the presence of only Pt(II) species on the surface pointing to the stability of the Pt oxidation state irrespective of the shut down conditions employed. Moreover the absence of metallic platinum peaks establishes the stability of lattice incorporated Pt even under the highly reducing reaction conditions as well as various shut down conditions.

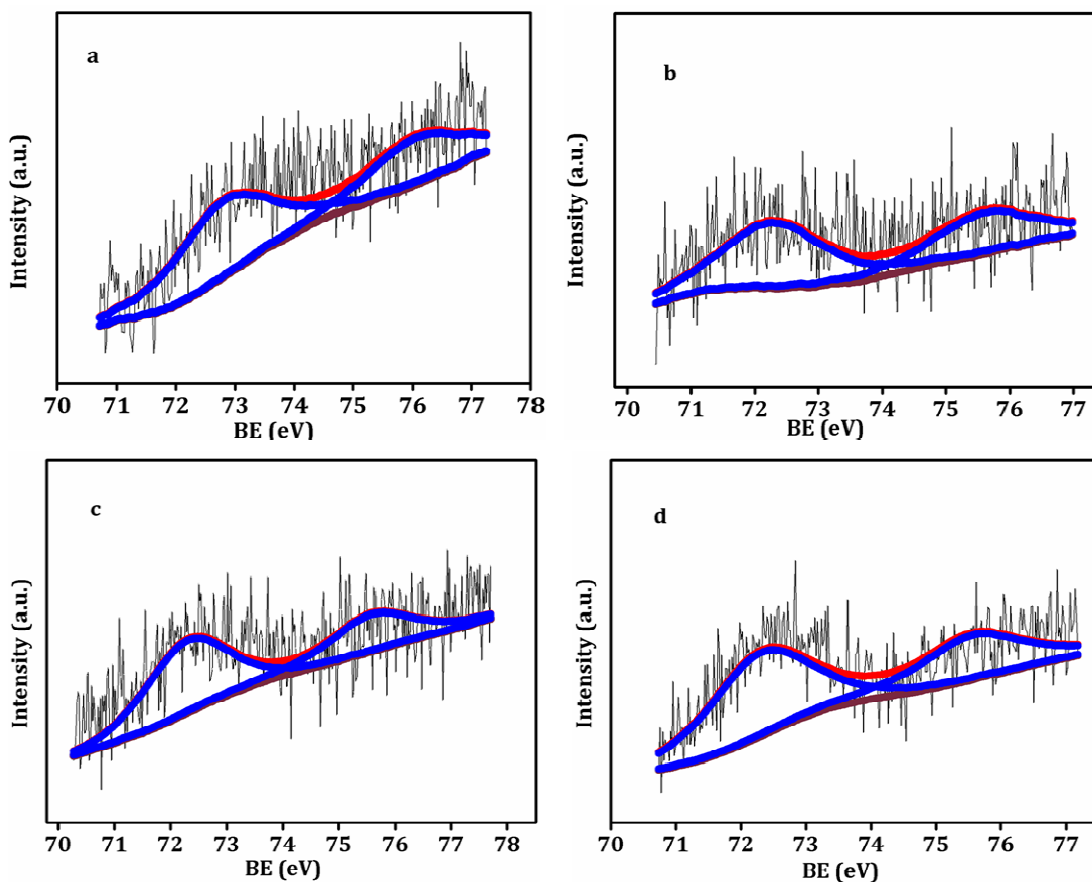


Figure 2A.14. Pt-4f XP spectra of BaCe_{0.98}Pt_{0.02}O_{3- δ} (a) before and after reactor shut down under (b) nitrogen, (c) reformate feed and (d) reformate feed with steam up to 80 °C and keeping for 1 h; Black: observed, red: fitted, blue; Pt(II).

The changes occurring to the cerium state under the various shut down atmospheres are also worthwhile to investigate and the Ce-3d XP spectra of the 2 mol% Pt doped BaCeO₃ before and after the shut down cycles are displayed in figure 2A.15.

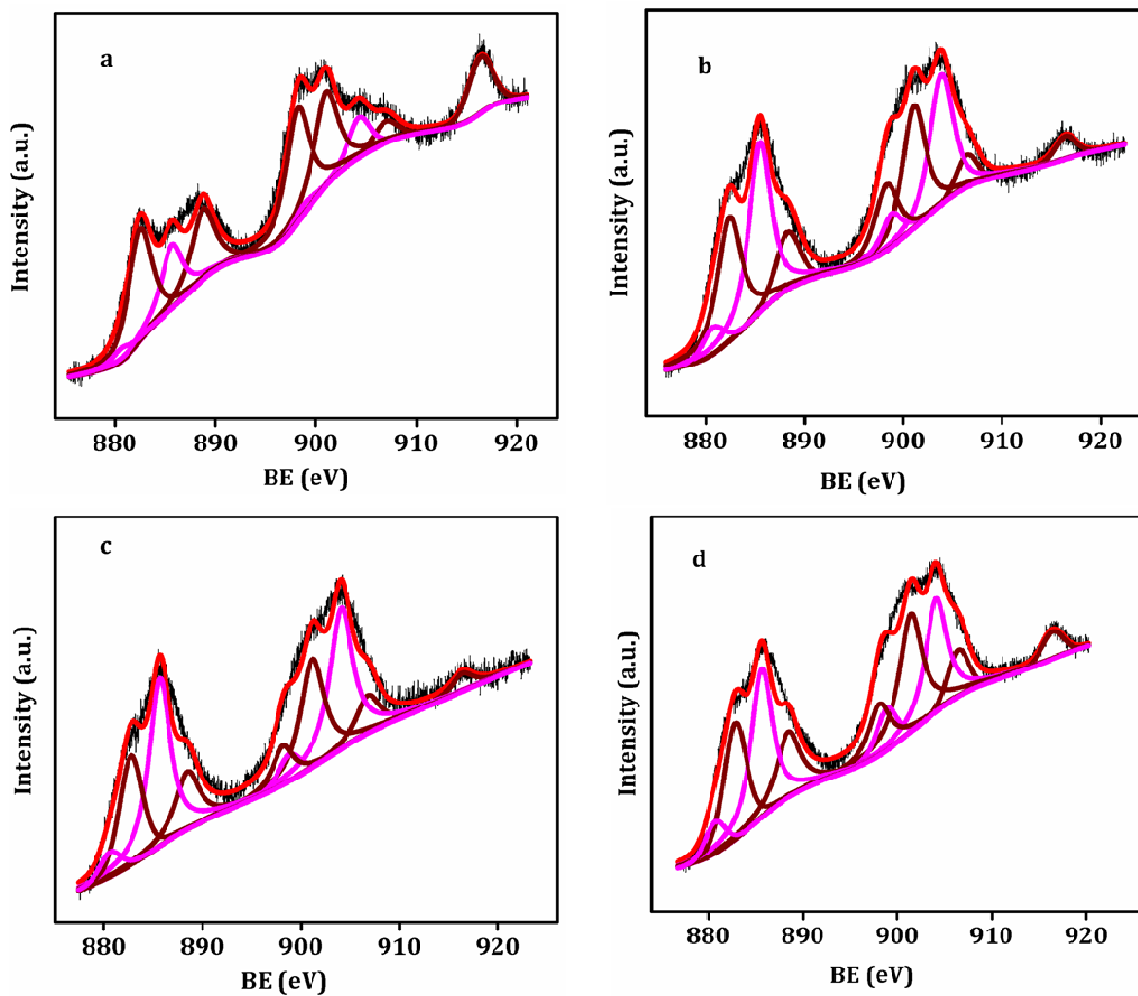


Figure 2A.15. Ce-3d XP spectra of BaCe_{0.98}Pt_{0.02}O_{3- δ} . (a) before and after reactor shut down under (b) nitrogen, (c) reformate feed and (d) reformate feed with steam up to 80 °C and keeping for 1 h. Black: observed, red: fitted, brown: Ce(IV) and pink: Ce(III).

The deconvolution of Ce-3d spectra obtained for 2 mol% Pt doped BaCeO₃ suggests that all the fresh and spent catalysts contain both Ce(IV) and Ce(III) states. The relative concentrations of Ce(III) and Ce(IV) were calculated using the area of the respective Ce3d_{5/2} structures as described by others [44-46]. The three peaks (~882.5,

888.9, and 898.2 eV) representing 3d_{5/2} state originate from the Ce(IV) states and the peaks (~880.5 and 885.7 eV) correspond to the Ce(III) 3d_{5/2} states. The relative concentrations determined using respective total peak area to the total 3d_{5/2} peak area suggest that the percentage of Ce(III) on the surface for all the spent catalysts were higher than that present on the surface of the fresh catalyst. The concentration of Ce(III) increases from ~20 % to 40 % for the shut down condition-I and condition-III while it increases to ~48 % for the shut down condition-II. This observation points to higher extent of reduction for the reformat shut down condition compared to the other instances. As determined in the case of oxidative shut down, the Pt: Ce ratio was calculated using the ratio of area of Pt4f_{7/2} to the total area of the Ce3d_{5/2} lines. This yields a ratio of 0.012 for the fresh catalyst and 0.010, 0.012 and 0.011 for the catalyst shut down under conditions, I, II and III respectively. This suggests that the concentration of platinum remains more or less same after the shut down cycles and hence the activity remains similar for the activity cycles before and after shut down.

2A.4. Conclusions

The stabilization of ionic platinum in the lattice sites of BaCeO₃ perovskite is achieved using wet chemical synthesis method. Analysis of the structure using various characterization techniques including neutron diffraction and PXRD, revealed the substitution of platinum in cerium sites. The increase in platinum substitution resulted in an increase in oxygen deficiency, suggesting the incorporation of Pt(II) in place of Ce(IV). This stabilized lattice incorporated ionic platinum is found to be active for WGS reaction. PXRD and XPS techniques are used to follow the evolution of Pt species after the shut down procedure in the reactor. The activity increased after shut down in air and is attributed to the surface enrichment of ionic Pt species. Egress of metallic platinum is not observed with the catalyst recovered after shut down. The stability of the ionic platinum incorporated in the BaCeO₃ lattice is further tested by employing shut down conditions which are proposed to cause different deactivation mechanisms. Hence the catalyst is subjected to the shut down conditions under nitrogen, reformat feed and steam. The catalyst is found to be stable under all the conditions employed. The barium ion present in the A-site may have helped in the removal of carbonate

formed under the reaction conditions and prevents the catalyst from deactivation caused by the blocking of the active sites. The perovskite structure is thought to be able to tolerate cerium reduction with the generation of oxygen vacancies. This indicates that deactivation associated with over reduction of cerium reported for CeO₂ is avoided here. The catalytic activity can be improved either by using methods such as oxidative treatment to enhance the surface ionic platinum or by developing new synthetic strategies to increase the surface area of the catalyst sufficiently. Such kind of materials with active ionic noble metal species stabilized in stable lattices and accessible to reactants in sufficient quantities can be considered as model catalysts where sintering problems associated with supported noble metal catalysts are addressed.

References

1. Nishihata, Y.; Mizuki, J.; Akao, T.; Tanaka, H.; Uenishi, M.; Kimura, M.; Okamoto, T.; Hamada, N. *Nature* **2002**, *418*, 164.
2. Li, J.; Singh, U. G.; Bennett, J. W.; Page, K.; Weaver, J. C.; Zhang, J.; Proffen, T.; Rappe, A. M.; Scott, S. L.; Seshadri, R. *Chem. Mater.* **2007**, *19*, 1418.
3. Singh, U. G.; Li, J.; Bennett, J. W.; Rappe, A. M.; Seshadri, R.; Scott, S. L. *J. Catal.* **2007**, *249*, 349.
4. Kreuer, K. D. *Annu. Rev. Mater. Res.* **2003**, *33*, 333.
5. Kruth, A.; Irvine, J. T. S. *Solid State Ionics* **2003**, *162*, 83.
6. Iwahara, H.; Asakura, Y.; Katahira, K.; Tanaka, M. *Solid State Ionics* **2004**, *168*, 299.
7. Scherban, T.; Villeneuve, R.; Abello, L.; Lucazeau, G. *Solid State Ionics* **1993**, *61*, 93.
8. Norby, T. *Solid State Ionics* **1999**, *125*, 1.
9. Trovarelli, A. *Catal. Rev.-Sci. Eng.* **1996**, *38*, 439.
10. Sandoval, A.; Gomez-Cortes, A.; Zanella, R.; Diaz, G.; Saniger, J. M. *J. Mol. Catal. A: Chem.* **2007**, *278*, 200.
11. Trovarelli, A.; de Leitenburg, C.; Boaro, M.; Dolcetti, G. *Catal. Today* **1999**, *50*, 353.
12. Toby, B. H. *J. Appl. Crystallogr.* **2001**, *34*, 210.
13. Rodriguez-Carvajal, J. *Physica B.* **1993**, *192*, 55.
14. Knight, K.S. *Solid State Ionics* **1994**, *74*, 109.

15. Giannici, F.; Longo, A.; Balerna, A.; Kreuer, K. -D.; Martorana, A. *Chem. Mater.* **2007**, *19*, 5714.
16. Malavasi, L.; Ritter, C.; Chiodelli, G. *Chem. Mater.* **2008**, *20*, 2343.
17. Pagnier, T.; Charrier-Cougoulic, I.; Ritter, C.; Lucazeau, G. *Eur. Phys. J. Appl. Phys.* **2000**, *9*, 1.
18. Chen, F. L.; Sorensen, O. T.; Meng, G. Y.; Peng, D. K. *J. Eur. Ceram. Soc.* **1998**, *18*, 1389.
19. Jacobson, A. J.; Tofield, B. C.; Fender, B. E. F. *Acta Cryst.* **1972**, *B28*, 956.
20. Knight, K. S.; Bonanos, N. *Mater. Res. Bull.* **1995**, *30*, 347.
21. Lopez, M. C. B.; Fourlaris, G.; Rand, B.; Riley, F. L. *J. Am. Ceram. Soc.* **1999**, *82*, 1777.
22. Saini, M.; Vivekanand, K.; Poddar, P.; Murty, K. V. G. K.; Thushara, K. S.; Gopinath, C. *S. Int. J. Nanotechnol.* **2010**, *7*, 919.
23. Gopinath, C. S.; Subramanian, S.; Prabhu, P. S.; Rao, M. S. R.; Rao, G. V. S. *Physica C* **1993**, *218*, 117.
24. Malavasi, L.; Tealdi, C.; Ritter, C.; Pomjakushin, V.; Gozzo, F.; Diaz-Fernandez, Y. *Chem. Mater.* **2011**, *23*, 1323.
25. Takeuchi, K.; Loong, C. K.; Richardson, J. W., Jr.; Guan, J.; Dorris, S. E.; Balachandran, U. *Solid State Ionics* **2000**, *138*, 63.
26. Pynn R. Neutron scattering – A non-destructive microscope for seeing inside matter. In: Liang L, Rinaldi R, Schober H, editors, *Neutron Applications in Earth, Energy, and Environmental Sciences*, Springer, New York; 2009.
27. Ruettinger, W.; Ilinich, O.; Farrauto, R. J. *J. Power Sources* **2003**, *118*, 61.
28. Goshima, H.; Tagawa, T.; Yamada, H.; Kawashima, Y. Proceedings of international symposium on EcoTopia science 2007, ISETS07, pp 329–331.
29. Nishimura, S.; Shishido, T.; Ebitani, K.; Teramura, K.; Tanaka, T. *Appl. Catal. A: Gen.* **2012**, *2*, 1685.
30. Ilinich, O.; Ruettinger, W.; Liu, X.; Farrauto, R. J. *Catal.* **2007**, *247*, 112.
31. Liu, X.; Ruettinger, W.; Xu, X.; Farrauto, R. *Appl. Catal. B: Environ.* **2005**, *56*, 69.
32. Kam. R.; Scott, J.; Amal, R.; Selomulya, C. *Chem. Eng. Sci.* **2010**, *65*, 6461.
33. Ruettinger, W.; Liu, X.; Farrauto, R. J. *Appl. Catal. B: Environ.* **2006**, *65*, 135.

34. Zalc, J. M.; Sokolovskii, V.; Loffler, D. G. *J. Catal.* **2002**, *206*, 169.
35. Denkwitz, Y.; Karpenko, A.; Plzak, V.; Leppelt, R.; Schumacher, B.; Behm, R. J. *J. Catal.* **2007**, *246*, 74.
36. Scholten, M. J.; Schoonman, J.; van Miltenburg, J. C.; Oonk, H. A. J. *Solid State Ionics* **1993**, *61*, 83.
37. Bancroft, G. M.; Adams, I.; Coatsworth, L. L.; Bennewitz, C. D.; Brown, J. D.; Westwood, W. D. *Anal. Chem.* **1975**, *47*, 586.
38. Drawdy, J. E.; Hoflund, G. B.; Gardner, S. D.; Yngvadottir, E.; Schryer, D. R. *Surf. Interface Anal.* **1990**, *16*, 369.
39. Bak, K.; Hilaire, L. *Appl. Surf. Sci.* **1993**, *70–71*, 191.
40. Rynkowski, J.; Farbotko, J.; Touroude, R.; Hilaire, L. *Appl. Catal. A: Gen.* **2000**, *203*, 335.
41. Yang, X.; Zhang, W.; Xia, C.; Xiong, X.; Mu, X.; Hu, B. *Catal. Commun.* **2010**, *11*, 867.
42. Goguet, A.; Burch, R.; Chen, Y.; Hardacre, C.; Hu, P.; Joyner, R. W.; Meunier, F. C.; Mun, B. S.; Thompsett, D.; Tibiletti, D. *J. Phys. Chem. C* **2007**, *111*, 16927.
43. Kim, C. H.; Thompson, L. T. *J. Catal.* **2005**, *230*, 66.
44. Karpenko, A.; Leppelt, R.; Cai, J.; Plzak, V.; Chuvilin, A.; Kaiser, U.; Behm, R. J. *J. Catal.* **2007**, *250*, 139.
45. Truffault, L.; Ta, M.-T.; Devers, T.; Konstantinov, K.; Harel, V.; Simmonard, C.; Andreatza, C.; Nevirkovets, I. P.; Pineau, A.; Veron, O.; Blondeau, J. -P. *Mater. Res. Bull.* **2010**, *45*, 527.
46. Paparazzo, E. *Mater. Res. Bull.* **2011**, *46*, 323.

Part B

**Synthesis, Characterization and WGS Activity
Studies of $\text{BaCe}_{0.98-x}\text{Y}_x\text{Pt}_{0.02}\text{O}_{3-\delta}$; ($x = 0.02, 0.04,$
 $0.06, 0.10, 0.20,$ and 0.30): Role of Oxygen
Vacancies on WGS Activity**

2B.1. Introduction

The mechanism of heterogeneous catalysis reactions generally depends on the type of reaction. In the case of supported metal catalysts, metallic particles are generally believed to be the active component, while support is considered as inert and in most of the cases, its role is limited to stabilize the active particles or providing acidic or basic sites [1, 2]. However, many reports employing reducible supports like ceria suggest that support also plays significant role in the mechanism and its properties are also crucial in determining the activity [3-5]. Various investigations indicate that noble metals supported on ceria catalyse the WGS reaction via redox mechanism involving the dissociative adsorption of water molecules occurring on the oxygen vacancies present in the ceria [6-9].

Most of the investigations on supported metal catalysed reactions focus on the structure, shape or redox aspects of the catalysts. Despite the fact that defects such as oxygen vacancies are proposed to actively participate in the mechanism of many reactions, studies which clearly establish their role hardly exist in the literature. Moreover the dependence of oxygen vacancies on catalytic activity is difficult to study with the conventional supported systems, as systematic tuning of oxygen vacancies is difficult in these systems. In this context, stable structured lattices like perovskites can be employed for such a study since they tolerate and stabilise sufficient concentration of oxygen vacancies. Doped and undoped BaCeO_3 are well known proton conductors and the conduction is suggested to occur through the oxygen vacancies present in the system. Various dopants like Y, Gd, Eu, Yb, Nb etc. have been used to systematically induce oxygen vacancies in the BaCeO_3 [10-14]. In the case of yttrium doped BaCeO_3 , up to 30 mol% dopant substitution is achieved [15, 16]. There is general agreement between researchers that the crystal structure of undoped BaCeO_3 and those doped up to 10 mol% Y belongs to the orthorhombic (space group $Pnma$) system. However, no definite structure is yet suggested for the system with dopant concentration higher than 10 mol%. The possible structures include rhombohedral $R\bar{3}c$ and monoclinic $I2/m$ or a mixture of both. This variation in crystal structures can be attributed to the sensitiveness to preparation and processing conditions employing different atmospheres and various calcination temperatures. The development of the catalyst system $\text{BaCe}_{1-x}\text{Pt}_x\text{O}_{3-\delta}$ ($x = 0.02, 0.04 \text{ \& } 0.06$)

where the platinum is stabilized in ionic form and active for WGS reaction is already discussed in the chapter 2A. In the study described in the present chapter, our objective is to systematically enhance oxygen vacancies by progressive doping of the Y(III) (up to 30 mol%) in the Ce(IV) site of $\text{BaCe}_{0.98}\text{Pt}_{0.02}\text{O}_{3-\delta}$ where the active cationic Pt is already present and to investigate the WGS activity of a series of such compounds with the assumption that the variation in activity can only be attributed to the variation in oxygen vacancy. All the materials were synthesized using combustion method followed in the work described in chapter 2A. The synthesized materials were characterized using various techniques and their water gas shift activities were compared. Moreover the structural variations caused by the incorporation of yttrium were also studied and the effect of structural variations in catalytic activity was also examined. It is observed that not the extent but the structural characteristics of oxygen vacancies play a decisive role in enhancing WGS activity.

2B.2. Experimental section

2B.2.1. Synthesis of $\text{BaCe}_{0.98-x}\text{Y}_x\text{Pt}_{0.02}\text{O}_{3-\delta}$ ($x = 0.02, 0.04, 0.06, 0.10, 0.20$ & 0.30)

Pt and Y codoped BaCeO_3 were synthesized using combustion method employing citric acid as described in the chapter 2A. Barium nitrate (0.003 mol) (Aldrich), ceric ammonium nitrate (0.003 mol) (Aldrich), appropriate quantities of tetrammine platinum nitrate (Aldrich) and yttrium nitrate (Aldrich) were dissolved in 50 ml of water one after the other. Citric acid monohydrate (0.012 mol) (Merck) was added to the solution. Aqueous ammonia was added to adjust the pH of the solution to 7. The solution was then heated at 90 °C to evaporate water. The resulted gel was heated at 400 °C to remove organic and other volatile components. The powder obtained was ground well and calcined at 900 °C for 8 h.

2B.2.2. Characterization

The details of the instruments and procedures used for PXRD, Rietveld refinement, HRTEM, and ICP-AES are same as those described in chapter 2A in section 2A.2.2. Variable temperature in-situ PXRD experiments were carried out in an Anton-Paar XRK900 reaction chamber under various atmospheres. Data collection under 5 % H_2/Ar and 10 % O_2/He

was carried out with a step size of 0.008° and a time per step of 25.7 s for 2θ range $26.5-84.5^\circ$ and 0.008° and 100 s for 2θ range $38-42^\circ$ respectively. In situ variable temperature XRD experiments using a reformat feed with a composition of 40.3 % H_2 , 10.1 % CO, 14.5 % CO_2 and balance nitrogen, saturated with water vapour by bubbling the feed through a flask containing water, was carried up to $400^\circ C$. Data collection was done at intervals of $100^\circ C$ after keeping for half an hour at each temperature with a step size of 0.008° and time per step of 42.5 s for the 2θ range $26.5-84.5^\circ$ and step size of 0.008° and a time per step of 100 s for the 2θ range $38-42^\circ$ respectively.

X-ray photoelectron spectroscopic (XPS) measurements were carried out on a VG Micro Tech ESCA 300 instrument at a pressure of $>1 \times 10^{-9}$ Torr with a pass energy of 50 eV and electron take off angle 60° , and the overall resolution was ~ 0.1 eV. All binding energies were referenced to the C 1s peak (285 eV) arising from adventitious carbon. The surface areas of the samples were determined by N_2 adsorption at the temperature of liquid nitrogen using Autosorb iQ Quantachrome system. The samples were degassed at $300^\circ C$ under vacuum for 6 h prior to the analysis to remove the adsorbed moisture on the catalyst surface. Specific surface area was calculated using the BET model at relative pressure of $P/P_0 = 0.05 - 0.3$. Thermogravimetric analysis was carried out on a METTLER-TOLEDO TGA/SDTA851e instrument. All the samples were preheated under Helium with a gas flow of 40 ml/min at $120^\circ C$ for 1 h and then cooled down to room temperature. Again the samples were heated to $500^\circ C$ at a rate of $5^\circ C/min$ under Helium with the same flow rate. Finally the samples were heated to $500^\circ C$ with a heating rate of $5^\circ C/min$ under air with a flow rate of 40 ml/min.

2B.2.3. Catalytic set up

The set up for catalytic activity measurement used was the same as that described in chapter 2A in the section 2A.2.3. But the composition of the reformat feed used was 40.3 % H_2 , 35.1 % N_2 , 10.1 % CO and 14.5 % CO_2 .

2B.3. Results and discussion

2B.3.1. Synthesis and structural characterisation

In all the materials synthesised, the molar concentration of Pt was kept at 2 mol% where as the concentration of Y was progressively increased as 2, 4, 6, 10, 20 and 30 %. The concentrations of platinum and yttrium present in the synthesized materials were determined using ICP-AES technique and the results are shown in table 2B.1.

Table 2B.1. Concentrations of Pt and Y in $\text{BaCe}_{0.98-x}\text{Y}_x\text{Pt}_{0.02}\text{O}_{3-\delta}$ obtained from ICP-AES analysis.

Compound	x	Pt		Y	
		Theoretical wt %	Experimental wt %	Theoretical wt %	Experimental wt %
$\text{BaCe}_{0.98-x}\text{Y}_x\text{Pt}_{0.02}\text{O}_{3-\delta}$	0.02	1.2	1.14	0.55	0.47
	0.04	1.2	1.06	1.09	0.90
	0.06	1.21	1.14	1.65	1.55
	0.10	1.21	1.17	2.76	2.60
	0.20	1.23	1.16	5.62	5.05
	0.30	1.25	1.13	8.57	7.97

The materials are henceforth represented as BC2PxY where x represents the molar concentration of Y for convenience. The ideal cubic structure of BaCeO_3 perovskite contains a three-dimensional network of identical, corner-shared regular CeO_6 octahedra with 12 coordinated barium present in the cuboctahedral cavity. However, the cooperative distortion and the rotation of the CeO_6 octahedra often result in non cubic structures such as orthorhombic, rhombohedral and monoclinic structures. The cooperative buckling of CeO_6 octahedra and small displacement of the barium atom result in the orthorhombic phase with two crystallographic sites for oxygen atoms. The undoped BaCeO_3 is reported to crystallize in the orthorhombic crystal system. The Pt and Y occupy the Ce-site in the doped samples as described in figure 2B.1.

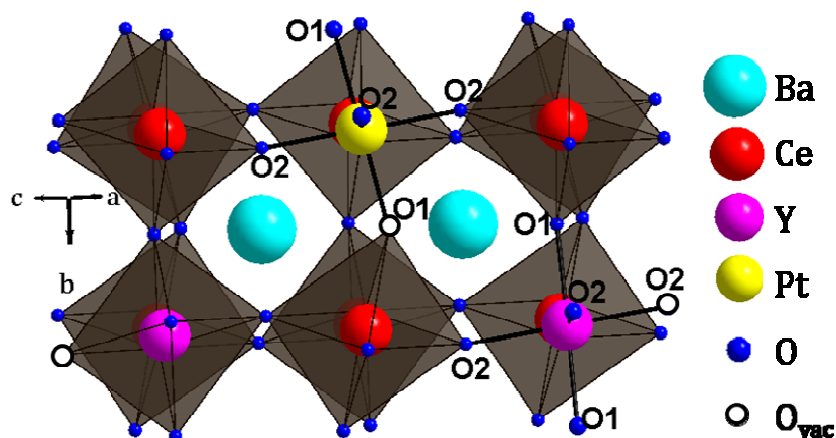


Figure 2B.1. Crystal structure of $\text{BaCe}_{0.98-x}\text{Y}_x\text{Pt}_{0.02}\text{O}_{3-\delta}$.

The structural characterization of the synthesized materials was done using PXRD technique and the diffraction patterns of all the Pt and Y doped BaCeO_3 perovskites are displayed in figure 2B.2 along with that of BaCeO_3 for comparison.

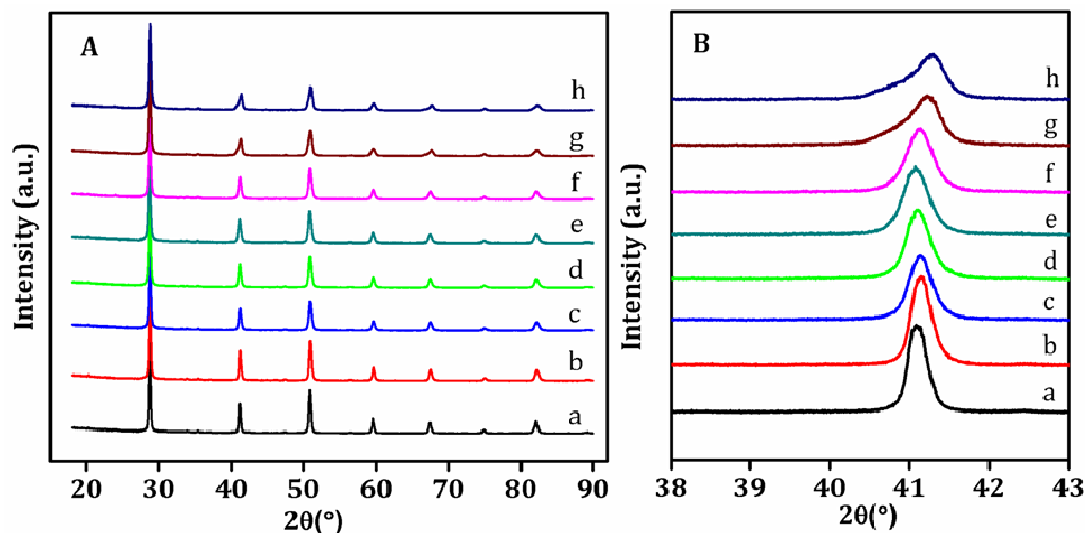


Figure 2B.2. (A) PXRD patterns of (a) BaCeO_3 , $\text{BaCe}_{0.98-x}\text{Y}_x\text{Pt}_{0.02}\text{O}_{3-\delta}$ with (b) $x = 0$, (c) $x = 0.02$, (d) $x = 0.04$, (e) $x = 0.06$, (f) $x = 0.10$, (g) $x = 0.20$ and (h) $x = 0.30$; (B) 2θ region showing peaks corresponding to (202) and (040) planes showing the orthorhombic to monoclinic transition as Y concentration increases.

As mentioned in section 2B.1., BaCeO_3 and its doped versions up to 10 mol% dopant at the Ce-site are reported to crystallize in the orthorhombic system. But when the amount

of the dopant increases above 10 mol%, the crystal system changes to rhombohedral or monoclinic or a mixture of both phases depending on the conditions used for the synthesis. In this work, all the doped materials are found to crystallize in the orthorhombic system ($Pnma$, JCPDS-82-2372) up to 10 mol% Y substitution [17]. However, further increase in the yttrium concentration results in the structural distortion to monoclinic system ($I2/m$, JCPDS-70-6753) [15]. The absence of reflections corresponding to metallic Pt and yttrium oxide phases suggests successful incorporation of platinum and yttrium in the lattice. But traces of impurities of $BaCO_3$ and CeO_2 can be seen in the samples as indicated by the presence of corresponding peaks. A closer examination of the peak near 41 deg consisting of (202) and (040) planes (Figure 2B), shows an interesting trend; up to 6 mol%, shift to lower angles is small, but the peak shift to higher angles for the BC2P10Y sample indicated substantial reduction in the cell parameters. The peak shifted further to higher angles with further increase in the Y percentage to 20 and 30. Moreover an asymmetry can be observed for the peak for monoclinic BC2P20Y and BC2P30Y compounds which is attributed to the splitting of peak corresponding to the (202) plane to 202 and $(20\bar{2})$ planes arising due to the β -angle deviation from the 90° , unlike in the case of orthorhombic system where these planes are equivalent. This kind of peak asymmetry is not observed for the BC2P10Y indicating that the structure remains in the orthorhombic system at this level of dopant concentration.

Rietveld refinement of the PXRD patterns was carried out to extract more information regarding the structure. The patterns were refined with orthorhombic $Pnma$ space group upto 10 mol% Y substitution while monoclinic $I2/m$ was used for the rest of the materials. We have already investigated the structure of Pt substituted $BaCeO_3$ and studied the substitution of Pt(II) in place of Ce(IV) using PXRD and neutron diffraction experiments and is described in chapter 2A. For the 2 mol% Pt substituted compound, oxygen vacancies are found to be created in the axial O1 sites. Similar kind of observation is reported in the case of Pd doped $BaCeO_3$ at lower dopant concentration [18]. But neutron diffraction experiments and local structure analysis performed to investigate the structural evolution with temperature, of the Y doped $BaCeO_3$ proton conducting oxide by the group of Dr. Lorenzo Malavasi in University of Pavia, indicated that for higher percentages of Y

substitution, the oxygen vacancies are created in the in-plane or equatorial O2 sites [19, 20]. These facts suggest the creation of oxygen vacancies in both O1 and O2 sites in $\text{BaCe}_{1-x}\text{Y}_x\text{Pt}_{0.02}\text{O}_{3-\delta}$, where Pt and Y are simultaneously doped in the Ce site. Hence during refinement, we fixed the oxygen occupancy of O1 based on the results of the refinement of the neutron diffraction data for the 2 mol% Pt doped BaCeO_3 given in chapter 2A and that of O2 based on the Y concentration as reported by others. The examination of the nature of the platinum on the surface of the representative samples viz., BC2PxY ($x = 6, 10$ and 20) were carried out using XPS and the corresponding Pt-4f spectra are shown in figure 2B.3.

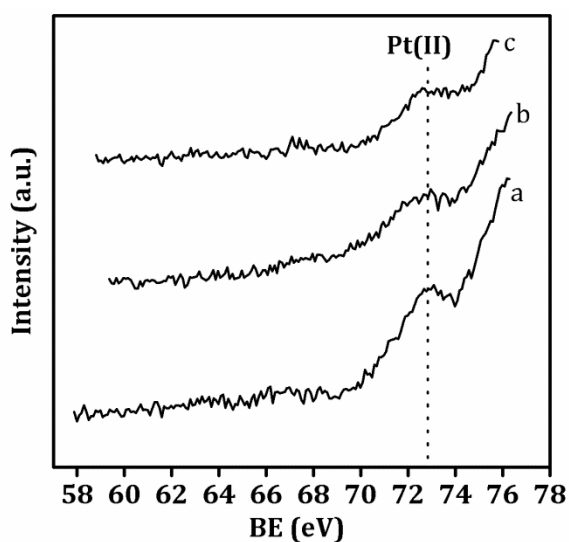


Figure 2B.3. Pt-4f XP spectra of $\text{BaCe}_{0.98-x}\text{Y}_x\text{Pt}_{0.02}\text{O}_{3-\delta}$ with (a) $x = 0.06$, (b) $x = 0.10$ and (c) $x = 0.20$.

The oxidation state of surface platinum present in all the materials is found to be +2 suggesting that the incorporation of Y has not affected the state of platinum in the materials. The platinum and yttrium occupancies were fixed based on the elemental analysis. The plots obtained after the Rietveld refinement for all the materials are shown in figure 2B.4, and the structural parameters obtained are tabulated in table 2B.2.

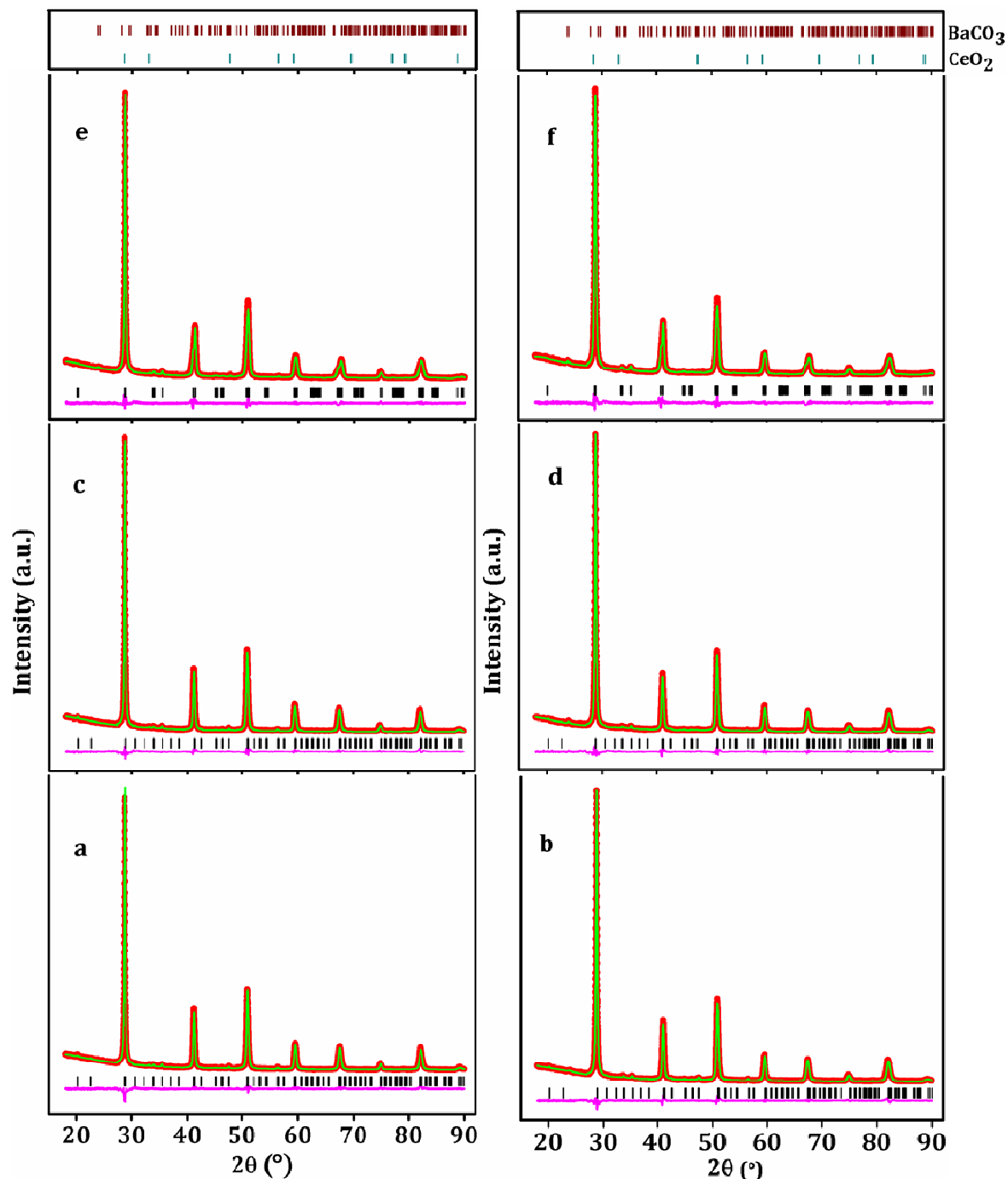


Figure 2B.4. Rietveld profile fits for the PXRD patterns of $\text{BaCe}_{0.98-x}\text{Y}_x\text{Pt}_{0.02}\text{O}_{3-\delta}$ with (a) $x = 0.02$, (b) $x = 0.04$, (c) $x = 0.06$, (d) $x = 0.10$, (e) $x = 0.20$ and (f) $x = 0.30$. Red line represents experimental data, green line is the Rietveld fit and pink line represents difference plot. Vertical lines at the top of the figure are the expected positions for the impurity phases BaCO_3 and CeO_2 .

Table 2B.2. Crystal structures of $\text{BaCe}_{0.98-x}\text{Y}_x\text{Pt}_{0.02}\text{O}_{3-\delta}$ as obtained from Rietveld refinement of PXRD data.

Parameters	x in $\text{BaCe}_{0.98-x}\text{Y}_x\text{Pt}_{0.02}\text{O}_{3-\delta}$					
	0.02	0.04	0.06	0.10	0.20	0.30
Space group	Pnma	Pnma	Pnma	Pnma	I2/m	I2/m
χ^2	1.928	1.789	1.802	1.828	1.97	2.253
wRp (%)	6.15	5.76	5.63	5.75	5.85	6.14
Rp (%)	4.66	4.11	4.09	4.21	4.23	4.46
a (Å)	6.2105(4)	6.2078(8)	6.1989(5)	6.2158(11)	6.2338(2)	6.2342(3)
b (Å)	8.7661(3)	8.7596(4)	8.7419(3)	8.7563(2)	8.7521(6)	8.7523(8)
c (Å)	6.2205(3)	6.2080(9)	6.2074(4)	6.2136(12)	6.2054(4)	6.2072(5)
β (°)					90.471(4)	90.517(5)
V(Å ³)	338.651(5)	337.575(5)	336.377(5)	338.195(5)	338.547(7)	338.674(8)
Ba x	0.4913(5)	0.4878(3)	0.4886(3)	0.4869(3)	0.2438(8)	0.2435(10)
z	-0.0025(14)	-0.0015(20)	-0.0011(11)	0.0064(5)	0.7549(5)	0.7586(10)
O1 x	0.5763(47)	0.4300(41)	0.4572(44)	0.4269(42)	0.1927(36)	0.1948(36)
z	0.5953(46)	0.5951(45)	0.5802(39)	0.6168(38)	0.3560(48)	0.3773(41)
O2 x	0.2328(77)	0.2481(41)	0.2409(37)	0.2585(37)	0	0
y	0.0354(13)	0.0324(13)	0.0407(13)	0.0144(29)	0.3023(25)	0.2847(38)
z	0.2607(64)	0.2434(60)	0.2555(58)	0.2257(29)	0	0
O3 y					0.2555(44)	0.2503(66)
O1 occ	0.876	0.876	0.876	0.876	0.876	0.876
O2 occ	1.0438	1.0398	1.0339	1.0245	1.003	0.9795
O3 occ						
BaCO ₃ (wt%)			1.89	2.05	1.29	1.52
CeO ₂ (wt%)	1.48	1.87	2.08		1.26	

For $x \leq 0.10$: Ce/Pt/Y at (0,0,0); Ba (x,0.25,y); O1(x,0.25,z); and for $x = 0.20$ and 0.30 : Ce/Pt/Y at (0.25,0.25,0.25); Ba (x,0,z); O1 (x,0,z); O3 (0.5,y,0)

Even though, the higher concentration of yttrium substitution changes the crystal system, it induces only small changes in the structure as can be observed from the small

variations in the lattice parameters and a small distortion in the basal plane as evident from the small change in the β angle from ideal 90° to 90.47° and 90.52° for the BC2P20Y and BC2P30Y respectively. In these monoclinic structures also, the oxygen vacancies are reported to be created in the equatorial O2 and O3 sites.

A clear picture of the structural distortion induced by the systematic incorporation of yttrium can be evolved with the help of plots of pseudocubic cell volume, BO_6 octahedron volume and pseudocubic cell parameters. The corresponding plots with respect to the Y substitution are displayed in figure 2B.5. The pseudocubic cell volume (calculated after neglecting the small monoclinic distortion, $\beta \neq 90^\circ$) of the materials is initially found to decrease from $338.651(5) \text{ \AA}^3$ for BC2P2Y to $336.377(5) \text{ \AA}^3$ for BC2P6Y and then increased to $338.195(5)$ for BC2P10Y and remains more or less same for further increase in Y concentration. Earlier reports on yttrium substitutions in BaCeO_3 focus on higher dopant concentrations equal to or greater than 10 % and found only marginal changes in cell volume when compared to the undoped BaCeO_3 . In the present work also, same observation is made when comparing 2 and 10 % substituted compounds. But smaller variations in the lower Y concentration range (4 and 6 mol%) resulted in significant reduction in the cell volume. Since the crystallographic radii of Ce(IV) (1.01 Å) and Y(III) (1.04) are almost same, the incorporation is not expected to have an effect on the structure. So the reduction in the cell volume can be attributed to the creation of oxygen vacancies consequent to the Y incorporation. However, a larger extent of yttrium doping (≥ 0.10) results in an impact of size effect on the structure. Similar kind of effect is not observed in the case of octahedron volume where the volume gradually decreased from 2 to 10 mol%. So the increase in cell volume for 10 mol% substituted sample can be attributed to the polyhedral distortions. For BC2P20Y and BC2P30Y, the higher concentration of the yttrium results in higher concentration of oxygen vacancies and to accommodate these, the structure undergoes relaxation to monoclinic system without having an effect on the cell volume. It can be noticed that the octahedral volume drastically reduces from orthorhombic to monoclinic systems. But it does not vary much for both the monoclinic structures pointing to the fact that the size effect becomes predominant after 20 mol%. BC2P10Y seems to be the transition point between orthorhombic and monoclinic

structures. However, the peak near 41° consisting reflections corresponding to (202) and (040) planes did not show any splitting corresponding to the monoclinic system and remains symmetric. In addition, the refinement of the diffraction pattern of the material using $I2/m$ space group did not yield satisfactory fitting parameters ruling out monoclinic system for the compound. These facts suggest that the structure remains orthorhombic at 10 mol% Y substitution. The gradual decrease in octahedral volume is the indication of the increase in oxygen vacancies.

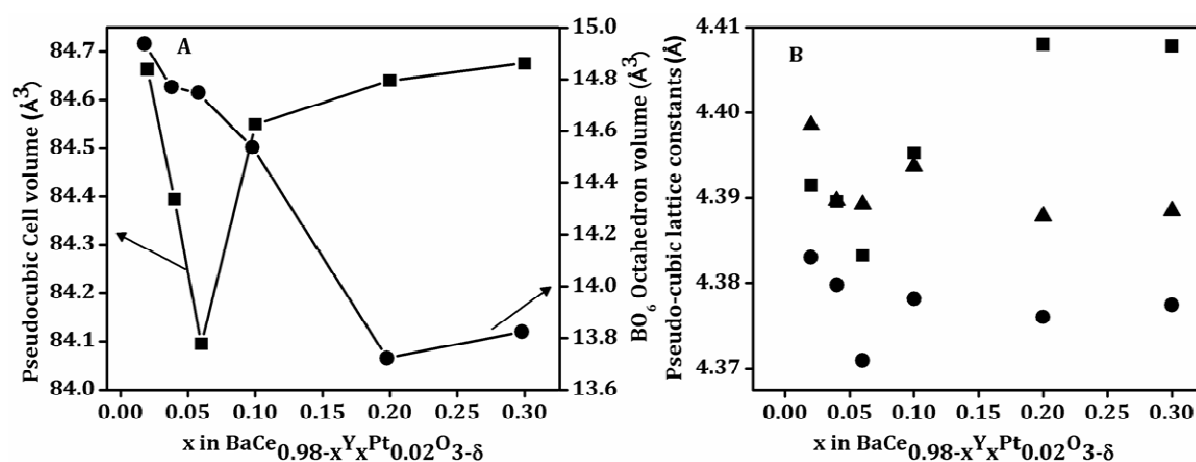


Figure 2B.5. (A) Pseudo-cubic cell volume, BO_6 octahedron volume and (B) Pseudo-cubic cell parameters $\blacksquare = a$, $\bullet = b$, and $\blacktriangle = c$ of $\text{BaCe}_{0.98-x}\text{Y}_x\text{Pt}_{0.02}\text{O}_{3-\delta}$ as a function of substitution x as obtained from Rietveld refinement of PXRD data. BO_6 octahedron volume was calculated considering total volume of four component tetrahedra.

An examination of the pseudocubic lattice parameters shows that the three axes lengths decreased for low yttrium percentages and then increased for BC2P10Y. However, with further increase in Y concentration, the b and c axes lengths remained more or less the same, but the a axis length increased considerably, indicating that structural relaxation occurs along the a axis for the monoclinic compounds. This observation may point to the fact that after a particular concentration, the oxygen vacancies start repelling each other resulting in an elongation of the cell lengths. So in these cases, the oxygen vacancies may be distributed anisotropically along the a axis. But it is very clear from the pseudo-cubic cell

parameter plot that the distribution of cell parameters for monoclinic structures is much wider when compared to the orthorhombic ones. To understand more about the changes occurring to the bonding characteristics with yttrium substitution, octahedral bond lengths and angles are compared (Table 2B.3).

Table 2B.3. Bond lengths and bond angles for $\text{BaCe}_{0.98-x}\text{Y}_x\text{Pt}_{0.02}\text{O}_{3-\delta}$ as obtained from the Rietveld refinement of PXRD data.

Parameter	x in $\text{BaCe}_{0.98-x}\text{Y}_x\text{Pt}_{0.02}\text{O}_{3-\delta}$					
	0.02	0.04	0.06	0.10	0.20	0.30
O1-Ce (Å)	2.318(10)	2.309(8)	2.257(6)	2.351(9)	2.313(10)	2.352(9)
O2-Ce (Å)	2.249(44)	2.252(32)	2.240(31)	2.273(21)	2.237(6)	2.211(7)
	2.197(43)	2.174(31)	2.205(32)	2.139(22)	2.208(4)*	2.209(5)*
Δd	0.000506	0.000587	0.000085	0.00165	0.000439	0.00088
Ce-O2-Ce (°)	162.72(215)	165.22(150)	161.30(149)	169.94(107)	156.39(0)	164.07(0)
Ce-O1-Ce (°)	141.92(0)	143.01(0)	151.08(0)	137.24(0)	142.15(0)	136.97(0)
Ce-O3-Ce (°)					177.73(0)	180.00(183)

*O3-Ce/Y/Pt

The Ce/Y/Pt-O octahedral distortion parameter Δd which directly gives information regarding the environment of oxygen ions around the B-site can be defined as [19],

$$\Delta d = 1/6 \sum_{n=1}^6 \left[\frac{d_n - d}{d} \right]^2,$$

where d is the mean Ce/Y/Pt-O bond distance and d_n are the individual Ce/Y/Pt-O bond distances. For the 2 and 4 mol% yttrium substitution, the Δd values are similar, but for the BC2P6Y the value (0.000085) is found to be the least, 10 fold less than the values obtained for other members. This points to a highly symmetric environment of oxygen ions around the B-site in the latter compound. The most distorted system is the BC2P10Y, as observed with a higher Δd value possibly due to the tilting of octahedra. This supports the

observed with a higher Δd value possibly due to the tilting of octahedra. This supports the earlier observation of change in lattice parameters and cell volume. The tilting of octahedra can be further understood with the help of B-O-B bond angles. It can be noted that the bond angles deviate to a greater extent from the ideal 180° for the Ce/Y/Pt -O1- Ce/Y/Pt than Ce/Y/Pt-O2-Ce/Y/Pt. This suggests that the octahedral tilting along b axis is much more severe than that along ac plane. In addition, both the bond angles are least for BC2P6Y compound indicating octahedral tilting and distortion is minimal in this compound. Similarly the Ba-O bond lengths are also obtained for all the compounds and are displayed in table 2B.4.

Table 2B.4a. O-Ba bond lengths of $\text{BaCe}_{0.98-x}\text{Y}_x\text{Pt}_{0.02}\text{O}_{3-\delta}$; $x \leq 0.1$ obtained from Rietveld refinement of PXRD patterns.

Parameters	$\text{BaCe}_{0.98-x}\text{Y}_x\text{Pt}_{0.02}\text{O}_{3-\delta}$			
	$x = 0.02$	$x = 0.04$	$x = 0.06$	$x = 0.10$
O2-Ba (Å)	3.432(32)	3.325(23)	3.428(23)	3.277(23)
	3.219(29)	3.283(24)	3.283(22)	3.144(23)
	2.966(35)	2.969(26)	2.869(26)	3.152(24)
Δd	2.837(34)	2.855(26)	2.851(26)	2.850(24)
	0.00541	0.004164	0.006649	0.002528
O1-Ba (Å)	3.677(31)	2.531(28)	2.608(26)	3.812(25)
	3.754(32)	2.806(25)	2.945(25)	3.564(25)
	2.558(32)	3.511(25)	3.612(26)	2.448(25)
Δd	2.643(31)	3.720(28)	3.331(25)	2.841(25)
	0.031498	0.024281	0.014871	0.029759

Table 2B.4b. O-Ba bond lengths of $\text{BaCe}_{0.98-x}\text{Y}_x\text{Pt}_{0.02}\text{O}_{3-\delta}$; $x > 0.1$ obtained from Rietveld refinement of PXRD patterns.

Parameters	$\text{BaCe}_{0.98-x}\text{Y}_x\text{Pt}_{0.02}\text{O}_{3-\delta}$	
	$x = 0.20$	$x = 0.30$
O2-Ba (Å)	2.844(14)	3.288(27)
	3.415(17)	2.953(23)
Δd	0.008323	0.00288
O3-Ba (Å)	3.061(25)	3.102(44)
	3.131(25)	3.090(44)
Δd	0.000151	0.0000037
O1-Ba (Å)	3.583(26)	3.853(26)
	3.746(31)	3.608(26)
	2.803(26)	2.853(26)
	2.493(31)	2.385(26)
Δd	0.027548	0.0341

The Ba-O1 bond lengths are much more distributed than the Ba-O2 values as indicated by a higher Δd value for the former in all the compounds. The enhanced symmetry of BC2P6Y can be further understood from the BaO_n polyhedra also. These studies revealed the unique nature of $\text{BaCe}_{0.92}\text{Pt}_{0.02}\text{Y}_{0.06}\text{O}_{3-\delta}$ with respect to the symmetric environment around the B ion compared to other structures.

HRTEM analysis was carried out and the representative images and lattices of BC2P6Y and BC2P20Y are shown in figure 2B.6. The particles are of approximately 100 nm size range and the lattice fringe analysis of a number of images shows the presence of perovskite only.

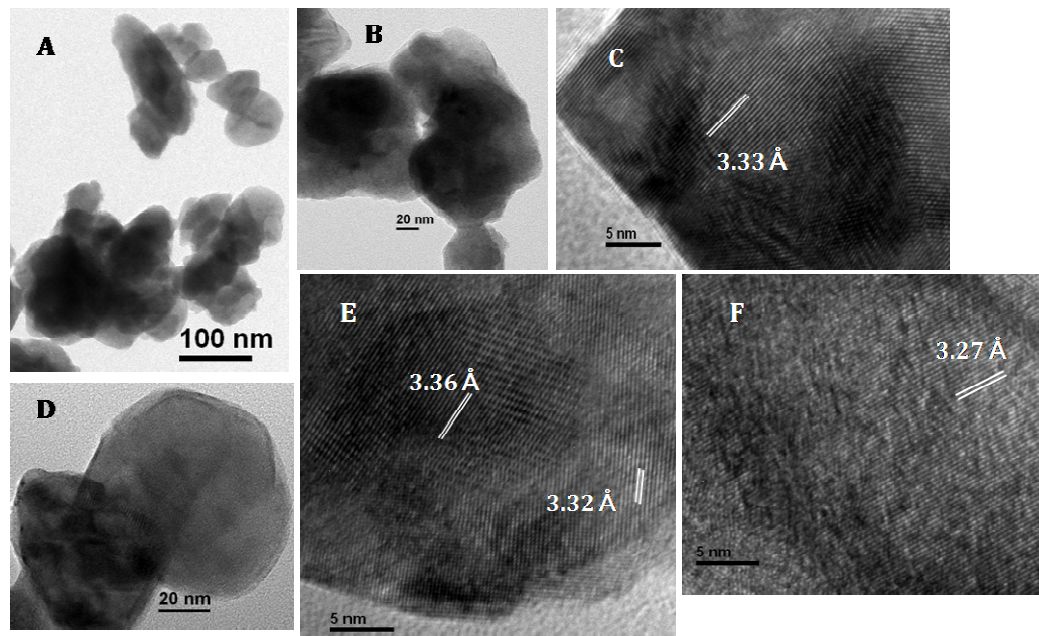


Figure 2B.6a. (A, B, & D) HRTEM images and (C, E & F) lattice fringes of $\text{BaCe}_{0.92}\text{Y}_{0.06}\text{Pt}_{0.02}\text{O}_{3-\delta}$.

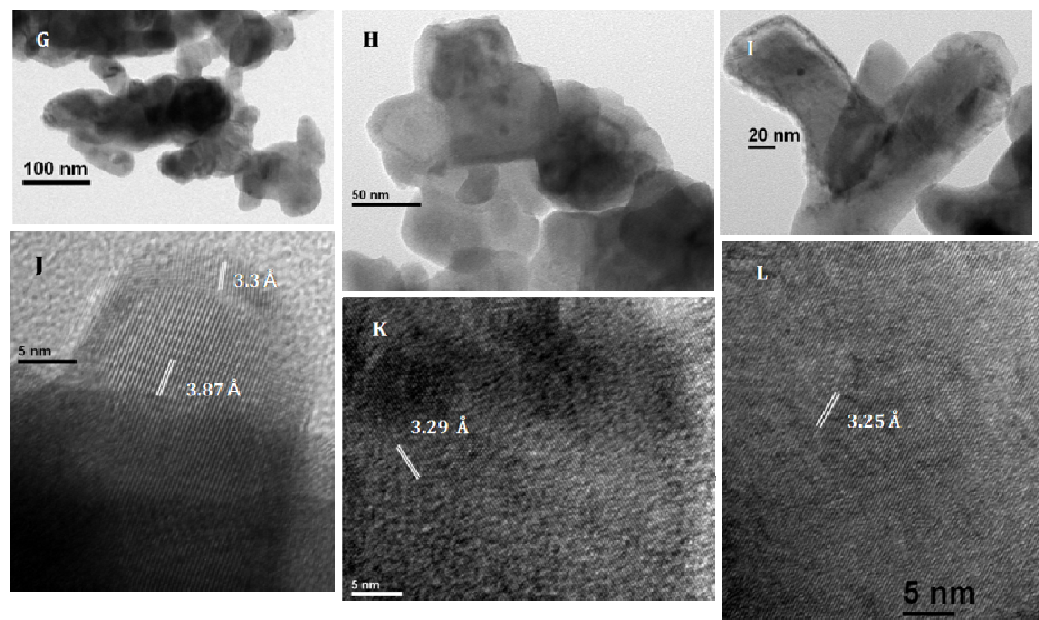


Figure 2B.6b. (G, H, & I) HRTEM images and (J, K & L) lattice fringes of $\text{BaCe}_{0.78}\text{Y}_{0.20}\text{Pt}_{0.02}\text{O}_{3-\delta}$.

2B.3.2. Catalytic activity testing

Water activation on oxygen vacancies present in the reducible oxide supports is considered as an important step in WGS reaction. In the catalyst systems used in the present study, ionic platinum, which can activate the CO molecules, is present in same amount in all the systems but the oxygen vacancies present varies depending on the Y content. So a correlation of the activity data with the yttrium content is expected to reveal the role of oxygen vacancies in the mechanism. This presents a series of catalysts whose activity variations depend only on the characteristics of the oxygen vacancy sites. The specific activities were determined based on the B atoms exposed on the perovskite particle surfaces obtained from N₂ adsorption study (table 2B.5).

Table 2B.5. Surface area obtained from N₂ adsorption.

x in BaCe _{0.98-x} Y _x Pt _{0.02} O _{3-δ}	Surface area (m ² /g)
0	9.174
0.02	7.577
0.04	8.626
0.06	8.327
0.10	8.839
0.20	8.56
0.30	7.982

As the HRTEM images of the representative samples reveal the particle sizes of the perovskites as 100 nm or larger, we assumed the chemical composition of the surface is same as that of bulk and hence a substitution of ~2 mol% Pt based on elemental analysis in the surface B positions was considered. The structure of perovskite was drawn with the help of “Diamond” software in the form of a sphere of ~1 nm radius and the number of B atoms was counted. This information was used to determine the number of B atoms in 1m² area. Since ~2 mol% (values obtained from ICP results are used) of the total B-site is

occupied by the platinum, its number per square meter was then calculated. After that the total number of surface platinum ions was determined using the weight of the catalyst and the surface area of the materials obtained from the N_2 adsorption. The obtained specific catalytic activities of all the materials along with that of 2 mol% Pt doped $BaCeO_3$ are displayed in figure 2B.7.

Initially the catalytic activity is found to increase with the yttrium substitution up to 6 mol% and then the activity drops and the 30 mol% Y doped sample displayed the least activity. This can be attributed to the fact that the increase in concentration of the oxygen vacancies help in facilitating the activity only up to a threshold concentration. The compound with 6 mol% Y substitution was found to display the highest activity of all the catalysts. The structural analysis described earlier revealed that this material has characteristic isotropic environment around the B ion. Reports suggest that isotropic coordination environment around the B ion facilitates ionic conduction through oxygen vacancies by lowering the energy barriers [21-23]. The BC2P10Y structure was found to have the highest distortion in the BO_6 octahedra. In the case of monoclinic structure, the breaking of symmetry in the Ce/Y site results in three different oxygen sites which can be expected to affect the activation energy for ion conduction. As the mechanism of both proton conduction and WGS reaction involve similar steps of water adsorption in the vacancy site and its dissociation, their energetics can be considered to be dependent on the coordination environment. So the higher activity of the BC2P6Y catalyst can be attributed to the presence of characteristic symmetric environment around the B ion which makes the adsorption and dissociation of water molecules energetically favourable.

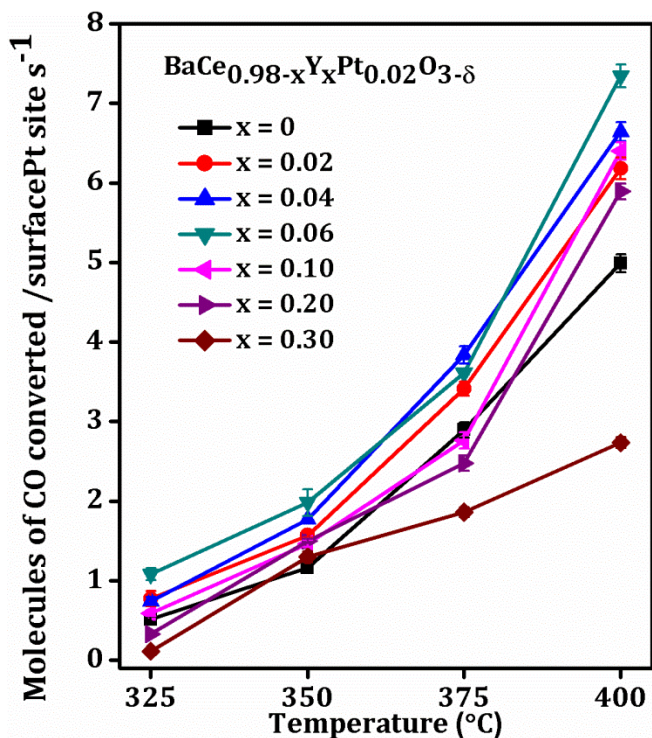


Figure 2B.7. Specific activities of $\text{BaCe}_{0.98-x}\text{Y}_x\text{Pt}_{0.02}\text{O}_{3-\delta}$ ($x=0$ to 0.3) under WGS conditions. Reformate composition: 40.3 % H_2 , 35.1 % N_2 , 10.1 % CO and 14.5 % CO_2 with a steam to CO ratio of 4.5 and GHSV 5000 h^{-1} .

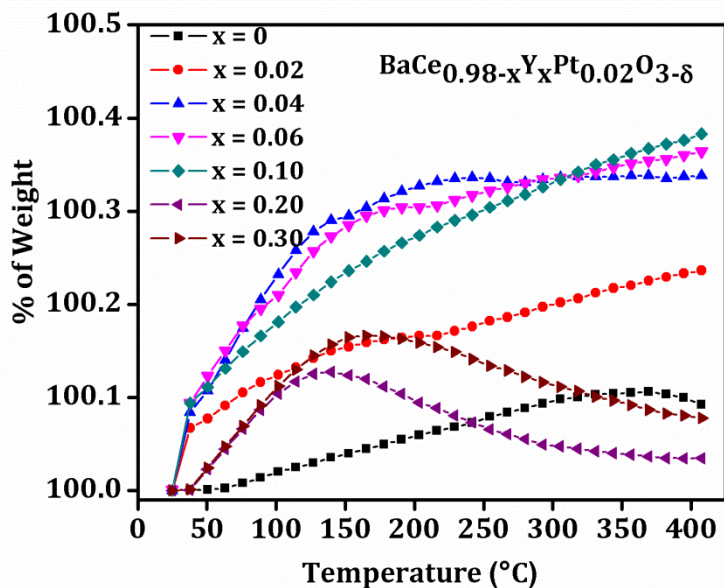


Figure 2B.8. Thermogravimetric profiles under air for $\text{BaCe}_{0.98-x}\text{Y}_x\text{Pt}_{0.02}\text{O}_{3-\delta}$ ($x=0$ to 0.3).

The catalytic activity of the materials was correlated with the oxygen uptake by thermogravimetric analysis under air up to the temperatures relevant to the WGS reaction and the obtained plots are displayed in figure 2B.8. The relation between oxygen vacancies and oxygen uptake are already reported by many groups [20, 24-26]. Initially the samples were preheated under Helium up to 500 °C to get reduced samples. This treatment enables the correlation of further weight change when heated in air to oxygen uptake or oxygen egress. It can be noticed that, for samples with a maximum of 10 mol% Y substitution, the oxygen uptake is found to increase with the temperature and the intake is found to be maximum at higher temperatures. The samples with 4, 6 and 10 mol% Y content showed highest oxygen uptake. Thermogravimetric profiles of the monoclinic structures, BC2P20Y and BC2P30Y are found to behave differently when compared to the orthorhombic structures. These materials showed increase in weight up to ~150 °C and then the weight started to decrease till 400 °C indicating an egress of oxygen from the lattice. This observation supports the structural studies where the monoclinic systems are found to behave very differently from the orthorhombic systems. The behavior of BC2P10Y similar to other low Y content orthorhombic structures further supports the assignment of orthorhombic crystal system to this compound from structural studies.

Yttrium doped BaCeO₃ compounds are well known proton conductors and it is understood that temperature can induce structural changes that can affect the characteristics and extent of oxygen vacancies. The structural changes occurring to the catalyst materials under WGS reaction conditions can be understood from the PXRD patterns (figure 2B.9) of the spent catalysts recovered after shutting down the reactor in N₂ atmosphere. When the concentration of Y, $x \leq 0.10$ in BC2P_xY, there is no structural change observed for the catalysts under reaction conditions. However, when $x > 0.10$, the structural transition from the monoclinic structure to the orthorhombic system is evident from the change in the asymmetric peak profile to the symmetric one after reaction. This indicates that the crystal structure is affected by the reaction conditions and consequently this transition might have some influence on the catalytic activity at these yttrium concentrations.

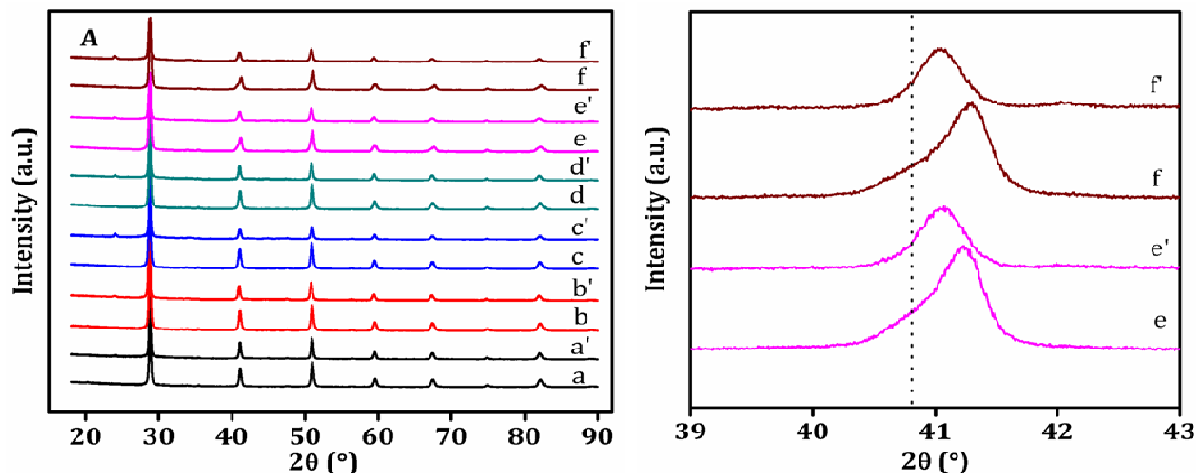
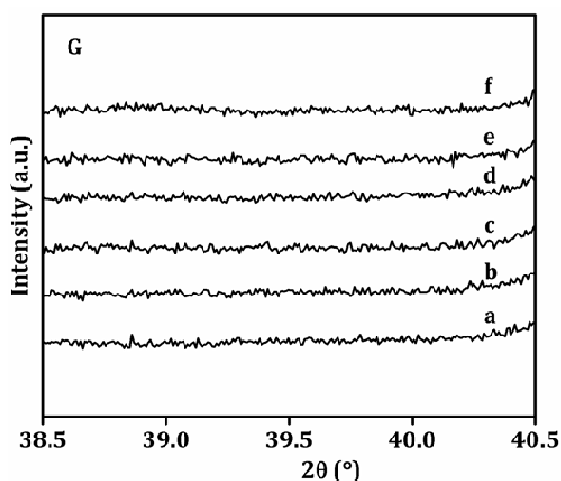


Figure 2B.9. (A) PXR patterns of BaCe_{0.98-x}Y_xPt_{0.02}O_{3-δ}, before (a) $x = 0.02$, (b) $x = 0.04$, (c) $x = 0.06$, (d) $x = 0.10$, (e) $x = 0.20$ and (f) $x = 0.30$ and after (a') $x = 0.02$, (b') $x = 0.04$, (c') $x = 0.06$, (d') $x = 0.10$, (e') $x = 0.20$ and (f') $x = 0.30$ WGS reaction. (B) 2θ region corresponding to [202] and [040] planes of BaCe_{0.98-x}Y_xPt_{0.02}O_{3-δ} before e) $x = 0.2$, f) $x = 0.3$ and after e') $x = 0.2$, f') $x = 0.3$ WGS reaction. Dotted line refers to the (20) peak.

In order to understand more about the structural changes occurring under different atmospheres, variable temperature PXR studies were carried out in reducing (5% H₂/Ar) as well as oxidizing (10% O₂/He) atmospheres and the results are depicted in figures 2B.10 and 2B.11 respectively. The structural studies using the obtained PXR patterns show that cationic Pt in all the materials is stable up to 900 °C under 5 % H₂/Ar as discernible by the absence of peaks corresponding to metallic Pt(111).



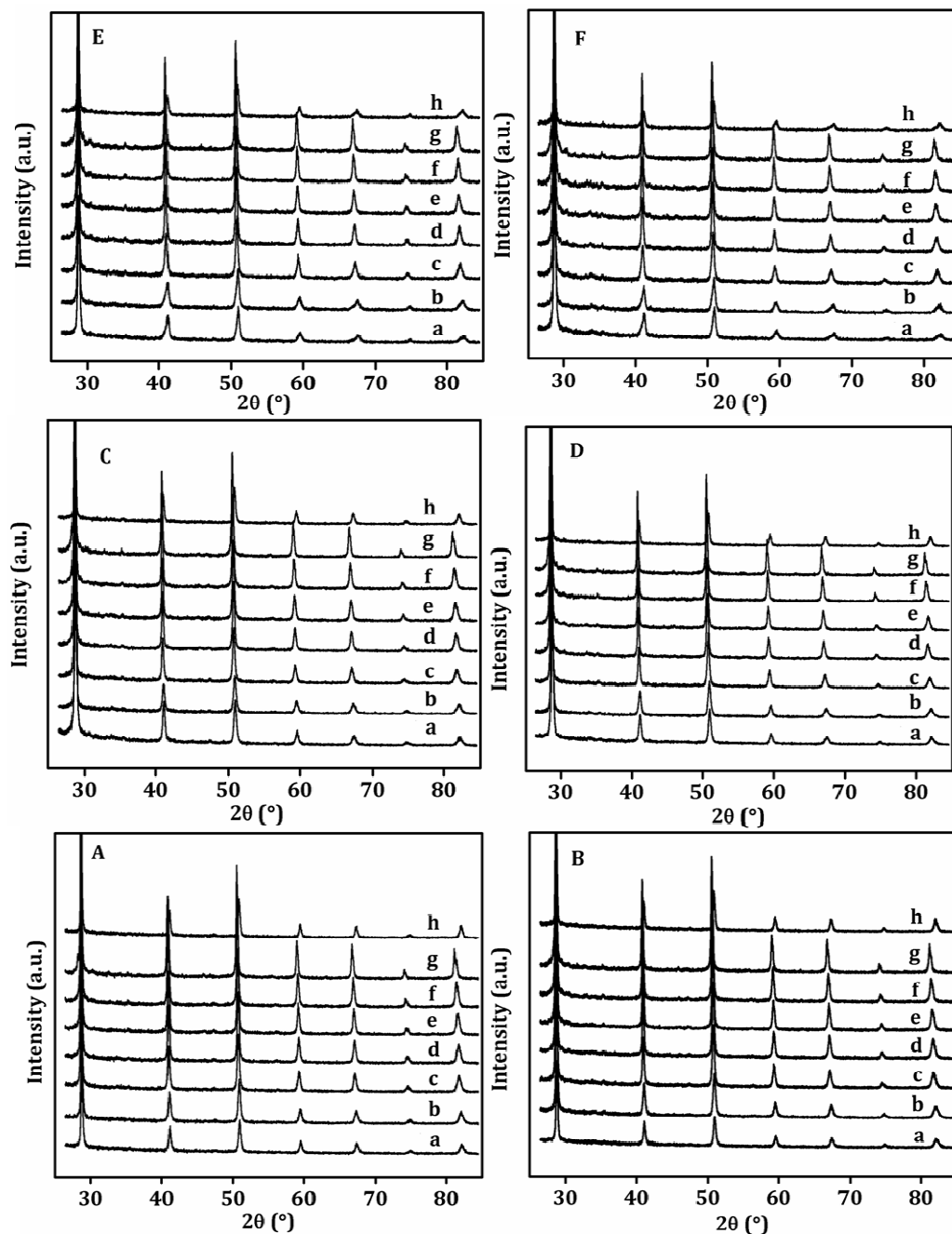


Figure 2B.10. In situ high temperature PXRD patterns of $\text{BaCe}_{0.98-x}\text{Y}_x\text{Pt}_{0.02}\text{O}_{3-\delta}$ with (A) $x = 0.02$, (B) $x = 0.04$, (C) $x = 0.06$, (D) $x = 0.10$, (E) $x = 0.20$ and (F) $x = 0.30$; (a) RT, (b) 150 °C, (c) 300 °C, (d) 450 °C, (e) 600 °C, (f) 750 °C, (g) 900 °C, (h) RT under 5 % H_2/Ar ; (G) 2 θ region where peak for metallic Pt(111) appear for $\text{BaCe}_{0.98-x}\text{Y}_x\text{Pt}_{0.02}\text{O}_{3-\delta}$ with (a) $x = 0.02$, (b) $x = 0.04$, (c) $x = 0.06$, (d) $x = 0.10$, (e) $x = 0.20$ and (f) $x = 0.30$ taken at 900 °C with slow scan speed.

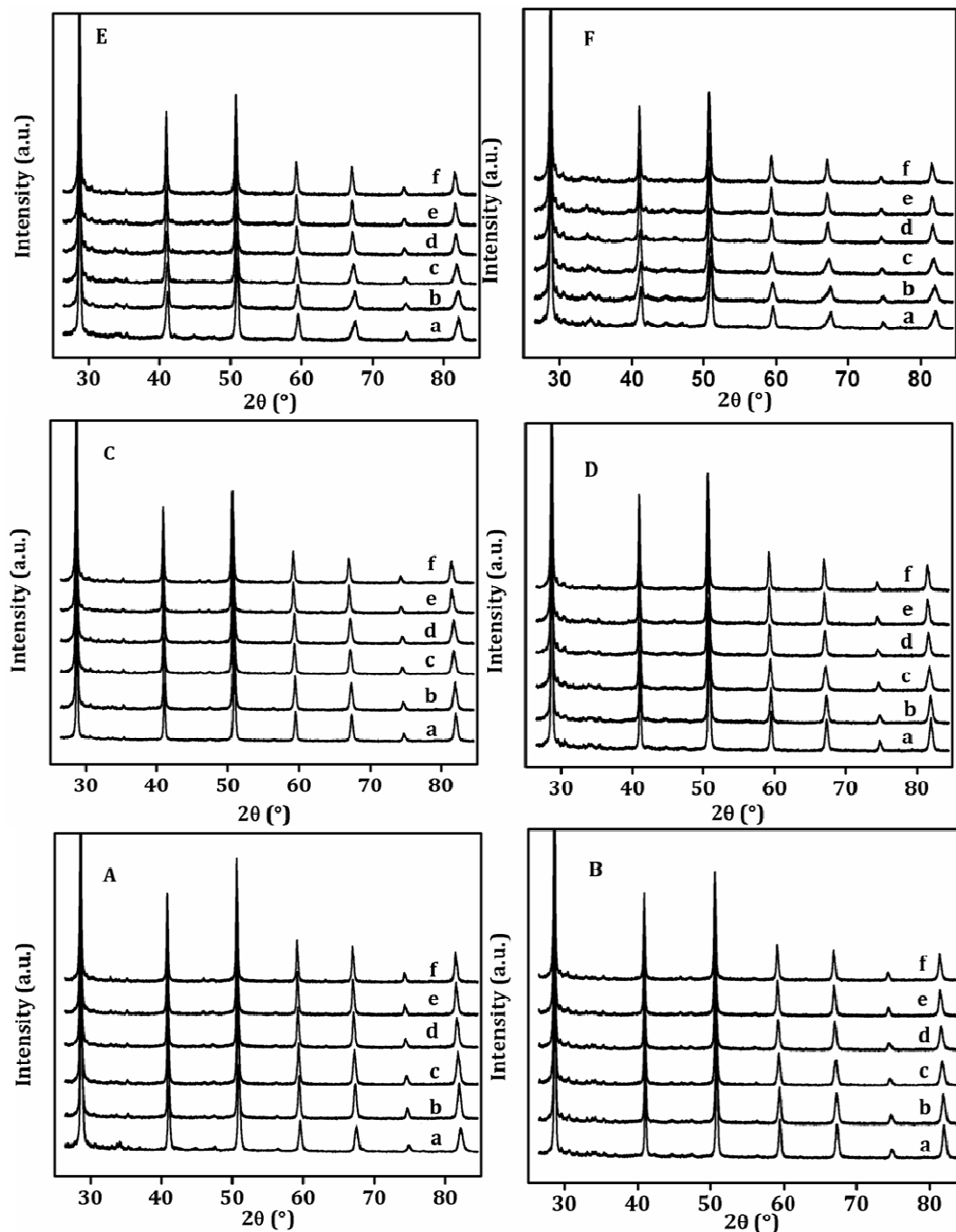


Figure 2B.11. In situ high temperature PXRD patterns of $\text{BaCe}_{0.98-x}\text{Y}_x\text{Pt}_{0.02}\text{O}_{3-\delta}$ with (A) $x = 0.02$, (B) $x = 0.04$, (C) $x = 0.06$, (D) $x = 0.10$, (E) $x = 0.20$ and (F) $x = 0.30$; (a) RT, (b) 150 °C, (c) 300 °C, (d) 450 °C, (e) 600 °C, and (f) 750 °C under 10 % O_2/He .

As observed in the PXRD analysis of the spent catalysts, the orthorhombic compounds having up to 10 mol% Y substitution, are structurally stable under both

oxidizing and reducing conditions employed. However, for the compounds with yttrium amount higher than 10 mol%, a structural transition from monoclinic to orthorhombic system starts at 150 °C (as indicated by a reduction in the β angle obtained from the Rietveld refinement of the pattern) under 5 % H₂/Ar and a complete transition could be observed at 300 °C. The structure remains in the orthorhombic system up to 900 °C; but when cooled to room temperature under the same atmosphere, the structure changes back to the initial monoclinic structure, which is different from the behavior seen with the spent catalyst recovered after WGS reaction. The reduced samples were then allowed to undergo heat treatment under 10 % O₂/He. The PXRD patterns show that under this condition also, the monoclinic structure underwent a similar kind of change to orthorhombic structure after 150 °C and regained the initial structure when cooled to room temperature. This structural change can be attributed to a reversible thermal effect only, which is independent of the atmospheres.

A thorough cell parameter refinement was done using GSAS-EXPGUI for the PXRD patterns of the compounds obtained at different temperatures and atmospheres and the results are given in figure 2B.12.

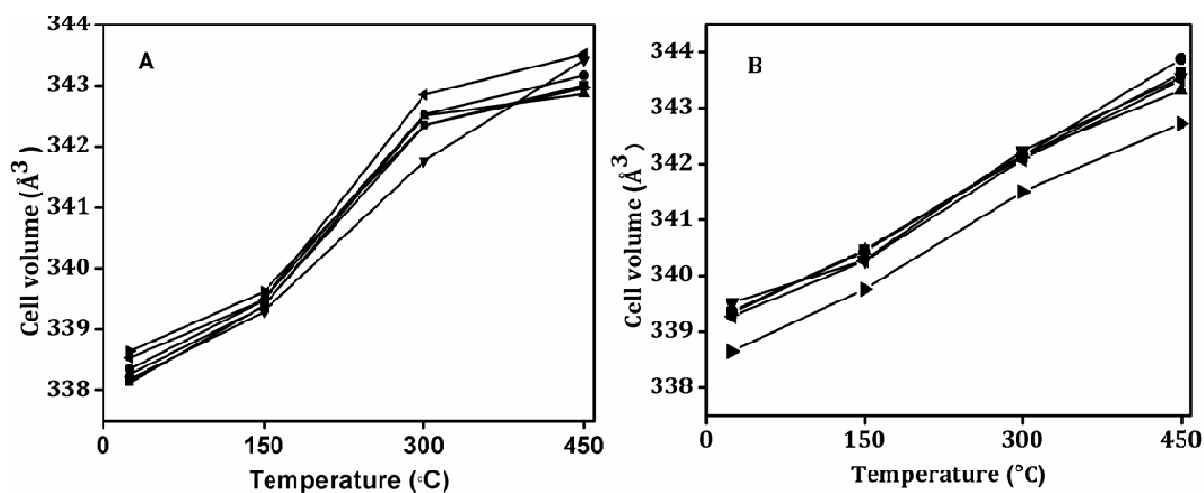


Figure 2B.12. Cell volume of BaCe_{0.98-x}Y_xPt_{0.02}O_{3-δ} under A) 5 % H₂/Ar and B) 10 % O₂/He with ■: x = 0.02, ●: x = 0.04, ▲: x = 0.06, ▼: x = 0.10, ◀: x = 0.20 and ▶: x = 0.30.

The cell volumes of all compounds irrespective of the atmospheres are found to increase with temperatures and no particular trend is observed with compounds of different Y content. The expansion of the cell with increase in temperature is already reported for Y incorporated BaCeO_3 proton conductors [20, 26]. The increase in cell volume under both reducing and oxidizing atmospheres support the fact that the effects are merely temperature induced. These results can be correlated with TGA studies described earlier where the monoclinic compounds showed a profile different from that of the orthorhombic compounds. The initiation of monoclinic to orthorhombic transition occurs at 150 °C as observed with a reduction in the β angle. Maxima in the oxygen uptake also occurs at around 150 °C after which egress of oxygen takes place. These observations correlate the structural change with oxygen uptake. Surprisingly the structural change to a less distorted orthorhombic structure at temperatures well below those significant for the activity studies has not influenced the activity positively. This observation also highlights the significance of characteristics of the oxygen vacancies and not their mere presence towards the catalytic activity. The capability of the structure to incorporate O_2 , which can also be extended to H_2O , seems to be important for WGS activity. But the structural change in reducing or oxidising atmospheres was found to be reversible while that under WGS reaction condition was shown to be irreversible. To investigate this difference in behaviour, in-situ PXRD studies under conditions similar to WGS reaction on representative samples from both structure families (BC2P6P from orthorhombic system and BC2P20P in monoclinic system) were conducted and the results are shown in figure 2B.13. Interestingly, in the case of monoclinic systems, an irreversible structural change to the orthorhombic system was observed. However, the structural change was found to be reversible under helium saturated with water vapour. This suggests that mere presence of water is not enough to induce the irreversible change.

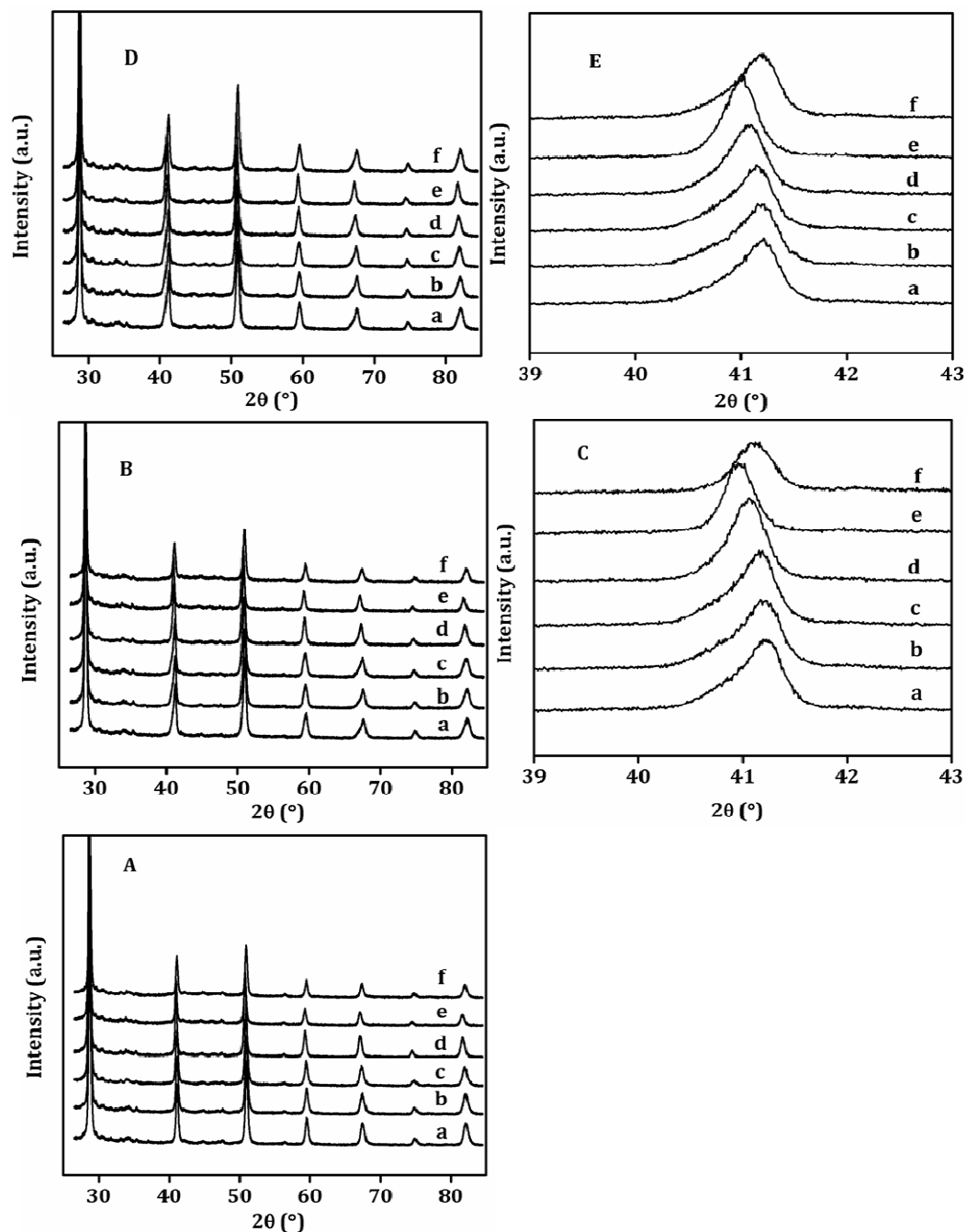


Figure 2B.13. In situ PXRD patterns of $\text{BaCe}_{0.98-x}\text{Y}_x\text{Pt}_{0.02}\text{O}_{3-\delta}$ with (A) $x = 0.06$ and (B) $x = 0.20$, (C) 2θ region showing monoclinic-orthorhombic transition for $x=0.20$ under reformat gas mixture of 40.3 % H_2 , 35.1 % N_2 , 10.1 % CO and 14.5 % CO_2 saturated with water vapour; (D) In situ PXRD patterns of $\text{BaCe}_{0.78}\text{Y}_{0.20}\text{Pt}_{0.02}\text{O}_{3-\delta}$ and (E) 2θ region showing monoclinic-orthorhombic transition for $x=0.20$ under helium saturated with water vapour; (a) RT, (b) 100 °C, (c) 200 °C, (d) 300 °C, (e) 400 °C, and (f) RT.

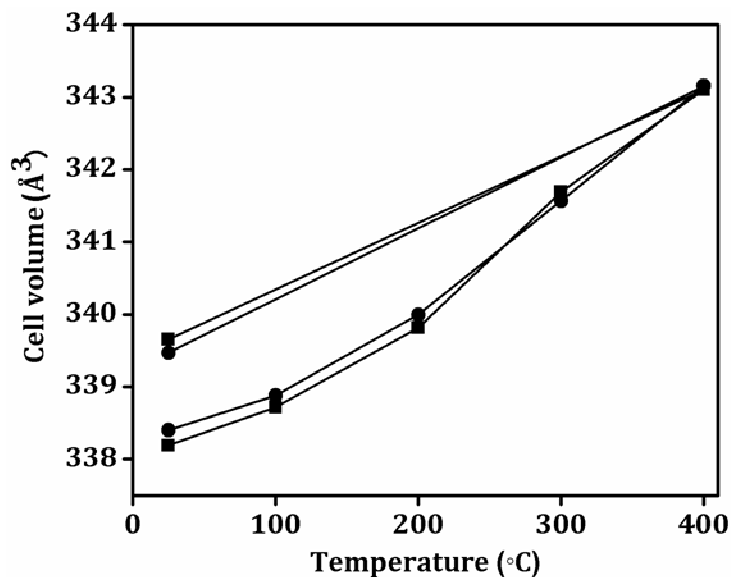


Figure 2B.14. Cell volume of $\text{BaCe}_{0.98-x}\text{Y}_x\text{Pt}_{0.02}\text{O}_{3-\delta}$ ■: $x = 0.06$ and ●: $x = 0.20$ under reformat gas mixture of 40.3 % H_2 , 35.1 % N_2 , 10.1 % CO and 14.5 % CO_2 saturated with water vapour.

Investigations reveal that in BaCeO_3 proton conductors, the increase in oxygen vacancies created with Y substitution resulted in the structural transition from orthorhombic to rhombohedral and monoclinic systems [15, 19]. Monoclinic structures accommodate more oxygen vacancies by undergoing a comparatively larger extent of octahedral tilting than the orthorhombic ones and are more distorted. The increase in the temperature, forces the compound to adopt the more ordered orthorhombic structure and when cooled to room temperature the structure returns to the initial one with no contribution from the atmospheres towards the structural change under oxidising and reducing conditions. The fact that the structure remains in the less oxygen vacant orthorhombic system under WGS reaction conditions means that the reaction mixture in the presence of water causes the reduction of the oxygen vacancies, a unique behaviour observed to be shown only in the presence of conditions similar to WGS reaction. Under these conditions, the oxygen vacancies might have been reduced by the induction of an oxide/hydroxide ion by the dissociation of water molecule in the oxygen vacancy site. This irreversible structural change caused by the reduction in the vacancy when CO was used

along with water directly indicated the significant role played by oxygen vacancies in WGS reaction.

2B.4. Conclusions

The role of oxygen vacancies in WGS reaction is investigated using a series of compounds based on BaCeO_3 codoped with Pt and Y. 2 mol% Pt doped BaCeO_3 was found to be moderately active for WGS reaction and the progressive doping of Y(III) in place of Ce(IV) in the range 2-30 mol% results in the systematic creation of oxygen vacancies in the system. Even though the creation of oxygen vacancies resulted in a reduction in the cell volume for lower Y concentration, further increase in oxygen vacancies for higher Y substitution forces the system to undergo structural distortion. Interestingly the compound with 6 mol% yttrium substitution was found to have the most symmetric environment around the B-ion and the same compound exhibited the best WGS activity. This led to the conclusion of existence of structure-activity relationship, where the symmetry around B-site ion energetically favours the dissociative adsorption of water molecules on the oxygen vacancies by lowering the activation energy barrier. In other words, the catalytic activity depends not on the concentration of oxygen vacancies but on their crystallographic characteristics. Moreover the ability of the oxygen vacant sites to uptake oxygen also determines the activity. Investigations to understand the stability of the materials using in-situ PXRD studies under reducing and oxidizing conditions revealed only a thermal expansion at higher temperatures for lower amount of Y substituted orthorhombic compounds, but a structural transition to orthorhombic system at high temperatures, which reversed upon cooling to RT, is observed for the high percentage Y containing monoclinic compounds. This reversible structural transition under H_2 , O_2 and water vapour is only temperature driven. However, when conditions similar to WGS reaction are used, the monoclinic to orthorhombic transition was found to be irreversible. The fact that WGS reaction conditions resulted in the permanent transition to a less oxygen vacant orthorhombic system clearly establishes the involvement of oxygen vacancies in the WGS reaction mechanism.

References

1. Astruc, D. Transition-Metal Nanoparticles in Catalysis: From Historical Background to the State-of-the Art. In Nanoparticles and Catalysis; Wiley-VCH Verlag GmbH & Co. KGaA: Weinheim, 2008.
2. Anderson, J. A.; Garcia, M. F. Supported Metals in Catalysis; Imperial College Press: London, 2005.
3. Trovarelli, A. *Catal. Rev.-Sci. Eng.* **1996**, *38*, 439.
4. Trovarelli, A.; de Leitenburg, C.; Boaro, M.; Dolcetti, G. *Catal. Today* **1999**, *50*, 353.
5. Sandoval, A.; Gomez-Cortes, A.; Zanella, R.; Diaz, G.; Saniger, J. M. *J. Mol. Catal. A: Chem.* **2007**, *278*, 200.
6. Bunluesin, T.; Gorte, R. J.; Graham, G. W. *Appl. Catal. B: Environ.* **1998**, *15*, 107.
7. Li, Y.; Fu, Q.; Flytzani-Stephanopoulos, M. *Appl. Catal. B: Environ.* **2000**, *27*, 179.
8. Bunluesin, T.; Gorte, R. J.; Graham, G. W. *Appl. Catal. B: Environ.* **1998**, *15*, 107.
9. Vindigni, F.; Manzoli, M.; Tabakova, T.; Idakiev, V.; Boccuzzi, F.; Chiorino, A. *Phys. Chem. Chem. Phys.* **2013**, *15*, 13400.
10. Scherban, T.; Villeneuve, R.; Abello, L.; Lucazeau, G. *Solid State Ionics* **1993**, *61*, 93.
11. Giannici, F.; Longo, A.; Deganello, F.; Balerna, A.; Arico, A. S.; Martorana, A. *Solid State Ionics* **2007**, *178*, 587.
12. Stevenson, D. A.; Jiang, N.; Buchanan, R. M.; Henn, F. E. G. *Solid State Ionics* **1993**, *62*, 279.
13. Knight, K. S.; Soar, M.; Bonanos, N. *J. Mater. Chem.* **1992**, *2*, 709.
14. Chen, F. L.; Sorensen, O. T.; Meng, G. Y.; Peng, D. K. *J. Eur. Ceram. Soc.* **1998**, *18*, 1389.
15. Takeuchi, K.; Loong, C. K.; Richardson, J. W., Jr.; Guan, J.; Dorris, S. E.; Balachandran, U. *Solid State Ionics* **2000**, *138*, 63.
16. Zhao, F.; Liu, Q.; Wang, S.; Brinkman, K.; Chen, F. *Int. J. Hydrogen Energy* **2010**, *35*, 4258.
17. Knight, K. S.; Bonanos, N. *J. Mater. Chem.* **1994**, *4*, 899.
18. Li, J.; Singh, U. G.; Bennett, J. W.; Page, K.; Weaver, J. C.; Zhang, J.-P.; Proffen, T.; Rappe, A. M.; Scott, S.; Seshadri, R. *Chem. Mater.* **2007**, *19*, 1418.
19. Malavasi, L.; Kim, H.; Proffen, T. *J. Appl. Phys.* **2009**, *105*, 123519-1.

20. Malavasi, L.; Ritter, C.; Chiodelli, G. *Chem. Mater.* **2008**, *20*, 2343.
21. Kreuer, K. D. *Annu. Rev. Mater. Res.* **2003**, *33*, 333.
22. Munch, W.; Kreuer, K. D.; Adams; Seifert, G.; Maier, J. *Phase Transitions* **1999**, *68*, 567.
23. Islam, M. S.; Davies, R. A.; Gale, J. D. *Chem. Mater.* **2001**, *13*, 2049.
24. Suescun, L.; Dabrowski, B.; Mais, J.; Remsen, S.; Richardson, J. W.; Maxey, E. R.; Jorgensen, J. D. *Chem. Mater.* **2008**, *20*, 1636.
25. Filimonov, D. S.; Liu, Z. K.; Randall, C. A. *Mater. Res. Bull.* **2002**, *37*, 2373.
26. Chen, Q.; El Gabaly, F.; Aksoy Akgul, F.; Liu, Z.; Mun, B. S.; Yamaguchi, S.; Braun, A. *Chem. Mater.* **2013**, *25*, 4690.

Chapter 3

Synthesis, Characterization and WGS Activity

Studies of $\text{LaB}_{1-x}\text{Pt}_x\text{O}_{3-\delta}$; (B = Mn, Fe, and Co):

Activity and Stability of Cationic Pt

3.1. Introduction

We have already demonstrated the stabilization of cationic platinum in the lattice sites of BaCeO_3 in an attempt to minimise sintering of noble metal nanoparticles and attendant deactivation frequently encountered with conventional oxide supported noble metal catalysts used in industrial processes. The stabilization of noble metals can be attempted in other perovskite lattices also. Lanthanum based perovskites (LaBO_3) with B-site occupied by first row transition metals are extensively studied for various applications including catalysis [1-5]. These perovskites are reported to be active for a number of heterogeneous reactions such as oxidation [6-8], hydrogenation of carbon oxides [9], electrocatalysis [10], photocatalysis [11], Water Gas Shift reaction [12, 13] etc. In addition, they are used as supports for catalytically active metals as they facilitate redox reactions on account of their ability to adapt multiple oxidation states and also they can tolerate and stabilize sufficient amount of oxygen vacancies [14, 15]. Recently these perovskites are found to be able to stabilize active noble metal against sintering in three way catalysis. The active palladium ions incorporated in the lattices of lanthanum ferrite perovskite is suggested to egress and ingress depending on the oxygen rich and lean conditions [16, 17]. These reports emphasise the importance of the stabilization by lattice incorporation of active metallic species in the lanthanum based perovskites. However, the strategy followed in the present study relies on the permanent incorporation of active metals as ions which are stable inside the lattice even under drastic conditions. The substitution of Pt in LaBO_3 perovskites has added advantage as their phase formation can be achieved with lower synthesis temperatures, which makes the properties of the materials ideal for catalytic application. In addition, a number of elements can be possible at the B-site, which themselves are known for catalytic activity and hence the combined effect of these transition metals along with the cationic platinum can be investigated. Of all the combinations possible with the first row transition metals for the perovskite, LaMnO_3 presents a unique structural system with oxidative nonstoichiometry due to the presence of Mn(IV) ions along with Mn(III) ions [18, 19]. Recent studies revealed that these materials indeed have cation vacancies ruling out the earlier concept of interstitial oxygen ions [20, 21]. However, these are

regarded as oxygen excess materials for convenience. So a catalytic system comprising this perovskite along with the platinum is ideal to investigate the role of oxygen vacancies in processes involving redox mediated mechanism.

The work presented in this chapter describes the synthesis, characterisation and WGS activity of $\text{LaB}_{1-x}\text{Pt}_x\text{O}_{3-\delta}$ perovskite system where B represents Mn, Fe and Co. It is established that platinum could be stabilized in ionic form in LaFeO_3 and LaCoO_3 perovskites, whereas the substitution of Mn by Pt in LaMnO_3 could not be achieved under various synthesis conditions. The activities of these catalysts are compared with the Pt impregnated perovskites and mixed oxides and the results bring out the advantage of perovskite over the mixed oxide system in catalysis.

3.2. Experimental section

3.2.1. Synthesis

LaFeO_3 and substituted LaFeO_3 containing various amounts of Pt (2, 4 and 6 mol%) were synthesised by combustion method using glycine. 3 mmol each of $\text{La}(\text{NO}_3)_3 \cdot 6\text{H}_2\text{O}$ and $\text{Fe}(\text{NO}_3)_3 \cdot 9\text{H}_2\text{O}$ (Sigma–Aldrich) were dissolved in 40 mL water. 2 mmol of glycine (Merck) was added to it. Appropriate amount of tetraammine platinum nitrate (Sigma–Aldrich) was added for the Pt doped sample. The solution was heated to 90 °C to get a brown coloured gel. The gel was pyrolysed at 400 °C to remove organic materials. A reddish brown powder was obtained and was ground well. It was then calcined at 600 °C for 6 h to get the Pt doped LaFeO_3 .

In case of LaBO_3 (B = Co, Mn) along with Pt substituted samples, 3 mmol each of $\text{La}(\text{NO}_3)_3 \cdot 6\text{H}_2\text{O}$ (Sigma–Aldrich) and $\text{Co}(\text{NO}_3)_2 \cdot 6\text{H}_2\text{O}$ or $\text{Mn}(\text{OAc})_2 \cdot 4\text{H}_2\text{O}$ (Merck) were dissolved in 40 mL water. 12 mmol of citric acid monohydrate (Merck) was added to it. Appropriate amount of tetraammine platinum nitrate (Sigma–Aldrich) was added for the Pt doped sample. The temperature was increased to 90 °C to get a gel. The gel was pyrolysed at 400 °C to remove organic materials. The obtained precursor powder was ground well and calcined at 600 °C for 6 h for Pt doped LaCoO_3 . To get Pt doped LaMnO_3 , the powder was calcined at different temperatures, viz. 600 °C for 60 h or 700

°C for 6 h or 900 °C for 6 h. For the preparation of undoped LaMnO₃ perovskite, the calcination was done at 600 °C for 9 h.

3.2.2. Characterisation

The details of the instruments and procedures used for PXRD, Rietveld refinement, HRTEM, ICP-AES and surface area measurements are same as those described in chapter 2A in section 2A.2.2. Synchrotron X-ray diffraction (SXR) experiments were carried out at Angle Dispersive X-ray Diffraction (ADXRD) beamline at Indus-2 synchrotron source. The beamline is equipped with Si(311) crystal pair based double crystal monochromator and two experimental stations; a six circle diffractometer (Huber 5020) with scintillation detector and an image plate area detector (MAR 345) [22]. SXR measurements reported here were performed using the Image Plate.

XANES (X-Ray Absorption Near Edge Structure) measurements were carried out at the same beamline. The energy band pass at 8 keV is ~0.8 eV and the energy reproducibility is ~50 meV. Pt L₃-edge XANES was collected in fluorescence mode using an energy dispersive detector (VERTEX-EX). The spectra were normalised to incident photon energy using an ionisation chamber. For the XPS analysis discussed for LaMnO₃ system, instrument described in section 2B.2.2. of chapter 2B was used. For XPS measurements described for the LaFeO₃ and LaCoO₃ systems, VSW scientific instrument (UK) with twin anode facility was used. For the present samples, Al K α source (resolution ~ 0.9 eV) was employed. Binding energy correction was done using the reference of graphitic C 1s peak, while Au sample served as an external reference for resolution and binding energy reference. The photoelectrons were detected using a concentric hemispherical analyzer with pass energy of 40 eV. For adventitious carbon, 285 eV was taken as the reference binding energy for charge correction. Data processing was performed with the XPSPEAK41 software and the spectra were deconvoluted using Gaussian and Lorentzian lines after subtracting a Shirley background.

3.2.3. Catalytic testing

The set up for catalytic activity measurement used was the same as that described in chapter 2A in section 2A.2.3.

3.3. Results and discussion

Soft wet chemical routes using citric acid and glycine were employed which enable the synthesis of the pure phase compound with smaller particles at relatively lower temperatures. The synthesized compounds have the stoichiometry $\text{LaFe}_{1-x}\text{Pt}_x\text{O}_{3-\delta}$ ($x = 0.02, 0.04$ and 0.06) and $\text{LaB}_{1-x}\text{Pt}_x\text{O}_{3-\delta}$ ($x = 0.02, 0.04$, $B = \text{Mn, Co}$) corresponding to the weight percentages 1.6, 3.1 and 4.7 respectively. The PXRD patterns of all the Pt doped perovskites are given in figure 3.1.

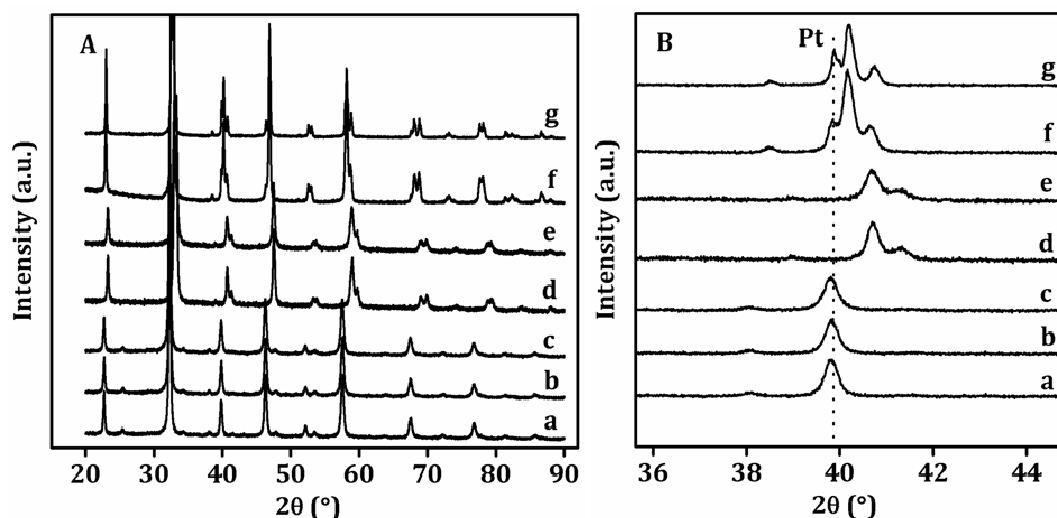


Figure 3.1. (A) PXRD patterns of $\text{LaB}_{1-x}\text{Pt}_x\text{O}_{3-\delta}$ ($B = \text{Fe, Co and Mn}$). For Fe (a) $x = 0.02$, (b) $x = 0.04$, (c) $x = 0.06$; for Co (d) $x = 0.02$, (e) $x = 0.04$ and for Mn (f) $x = 0.02$ and (g) $x = 0.04$. (B) 2θ region where Pt(111) reflection appear.

In case of LaFeO_3 perovskite, the incorporation of ionic platinum could not be understood from the PXRD patterns as the peak positions of the perovskite as well as Pt metal overlap. However, in the other two cases the peak positions of the perovskites and Pt are well separated. Reflections corresponding to the metallic platinum are not observed in the case of Pt doped LaCoO_3 perovskites where as metallic Pt peaks are

easily distinguishable in the patterns of LaMnO_3 which was synthesized at $900\text{ }^\circ\text{C}$. So in order to understand more about the resistance to Pt incorporation in LaMnO_3 , synthesis conditions utilizing different calcination temperatures are used. So the Pt doping in LaMnO_3 system will be discussed separately from the other two systems.

3.3.1. Pt doping in LaMnO_3 system

3.3.1.1. Synthesis

Stoichiometric LaMnO_3 is reported to be synthesized under very low oxygen partial pressures at $1200\text{ }^\circ\text{C}$ [23]. The structure belongs to orthorhombic crystal system and is formed as a result of the Jahn-Teller distortion of the oxide octahedron around the Mn ion. All other synthesis methods results in oxygen excess materials. According to the reports, when Mn(IV) concentration is greater than 21 %, the structure changes from orthorhombic to rhombohedral [24]. The lanthanum manganite perovskite with excess oxygen can be converted to oxygen deficient ones by reduction [25]. Various substitution studies are also carried out by many groups, but most of them concentrate on La-site substitution [26-29]. Few reports suggest that aliovalent substitution at the Mn-site leads to the formation of more Mn(IV) ions rather than the creation of oxygen vacancies [30-33]. In the present study, Pt incorporation (4 mol% equivalent to ~3 wt%) is attempted at the Mn site of LaMnO_3 perovskite at various calcination temperatures ($600, 700$ & $900\text{ }^\circ\text{C}$) to observe the effect of temperature on the extent of substitution as well as stability. The catalysts are referred henceforth as MP_x for the samples for convenience, where x represents the calcination temperature. The amount of Pt in all the materials is found to be approximately 3 wt% according to the elemental analysis by ICP-AES as shown in table 3.1.

Table 3.1. Pt concentrations of 4 mol% Pt doped LaMnO_3 calcined at different temperatures, obtained from ICP-AES analysis.

Compound	Calcination Temperature ($^{\circ}\text{C}$)	Theoretical wt% of Pt	Experimental wt% of Pt
4 mol% Pt doped LaMnO_3	600	3.15	2.85
	700	3.15	2.92
	900	3.15	3.05

3.3.1.2. Structural characterisation

Phase analysis and structural characterization were done using PXRD studies and the patterns of the samples calcined at different temperatures are shown in figure 3.2. The structure of all the materials including that of the parent perovskite belongs to the rhombohedral system. When the material has oxygen excess nature, rhombohedral system is preferred [34]. This indicates that the samples contain higher concentration of tetravalent ions at the B-site with the concomitant presence of La vacancies.

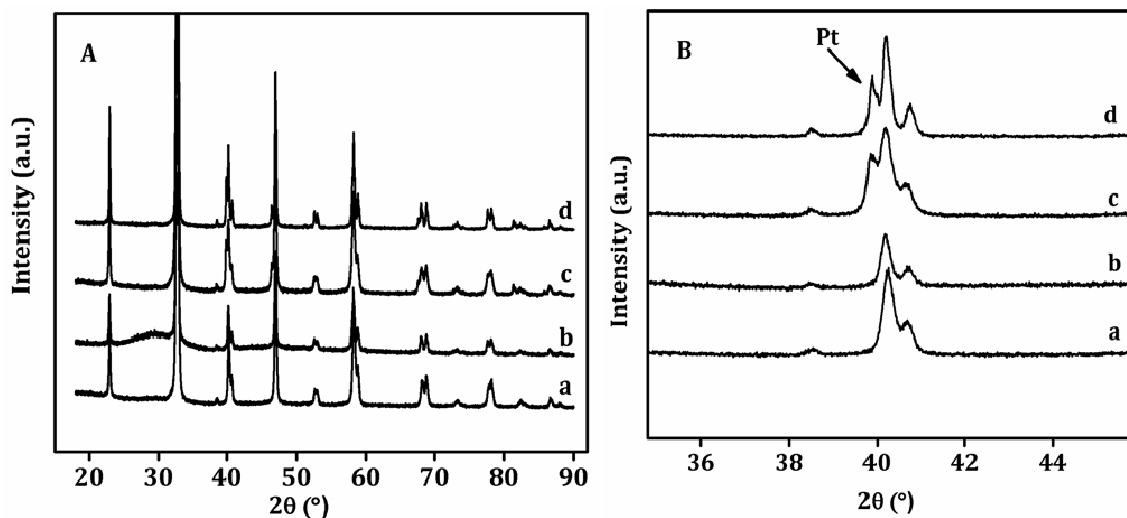


Figure 3.2. (A) PXRD patterns of (a) LaMnO_3 , and 4 mol% Pt doped LaMnO_3 calcined at (b) 600 $^{\circ}\text{C}$, (c) 700 $^{\circ}\text{C}$ and (d) 900 $^{\circ}\text{C}$; (B) 2θ region where Pt(111) reflections appear.

The parent perovskite completely crystallizes at 600 °C without any impurity. However, the Pt doped sample calcined at 600 °C is found to contain an amorphous phase, which was not eliminated by repeated calcination at the same temperature. This amorphous structure may correspond to poorly crystallized perovskite phase. Two-theta region where peak corresponding to (111) plane of fcc cell of Pt is expected, is given in figure 3.2B. The interesting thing to be noted here is the absence of peaks corresponding to metallic Pt or PtO/PtO₂ in the PXRD pattern. This observation points to either lattice incorporation of ionic Pt or presence of highly dispersed PtO_x phase interacting with the amorphous phase not detectable by PXRD. Furthermore, the PXRD patterns suggest that the presence of Pt species in the system somehow affects the formation of perovskite phase. This fact is further supported by the observation that the PXRD pattern of the sample calcined at 700 °C did not show the presence of the amorphous phase but show metallic Pt peaks. When the sample is calcined at 900 °C, the platinum completely comes out as metallic platinum.

More structural information is retrieved by carrying out Rietveld refinement of the PXRD patterns using GSAS-EXPGUI program. Since the PXRD pattern of MP600 did not show any metallic Pt peaks, the model based on the Pt substitution at the B-site is used. For the rest of the samples, separate phases of perovskite and metallic Pt are used. As the refinement of the PXRD pattern of MP600 with two separate phases did not invoke any significant difference in the structural parameters, further discussions are based on the initial model. Particle sizes are also determined from line broadening. The refinement plots are displayed in figure 3.3 and the structural parameters obtained are tabulated in table 3.2. Since the crystallographic radius of Pt(IV) and Mn(IV) are 0.765 and 0.67 Å respectively, a substitution of the latter by the former may have a direct effect on the cell parameters. But surprisingly no particular trend is observed. The Mn-O bond distances of all the samples are also determined and do not show much variation. These observations rule out the possibility of lattice incorporation of Pt in the MP600 sample and suggest that platinum exists as PtO_x phase on the surface. The estimation of platinum phase fraction indicates that it increases from ~2.7 to 3 wt% when the calcination temperature increases from 700 to 900 °C.

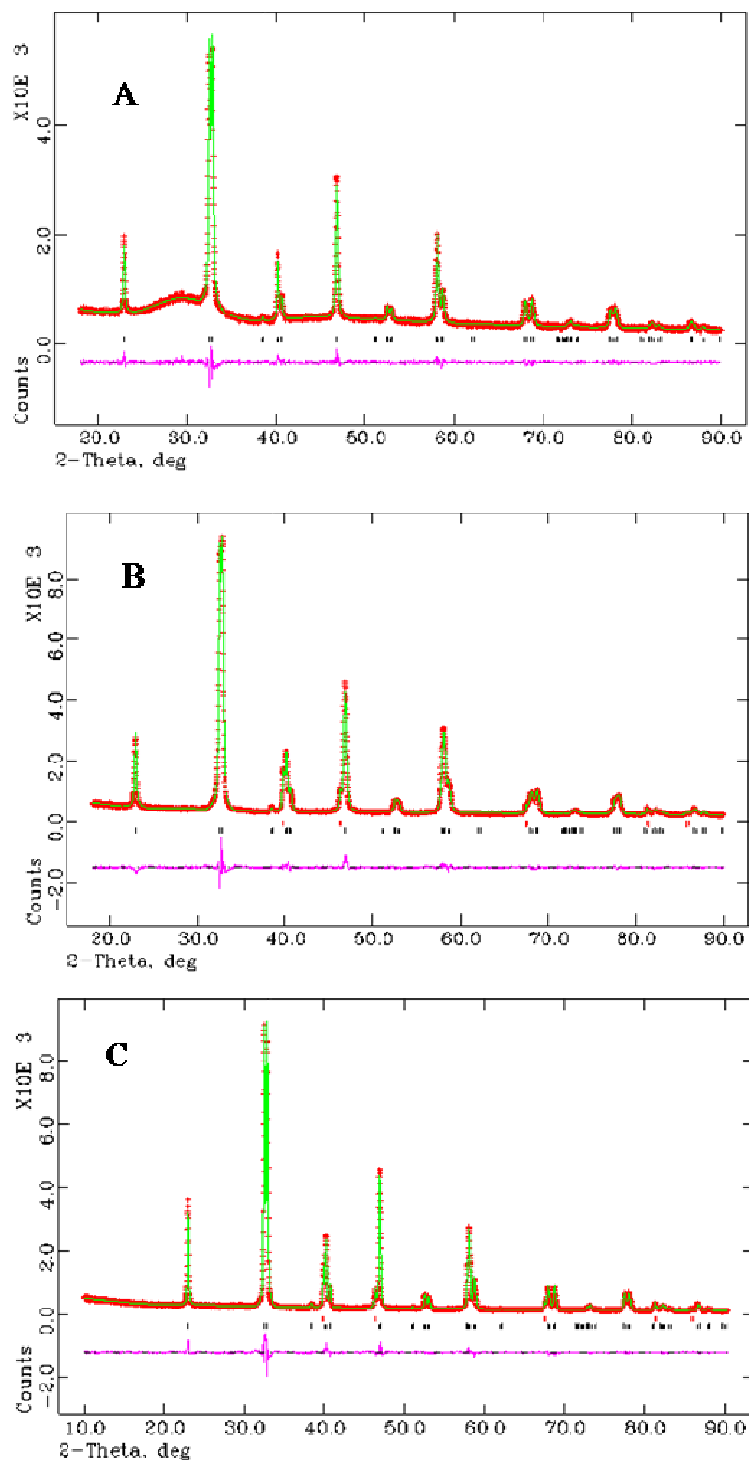


Figure 3.3. Rietveld refinement of PXRD patterns of 4 mol% Pt doped LaMnO₃ synthesised at (A) 600 °C, (B) 700 °C and (C) 900 °C.

Table 3.2. Crystal structures of Pt doped LaMnO₃ as obtained from Rietveld refinement of PXRD data.

Parameters	MP600	MP700	MP900
χ^2	1.043	1.704	1.573
wRp (%)	4.42	5.75	6.74
Rp (%)	3.48	4.51	5.23
a (Å)	5.5110(0)	5.5082(0)	5.5121(0)
b (Å)	5.5110(0)	5.5082(0)	5.5121(0)
c (Å)	13.3159(2)	13.3295(2)	13.3104(1)
01x	0.4499(7)	0.4494(6)	0.4508(5)
y	0	0	0
z	0.25	0.25	0.25
Pt particle size (nm)	Not observed	70	75
LaMnO ₃ Phase fraction (%)	100	97.287	97.003
Pt Phase fraction (%)	0	2.713	2.997
Mn-O bond distance (Å)	1.959	1.96	1.959

La at (0,0,0.25) and Mn at (0,0,0)

3.3.1.3. Textural characterisation

The information regarding the nature and particle size of the MP600 sample was obtained using HRTEM studies. The images shown in figure 3.4 indicate that the particles are irregularly shaped and amorphous porous structures are visible in some

regions. The presence of porous structures in the HRTEM images supports the appearance of amorphous phase in the PXRD of the MP600 sample. Furthermore, other than the lattices corresponding to the (110) plane of perovskite, those of the crystalline orthorhombic PtO_2 corresponding to (110) and (020) planes in a few regions can also be observed. The PtO_2 may be existing as a thin layer on the surface of the perovskite and thus not detected by PXRD.

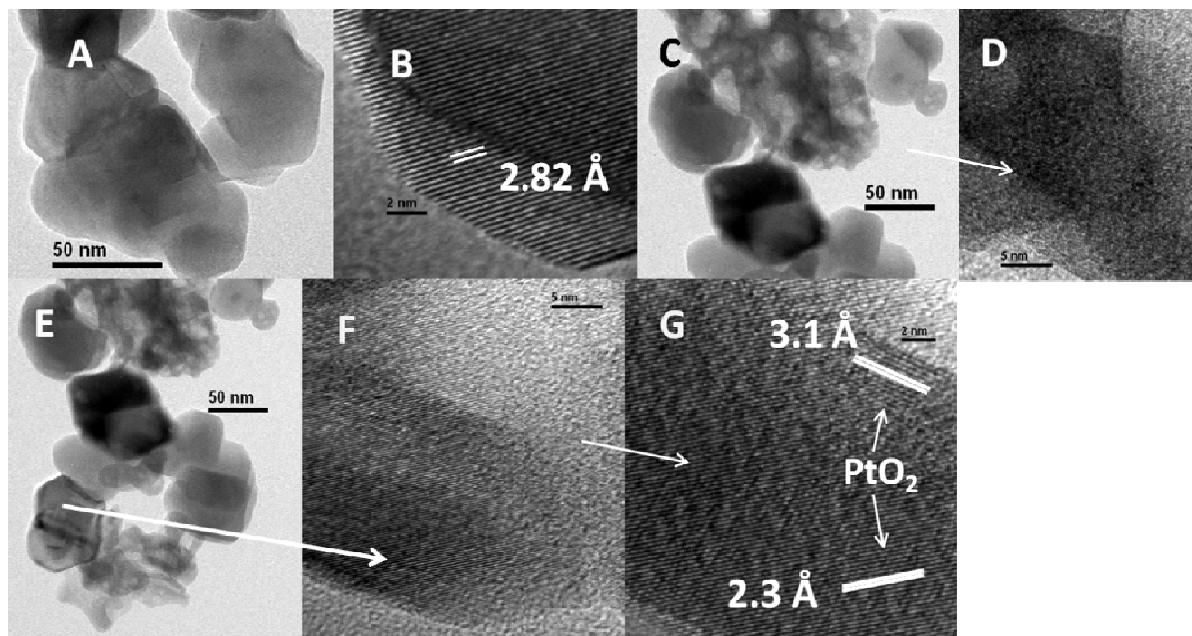


Figure 3.4. (A) HRTEM images of MP600; (B) LaMnO_3 lattice showing (110) plane, (C, D) amorphous structure, (E-G) PtO_2 .

These results suggest that the Pt doped compound calcined at 600 °C contain platinum as PtO_2 , strongly interacting with the amorphous structure, which undergo reduction when calcined at higher temperatures. This indicates the reluctance of Pt incorporation in the lattice sites of LaMnO_3 perovskites.

3.3.1.4. Surface characterisation

The surface characterisation of MP600 sample was carried out using XPS. Pt-4f and Mn-2p XP spectra for MP600 are shown in figure 3.5. The surface of the sample is clearly found to contain Pt(IV) species. No metallic Pt peak is observed which is in

agreement with the observations from PXRD and HRTEM of a possible PtO_2 surface layer. The incorporation of Pt(IV) may have direct consequence on the oxidation state of the Mn ion which ideally undergo reduction. However, the surface of the sample is found to contain a mixture of Mn(III) and (IV) states as observed by various other groups [35-38]. Reports suggest that the surface of the unsubstituted LaMnO_3 is also found to consist of sufficient amount of Mn(IV) depending on the synthesis conditions, viz., the calcination temperature and oxygen partial pressure [39]. A semi empirical estimation using the relative intensities indicate a Mn(III) to Mn(IV) ratio to be 1:0.9 for the MP600 sample. This evidences a clear resistance for Pt incorporation into the lattice, possibly due to the inherent oxygen excess nature of the matrix.

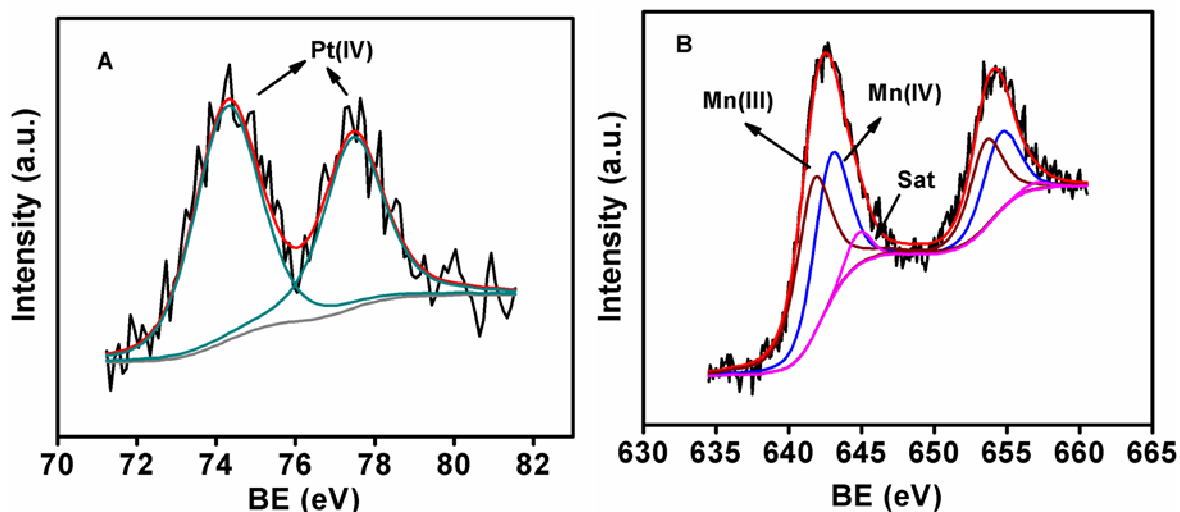


Figure 3.5. (A) Pt-4f and (B) Mn-2p XP spectra of MP600. Black: observed, red: fitted, green; Pt(IV), Brown: Mn(III), blue: Mn(IV) and pink: satellite peaks.

3.3.1.5. Catalytic activity

The catalytic activities of the samples calcined at various calcination temperatures were studied using WGS reaction. The experiments were carried out with a reformat feed having composition of 40.3 % H_2 , 35.1 % N_2 , 10.1 % CO and 14.5 % CO_2 with a GHSV of 5000 h^{-1} with steam to CO ratio 4.5 and the activity data are represented in figure 3.6.

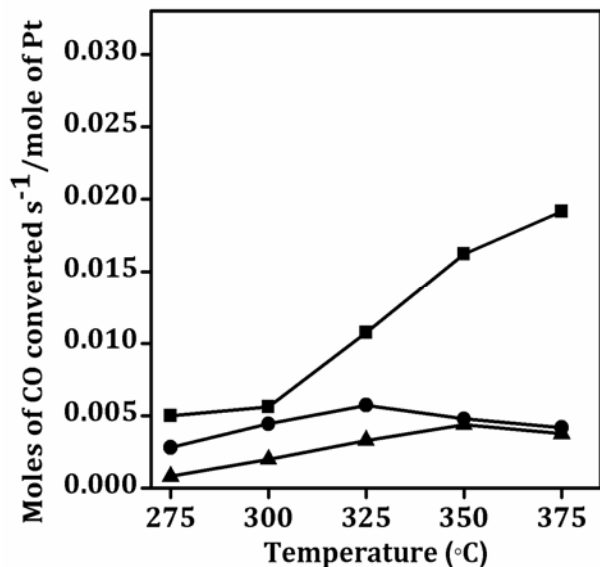


Figure 3.6. CO conversion measured over Pt doped LaMnO_3 calcined at ■: 600 °C, ●: 700 °C and ▲: 900 °C under WGS conditions. Reformate composition 40.3 % H_2 , 35.1 % N_2 , 10.1 % CO and 14.5 % CO_2 ; steam to CO ratio 4.5 and GHSV 5000 h^{-1} . Total amount of Pt is considered for calculating the conversions.

From the activity data, it becomes clear that MP600 catalyst exhibits appreciable WGS activity after 300 °C whereas samples MP700 and MP900 display very poor activity. This is surprising since MP600 catalyst possesses excess oxygen rather than oxygen vacancies, the latter being proposed to play a significant role in the mechanism of WGS reaction. The activity of MP600 can be attributed to the metallic Pt nanoparticles formed by the reduction of PtO_x phase upon exposing to the highly reducing atmosphere of WGS reaction. These particles undergo sintering at high temperature calcination and thus are not active.

3.3.1.6. Surface and structural characterization of spent catalysts

The changes occurring on the surface of the MP600 catalyst after exposing to the WGS reaction conditions were studied with the help of XPS. The Pt-4f and Mn-2p XP spectra of MP600 after WGS reaction are shown in figure 3.7.

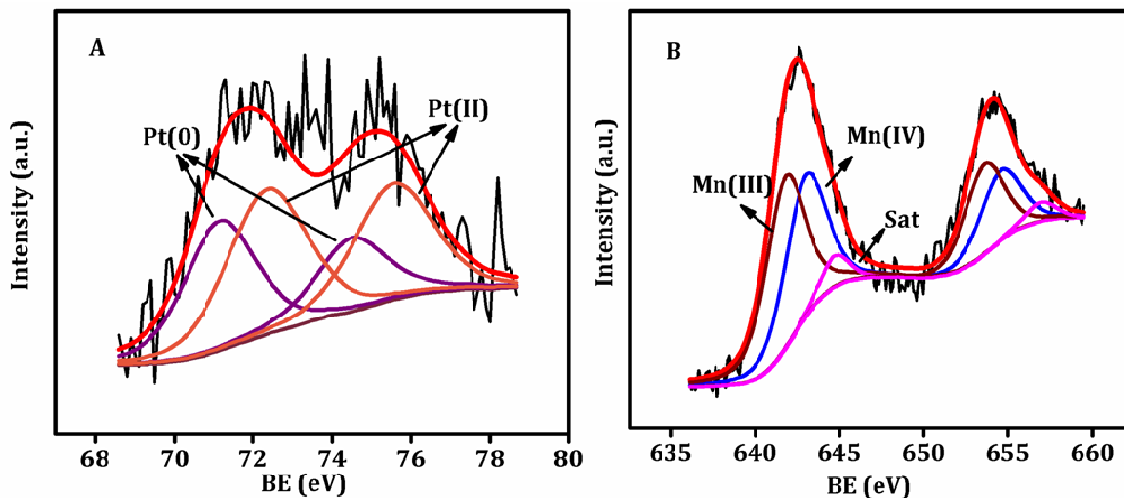


Figure 3.7. (A) Pt-4f and (B) Mn-2p XP spectra of MP600 after WGS reaction; Black: observed, red: fitted, violet: Pt(0), orange: Pt(II), brown: Mn(III), blue: Mn(IV) and pink: satellite peaks.

The presence of peaks at ~ 71.2 eV and ~ 72.4 eV binding energies indicated the presence of both Pt(0) and Pt(II) states on the surface of the catalyst after the reaction. This indicates that Pt species on this material is reduced to a reasonable extent. But the fact that platinum undergoes incomplete reduction even under the harsh reducing conditions of the WGS reaction suggests that the amorphous phase stabilises the PtOx species sufficient enough to withstand the conditions exposed. The Mn-2p XP spectra revealed that both Mn(III) and Mn(IV) states are present on the surface of the spent catalyst. But the Mn(III) to Mn(IV) ratio is found to increase to 1:0.8, showing a 15 % increase in the amount of Mn(III) compared to that observed in the case of fresh catalyst and the cause of reduction is obviously the reducing atmosphere of WGS reaction.

These studies clearly indicate that reducing reaction conditions affected the catalysts. To understand more about the structural changes occurring under the reaction conditions, PXRD analysis was carried out. PXRD patterns of MP600 before and after WGS reaction are shown in figure 3.8. The PXRD pattern of the spent catalyst is different from that of the fresh catalyst. The pattern of the spent catalysts is found to match with the reported pattern for the less oxygen excess orthorhombic LaMnO_3

(space group $Pnma$) [40]. The reducing reaction conditions result in the increase of Mn(III) which is clear from the XPS analysis, resulting in less number of La vacancies and thus undergoes a structural change to the orthorhombic system. In addition, it can be seen that the fraction of amorphous phase decreases after reaction. This observation together with the partial reduction of the PtOx phase give further evidence of the interaction of the amorphous phase and PtOx phase which stabilises the latter at lower calcination temperatures.

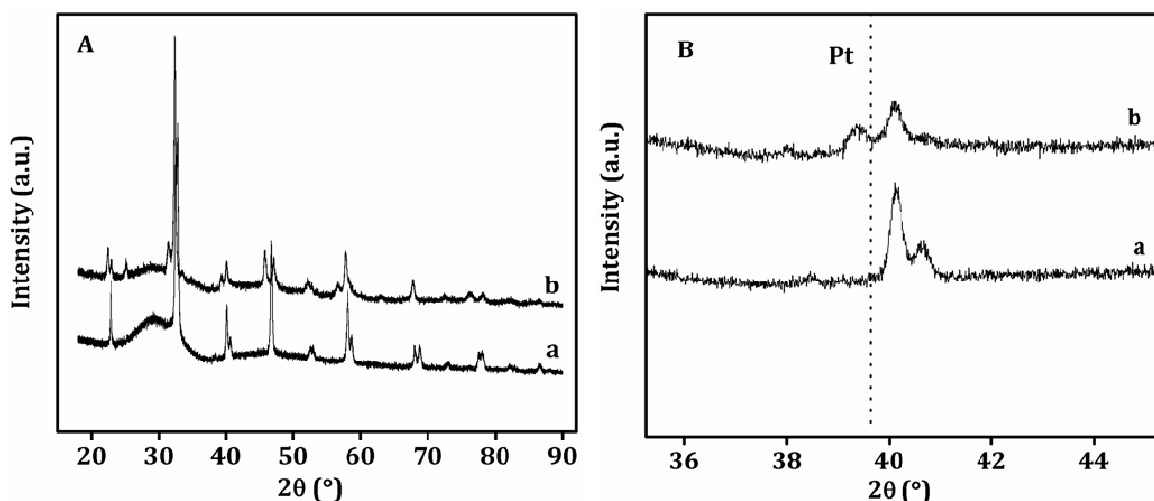


Figure 3.8. (A) PXRD patterns of MP600 (a) before and (b) after WGS reaction, and (B) 2θ region where Pt(111) reflection appear.

It can be seen that the metallic Pt reflections are overlapped by the perovskite reflections in the spent catalysts. So the presence of small amount of metallic Pt which may be dispersed on the surface was not visible in the PXRD of the spent catalysts.

HRTEM analysis of the MP600 sample after WGS reaction was also carried out and the representative images are shown in figure 3.9. The porous structures are less in this sample compared to the fresh one. In addition to the perovskite lattices, those of tetragonal PtO (figure 3.9C), metallic Pt (figure 3.9E) and orthorhombic PtO₂ (figure 3.9F) are also observed.

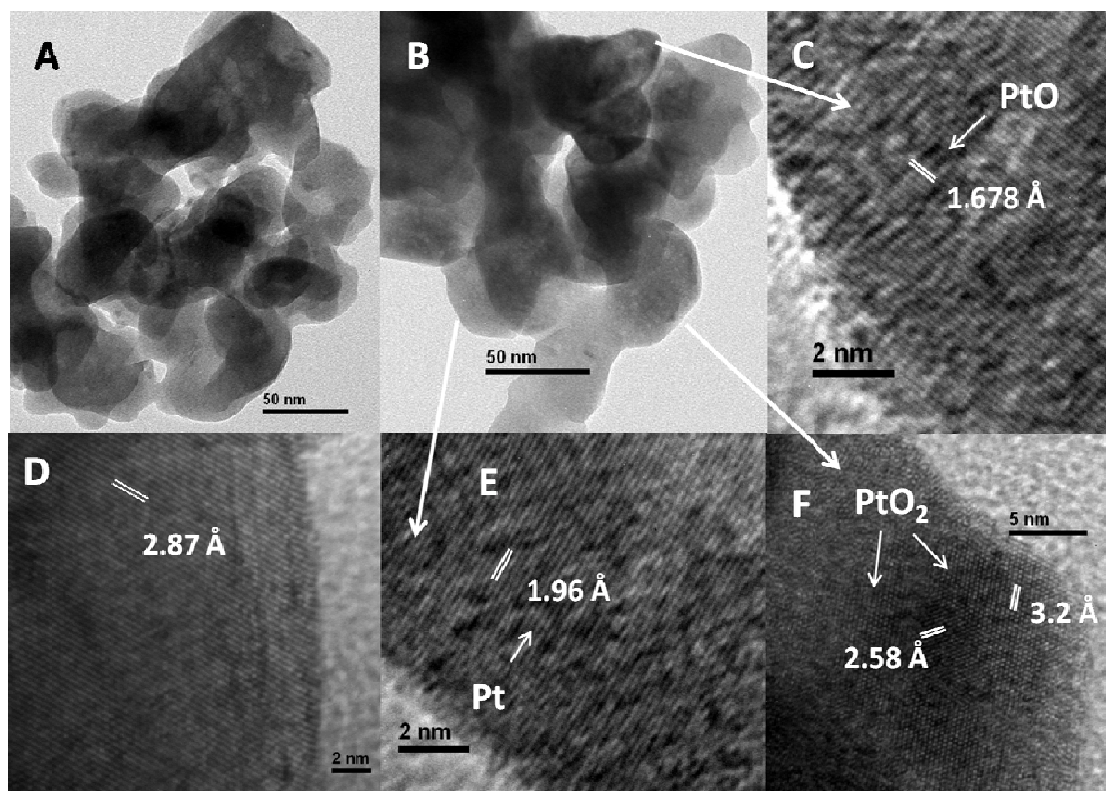


Figure 3.9. (A, B) HRTEM images of MP600 after WGS reaction showing lattices of (C) PtO, (D) LaMnO₃ showing (020) planes, (E) metallic Pt and (F) PtO₂.

It can be seen in the figure 3.9F that a part of the amorphous region shows structural ordering and few lattice planes corresponding to PtO₂. This observation strongly supports the structural change of the PtO_x species interacting with the amorphous phase to the metallic Pt and oxide compounds during reaction. It also supports the observation that more metallic Pt is present when the amount of amorphous phase decreases.

3.3.2. Pt doping in LaFeO₃ and LaCoO₃ systems

3.3.2.1. Structural characterisation

As mentioned in section 3.3, the synthesised compounds have the stoichiometry LaFe_{1-x}Pt_xO_{3-δ} ($x = 0.02, 0.04$ and 0.06) and LaCo_{1-x}Pt_xO_{3-δ} ($x = 0.02$ and 0.04) corresponding to the weight percentages 1.6, 3.1 and 4.7 respectively. Henceforth, these phases will be referred to as BPt_x (B = Fe & Co; $x =$ moles of Pt) for convenience. The

concentrations of platinum present in the materials were determined using ICP-AES and the results are given in table 3.3.

Table 3.3. Pt concentrations determined using ICP-AES technique.

Compound	x	Theoretical wt% of Pt	Experimental wt% of Pt
LaFe _{1-x} Pt _x O _{3-δ}	0.02	1.59	1.41
	0.04	3.14	3.04
	0.06	4.66	3.98
LaCo _{1-x} Pt _x O _{3-δ}	0.02	1.57	1.44
	0.04	3.11	2.99

Since the PXRD patterns for the FePt_x samples were not useful to establish the incorporation of ionic Pt in their lattice sites, diffraction experiments using synchrotron X-rays were carried out for all the samples which enabled to obtain high resolution data. In the case of CoPt_x, the peak positions of metallic Pt and perovskite are well separated and the absence of peaks corresponding to metallic Pt indicates the incorporation of cationic Pt in its lattices. However, in the case of FePt_x, even these experiments could not separate the peak positions of metallic Pt and LaFeO₃. XANES experiments using synchrotron X-rays were carried out for the highest Pt containing sample FePt0.06 to unambiguously conclude the Pt incorporation in the lattice. The experiments were carried out for MnPt0.04 also, where Pt is present in metallic state as shown by PXRD. XANES region corresponds to the transitions of core electrons to non-bound levels, the probability of which is so high to result in a sudden raise of absorption leading to an absorption edge. XANES spectrum is characteristic of local atomic environment and valence states of the element. Since the absorption peak area is directly proportional to the d-hole density of the element, the intensity of the white line directly indicates the formal valence of the element [41, 42]. Normalised Pt-L3 XANES spectra of FePt0.06 and MnPt0.04 are shown in figure 3.10.

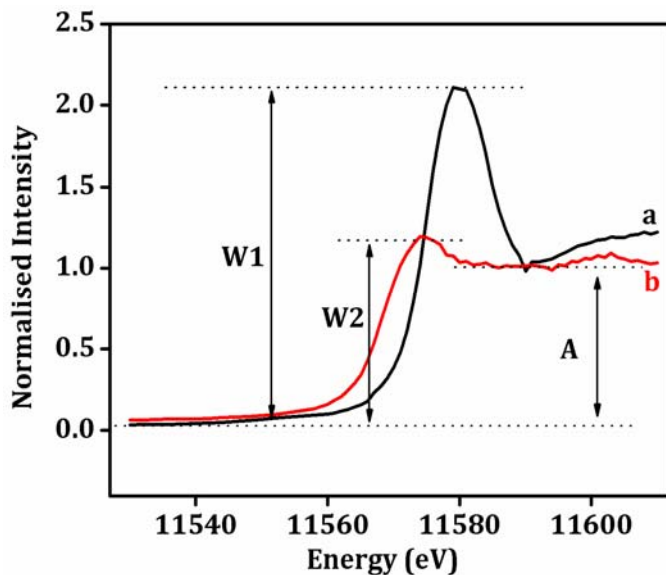


Figure 3.10. Pt L3 XANES spectra of (a) $\text{LaFe}_{0.94}\text{Pt}_{0.06}\text{O}_{3-\delta}$ and (b) $\text{LaMn}_{0.96}\text{Pt}_{0.04}\text{O}_3$. The spectra are normalised by the incident intensity to a step edge of unity.

The height of the white line (marked 'W' in the figure) with respect to the shoulder (marked 'A' in the figure) in XANES spectra is reported to be in direct relationship with the valence state of Pt by a linear empirical relation, obtained by studies conducted using complexes having Pt(II) and Pt(IV) valence states [43]. The ratios obtained for the $\text{FePt}_{0.06}$ and $\text{MnPt}_{0.04}$ are 2.14 and 1.18, respectively. The reported values for Pt(IV) and Pt(II) oxidation states are 2.5 and 1.5 respectively [43]. A value of 1.18 for $\text{MnPt}_{0.04}$ indicates that the valence state of Pt in this compound is lower than +2 and hence metallic in agreement with the PXRD results. The ratio between 1.5 and 2.5 for $\text{FePt}_{0.06}$ indicates that Pt exists in both oxidation states, +2 and +4 with more amount of latter in this compound and is incorporated in the lattice. In addition, the position of the edge gives information regarding the average valence state of the element present. The absorption edge of higher oxidation state ions is reported to be blue shifted compared to those of the lower valent ions. According to the literature, a shift in the edge energy of the order of 2.2 eV corresponds to change in the valence state from +2 to +4 [43]. In the present work, we observed a shift of 4.2 eV which indicates the change in the valence state more than +2. These results compel us to conclude that

Pt could be successfully incorporated in the lattice sites of LaBO_3 perovskites where, B = Fe and Co.

The refinement of PXRD patterns obtained with the help of synchrotron X-rays for all the materials were then carried out using GSAS-EXPGUI program to obtain more structural information. The basic model consists of Pt substituted in B site of LaBO_3 (B = Fe and Co). The resulted plots are displayed in figure 3.11 and structural parameters are listed in the table 3.4.

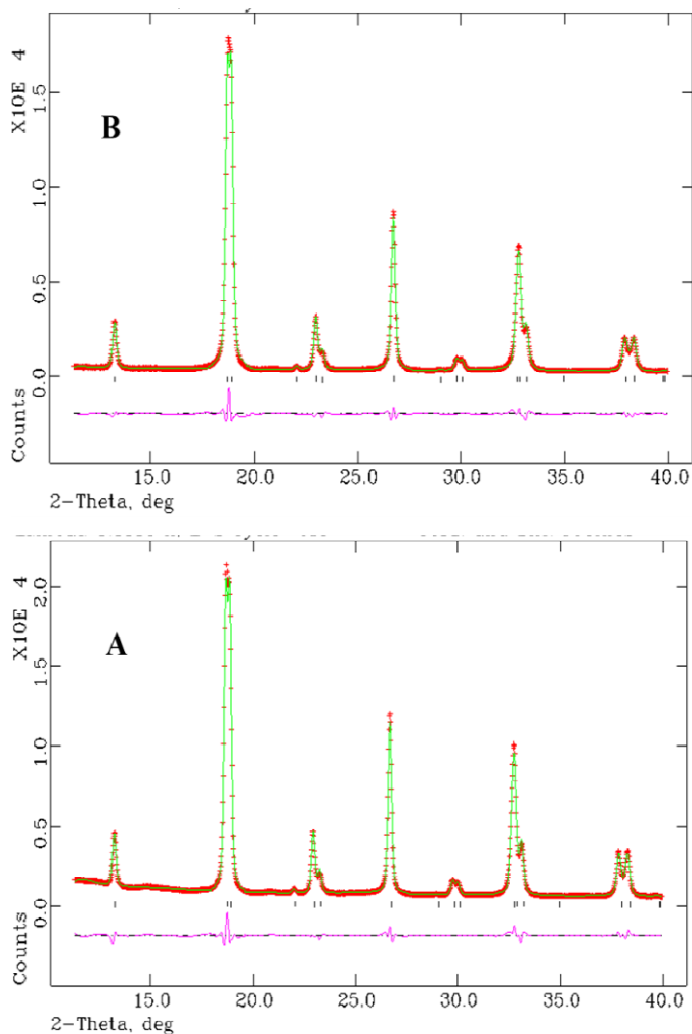


Figure 3.11a. Rietveld refinement of the synchrotron XRD pattern of $\text{LaCo}_{1-x}\text{Pt}_x\text{O}_{3-\delta}$ with (A) $x = 0.02$, and (B) $x = 0.04$.

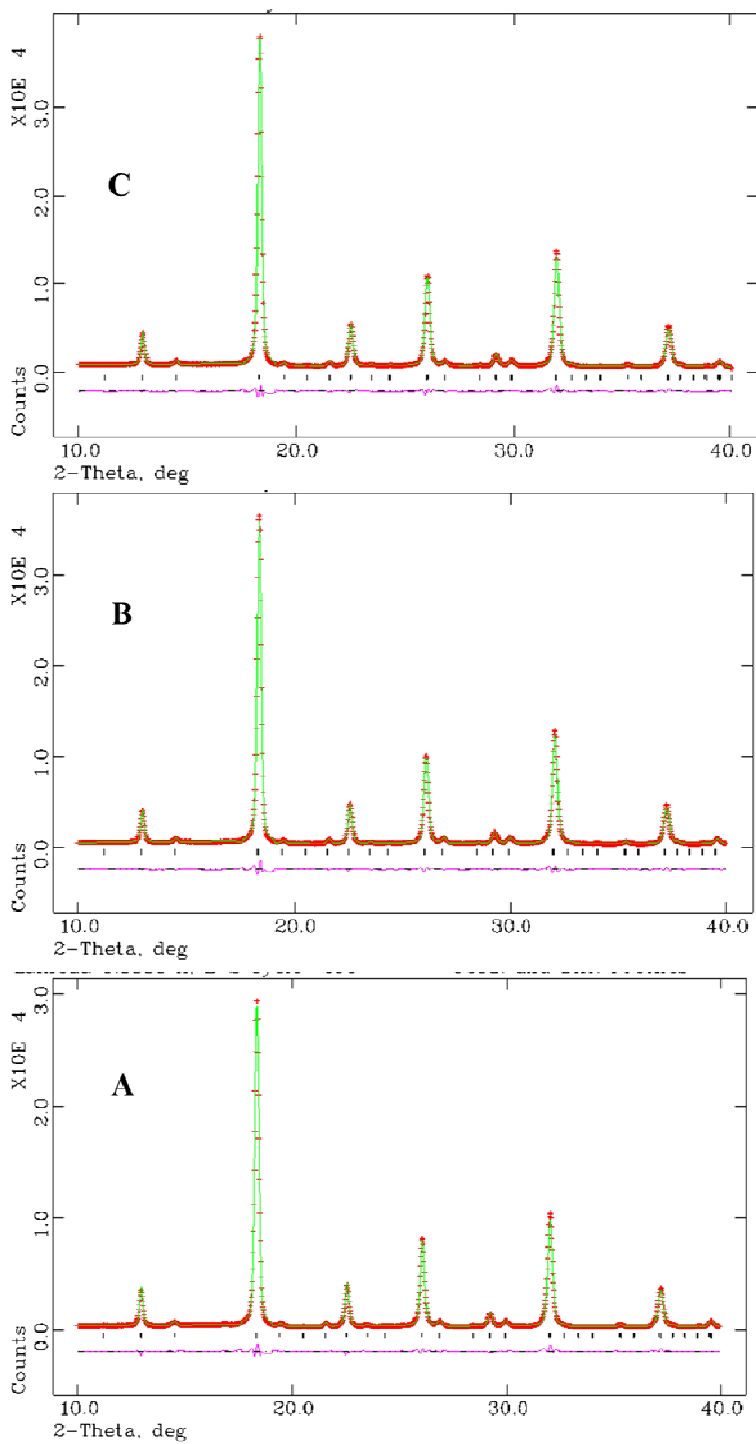


Figure 3.11b. Rietveld refinement of the synchrotron XRD pattern of LaFe_{1-x}Pt_xO_{3-δ} with (A) x = 0.02, (B) x = 0.04 and (C) x = 0.06.

Table 3.4a. Crystal structures of $\text{LaCo}_{1-x}\text{Pt}_x\text{O}_{3-\delta}$ as obtained from Rietveld refinement of synchrotron XRD data.

Parameters	$\text{LaCo}_{1-x}\text{Pt}_x\text{O}_{3-\delta}$	
	$x = 0.02$	$x = 0.04$
χ^2	2.79	2.582
wRp (%)	4.18	5.22
Rp (%)	3.13	3.88
a(Å)	5.4383(1)	5.4439(1)
b(Å)	5.4383(1)	5.4439(1)
c(Å)	13.1200(3)	13.1366(4)
01x	0.4522(13)	0.4513(12)
y	0	0
z	0.25	0.25
Uiso-La	0.0144(5)	0.0273(5)
Uiso-Co	0.0083(7)	0.0224(8)
Uiso-O	0.0279(20)	0.0363(18)

La at (0,0,0.25) and Co/Pt at (0,0,0)

Table 3.4b. Crystal structures of $\text{LaFe}_{1-x}\text{Pt}_x\text{O}_{3-\delta}$ as obtained from Rietveld refinement of synchrotron XRD data.

Parameters	$\text{LaFe}_{1-x}\text{Pt}_x\text{O}_{3-\delta}$		
	$x = 0.02$	$x = 0.04$	$x = 0.06$
χ^2	3.461	3.101	3.623
wRp (%)	5.85	4.91	4.89
Rp (%)	4.15	3.34	3.44
a(Å)	5.5610(7)	5.5608(7)	5.5643(7)
b(Å)	7.8470(15)	7.8494(15)	7.8506(13)
c(Å)	5.5512(12)	5.5526(11)	5.5545(10)

Lax	0.0227(3)	0.0226(2)	0.0223(3)
y	0.25	0.25	0.25
z	0.0011(23)	-0.0007(22)	0.0039(14)
O1x	0.4880(22)	0.4901(21)	0.4918(23)
y	0.25	0.25	0.25
z	0.0608(100)	0.0702(80)	0.0460(102)
O2x	0.2751(31)	0.2780(28)	0.2743(33)
y	0.0512(32)	0.0472(34)	0.0512(27)
z	-0.2709(33)	-0.2713(33)	-0.2683(37)
Ptocc	0.0177	0.0386	0.0512
LaUiso	0.0249(6)	0.0230(5)	0.0233(6)
FeUiso	0.0180(8)	0.0146(7)	0.0209(8)

Fe/Pt at (0,0,0.5)

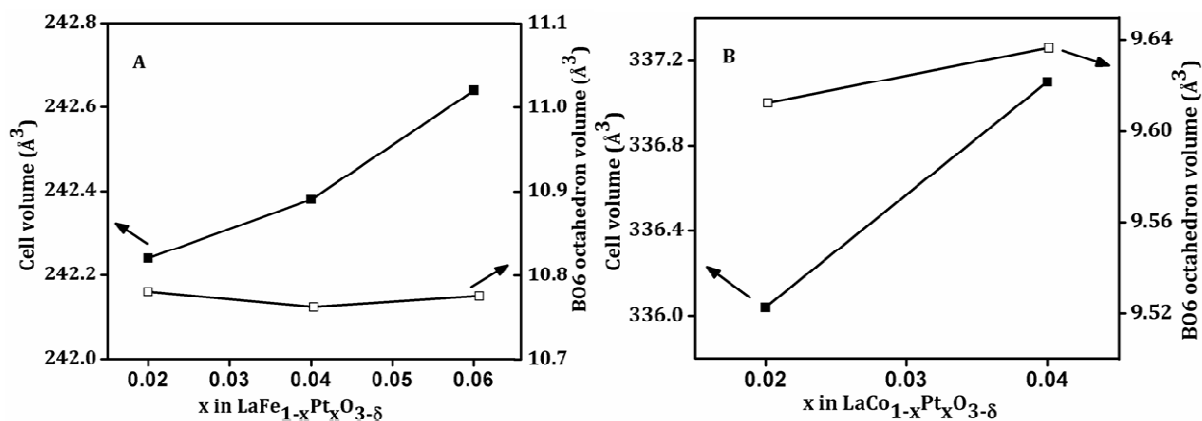


Figure 3.12. Cell volume and octahedron volume plots of $\text{LaB}_{1-x}\text{Pt}_x\text{O}_{3-\delta}$. (A) B = Fe and (B) B = Co as a function of substitution x as obtained from Rietveld refinement of synchrotron XRD data.

HRTEM studies were carried out on selected samples (figure 3.13) and in the cases of FePt0.04 and CoPt0.04, only perovskite lattices could be identified. Textural properties also are found to be similar for all the catalysts (table 3.5).

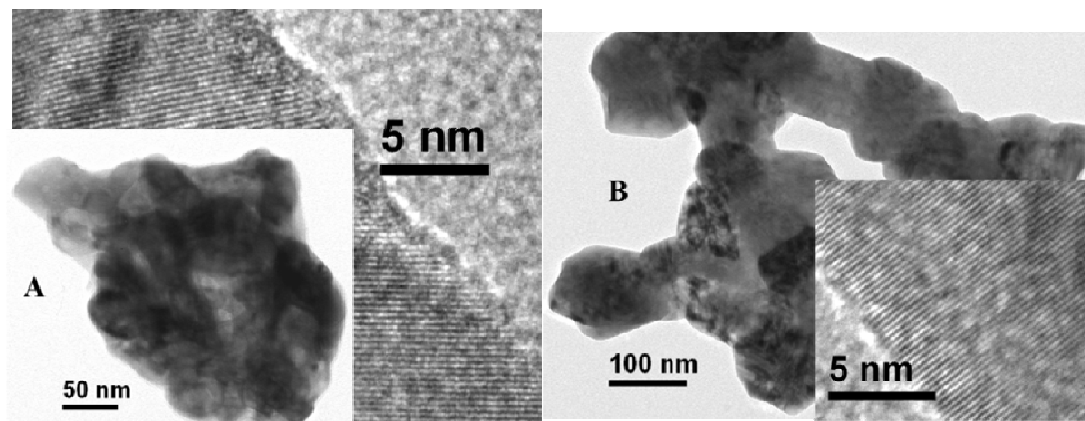


Figure 3.13. HRTEM images of $\text{LaB}_{0.96}\text{Pt}_{0.04}\text{O}_{3-\delta}$, (A) B= Fe and (B) B = Co.

Table 3.5. Surface area analysis of $\text{LaB}_{0.96}\text{Pt}_{0.04}\text{O}_{3-\delta}$, (B = Fe and Co).

Compound	Surface area (m^2/g)
$\text{LaFe}_{0.96}\text{Pt}_{0.04}\text{O}_{3-\delta}$	13.284
$\text{LaCo}_{0.96}\text{Pt}_{0.04}\text{O}_{3-\delta}$	7.919

3.3.2.2. Surface characterisation

The examination of the surface of both $\text{FePt}_{0.04}$ and $\text{CoPt}_{0.04}$ was done to understand the oxidation states of B ion and Pt ion. Pt-4f XP spectra and the corresponding Fe-2p and Co-2p XP spectra of $\text{FePt}_{0.04}$ and $\text{CoPt}_{0.04}$ are shown in figure 3.14. In all the cases, multiple oxidation states for the ions are detected. Both Pt(II) and Pt(IV) states are found on the surface of Co and Fe perovskites. But no peaks corresponding to metallic species are observed in both the cases. Figure 3.14B representing XP spectrum in the Co-2p region for $\text{CoPt}_{0.04}$ shows an asymmetric peak at BE ~ 781 eV which can be deconvoluted into two components attributable to Co(III) and Co(II) [44, 45]. The presence of shake-up satellite peak at ~ 787 eV is characteristic of Co(II) in a high spin state. For the $\text{FePt}_{0.04}$ sample (figure 3.14D), the asymmetric peak in the Fe-2p region observed at BE ~ 711 eV could be resolved into Fe(II) and Fe(III) components [46-48]. The broad satellite peak at ~ 715 eV is characteristic of Fe(II) species.

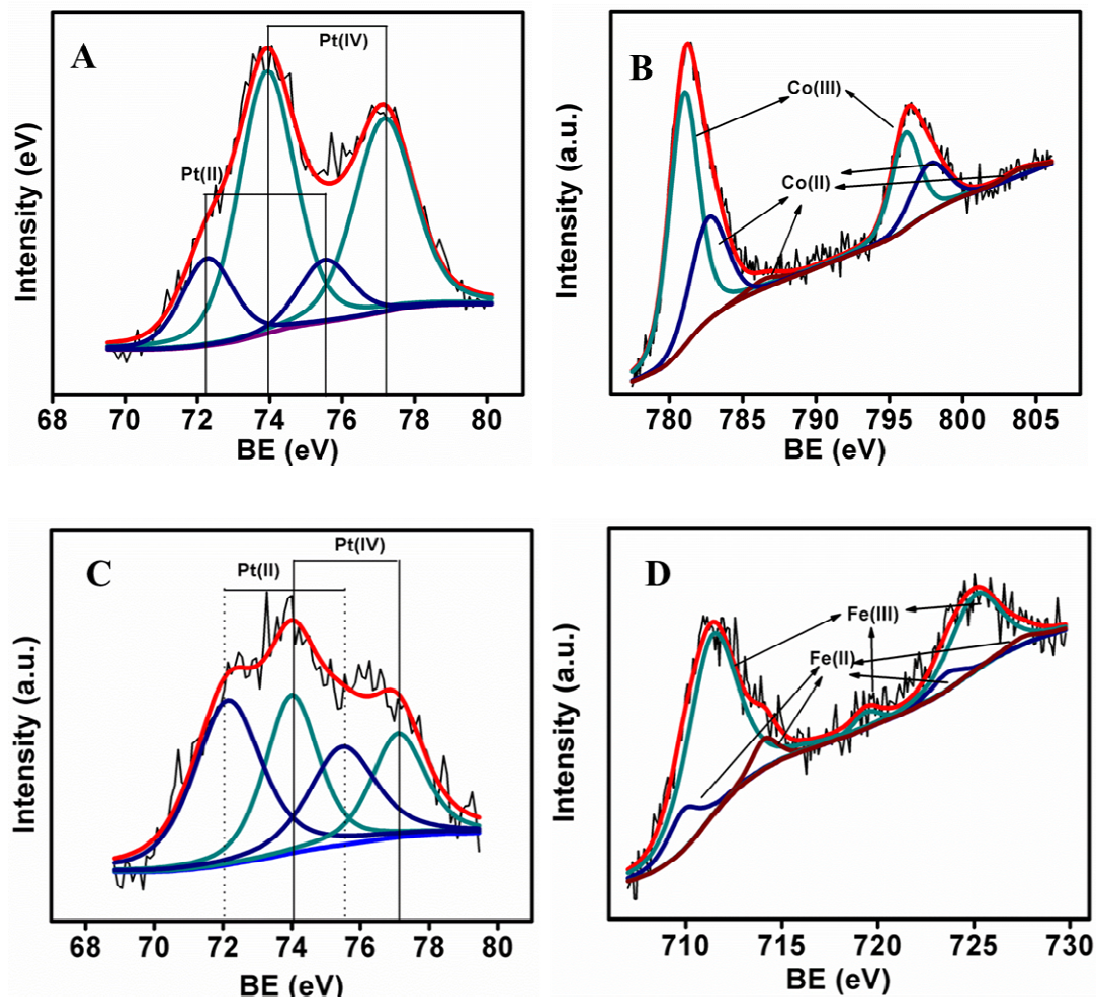


Figure 3.14. (A) Pt-4f and (B) Co-2p XP spectra of $\text{LaCo}_{0.96}\text{Pt}_{0.04}\text{O}_{3-\delta}$ and (C) Pt-4f and (D) Fe-2p XP spectra of $\text{LaFe}_{0.96}\text{Pt}_{0.04}\text{O}_{3-\delta}$.

A semi-quantitative estimation of the different oxidation states present was attempted by comparing their intensities. In the case of $\text{CoPt}_{0.04}$, the ratio of Pt(IV) to Pt(II) states is determined as 1:0.3. Since majority of the Pt exists in +4 state, a corresponding reduction of Co(III) to Co(II) [Co(III): Co(II) = 1: 0.39] compensates for the excess charge, leading to oxygen deficiency ($\delta = 0.25$). Similarly, the ratio of Pt(IV) to Pt(II) in the case of FePt_x is found to be 1:1 with a corresponding Fe(III):Fe(II) ratio of 1:0.22 ($\delta = 0.17$). The higher reduction potential of Co redox system compared to that of the Fe counterpart (ie. Fe(III)-Fe(II) - +0.77V; Co(III)-Co(II) - +1.82V) might have caused the presence of higher percentage of Pt(IV) in the former system. Hence the

reduction of Co(III) occurred more easily than the Fe(III) with the possibility of Pt existing in higher oxidation state in the Co system. The parent perovskite LaFeO_3 is reported to contain Fe(III) ions only on the surface [49, 50], while the LaCoO_3 is found to consist of both +3 and +2 states [51]. In the present work, both the +2 and +3 states are observed on the surface of both the Fe and Co systems resulting in the redox systems ideal for catalysis.

3.3.2.3. Catalytic activity and structural correlation

WGS activities of series of metals and oxides have been reported extensively in the literature. It is observed that with some metals such as Ni, Co, Ru etc. in the catalyst formulation, under real reformat conditions in presence of excess of hydrogen, CO or CO_2 hydrogenation is possible leading to the formation of alkanes [52-56]. But the extent of formation of higher alkanes is found to be suppressed in presence of water leading only to the formation of methane [57]. Some researchers suggest that the CO adsorption strengths of the metals decide in which way the reaction should proceed. If the adsorption is strong, methanation is preferred [58, 59]. The present systems consist of Pt and Fe, both known to favour WGS reaction [60] and Co, which is reported to be active for methane formation [61]. Hence these are ideal systems to study the combined effect of Pt and the corresponding B ions towards the WGS activity. Catalytic activity testing was done for FePt0.04 sample and the activity data in comparison with the 3 wt% Pt impregnated LaFeO_3 and mixed oxides system $\text{La}_2\text{O}_3\text{-Fe}_2\text{O}_3$ is displayed in figure 3.15. This comparison was necessary to assess the difference in activity of incorporated ionic Pt and Pt nanoparticles supported on perovskite oxides and simple binary oxides.

The FePt0.04 catalyst having ionic Pt is observed to be active only after 300 °C where as the impregnated catalysts with metallic platinum species are active for the entire temperature range used in this study. But the activities are found to be similar at higher temperatures. From this study we can conclude that ionic Pt species together with the oxygen vacancies is active for WGS reaction.

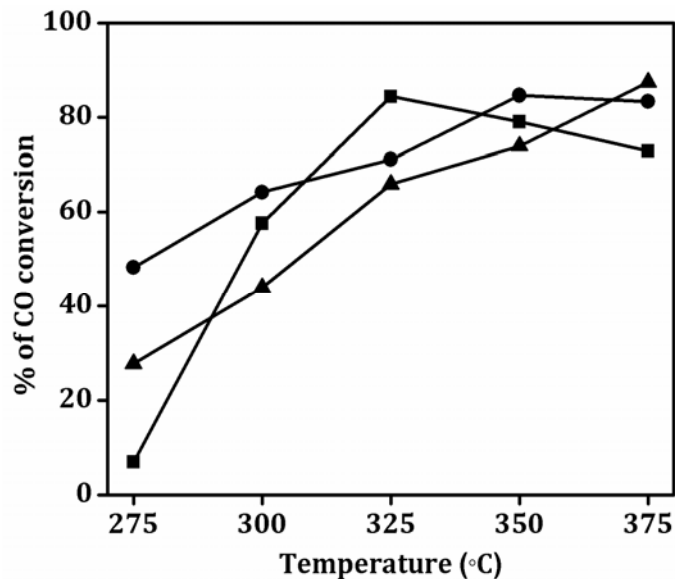


Figure 3.15. CO conversion measured over ■:LaFe_{0.96}Pt_{0.04}O_{3-δ}, ●: 3 wt% Pt impregnated LaFeO₃, and ▲: 3 wt% Pt impregnated La₂O₃-Fe₂O₃ catalysts under WGS conditions. Reformate composition of 37.9 % H₂, 13.5 % CO, 19.6 % CO₂ and balance N₂ with a steam to CO ratio of 4.5 and GHSV 5000 h⁻¹.

WGS activity data for CoPt_{0.04} and 3 wt% Pt impregnated LaCoO₃ and La₂O₃-Co₃O₄ binary oxide systems are shown in figure 3.16. All the Co catalysts exhibited very high activity after 300 °C and the CO conversion for the CoPtx perovskites is comparable to that of the impregnated samples. On further analysis, it is understood that all the Co catalysts exhibited small extent of CO hydrogenation also, along with H₂ generation even in presence of water, unlike in the case of Fe catalysts where only WGS reaction is observed. Figure 3.16B represents the methane formation found with the Pt doped and impregnated Co catalysts. In the case of CoPt_{0.04}, a drastic reduction in CO concentration is observed at 300 °C and a reduction in H₂ concentration is observed along with formation of 2 % CH₄. At higher temperatures, CH₄ concentration is reduced to traces and H₂ concentration increased indicating a suppression of methane formation.

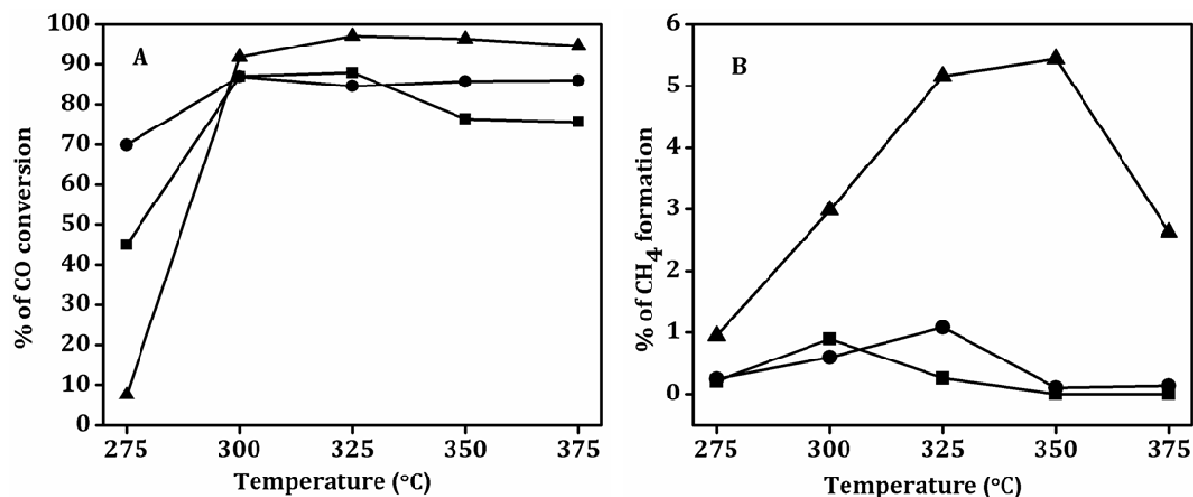


Figure 3.16. (A) CO conversion measured over ■: LaCo_{0.96}Pt_{0.04}O_{3-δ}, ●: 3 wt% Pt impregnated LaCoO₃, and ▲: 3 wt% Pt impregnated La₂O₃-Co₃O₄ catalysts under WGS conditions. Reformate composition of 37.9 % H₂, 13.5 % CO, 19.6 % CO₂ and balance N₂ with a steam to CO ratio of 4.5 and GHSV 5000 h⁻¹. (B) Methane formation observed with the Co catalysts under the same conditions described above.

This behaviour of Co-based catalysts towards hydrogenation reaction in presence of excess of hydrogen is in agreement with previous reports [61]. However, the interesting point to be noted here is that even in the presence of Pt ion, which is active for WGS, Co exhibits its characteristic behavior. The CO conversions (WGS or alkane formation) were obtained using the parent perovskites without any Pt content to understand more about the combined effect of Co and Pt. Figure 3.17 displays the CO conversion of the parent perovskites LaBO₃ (B= Fe and Co). Both the catalysts are found to show very poor activity under WGS conditions.

These observations put an emphasis on the facts that Fe and Co ion systems show their characteristic activity only in the presence of platinum and Pt is necessary to enhance the activity of Fe and Co systems. In addition, WGS reaction with these catalysts proceeds through a mechanism involving both Pt and B ions in the perovskite.

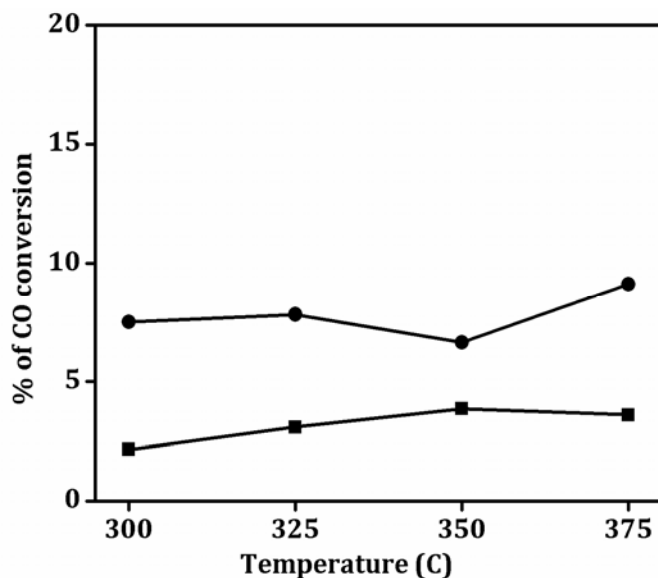


Figure 3.17. CO conversion measured over ■: LaFeO₃ and ●:LaCoO₃ catalysts under WGS conditions. Reformate composition of 37.9 % H₂, 13.5 % CO, 19.6 % CO₂ and balance N₂ with a steam to CO ratio of 4.5 and GHSV 5000 h⁻¹.

Furthermore, a comparison of the CH₄ formation with the Pt doped and impregnated Co catalysts revealed that even though the CO conversion activity is similar for all the catalysts, the extent of methane formation is found to be very high for the catalyst with Pt impregnated on the binary oxides (La₂O₃ + spinel-Co₃O₄). When perovskites are used either as supports for the Pt nanoparticles or to stabilize the cationic Pt, the CH₄ formation is found to be greatly suppressed. This observation points to the fact that the activity is influenced by the chemical nature of the B ion also, as the structural environment of Co in both Co₃O₄ spinel and LaCoO₃ perovskite are different.

3.3.2.4. Characterisation of spent catalysts

The structure of the catalysts after subjecting to the WGS reaction condition was examined using PXRD and the diffraction patterns of both the FePt0.04 and CoPt0.04 before and after WGS reaction are shown in figure 3.18. The patterns of the spent catalysts showed no peaks corresponding to metallic Pt. Also the perovskite structure is found to be stable enough to withstand the reaction conditions.

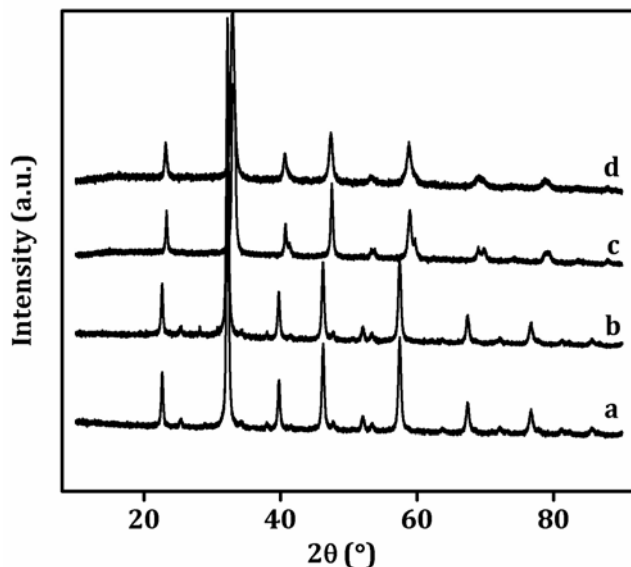


Figure 3.18. XRD patterns of $\text{LaFe}_{0.96}\text{Pt}_{0.04}\text{O}_{3-\delta}$ (a) before and (b) after WGS reaction and $\text{LaCo}_{0.96}\text{Pt}_{0.04}\text{O}_{3-\delta}$ (c) before and (d) after WGS reaction.

However, a small percentage of metallic Pt formed during the reaction which may be highly dispersed and hence not detected by XRD, can be expected as reported in previous studies of similar systems. Hence, XPS was used to investigate this and also to understand the changes occurring to the oxidation states during WGS reaction. Pt-4f and the corresponding Fe-2p and Co-2p XP spectra of FePt0.04 and CoPt0.04 are shown in figure 3.19.

Pt-4f spectra revealed that small amount of metallic Pt is present in the cases of both Fe and Co systems after subjecting to the reaction conditions. Intensity based calculations suggest that in CoPt0.04 spent catalyst, ~ 0.01 mol of Pt(0) is present along with 0.02 and 0.01 mol of Pt(II) and Pt(IV) respectively. When compared with the fresh catalyst, the amount of Pt(IV) decreased by three fold while Pt(II) concentration increased by two fold. But a corresponding oxidation of Co(II) is not observed and the oxygen deficiency (δ) is enhanced to 0.364. For the spent FePt0.04, 0.008 mol of Pt(0) is found on the surface with a corresponding decrease in both Pt(II) and Pt(IV) unlike CoPt0.04, where Pt(IV) decreased more drastically. In addition, 0.13 mol of Fe(III) is reduced to Fe(II) increasing the oxygen deficiency on the surface to 0.2.

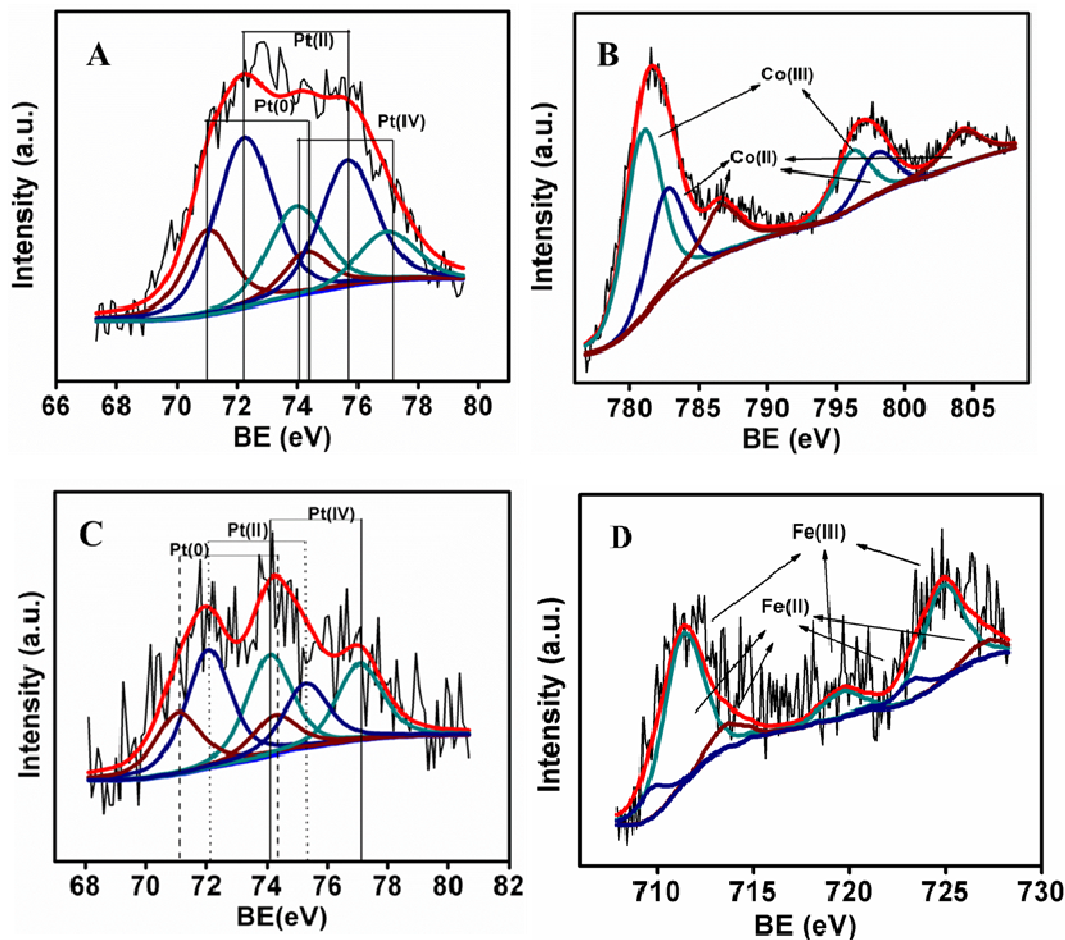


Figure 3.19. (A) Pt-4f and (B) Co-2p XP spectra of LaCo_{0.96}Pt_{0.04}O_{3-δ} and (C) Pt-4f and (D) Fe-2p XP spectra of LaFe_{0.96}Pt_{0.04}O_{3-δ} after WGS reaction.

But the fact that under the highly reducing WGS reaction conditions, a full reduction to metallic Pt does not occur in both the systems, indicates a structural stabilisation of ionic Pt in the lattice. Lesser extent of reduction of Pt to metallic state in Fe system and its attendant higher activity in WGS may indicate a correlation to ionic Pt species being active for WGS reaction.

3.4. Conclusions

Incorporation of cationic platinum was attempted in the B site of LaBO₃ (B = Mn, Fe and Co) perovskites to stabilize it against sintering and was found to be successful only in the case of Fe and Co perovskites at the temperatures under study and not in case of Mn. Highly sintered Pt particles on the surface of LaMnO₃ were found and it is

possible that the inability of the LaMnO_3 perovskite lattice to incorporate Pt in the lattice may have led to the agglomeration.

In order to understand the extent of Pt incorporation in the LaMnO_3 system, Pt doping was attempted at different calcination temperatures. In the doped system synthesized at lower temperatures, presence of metallic Pt was not detected. But when compared to the unsubstituted LaMnO_3 , Pt doped LaMnO_3 was found to have a persistent amorphous phase impurity at lower synthesis temperatures. With the help of PXRD, HRTEM and XPS studies, it is demonstrated that Pt exists as PtO_x phase which is stabilised by the amorphous structure at lower calcination temperature. When high temperatures are used for calcination, the amorphous phase disappeared and metallic Pt appeared. Pt doped sample synthesized at $600\text{ }^\circ\text{C}$ with partially stabilized PtO_x by amorphous phase was found to be moderately active. Since the support is oxygen excess, the activity can only be attributed to $\text{Pt}(0)$ particles and the role of support through oxygen vacancies is minimal in this system. At higher calcination temperatures, $\text{Pt}(0)$ particles underwent sintering and these samples consequently exhibited poor activity.

The incorporation of cationic Pt in LaFeO_3 and LaCoO_3 was established with the help of PXRD using synchrotron X-rays, XANES and XPS. Water gas shift activity of these catalysts was tested and Pt doped Co and Fe perovskite catalysts showed $\sim 90\%$ CO conversion above $300\text{ }^\circ\text{C}$. XPS studies revealed the presence of multiple oxidation states (+4 and +2) for Pt in these compounds. A reduction of the B ions from the ideal state of +3 was observed for compensating the charge of $\text{Pt}(\text{IV})$, which was in turn found to enhance the oxygen vacancies on the surface. Small amount of methane formation along with hydrogen formation was found to occur with Pt doped Co perovskite while WGS activity was observed exclusively with Pt doped Fe perovskite. This is an expected result in line with previously studied preferences of Co and Fe oxides. The WGS activity of the Pt doped LaCoO_3 was compared with that of the same amount Pt impregnated on LaCoO_3 and $\text{La}_2\text{O}_3\text{-Co}_3\text{O}_4$ mixed oxide systems. The extent of methanation at maximum conversion when perovskite catalysts are used was very low in comparison to Pt

impregnated on mixed oxide support. It is possible that in the case of Pt doped catalyst, ionic Pt species in tandem with oxygen vacancies capable of acting as water adsorption sites may be enhancing WGS activity suppressing CO or CO₂ hydrogenation. In both Co and Fe catalysts, a small extent of Pt reduction to metallic state occurred under reducing conditions of WGS reaction. The fact that most of the Pt exist in oxidized form also indicates that it is stabilised in lattice points and hence resistant to sintering to a large extent.

References

1. Pena, M. A.; Fierro, J. L. G. *Chem. Rev.* **2001**, *101*, 1981.
2. da Conceicao, L.; Silva, A. M.; Ribeiro, N. F. P.; Souza, M. M. V. M. *Mater. Res. Bull.* **2011**, *46*, 308.
3. Petric, A.; Huang, P.; Tietz, F. *Solid State Ionics* **2000**, *135*, 719.
4. Lim, D. -K.; Im, H. -N.; Kim, J.; Song, S. -J. *J. Phys. Chem. Solids* **2013**, *74*, 115.
5. Choi, Y.; Lynch, M. E.; Lin, M. C.; Liu, M. J. *J. Phys. Chem. C* **2009**, *113*, 7290.
6. Kim, C. H.; Qi, G.; Dahlberg, K.; Li, W. *Science* **2010**, *327*, 1624.
7. Eyssler, A.; Winkler, A.; Safonova, O.; Nachtegaal, M.; Matam, S. K.; Hug, P.; Weidenkaff, A.; Ferri, D. *Chem. Mater.* **2012**, *24*, 1864.
8. Shu, J.; Kaliaguine, S. *Appl. Catal. B: Environ.* **1998**, *16*, L303.
9. Brown Bourzutschky, J. A.; Homs, N.; Bell, A. T. *J. Catal.* **1990**, *124*, 52.
10. Savinell, R. F. *Nat. Chem.* **2011**, *3*, 501.
11. Hwang, D. W.; Kim, H. G.; Kim, J.; Cha, K. Y.; Kim, Y. G.; Lee, J. S. *J. Catal.* **2000**, *193*, 40.
12. Watanabe, R.; Sekine, Y.; Takamatsu, H.; Sakamoto, Y.; Aramaki, S.; Matsukata, M.; Kikuchi, E. *Top. Catal.* **2010**, *53*, 621.
13. Sekine, Y.; Takamatsu, H.; Aramaki, S.; Ichishima, K.; Takada, M.; Matsukata, M.; Kikuchi, E. *Appl. Catal. A: Gen.* **2009**, *352*, 214.
14. Dacquin, J. P.; Lancelot, C.; Dujardin, C.; Cordier-Robert, C.; Granger, P. *J. Phys. Chem. C* **2011**, *115*, 1911.
15. Zhou, K.; Chen, H.; Tian, Q.; Hao, Z.; Shen, D.; Xu, X. *J. Mol. Catal. A: Chem.* **2002**, *189*, 225.

16. Nishihata, Y.; Mizuki, J.; Akao, T.; Tanaka, H.; Uenishi, M.; Kimura, M.; Okamoto, T.; Hamada, N. *Nature* **2002**, *418*, 164.
17. Uenishi, M.; Tanaka, H.; Taniguchi, M.; Tan, I.; Sakamoto, Y.; Matsunaga, S. -I.; Yokota, K.; Kobayashi, T. *Appl. Catal. A: Gen.* **2005**, *296*, 114.
18. De Souza, R. A.; Islam, M. S.; Ivers-Tiffée, E. *J. Mater. Chem.* **1999**, *9*, 1621.
19. Kuo, J. H.; Anderson, H. U.; Sparlin, D. M. *J. Solid State Chem.* **1989**, *83*, 52.
20. Malavasi, L.; Ritter, C.; Mozzati, M. C.; Tealdi, C.; Islam, M. S.; Bruno-Azzoni, C.; Flor, G. *J. Solid State Chem.* **2005**, *178*, 2042.
21. Van Roosmalen, J. A. M.; Cordfunke, E. H. P.; Helmholdt, R. B.; Zandbergen, H. W. *J. Solid State Chem.* **1994**, *110*, 100.
22. Sinha, A. K.; Sagdeo, A.; Gupta, P.; Kumar, A.; Singh, M. N.; Gupta, R. K.; Kane, S. R.; Deb, S. K. *AIP Conf. Proc.* **2011**, *1349*, 503.
23. Topfer, J.; Goodenough, J. B. *Chem. Mater.* **1997**, *9*, 1467.
24. Goodenough, J. B.; Wold, A.; Arnott, R. J.; Menyuk, N. *Phys. Rev.* **1961**, *124*, 373.
25. Cortes-Gil, R.; Arroyo, A.; Ruiz-Gonzalez, L.; Alonso, J. M.; Hernando, A.; Gonzalez-Calbet, J. M.; Vallet-Regi, M. *J. Phys. Chem. Solids* **2006**, *67*, 579.
26. Zhang, C.; Hua, W.; Wang, C.; Guo, Y.; Guo, Y.; Lu, G.; Baylet, A.; Giroir-Fendler, A. *Appl. Catal. B: Environ.* **2013**, *134–135*, 310.
27. Licci, F.; Turilli, G.; Ferro, P.; Ciccarone, A. *J. Am. Ceram. Soc.* **2003**, *86*, 413.
28. Hildrum, R.; Aasland, S.; Johannesen, O. *Solid State Ionics* **1993**, *66*, 207.
29. Kuznetsov, M. V.; Parkin, I. P.; Caruana, D. J.; Morozov, Y. G. *J. Mater. Chem.* **2004**, *14*, 1377.
30. Park, J. H.; Cheong, S. W.; Chen, C. T. *Phys. Rev. B* **1997**, *55*, 11072.
31. Khan, W.; Naqvi, A. H.; Gupta, M.; Husain, S.; Kumar, R. *J. Chem. Phys.* **2011**, *135*, 054501.
32. Wang, J.; Su, Y.; Wang, X.; Chen, J.; Zhao, Z.; Shen, M. *Catal. Commun.* **2012**, *25*, 106.
33. Vertruyen, B.; Flahaut, D.; Hebert, S.; Maignan, A.; Martin, C.; Hervieu, M.; Raveau, B. *J. Magn. Magn. Mater.* **2004**, *280*, 75.
34. Alonso, J. A.; Martinez-Lope, M. J.; Casis, M. T.; Munoz, A. *Solid State Commun.* **1997**, *102*, 7.

35. Ponce, S.; Pena, M. A.; Fierro, J. L. G. *Appl. Catal. B: Environ.* **2000**, *24*, 193.
36. Lee, Y. N.; Lago, R.M.; Fierro, J. L. G.; Cortes, V.; Sapina, F.; Martinez, E. *Appl. Catal. A: Gen.* **2001**, *207*, 17.
37. Wu, X.; Liang, Q.; Weng, D.; Fan, J.; Ran, R. *Catal. Today* **2007**, *126*, 430.
38. Liu, L.; Yu, Q.; Zhu, J.; Wan, H.; Sun, K.; Liu, B.; Zhu, H.; Gao, F.; Dong, L.; Chen, Y. *J. Colloid Interface Sci.* **2010**, *349*, 246.
39. Tofield, B. C.; Scott, W. R. *J. Solid State Chem.* **1974**, *10*, 183.
40. Norby, P.; Andersen, I. G. K.; Andersen, E. K. *J. Solid State Chem.* **1995**, *119*, 191.
41. Poverenov, E.; Efremenko, I.; Frenkel, A. I.; Ben-David, Y.; Shimon, L. J. W.; Leituss, G.; Konstantinovski, L.; Martin, J. M. L.; Milstein, D. *Nature* **2008**, *455*, 1093.
42. Xu, W.; Si, R.; Senanayake, S. D.; Llorca, J.; Idriss, H.; Stacchiola, D.; Hanson, J. C. Rodriguez, J. A. *J. Catal.* **2012**, *291*, 117.
43. Hall, M. D.; Foran, G. J.; Zhang, M.; Beale, P. J.; Hambley, T. W. *J. Am. Chem. Soc.* **2003**, *125*, 75245.
44. Hueso, J. L.; Caballero, A.; Ocana, M.; Gonzalez-Elipe, A. R. *J. Catal.* **2008**, *257*, 334.
45. Brundle, C. R.; Chuang, T. J.; Wandelt, K. *Surf. Sci.* **1977**, *68*, 459.
46. Rosynek, M. P.; Polansky, C. A. *Appl. Catal.* **1991**, *73*, 97.
47. Wang, C. -T.; Ro, S. -H. *J. Non-Cryst. Solids* **2006**, *352*, 35.
48. Lin, T. -C.; Seshadri, G.; Kelber, J. A. *Appl. Surf. Sci.* **1997**, *119*, 83.
49. Rosmaninho, M. G.; Tristao, J. C.; Moura, F. C. C.; Lago, R. M.; Araujo, M. H.; Fierro, J. L. G. *Anal. Bioanal. Chem.* **2010**, *396*, 2785.
50. Chainani, A.; Mathew, M.; Sarma, D. D. *Phys. Rev. B* **1993**, *48*, 14818.
51. Tejuca, L. G.; Bell, A. T.; Fierro, J. L. G.; Pena, M. A. *Appl. Surf. Sci.* **1988**, *31*, 301.
52. Yaccato, K.; Carhart, R.; Hagemeyer, A.; Lesik, A.; Strasser, P.; Volpe Jr., A. F.; Turner, H.; Weinberg, H.; Grasselli, R. K.; Brooks, C. *Appl. Catal. A: Gen.* **2005**, *296*, 30.
53. Lin, J. -H.; Biswas, P.; Gulians, V. V.; Misture, S. *Appl. Catal. A: Gen.* **2010**, *387*, 87.
54. Habazaki, H.; Yamasaki, M.; Zhang, B. -P.; Kawashima, A.; Kohno, S.; Takai, T.; Hashimoto, K. *Appl. Catal. A: Gen.* **1998**, *172*, 131.
55. Somorjai, G. A. *Catal. Rev.-Sci. Eng.* **1981**, *23*, 189.

56. Hwang, K. -R.; Lee, C. -B.; Ryi, S. -K.; Park, J. -S. *Int. J. Hydrogen Energ.* **2012**, *37*, 6626.
57. Panagiotopoulou, P.; Kondarides, D. I.; Verykios, X. E. *Appl. Catal. A: Gen.* **2008**, *344*, 45.
58. Coenen, J. W. E.; van Nesselrooy, P. F. M. T.; de Croon, M. H. J. M.; van Dooren, P. F. H. A.; van Meerten, R. Z. C. *Appl. Catal.* **1986**, *25*, 1.
59. Sehested, J.; Dahl, S. R.; Jacobsen, J.; Rostrup-Nielsen, J. R. *J. Phys. Chem. B* **2004**, *109*, 2432.
60. Xu, L.; Wu, Z.; Jin, Y.; Ma, Y.; Huang, W. *Phys. Chem. Chem. Phys.* **2013**, *15*, 12068.
61. Schanke, D.; Vada, S.; Blekkan, E. A.; Hilmen, A. M.; Hoff, A.; Holmen, A. *J. Catal.* **1995**, *156*, 85.

Chapter 4

Synthesis, Characterization, WGS and CO Oxidation

Activity of $\text{Ag}_2\text{Cu}_2\text{O}_3$ and $\text{Ag}_2\text{Cu}_2\text{O}_4$: Catalytic

Activity of Compounds with Low Coordinated

Metal Centers

4.1. Introduction

As mentioned in the Chapter 1, section 1.5, metals such as silver and copper, active for various reactions, when present in low coordinated form present an interesting system to explore the catalytic activity of coordinatively unsaturated sites. Such materials can be envisaged to provide ideal catalytic sites via coordination of reactant molecules. Recently developed $\text{Ag}_2\text{Cu}_2\text{O}_3$ and $\text{Ag}_2\text{Cu}_2\text{O}_4$ are examples of such systems where low coordinated silver and copper are interconnected. $\text{Ag}_2\text{Cu}_2\text{O}_3$ has an open channel structure and the oxidation states of Ag and Cu are +1 and +2 respectively [1, 2]. On the other hand, $\text{Ag}_2\text{Cu}_2\text{O}_4$ has a layered structure with Ag and Cu having oxidation states larger than the usual +1 and +2 [3-7].

Even though conventional catalysts are based on metal nanoparticles supported on high surface area materials for inducing better dispersion, in recent times, there have been some strong evidences of catalytic activity of ionic species as described in chapter 1, section 1.4. Also, a few reports mention the importance of ionic species in the interface of metal nanoparticles and oxide support in activating reactant molecules. This is especially true in case of facilitating CO adsorption and oxidation which can be considered as the elementary step in WGS as well as CO oxidation reactions [8].

In this context, the compound oxides of Ag and Cu form an interesting alternative due to the presence of stable ionic species as coordinatively unsaturated sites. Even though copper and silver based catalysts are already tested for WGS as well as CO oxidation reactions [9-12], compounds with low coordinated metal sites based on them have not been studied as catalysts for these processes. According to the redox mechanism for WGS reaction, CO adsorbs on transition metal sites and reacts with oxygen from the reducible support, which in turn is reoxidized by H_2O [13]. Both the CO oxidation and water-gas shift reaction on ceria-based catalysts are proposed to be controlled by the same two steps, transfer of oxygen from ceria to the metal interface and re-oxidation of ceria. It is reported that on TiO_2 , oxidized or reduced copper adsorb CO, while metallic silver practically does not adsorb CO; only oxidized Ag can adsorb CO strongly [14]. So a compound containing these two metals in oxidized form is expected

to show CO oxidation capability which is the most important step in both the above reactions. The CO which gets adsorbed on the ionic silver or copper can react with oxygen from the lattice which in turn can get oxidized by water or oxygen.

In this study, two conditions are used, viz., reducing and oxidizing for following the capability of these compounds for activating CO by choosing the above two reactions; Water Gas Shift and CO oxidation. Very different behaviours are observed from the two compounds in regards to activity and stability under the reaction conditions.

4.2. Experimental section

4.2.1. Synthesis

$\text{Ag}_2\text{Cu}_2\text{O}_3$ and $\text{Ag}_2\text{Cu}_2\text{O}_4$ samples were prepared as previously reported [2, 3]. To synthesise $\text{Ag}_2\text{Cu}_2\text{O}_3$, equimolar amounts (3.2 mmol) of $\text{Cu}(\text{NO}_3)_2 \cdot 3\text{H}_2\text{O}$ (Merck, 99.5 %) and AgNO_3 (Merck, 99.98 %) were dissolved in 2 mL of water, and the solution was then poured into 4 mL of a 3 M NaOH solution, while stirring vigorously. A dark-green precipitate formed. Added 100 ml more of water and the stirring was continued for 1 h. The dark solid was then filtered, washed with distilled water and dried. For the precipitation of $\text{Ag}_2\text{Cu}_2\text{O}_4$, combined saturated aqueous solutions of 1.205 g (5 mmol) AgNO_3 (Merck, 99 %) and 0.85 g (5 mmol) $\text{Cu}(\text{NO}_3)_2 \cdot 3\text{H}_2\text{O}$ (Merck, 99 %) was added to a solution of 3.0 g KOH (Merck) and 1.5 g $\text{K}_2\text{S}_2\text{O}_8$ (Merck) in 150 ml water at 90 °C. The obtained black precipitate was filtered off, washed with deionized water and dried in air at 70 °C.

4.2.2. Characterisation

The details of the instruments and procedures used for PXRD and in situ high temperature XRD experiments are same as those described in chapter 2A in section 2A.2.2.

4.2.3. Catalytic Testing

The set up for catalytic activity measurement used for WGS reaction was the same as that described in chapter 2A in the section 2A.2.3.

The same set up for WGS reaction was used for CO oxidation also. The activity tests were carried out under atmospheric pressure. A reaction gas containing 5 % v/v CO was passed over 0.25 cc of the catalyst. The activity data were collected with a GHSV of 20000 h⁻¹ and a CO to steam ratio 1: 3. The conversion reported here was carried out in the steady state where the catalyst temperature is ramped at 2 °C min⁻¹ and held at various temperatures for 15 min for equilibration. The reactor outflow was analyzed using a NUCON gas chromatograph equipped with a Carbosphere column and a thermal conductivity detector.

4.3. Results and discussion

4.3.1. Structural characterization and WGS activity studies

Ag₂Cu₂O₃ and Ag₂Cu₂O₄ were synthesized by the already reported coprecipitation method at low temperatures (RT and 90 °C respectively) [2, 3]. PXRD technique used for the structure analysis confirms the formation of single phase compounds (figure 4.1) without any impurity and matches with the reported patterns.

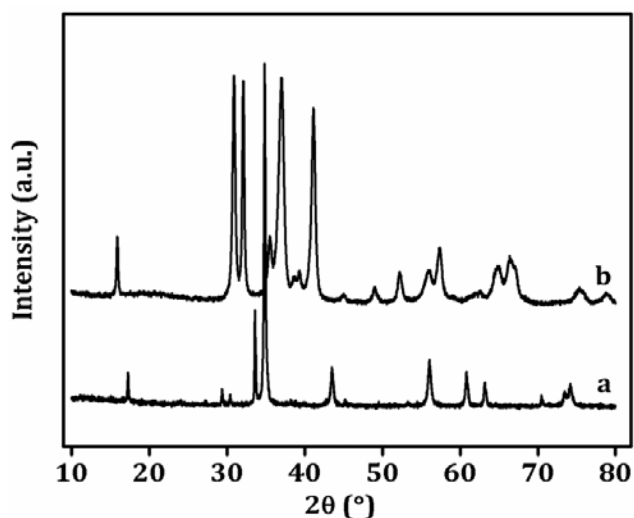


Figure 4.1. PXRD patterns of (a) Ag₂Cu₂O₃ and (b) Ag₂Cu₂O₄.

Earlier reports on the stability of these compounds suggest that under Ar or Ar/H₂ atmospheres, Ag₂Cu₂O₃ suffers a single step decomposition to yield metallic Ag and Cu at 340 and 260 °C respectively, while it decomposes to Ag and CuO under air or oxygen at around 350-360 °C [2]. Ag₂Cu₂O₄ decomposes first to Ag₂Cu₂O₃ at 280 °C and then to metallic Ag and CuO at 310 °C [3]. When stored in Ar atmosphere, it decomposes to Ag₂O and CuO within few days, though it is unaffected by moisture or air. Initially, both the catalysts were tested for WGS activity. The Ag₂Cu₂O₃ compound was found to convert ~93 % of the CO in the stream to CO₂ at 115 °C, but a corresponding increase in the hydrogen concentration was not observed. After 20 minutes at the same temperature, CO conversion dropped to zero pointing to a possible change in the structure of the material during the reaction conditions even at temperatures as low as 115 °C. In order to understand the structural changes which occurred and what conditions did affect the activity, the catalyst was subjected to various gas atmospheres, viz., reformat mixture with steam, reformat mixture alone and steam with N₂ within the reactor itself up to 115 °C and the samples obtained after the treatments were analysed using PXRD technique. The results are plotted in figure 4.2.

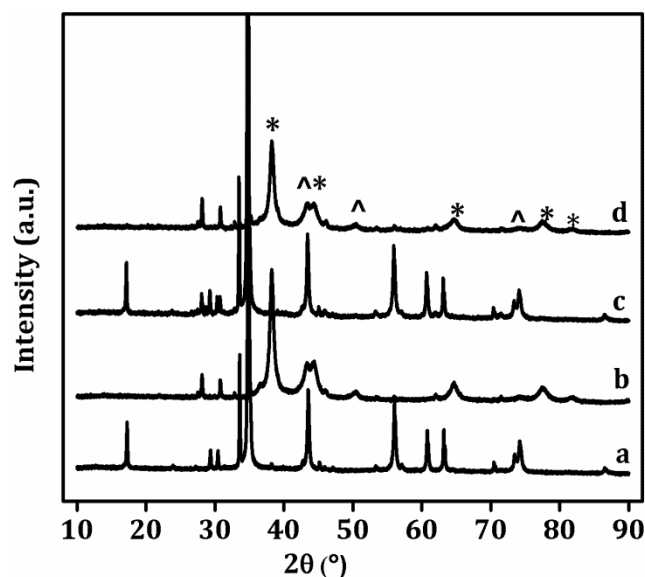


Figure 4.2. PXRD patterns of Ag₂Cu₂O₃ (a) before, (b) after WGS reaction, after subjecting to (c) steam with N₂ and (d) reformat mixture alone; *: Ag, ^: Cu.

It is apparent that steam did not affect the catalyst; however the reformat mixture did result in structural collapse to metallic silver and copper. There was no change in the concentration of hydrogen observed, but the concentration of CO_2 increased from 14.5 to 24 %. The absence of hydrogen production observed under water gas shift reaction conditions indicates that instead of WGS reaction, a mere CO oxidation occurred as the decrease in CO concentration and increase in CO_2 concentration could be balanced. The oxygen required for the reaction was probably provided by the decomposition of the catalyst itself which was supported by the fact that the CO_2 production lasted for only a few minutes. It is also possible that CO adsorption is facilitated on the coordinatively unsaturated sites and a subsequent abstraction of lattice oxygen leads to structural collapse. Apparently, the catalyst is not able to dissociate water and replenish the lattice oxygen thereby stabilizing the structure, at such low temperatures at which the catalyst decomposes. It is obvious that the harsh reduction conditions affect the catalyst structure and to understand the extent of structure stability, we carried out in situ high temperature XRD studies with 10 % H_2/N_2 and the results are plotted in figure 4.3.

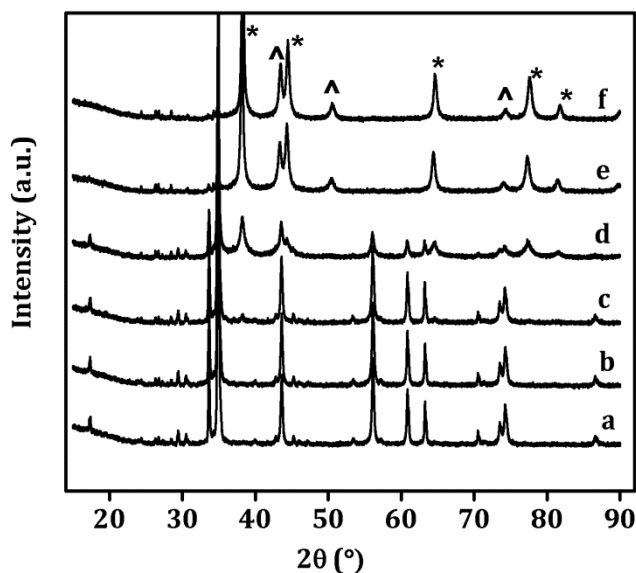


Figure 4.3. In situ high temperature PXRD patterns of $\text{Ag}_2\text{Cu}_2\text{O}_3$ (a) RT, (b) 50 °C, (c) 100 °C, (d) 150 °C, (e) 200 °C and (f) RT, under 10 % H_2/N_2 ; *: Ag, ^: Cu.

It can be observed that the sample decomposes above 100 °C to metallic Ag and Cu under 10 % H₂/N₂ conditions. The WGS reactant gas stream contains almost 40 % H₂ and this might have resulted in the structural collapse at a much lower temperature. Hence it is not clear whether lattice abstraction of oxygen led to the collapse of the structure or the harsh conditions also played a role in it.

The oxidation of the Ag₂Cu₂O₃ results in the formation of Ag₂Cu₂O₄, in which one oxygen atom is excess. WGS activity of this material was also studied. Surprisingly the material exhibited complete inactivity towards WGS reaction. Here, unlike in the case of Ag₂Cu₂O₃, no CO conversion is observed at anytime. The PXRD pattern of the catalyst after reaction at 150 °C is compared with that of the fresh catalyst and the plot is displayed in figure 4.4. Here also the compound is found to undergo decomposition to metallic silver and copper under WGS conditions.

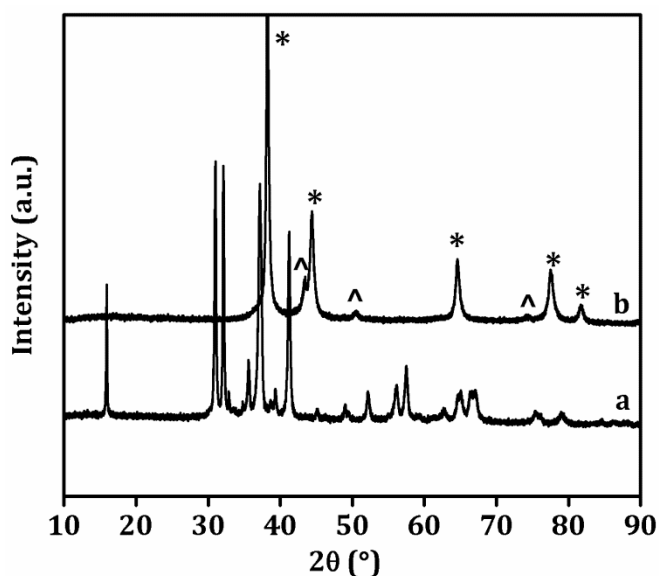


Figure 4.4. PXRD patterns of Ag₂Cu₂O₄ (a) before and (b) after WGS reaction; *: Ag, ^: Cu.

Even though both the materials have similar coordination environments for Ag and Cu and also undergo similar decomposition profiles, they show marked difference in behavior towards CO oxidation activity. This has to be attributed to the difference in

lattice oxygen abstraction step by CO. In $\text{Ag}_2\text{Cu}_2\text{O}_4$, apparently the structure collapses before it is energetically possible to do so.

4.3.2. CO oxidation activity studies

It became clear that $\text{Ag}_2\text{Cu}_2\text{O}_3$ is capable of converting CO present in the stream to CO_2 as long as the oxygen supply is there. Hence, this catalyst was further used to explore CO oxidation activity and the results are displayed in figure 4.5.

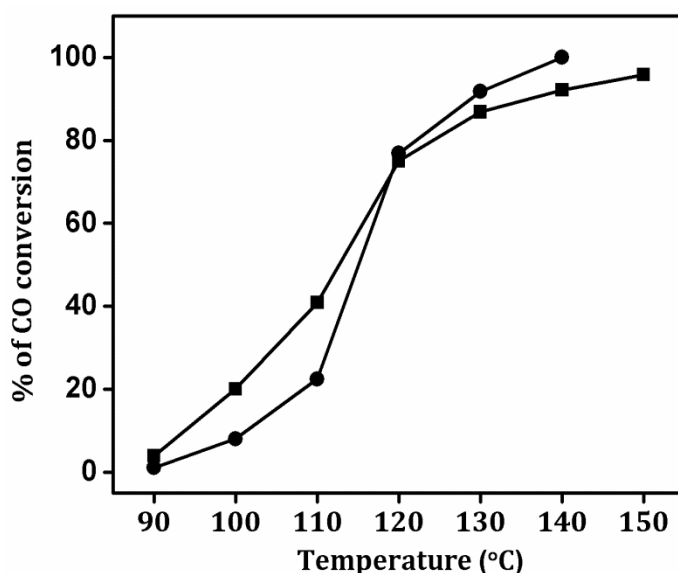


Figure 4.5. CO conversion measured over ■: $\text{Ag}_2\text{Cu}_2\text{O}_3$ and ●: $\text{Ag}_2\text{Cu}_2\text{O}_4$. GHSV: 20000 h^{-1} ; CO: O_2 = 1: 3.

The $\text{Ag}_2\text{Cu}_2\text{O}_3$ material was found to yield 96 % CO conversion at temperature as low as 150 °C. The PXRD analysis (figure 4.6) of the material shows that only a negligible amount of metallic silver appeared after CO oxidation. However, in case of $\text{Ag}_2\text{Cu}_2\text{O}_4$, the material undergoes complete decomposition, but exhibits almost similar activity as $\text{Ag}_2\text{Cu}_2\text{O}_3$. As expected, CO adsorption is facilitated on the ionic active sites. The dissociation energies of H_2O and O_2 are comparable and since we did not observe any H_2O dissociation in the presence of steam at ~115 °C, O_2 adsorption in the vacancy site and subsequent dissociation has to be ruled out. Hence a reaction based on Eley-Rideal mechanism in which adsorbed CO reacts with gaseous O_2 molecule [15], may

play the dominant role even under excess of O_2 . Such a mechanism for WGS reaction is not plausible without involving the H_2O dissociation step which is not energetically possible in both the compounds. In the absence of O_2 , CO apparently abstracts the O from lattice, in case of $Ag_2Cu_2O_3$. In $Ag_2Cu_2O_4$, this does not occur possibly due to the structural difference and absence of conducive adsorption sites. This leads to structural collapse and further reaction occurs on the metal nanoparticle surfaces.

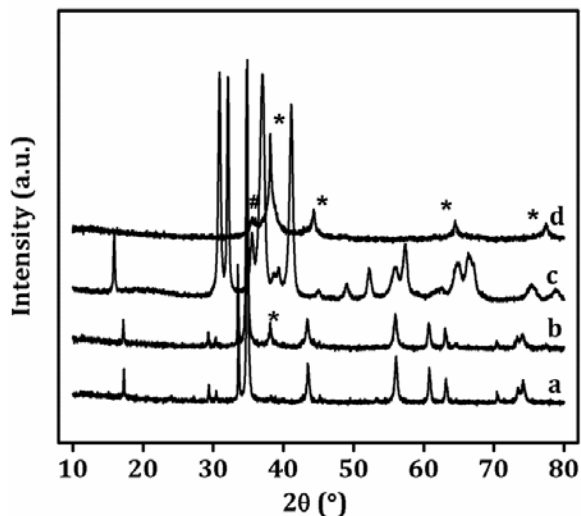


Figure 4.6. XRD patterns of (a) $Ag_2Cu_2O_3$ and (c) $Ag_2Cu_2O_4$ before and (b) $Ag_2Cu_2O_3$ and (d) $Ag_2Cu_2O_4$ after CO oxidation. #: CuO and *: Ag.

The structural peculiarity of $Ag_2Cu_2O_3$ and the stability it retains by incorporating another O per unit cell vis-à-vis $Ag_2Cu_2O_4$ probably presents energetically favourable adsorption sites making it a better catalyst than $Ag_2Cu_2O_4$. This study shows that $Ag_2Cu_2O_3$ can be tuned to a highly active catalyst for CO oxidation and other redox reactions if suitable water/ O_2 dissociation sites could be created.

4.4. Conclusions

Low coordination compounds with active metals viz. silver and copper in low coordination geometries, $Ag_2Cu_2O_3$ and $Ag_2Cu_2O_4$ are synthesised. $Ag_2Cu_2O_3$ exhibited very high CO conversion activity at very low temperatures under WGS reaction conditions while $Ag_2Cu_2O_4$ displayed no activity at all. Structural characterizations indicated that both the materials are unstable under WGS conditions. Further analysis

indicated that only CO oxidation occurred and not hydrogen production under the reaction conditions. CO oxidation carried out over both the catalysts indicated that both exhibited very high activity at temperatures ~ 150 °C. PXRD characterization indicated that small amount of metallic silver egress from the lattice in the case of $\text{Ag}_2\text{Cu}_2\text{O}_3$ where as the structure collapses to metallic silver and copper oxide in the case of $\text{Ag}_2\text{Cu}_2\text{O}_4$ after CO oxidation reaction. Eley-Rideal mechanism where only CO gets adsorbed on the surface site can be suggested for CO oxidation with these catalysts. It can also be suggested that the employment of methods by which oxygen can be replenished on the surface may enhance the CO oxidation activity of these compounds.

References

1. Gomez-Romero, P.; Tejada-Rosales, E. M.; Palacin, M. R. *Angew. Chem. Int. Edit.* **1999**, *38*, 524.
2. Tejada-Rosales, E. M.; Rodriguez-Carvajal, J.; Casan-Pastor, N.; Alemany, P.; Ruiz, E.; El-Fallah, M. S.; Alvarez, S.; Gomez-Romero, P. *Inorg. Chem.* **2002**, *41*, 6604.
3. Curda, J.; Klein, W.; Jansen, M. *J. Solid State Chem.* **2001**, *162*, 220.
4. Curda, J.; Klein, W.; Liu, H.; Jansen, M. *J. Alloy. Compd.* **2002**, *338*, 99.
5. Munoz-Rojas, D.; Ori, J.; Gomez-Romero, P.; Fraxedas, J.; Casan-Pastor, N. *Electrochem. Commun.* **2002**, *4*, 684.
6. Munoz-Rojas, D.; Fraxedas, J.; Ori, J.; Gomez-Romero, P.; Casan-Pastor, N. *Cryst. Eng.* **2002**, *5*, 459.
7. Munoz-Rojas, D.; Fraxedas, J.; Gomez-Romero, P.; Casan-Pastor, N. *J. Solid State Chem.* **2005**, *178*, 295.
8. Bunluesin, T.; Gorte, R. J.; Graham, G. W. *Appl. Catal. B: Environ.* **1998**, *15*, 107.
9. Honkala, K.; Hellman, A.; Gronbeck, H. *J. Phys. Chem. C* **2010**, *114*, 7070.
10. Hellman, A.; Klacar, S.; Gronbeck, H. *J. Am. Chem. Soc.* **2009**, *131*, 16636.
11. Rodriguez, J. A.; Liu, P.; Hrbek, J.; Perez, M.; Evans, J. *J. Mol. Catal. A: Chem.* **2008**, *281*, 59.
12. Rodriguez, J. A.; Evans, J.; Graciani, J. s.; Park, J. -B.; Liu, P.; Hrbek, J.; Sanz, J. F. *J. Phys. Chem. C* **2009**, *113*, 7364.

13. Li, Y.; Fu, Q.; Flytzani-Stephanopoulos, M. *Appl. Catal. B: Environ.* **2000**, *27*, 179.
14. Boccuzzi, F.; Chiorino, A.; Manzoli, M.; Andreeva, D.; Tabakova, T.; Ilieva, L.; Iadakov, V. *Catal. Today* **2000**, *75*, 169.
15. Peden, C. H. F.; Goodman, D. W.; Weisel, M. D.; Hoffmann, F. M. *Surf. Sci.* **1991**, *253*, 44.

Chapter 5

Summary and Conclusions

5.1. Summary

Chapter 1 presents a general introduction to the noble metal nanoparticles and their role in heterogeneous catalysis. Even though supported noble metal nanoparticles are reported to exhibit extreme activity towards several reactions, deactivation due to sintering of nanoparticles is a major problem associated with them. The chapter further presents a comprehensive review of literature on the sintering of metal nanoparticles and on some industrially important heterogeneous reactions like water gas shift reaction and CO oxidation where supported metal catalysts are important. In addition, it describes some of the reports where ionic species are suggested to act as active species contrary to the conventional idea of active metallic species. The chapter briefly describes the role of structured oxides such as perovskites in catalysis and also gives an introduction about the recently developed low coordination oxides based on catalytic active metals. Finally the scope and objective of the theses are stated.

Chapter 2A describes the synthesis of $\text{BaCe}_{1-x}\text{Pt}_x\text{O}_{3-\delta}$ and its structural evaluation by various characterization methods and in situ studies, in relation to the WGS reaction. This catalyst system is found to isolate efficiently cationic Pt species that are stable under reducing conditions. Structural characterizations point to the successful substitution of Pt(II) in Ce(IV) sites indicating an increase in oxygen vacancies with increase in Pt concentration. Cationic Pt stabilized in the BaCeO_3 lattice is found to be active for WGS. Metallic species are not identified in spent catalysts recovered under WGS conditions as well as after exposure to air during shutdown. Interestingly, after the first shutdown under air, a surface enrichment of ionic Pt species is observed which is thought to be responsible for the enhancement of WGS activity for the second cycle. We have further studied the variations in Pt states under other possible shut down conditions and it is observed that the catalyst system is stable and withstand harsh reaction conditions as well as various shut down conditions employed such as N_2 , reformat feed and reformat feed along with steam. BaCeO_3 is proposed to be an ideal perovskite lattice to stabilize ionic Pt, keeping it not only active but also sinter resistant under WGS conditions.

Chapter 2B describes the progressive doping of yttrium in the B site of $\text{BaCe}_{1-x}\text{Pt}_x\text{O}_{3-\delta}$ catalyst system so that oxygen vacancies are systematically enhanced to maintain electrical neutrality. Moreover, the Pt concentration was fixed at 2 mol% so that contribution from Pt remains same catalytically as well as structurally. The materials are synthesized and characterized using various techniques and their water gas shift activities are compared. Even though oxygen vacancies will be increased as Y content increases, we observe a distinct way in which structural variations accommodate the vacancies. At lower Y substitutions with orthorhombic structure, oxygen vacancy increase is reflected in the drastic reduction in cell volume and at higher Y concentrations, the oxygen vacancies are accommodated by structural distortions due to the creation of an isotropic environment. $\text{BaCe}_{0.92}\text{Pt}_{0.02}\text{Y}_{0.06}\text{O}_{3-\delta}$ having the least distorted Ce/Y/PtO6 octahedra, exhibited maximum WGS activity in the series. The isotropic environment around B ion in this compound energetically favors the adsorption and splitting of H_2O by lowering the energy barriers. This clearly indicates dependence on not the concentration of oxygen vacancies but on their crystallographic characteristics. Extensive in-situ powder XRD studies under reducing and oxidizing conditions revealed only a thermal effect at increasing temperatures for low Y substituted orthorhombic compounds. However, the monoclinic structures with higher concentrations of oxygen vacancies exhibited a phase transition to orthorhombic structure, usually with lower concentrations of oxygen vacancies, at 300 °C. This phase transition is found to be reversible under H_2 , O_2 and water vapour indicating it to be a thermal effect. But under WGS conditions, viz., CO and H_2O , the transition to a lower oxygen vacancy structure was irreversible. This clearly indicates that vacancy sites are involved in the WGS.

Chapter 3 reported synthesis, characterization and WGS activity of $\text{LaB}_{1-x}\text{Pt}_x\text{O}_{3-\delta}$ where B is Mn, Fe and Co. X-ray based characterization techniques indicated cationic Pt stabilization in the lattice sites of Fe and Co perovskites. In the case of Mn, highly sintered metallic Pt particles are observed. It is apparent that LaMnO_3 presents a challenge as a matrix for stabilizing ionic Pt species and the next section of the chapter describes a thorough study regarding the incorporation of cationic Pt in the oxygen

excess LaMnO_3 at different calcination temperatures. It is established that Pt incorporation in ionic form in LaMnO_3 is not possible and the Pt exists as PtO_2 at lower temperatures strongly interacting with the amorphous phase found along with the perovskite and reduced to metallic Pt at higher temperatures. Another important conclusion in this study is that crystalline PtO/PtO_2 are not as active as $\text{Pt}(0)$ for WGS.

In the case of Pt stabilized in LaFeO_3 catalyst, the WGS activity was $\sim 80\%$. Cationic Pt incorporated Co perovskites are shown to be highly active for WGS reaction, but a small amount of methanation is observed. It is also observed that methanation could be decreased and WGS enhanced in case of Pt doped or impregnated Co perovskites when compared to Pt impregnated mixed oxides. Ionic Pt species in tandem with oxygen vacancies capable of acting as water adsorption sites might be enhancing their WGS activity suppressing CO or CO_2 hydrogenation. In both Co and Fe catalysts, a small extent of Pt reduction to metallic state occurred under reducing conditions of WGS reaction. The fact that most of the Pt exist in oxidised form also indicates that it is stabilised in lattice points and hence resistant to sintering to a large extent. It is worth mentioning here that doping may be looked upon as a method for selectively enhancing one among two competing reactions as well as to improve overall thermal stability under reaction conditions.

Chapter 4 describes the synthesis of low coordination compounds, $\text{Ag}_2\text{Cu}_2\text{O}_3$ and $\text{Ag}_2\text{Cu}_2\text{O}_4$ and their catalytic activity towards WGS reaction and CO oxidation, to study the activity of coordinatively unsaturated active metals. We observed $\sim 90\%$ initial CO oxidation activity when $\text{Ag}_2\text{Cu}_2\text{O}_3$ was used as catalysts for WGS reaction with simultaneous decomposition of the catalyst. However when used for CO oxidation, the structure is retained with the appearance of a small percentage of metallic Ag. Interestingly, the oxygen rich $\text{Ag}_2\text{Cu}_2\text{O}_4$ catalyst did not show any activity in CO oxidation under WGS conditions and decomposed to metallic Ag and Cu. The compound shows CO oxidation activity under oxidizing conditions, but decomposes to Ag and CuO. This indicates that lattice oxygen takes part in oxidizing CO in the case of $\text{Ag}_2\text{Cu}_2\text{O}_3$, consequently destroying the structure whereas, this does not occur in case of $\text{Ag}_2\text{Cu}_2\text{O}_4$.

5.2. Conclusions

- ❖ Cationic Pt is stabilized in BaCeO_3 perovskite lattice and is stable up to high temperatures under reducing atmospheres.
- ❖ Cationic Pt is active for WGS reaction and withstands the harsh reaction conditions as well as all the shut down conditions employed.
- ❖ Oxygen vacancies are involved in the mechanism of WGS reaction.
- ❖ WGS activity depends not on the concentration of the oxygen vacancies but on their structural characteristics and the extent of favourable energetics of water adsorption.
- ❖ There is an inherent resistance to doping of Pt in LaMnO_3 due to its oxygen excess nature.
- ❖ Cationic Pt can be stabilized in LaBO_3 (B = Fe & Co).
- ❖ Cationic Pt together with B-site ion determines the activity and preference for WGS or CO methanation.
- ❖ Pt doped lanthanum based perovskites are not as stable as BaCeO_3 .
- ❖ Cationic species in $\text{Ag}_2\text{Cu}_2\text{O}_3$ catalyses CO oxidation.
- ❖ Incorporation of noble metals in the form of ions in stable lattices can be considered as a solution to minimise the problem of sintering of metallic particles and consequent deactivation of the catalyst.

List of Publications

1. Evidence of Cationic Pt Active for Water-Gas Shift Reaction: Pt-Doped BaCeO₃ Perovskite. **Thattarathody Rajesh**, Anakot K. Rajarajan, Chinnakonda S. Gopinath, and R. Nandini Devi, *J. Phys. Chem. C* **2012**, 116, 9526–9532.
2. Role of Oxygen Vacancies in Water Gas Shift Reaction: Activity Study on BaCe_{0.98-x}Y_xPt_{0.02}O_{3-δ} Perovskites. **Thattarathody Rajesh** and R. Nandini Devi, *J. Phys. Chem. C*, **2014**, 118, 20867–20874.
3. Effect of Pt Incorporation in LaBO₃ (B = Mn, Fe, Co) Perovskites on Water Gas Shift Activity. **Thattarathody Rajesh**, Anuj Upadhyay, Anil K. Sinha, Sudip K. Deb and R. Nandini Devi, *J. Mol. Catal. A: Chem.* **2014**, 395, 506-513.
4. Resistance to Ionic Pt Insertion in Oxygen Excess LaMnO₃ Perovskite Lattices and Its Effect in Water Gas Shift Reaction. **Thattarathody Rajesh** and R. Nandini Devi, *J. Mol. Catal. A: Chem.* **2014**, 395, 534-542.
5. Pt States in BaCe_{0.98}Pt_{0.02}O_{3-δ} during Start up and Shut down Operations under Different Conditions: Stability and Activity of Ionic Pt in Water Gas Shift Reaction. **Thattarathody Rajesh** and R. Nandini Devi, *Catal. Lett.* **2014**, 144, 2227-2232.
6. Confined Space Synthesis of Fully Alloyed and Sinter Resistant AuPd Nanoparticles Encapsulated in Porous Silica. Anupam Samanta, **Thattarathody Rajesh** and R. Nandini Devi. *J. Mater. Chem. A*, **2014**, 2, 4398-4405.

Contributions to Symposia/Conference

1. Presented a poster entitled "*Noble metal doped perovskite $BaCe_{1-x}Pt_xO_{3-\delta}$ as catalyst for Water Gas Shift Reaction*" at the "21st National Symposium on Catalysis for sustainable development (**CATSYMP-21**)" at CSIR-IICT, Hyderabad, India (11-13 February, 2013).
2. Participated and presented a poster entitled "*Noble metal doped perovskite $BaCe_{1-x}Pt_xO_{3-\delta}$ as efficient Water Gas Shift catalyst*" at the "9th International Congress on Catalysis and Automotive Pollution Control (**CAPoC9**)" at Universite Libre de Bruxelles, Brussels, Belgium (29-31 August, 2012).
3. Presented a poster entitled "*Synthesis, characterization and water gas shift activity of noble metal doped perovskite*" at "20th National Symposium on Catalysis (**CATSYMP-20**)" at IIT Madras, India (19-22 December, 2010).
4. Participated in symposium on "Catalysis for Sustainable Energy and Chemicals", 19th National Symposium on Catalysis, (**CATSYMP-19**) from January 18-21, 2009 at National Chemical Laboratory, Pune, India.

Appendix

Physicochemical Characterizations

Various physicochemical techniques can be used for the characterization of the perovskite materials. The principles of techniques, used in the present study like powder diffraction using laboratory or synchrotron X-rays or neutron, Rietveld refinement, ICP-AES, Surface area analysis using N₂ adsorption, HRTEM, XANES and XPS.

1. Powder Diffraction

Understanding and predicting the properties of scientific and technologically important materials require the exact knowledge of its structure. The structure of an idealized crystal lattice consists of periodic arrangement atoms and single crystal analysis is the most suitable technique to understand it. However, because of the unavailability of suitable single crystals in many cases and to extract information on the bulk material, alternative technique, powder diffraction is routinely used. Moreover it can be used for the determination of microstructural properties, disorder in materials, studies of macroscopic stresses in components, and texture of polycrystalline samples.

X-rays are electromagnetic waves having wavelengths of the order of 1Å, which is comparable with the spacing between lattice planes in crystals. X-ray diffraction, based on wide-angle elastic scattering of X-rays, is the most important and common tool to determine the structure of the materials characterized by the long range ordering. X-ray diffraction involves the measurement of the intensity of X-rays scattered from electrons or neutrons bound to atoms. Waves scattered at atoms at different positions arrive at the detector with a relative phase shift. Therefore, the measured intensities yield information about the relative atomic positions. The diffraction patterns gives information about structure formation, phase purity, degree of crystallinity, and unit cell parameters of the materials. The formation of a structural phase can be confirmed by comparing the powder diffraction patterns with that of pure reference phases distributed by International Center for Diffraction Data (ICDD).

The use of Bragg's equation is the easiest way to get to the structural information in powder diffraction, the derivation of which considers X-ray diffraction as a reflection of X-rays by sets of lattice planes. As the X-rays penetrate deeply, additional reflections occur at

thousands of consecutive parallel planes. The overlap of the scattered X-rays occurs since all are reflected in the same direction.

The Bragg's equation is $n\lambda = 2d\sin\theta$, where d is the interplanar spacing of parallel lattice planes and 2θ is the diffraction angle, the angle between the incoming and outgoing X-ray beams.

Sharp intensities emerge from the sample only at the special angles where Bragg's equation holds. For crystalline materials, the destructive interference results in a completely destruction of intensity in all the other directions. In the modern flat-plate powder X-ray diffractometer, used most commonly in industrial and academic laboratories, the divergent incident beam is allowed to reflect from the sample and converges at a fixed radius from the sample position. This configuration is commonly referred to as "Bragg-Brentano" geometry (shown in Figure 6). The spinning of sample about an axis normal to the flat plate results in a good powder average.

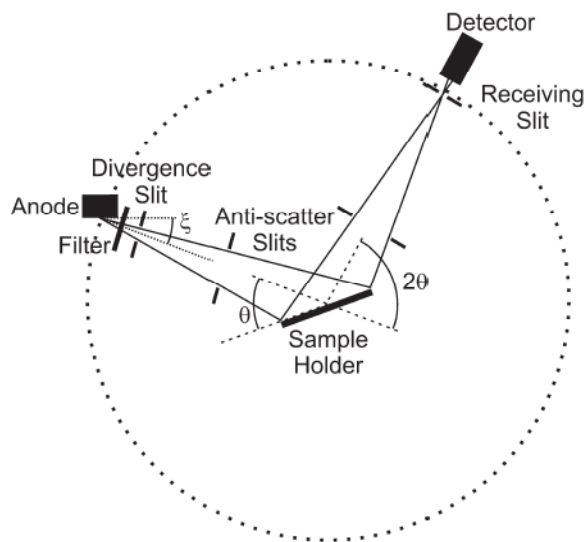


Figure 1. Schematic representation of Bragg-Brentano geometry.

Powder diffraction experiments, exploits X-rays from a laboratory generator or from a high energy storage ring (synchrotron radiation), or neutrons produced in a reactor or spallation source. A typical wavelength used lies in the range 0.1-5 Å, comparable with the spacings between lattice planes in crystals. Data can be collected in transmission or reflection modes, depending on the absorption of radiation by the sample. A brief

description of the different sources used for the powder diffraction experiments are given here.

1.1. Laboratory X-ray Sources

In a standard laboratory instrument, the X-rays are produced in a sealed-tube source where electrons, accelerated by a potential difference of up to 60 kV, bombard a metal anode inside a vacuum tube. This results in the formation of a characteristic radiation spectrum composed of discrete peaks arising from the filling of vacant level in the inner shell (created from the ejection of electron by the incoming electron) by a higher atomic level electron. The emission of an X-ray photon is characterised by the difference in energy between the two levels. A higher resolution copper X-ray spectrum consists of components labeled as $K_{\alpha 1}$ (1.54056Å) and $K_{\alpha 2}$ (1.54439Å). The most commonly used target element is Cu but Mo, Cr, Fe, Co, Ag and W are also used for specialist applications (. Cu tube is the most common choice for routine analysis, which gives X-rays of shortest wavelength above 1Å. Also relatively high power can be applied to the target because of the good thermal conductivity of copper.

Table 1. Approximate principle emission lines for various anode targets.

Anode	Cu	Mo	Cr	Fe	Co	Ag	W
$\lambda(K_{\alpha})$ Å	1.54	0.71	2.29	1.94	1.79	0.56	0.21

1.2. Synchrotron X-ray Sources

The synchrotron X-ray radiation has several advantages over laboratory sources like extreme intensity, high collimation in the vertical sense allowing the design of high resolution instruments, selection of wavelengths for a particular measurement etc. The underlying principle behind the ejection of synchrotron radiation is that when a fast moving charged particle is forced to follow a curved trajectory by applying a magnetic field it changes its velocity. In modern synchrotron radiation sources electrons or positrons are accelerated to speeds close to that of light and circulate in ultrahigh vacuum tubes, guided by arrays of magnets. The electrons are guided in a storage ring which consists of straight

section followed by a curved section where the electrons are forced into the next straight section using bending magnet and the radiation is emitted at these curved sections.

The spectrum of synchrotron radiation depends on the energy of the electrons in the storage ring, the curvature of their path, etc. Generally, the greater the electron energy or tighter the curvature (i.e. the higher the magnetic field) in the storage ring, the higher the energy of the emitted X-rays. The tunability of wavelength over a large range can be used for anomalous dispersion experiments or for depth profiling of thin films etc.

1.3. Neutron Scattering

Neutron radiation of sufficient intensity can be provided at research reactors and spallation neutron sources. A neutron even though uncharged has a magnetic moment as a result of its spin (spin of 1/2) and therefore it can approach the nucleus of atoms closely. This results in scattering of neutrons by nuclear forces or via spin-spin interactions with both nuclear magnetic moments and unpaired electrons in magnetic atoms or ions. The scattering cross section, σ , measured in barns ($1 \text{ barn} = 10^{-28} \text{ m}^2$) is used to describe the scattering of a neutron by a nucleus which is defined as equal to the effective area presented by the nucleus to the incoming neutron. The scattering occurs isotropically as the range of the neutron-nucleus interaction is tiny compared to the wavelength of the neutron making the nucleus essentially a point scatterer.

In the case of X-ray diffraction, the photons are scattered by the interaction of electron cloud of the material and this means that in presence of heavier atoms, it may be difficult to detect lighter atoms. However, most atoms have neutron scattering lengths of approximately equal in magnitude (as shown in table below) and hence neutron diffraction techniques are used to detect light elements such as oxygen or hydrogen.

Table 2. Scattering cross section for X-Rays and neutrons.

Element		${}^1\text{H}$	${}^6\text{C}$	${}^{25}\text{Mn}$	${}^{26}\text{Fe}$	${}^{28}\text{Ni}$	${}^{46}\text{Pd}$	${}^{67}\text{Ho}$	${}^{92}\text{U}$
σ_{coh} (barn)	X-ray	0.66	24	416	450	522	1406	2986	5631
	Neutron	1.76	5.55	1.75	11.22	13.30	4.39	8.06	8.90

The properties of a radiation source can be characterized by parameters such as spectral flux and brightness. Flux is the number of photons travelling through unit area in unit time.

The spectral brightness is defined as photon flux density in phase space about a certain frequency. This means the number of photons per unit time per unit area per unit solid angle

$$\text{Spectral flux} = \text{Photons s}^{-1}(\text{0.1\% bandwidth})^{-1}$$

$$\text{Brightness} = \text{Photons s}^{-1}\text{mrad}^{-2} (\text{0.1\%bandwidth})^{-1}$$

A comparison of brightness and flux of X-rays and neutrons from various sources is given in the following table.

Table 3. Brightness and flux for generalized X-ray and neutron sources.

Source type	Brightness ($\text{s}^{-1}\text{m}^{-2}\text{ster}^{-1}$)	Divergence (mrad^2)	Flux ($\text{s}^{-1}\text{m}^{-2}$)
Neutron reactor source	10^{15}	10×10	1×10^{11}
X-ray tube	10^{20}	0.5×10	5×10^{14}
Synchrotron bending magnet	10^{27}	0.1×5	5×10^{20}
Synchrotron undulator	10^{33}	0.01×0.1	1×10^{24}

1.4. Rietveld refinement

The development of Rietveld method in 1969 breaks out the application of powder diffraction method as a quantitative tool. Rietveld method is a powerful technique that makes use of the entire powder pattern instead of analyzing individual, non-overlapped, diffraction peaks for crystal structure refinement. The advantage of this method is that it calculates the entire powder pattern of a crystalline model, including various experimental and sample dependent effects. Rietveld method essentially tries to fit a structural model based on a number of crystal structure parameters to the experimental diffraction data. This model utilizes a least-squares approach where various parameters such as lattice parameters, atomic positions and parameters such as peak shape, background, scale factors, peak broadening, that describe the experimental and sample conditions, are allowed to vary to reach an agreement between the calculated and measured diffraction

profiles. However to employ this method, a good initial knowledge of the structure is needed which is refined by small adjustments. The method can be utilized to refine several powder or single crystal diffraction data including reactor neutron data, laboratory X-ray powder diffraction data, synchrotron powder diffraction data, time-of-flight neutron data from pulsed spallation sources, and to refinements of magnetic structures. Rietveld analysis is carried out mostly for the determination the structural parameters, but increasingly, the method is also used to determine relative amounts of the crystallographic phases, the preferred orientation, residual stress, crystallite size etc. The use of highly monochromatic parallel beam synchrotron radiation enabled us to get accurate atomic parameters, which in turn allows to extract useful information regarding bonding conditions and reaction mechanisms. This method further helps to quantitatively detect small amounts of polymorphic phases which are of great interest especially for pharmaceutical research and in the concrete business. Currently various softwares are available for the Rietveld refinement such as GSAS, GSAS-EXPGUI, Fullprof, TOPAS, JANA2000, Rietan etc.

2. Inductively Coupled Plasma-Optical Emission Spectroscopy

Inductively coupled plasma atomic emission spectroscopy (ICP-AES), or inductively coupled plasma optical emission spectrometry (ICP-OES), is an analytical technique used for the detection of trace metals. This technique exploits the fact that excited electrons emit energy at a wavelength characteristic to the element as they return to ground state. The intensity of this emission directly gives information about the concentration of the element present in the sample. The schematic representation of the ICP-AES instrument is shown in figure 7.

Plasma is a gaseous state of matter, a major part of which consists of free electrons and highly charged ions. It presents an effective medium for volatilization and atomization (and ionization) of liquid droplets. In plasma-based systems, the temperature normally reaches ~ 6000 to 10000 K which ensures effective excitation of atoms (generally greater than 90%) of approximately 60 elements including some nonmetals. The intense heat excites and in many cases ionizes atoms and finally emission of a photon occurs as electron relaxes (resonance fluorescence). Even though this technique is free of many problems, the excitation and subsequent emission of spectral lines for every element including the added

Ar to facilitate plasma generation present, leads to interferences. This problem is addressed in modern instruments via the use of specialised sequential monochromators.

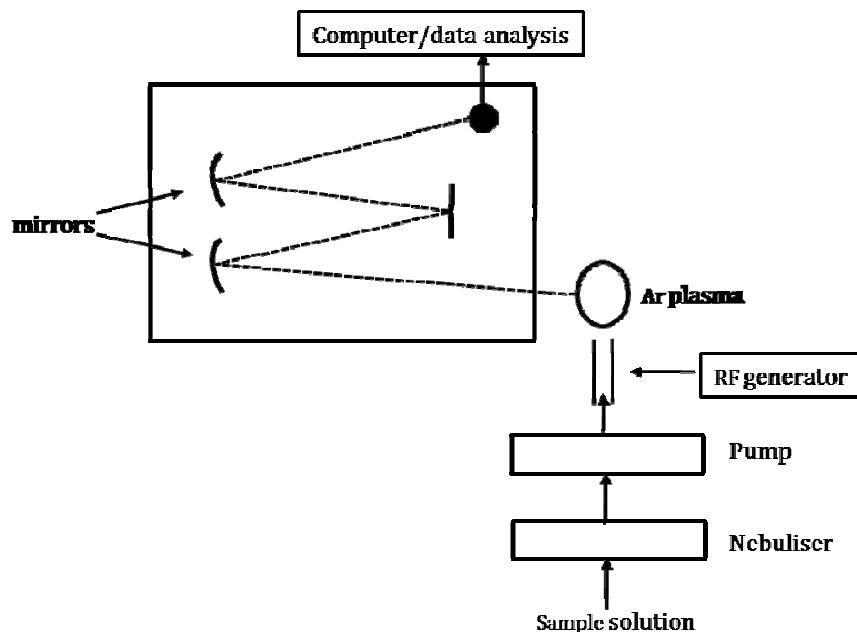


Figure 2. Schematic representation of ICP-AES instrument.

ICP-AES offers high selectivity between elements, high sensitivity, a large dynamic range, lower detection limits, multi-element detection, and fewer matrix interferences. An ICP-AES instrument consists of two parts; the inductively coupled plasma source and the atomic emission spectrometry detector. The clear solution of the sample is introduced to the nebulizer chamber using a peristaltic pump. The flow of sample and Ar gas through the small aperture of the nebulizer creates very small droplets that form a mist of micrometer sized particles in the chamber. Ar flow carries small droplets to the torch leaving larger droplets on the chamber walls and the latter are removed through a drain. In the plasma at temperatures of about 10000K, all the elements including Ar undergo evaporation, atomization, and excitations or ionizations. When these excited or ionized atoms leave the plasma, excited valence electrons relax to the ground state and emit a photon characteristic of the transition. This radiation consisting visible and UV radiation enters the monochromator through a small slit where the wavelengths are separated by gratings and/or prisms and are then captured and measured by a wide variety of detectors. The types and concentrations of the elements present in the sample can then be determined by

isolating the photon wavelengths. The calibration of instrument with commercially available standards helps to perform highly quantitative analysis.

3. Adsorption Isotherm and BET Method for surface area measurement

When a gas or vapour phase is brought into contact with a solid, part of it remains on the outside attached to the surface. In some cases the gas molecules (referred as adsorbate) are attached to the solid surface (referred as adsorbent) by a weak Vander Waals attraction. This type of adsorption known as physisorption (physical adsorption) can be utilized to characterise materials allowing for the determination of specific surface area, pore size distribution and pore volume.

The specific surface area of a powder is determined by measuring the amount of adsorbate gas corresponding to a monomolecular layer on the surface usually at the temperature of liquid nitrogen. The amount of gas adsorbed can be measured by a volumetric or continuous flow procedure. The most common adsorbate used is nitrogen; however, other adsorbates like Ar, CO, CO₂, O₂ are also used in some instances.

In 1938, S. Brunauer, P. H. Emmett, and E. Teller put forward a theory known as Brunauer–Emmett–Teller (BET) theory to explain the physisorption of gas molecules on a solid surface which forms the basis for the technique for the determination of the specific surface area of a material. The theory is based on the following hypotheses:

- (a) Gas molecules physically adsorb on a solid in layers infinitely.
- (b) There is no interaction between each adsorption layer.
- (c) The Langmuir theory can be applied to each layer.
- (d) Uppermost layer is in equilibrium with vapor phase.
- (d) First layer adsorption is governed by the heat of adsorption while heat of condensation can be used for higher layers.

With these assumptions, the following equation known as BET equation is derived.

$$\frac{1}{v\left\{\left(\frac{p_0}{p}\right)-1\right\}} = \left[\frac{c-1}{v_m c}\right] \left(\frac{p}{p_0}\right) + \left(\frac{1}{v_m c}\right),$$

where, p and p_0 are the equilibrium and the saturation pressure of adsorbates at the temperature of adsorption, v is the volume of adsorbed gas, v_m is the monolayer adsorbed gas quantity and c is the BET constant given as

$$c = \exp\left[\frac{(E_1-E_L)}{RT}\right],$$

where E_1 is the heat of adsorption for the first layer, and E_L is that for the second and higher layers and is equal to the heat of liquefaction.

The BET Equation is an adsorption isotherm and a straight line can be plotted (only in the p/p_0 range 0.05-0.35) known as BET plot with the factor $1/v[(p_0/p)-1]$ on the y-axis and p/p_0 on the x-axis. The value of v_m and c can be calculated from the values of slope (A) and Y-intercept (I) using the equations,

$$v_m = 1/(A+I) \text{ and } c = 1 + (A/I)$$

The BET method is widely used for the calculation of surface areas of solids in heterogeneous catalysis where the number of active sites depends on the surface area which in turn related to particle size, particle morphology, surface texturing and porosity.

The total surface area (S_{total}) and the specific surface area (S_{BET}) are then given by

$$S_{\text{total}} = (v_m N s)/V \text{ and } S_{\text{BET}} = S_{\text{total}}/ a,$$

where N is the Avogadro's number, s the adsorption cross section of the adsorbing species, V the molar volume of the adsorbate gas, and a the mass of the solid sample or adsorbent.

The single-point method may be employed directly for a series of powder samples of a given material for which the material constant C is much greater than unity.

4. High resolution Transmission Electron Microscopy (HRTEM)

Transmission electron microscopy uses high energy electrons which are accelerated to nearly the speed of light by applying a voltage of 300 kV to provide morphological, compositional and crystallographic information. When electron beam wavefront passes through a thin-section specimen of a material, electrons undergo scattering. These scattered electrons can be focused into an image or diffraction pattern using a system of electromagnetic lenses. The images can provide a highly magnified view of the structures in micro- and nanosized dimensions and ultimately, in the high resolution mode a direct map of atomic arrangements. The advantage of this technique is that it can provide information in real space (in the imaging mode) and reciprocal space (in the diffraction mode) simultaneously. The diffraction mode (electron diffraction) provides accurate information about the local crystal structure.

When electrons interact with sample, elastic scattering (change in path without loss in energy) and inelastic scattering (loss in energy by interaction with the electrons of the sample atoms) can occur. Electrons which are not scattered contribute positively to the

image, while electrons which are considerably deflected are prevented from doing so by apertures in the optical path. This results in the differences in light intensity (contrast) in the image according to the scattering abilities of areas in the sample. Generally the scattering efficiency increases with the atomic number. This means that heavy metals can form images with good contrast.

HRTEM can provide information about structure at spatial resolutions better than 0.2 nm. Individual atomic layers can be resolved in the case of most of the crystalline inorganic materials, including ceramics, semiconductors, and metals, at least in low-index zones. The possible applications include distribution and structure of defects, interfaces and grain boundaries, nano-crystalline features in amorphous films, small particle analysis in heterogeneous catalysts, sub-micron morphological features, diffusion, and phase transformations.

The image resolution is governed by the electron wavelength which depends on the speed of electrons. The various parts of a modern TEM are an illumination system, condenser lens system, an objective lens system, magnification system, and the data recording system. A set of condenser lens is used to focus the beam on the sample and objective lens collects all the electrons after interacting with the sample and form image of the sample, and determines the limit of image resolution. Finally, a set of intermediate lenses magnify the image and projects them on a phosphorous screen or a charge coupled device (CCD). HRTEM images are obtained when the point resolution of the microscope is sufficiently high and a crystalline sample is oriented along a zone axis. The HRTEM uses both the transmitted and the scattered beams to create an interference image which is actually a phase contrast image. The electron waves coming from the sample at very low angles interfere with itself when travelling through the objective lens. All electrons are finally combined at a point in the image plane. A large objective aperture allowing most of the beams to pass is crucial to obtain lattice images.

HRTEM has been extensively used for analyzing crystal structures and lattice imperfections in various types of materials. It can be used for the characterization of point defects, dislocations, stacking faults, and surface structures.

5. X-ray Absorption Near Edge Structure (XANES)

X rays are ionizing radiation that has sufficient energy to excite a core electron of an atom to an empty state below the ionization threshold or to the continuum which is above the ionization threshold. Different core electrons have distinct binding energies; consequently, if one plots the X-ray absorbance of a specific element as a function of energy of the energy of X-ray radiation, a sudden increase of absorption appears, which corresponds to absorption of the X-ray photon by a specific type of core electron. This gives rise to a so-called absorption edge in the X-ray absorption spectrum due to its vertical appearance. This sharp intense peak is sometimes referred as “white line” because in the past, X-ray absorption spectra were recorded using photographic plates, where strong absorption of certain wavelength after developing negative, appear as a white vertical stripe. Energies of absorption edges in X-ray absorption spectra reveal the identity of the corresponding absorbing elements. The name of the absorption edges are given according to the principle quantum number, n , of the excited electrons K for $n=1$, L for $n=2$, M for $n=3$, etc. The core-electron binding energy increases with increasing atomic number. However the L edge is in fact found to be consists of three distinct edges, named L_1 , L_2 , and L_3 in the order of decreasing energy. L_1 corresponds to excitation of a 2s electron. But the excitation of a 2p electron results in the splitting into two edges as a consequence of the spin-orbit coupling energy of the resulting $2p^5$ configuration. The higher energy of the $2p^5$ excited states is the $2P_{1/2}$ term corresponds to the L_2 edge. The lower energy state corresponds to the $2P_{3/2}$ excited state gives the L_3 edge. Even though the spin-orbit coupling energies of valence electron shells are relatively small, that of core shells can be quite large.

The structure found in the immediate neighborhood of the absorption edge, conventionally within 50 eV of the absorption edge, is referred to as X-ray Absorption Near Edge Structure (XANES) or near-edge x-ray absorption fine structure (NEXAFS). It is an element-specific technique. Moreover the analysis is sensitive to local bonding and it determines the partial density of the empty states of a molecule. XANES directly probes the angular momentum of the unoccupied electronic states which can be bound states or unbound states (continuum), discrete or broad, atomic or molecular. The dipole selection rule for transition determination is:

$$\Delta l = \pm 1, \Delta j = \pm 1, \Delta s = 0.$$

Commonly observed allowed transitions are tabulated below.

Table 4. Spin and orbitally allowed transitions for X-ray absorption.

Initial state	Final state
s	p
p	s, d
d	p, f
f	d, g

The experimental setup simply requires a monochromatically tunable light source and an electron energy analyzer. The XANES principle is based on the determination of the x-ray absorption coefficient μ depending on the photon energy $h\nu$ at a fixed angle of illumination, θ . However, this edge of the absorption coefficient is influenced by the energy of unoccupied electronic levels.

XANES spectra can be used to make qualitative fingerprint-like comparisons. The availability of representative library of reference spectra helps the identification of unknown element using spectral matching. Moreover XANES spectra can be used to determine oxidation state, to deduce three-dimensional structure, and as a probe of electronic structure. The energy of an edge increases as the oxidation state of the absorber increases. The electrostatic model explains this observation as atoms with a higher oxidation state have a higher effective nuclear charge thereby requiring more energetic X-ray for the excitation of a core electron. Another explanation treats the edge features as “continuum resonances”, which involves excitation of a core electron into a high-energy state (above the continuum) that has a finite lifetime. A potential well created by the absorbing and scattering (nearest neighbor) atoms can be considered as an example of this. The energy of the continuum state is directly related with the absorber–scatterer distance as $1/R^2$. Higher oxidation- state metals with shorter bond lengths will have an increase in edge energy.

The X-ray absorption can be measured by measuring X-ray fluorescence or transmittance.

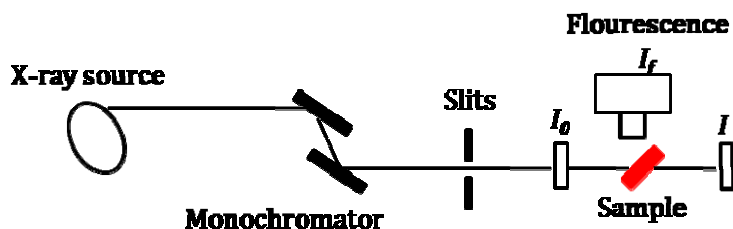


Figure 3. Schematic representation of XANES experimental setup.

The core hole states produced by the ejection of the electrons by X-ray photon are highly excited and one way of relaxation is by X-ray fluorescence where higher energy electron occupies the hole by emitting energy. The intensity of X-ray fluorescence is described by following equation.

$$\mu = (I_f/I_0)$$

The intensity of X-ray fluorescence is directly proportional to the X-ray absorption cross-section of the sample. In practice, energy-resolving solid-state fluorescence detectors are used to selectively distinguish fluorescent X-rays from backscattered ones.

Alternatively the X-ray absorption can be determined from the transmittance if the concentration of the sample is moderate. The intensity ratio of the incoming X-ray and the outgoing X-ray is proportional to the exponential of the absorption coefficient times the thickness. At the absorption edge, a sudden decrease in transmittance occurs. The obtained transmittance spectra are then usually converted to absorption spectra. X-ray Absorption is described by equation

$$\mu = \ln(I_0/I)$$

6 X-ray photoelectron spectroscopy

X-ray Photoelectron Spectroscopy (XPS) or Electron Spectroscopy for Chemical Analysis (ESCA) is based on the principle that when X-rays hit atoms, electrons are ejected. It is a typical surface-sensitive technique as only electrons that are generated in the top few atomic layers (mean free path ~ 1.5 nm) are detected, even though the absorption length of the X-rays is about 100 - 1000 nm. The technique provides quantitative information about the elemental composition of the surface of all kinds of solid material like insulators, conductors, polymers etc. The sample material is irradiated with monoenergetic soft x-rays causing electrons to be ejected. The measurement of kinetic energies of these ejected photoelectrons helps in the identification of the elements in the sample as each element

produces a characteristic set of XPS peaks at characteristic binding energy values. All elements except H and He can be detected. Moreover the relative concentrations of elements can be determined from the photoelectron intensities. The most important advantage of XPS is its ability to obtain information on chemical states from the variations in binding energies, or chemical shifts, of the photoelectron lines. Most modern instruments have detection limits for most of the elements in the parts per thousand ranges. Detection limits of parts per million (ppm) are possible under special conditions such as concentration at top surface or very long collection time.

In XPS, soft X-rays with energies range from 200-2000 eV are used. The development of synchrotron radiation sources has enabled high resolution studies with much wider and more complete energy range (5 - 5000 eV). A sample placed in ultra-high vacuum is irradiated with photons of energy, $h\nu$. Electrons of the atoms on the surface absorb the photons and leave the atom by using some of its energy to overcome the coulomb attraction of the nucleus, reducing its KE by its initial state BE. The kinetic energy of the ejected electron is related to the energy of the X-ray photon as

$$KE = h\nu - BE - \Phi$$

where BE represents the binding energy of the atomic orbital from which the electron ejected and Φ is the spectrometer work function which is an adjustable instrumental correction factor that accounts for the few eV of KE loss of the photoelectron as it becomes absorbed by the instrument's detector. An electron energy analyzer measures the kinetic energy distribution of the emitted photoelectrons and a photoelectron spectrum can thus be recorded.

The number of detected electrons is a measure for the elemental concentration. Atomic concentrations can be obtained by dividing the peak areas by standard sensitivity factors and normalizing to 100%. For bulk materials the surface concentrations can be determined with a 20% inaccuracy. However, in most cases, the surface composition varies as a function of depth, where the signal of an element in a lower layer will be attenuated more strongly than that in the top layer. In such cases either angle-resolved measurements or model calculations are performed to extract quantitative information.

The basic requirements for a XPS experiment are:

1. A fixed-energy radiation source. The most commonly employed X-ray sources are those giving rise to Mg K α radiation ($h\nu = 1253.6$ eV) and Al K α radiation ($h\nu = 1486.6$ eV).
2. An electron energy analyser. This separates the emitted electrons according to their KE, and measures the flux of emitted electrons of a particular energy. The most preferred design is a concentric hemispherical analyser (CHA) where an electric field is applied between two hemispherical surfaces to disperse the electrons according to their KE
3. A high vacuum environment which enables the emitted photoelectrons to be analysed without interference from gas phase collisions. XPS detectors must be operated under ultra-high vacuum (UHV, $P < 10^{-9}$ millibar) conditions in order to count the number of electrons with a minimum of error, as they are kept one meter away from the sample.